Marine Magnetic Survey Modeling:
Custom Geospatial Processing Tools for Visualizing and Assessing Marine Magnetic Surveys for Archaeological Resources

US Department of the Interior
Bureau of Ocean Energy Management
Office of Renewable Energy Programs

BOEM
Bureau of Ocean Energy Management

Marine Magnetic Survey Modeling:
Custom Geospatial Processing Tools for Visualizing and Assessing Marine Magnetic Surveys for Archaeological Resources

Authors

John C. Bright
David Conlin
Sage Wall

US Department of the Interior
Bureau of Ocean Energy Management
Office of Renewable Energy Programs

BOEM
BUREAU OF OCEAN ENERGY MANAGEMENT

DISCLAIMER

REPORT AVAILABILITY

CITATION

Bright, John C., David Conlin, and Sage Wall. 2014. Marine Magnetic Survey Modeling: Custom Geospatial Processing Tools for Visualizing and Assessing Marine Magnetic Surveys for Archaeological Resources. US Dept. of the Interior, Bureau of Ocean Energy Management, Office of Renewable Energy Programs, Herndon, VA. OCS Study BOEM 2014-615. 240 pp.

ABOUT THE COVER

Acknowledgements

Executive Summary

John C. Bright
National Park Service Submerged Resources Center

In March of 2013, the Bureau of Ocean Energy Management's Office of Renewable Energy Programs (BOEM OREP) contracted the National Park Service's Submerged Resources Center (NPS SRC) to develop a series of custom-scripted GIS tools to visualize and assess magnetic remote sensing data submitted to the agency by developers. This Inter-Agency Agreement was part of an ongoing collaboration between BOEM's OREP and the NPS SRC, originating in 2012 during a BOEM-led research initiative within the Massachusetts Wind Energy Area (MA WEA). The results of this work, the *Collaborative Archaeological Investigations within the Massachusetts Wind Energy Area*, were published by the Department of the Interior in October of 2013 and included the NPS SRC's comments on BOEM's current *Guidelines for Providing Geological and Geophysical, Hazards, and Archaeological Information Pursuant to 30 CFR Part 585*. Specifically, the NPS SRC identified several areas of potential improvement to the agencies guidelines for marine magnetic data collection and assessment.

These recommendations became the basis for a second collaboration focused specifically on the assessment of magnetic data sets. At the core of the SRC's recommendations was the need for BOEM to independently and quantitatively verify magnetic data submitted to the agency to ensure that the bureau is making an appropriate effort to protect submerged archaeological resources. Beyond simply visualizing acquired magnetic data, however, the tools needed to quantitatively assess magnetic datasets did not exist. Thus, BOEM and NPS partnered to develop a custom set of geospatial processing functions. Starting with a theoretical mathematical model, the team tested, validated, and refined this algorithm, which was then integrated into a series of custom-scripted ArcGIS tools. Magnetic data collected to test the mathematical model was then used to test the scripted tools. The tests produced an empirically verified and field-tested suite of geoprocessing functions that automate all data processing tasks associated with marine magnetic survey and produce statistics on the coverage of a given magnetic datasets in terms of detection thresholds across a range of ferromagnetic masses.

The following report outlines the mathematical algorithm developed to drive these processing functions, as well as the methodology and results from field testing operations. Additionally, each individual GIS tool is presented and described in terms of both its theoretical basis and practical applications. Attached in appendices are the release notes and operating instructions for the toolbox.

Contents

List of Figures

List of Tables

Abbreviations and Acronyms

ASMIS	Archeological Sites Management Information System (NPS)
B	Magnetic Density Flux
B_e	Earth's Ambient Magnetic Field, as sampled at a single time/location
BISC	Biscayne National Park
BOEM OREP	Bureau of Ocean Energy Management, Office of Renewable Energy Programs
CGS	Centimeter Gram Second System of Units
Δ	delta (change)
DGPS	Differential Global Positioning System
ESRI	Environmental Systems Research Institute (makers of ArcGIS)
FKNMS	Florida Keys National Marine Sanctuary
G	Gauss, unit of Magnetic Density Flux
γ	Gamma, unit of Magnetic Density Flux (10^5 G)
GGARCH	Guidelines for Providing Geological and Geophysical, Hazards, and Archaeological Information (BOEM)
GIS	Geographic Information System
GPS	Global Positioning System
HMS	His/Her Majesty's Ship (Royal Navy ship name prefix)
IAA	Inter-Agency Agreement
k	Volumetric Magnetic Susceptibility (unitless)
M	Magnetic Moment (emu)
σ	Magnetic Moment per Unit Mass ($\frac{emu}{g}$)
χ	Mass-Specific Magnetic Susceptibility ($\frac{cm^3}{g}$)
MA WEA	Massachusetts Wind Energy Area
NAD 83	North American Data, 1983
NPS SRC	National Park Service, Submerged Resources Center
NOAA NGDC	National Oceanic and Atmospheric Administration, National Geophysical Data Center
r	Distance (in magnetic modeling equation)
RSD	Relative Standard Deviation
SI	International System of Units
SRC	National Park Service, Submerged Resources Center
TIN	Triangulated Irregular Network
UTM	Universal Transverse Mercator
w	Mass (in magnetic modeling equation)

CHAPTER 1

INTRODUCTION

As part of an ongoing collaboration between the Bureau of Ocean Energy Management (BOEM) Office of Renewable Energy Programs (OREP) and the National Park Service Submerged Resources Center (NPS SRC), the two agencies embarked upon the testing and development of a marine magnetic survey modeling process subsequent to work completed during the 2012 Massachusetts Wind Energy Area (MA WEA) Baseline Survey (see BOEM 2013). During the Baseline Survey, SRC archaeologists were tasked with reviewing the requirements for Archaeological Resources Assessment Reports outlined in BOEM's *Guidelines for Providing Geological and Geophysical, Hazards, and Archaeological Information [GGARCH] Pursuant to 30 CFR Part 585* (BOEM 2012), including the use of magnetometers to detect archaeological resources. Internally, the SRC had been exploring ways to refine magnetic data collection, processing, and reporting for several decades. Collaboration with BOEM, therefore, offered an ideal means to effectively leverage time and resources towards mutually beneficial research.

Included in the final MA WEA report (BOEM 2013:175-178) are the NPS SRC's recommendations to BOEM involving magnetic survey design, data processing, data reporting, and survey confidence assessment. Many of these recommendations centered on verification and evaluation of magnetic datasets submitted by developers. Under the current version of GGARCH, applicants were only required to provide magnetic maps and lists of magnetic anomalies, yet it was demonstrated by NPS archaeologists how easily magnetic data can be distorted—intentionally or accidentally—throughout the acquisition and visualization process. To minimize the likelihood of this happening, the SRC recommended that BOEM independently verify all or portions of the magnetic data submitted to the agency. This would involve the agency re-processing raw magnetic data to confirm anomalies within the data, but also running the data through a quality assurance/quality control filter to determine levels of coverage throughout the survey area.

Concurrently, SRC also began development of a mathematical magnetic modeling algorithm to serve as the basis for several quantitative data assessment tools. This model, based on the physics of induced magnetism, described observed anomaly amplitude as a function of distance between the magnetic sensor and a mass of ferromagnetic material of a given magnetic moment (a metric of magnetic field strength). This mathematical relationship allows archaeologists to tailor survey designs to ensure hypothetical detection of specific objects, as well as to review a data set post-acquisition to assess varying thresholds of detection and coverage. In other words, the model informs survey design and dataset review in terms of theoretically detectable and undetectable masses, used as proxy for certain material culture items, on the basis of data point density, sensor altitude, and the presumed strength of an object's magnetic field.

At the conclusion of the 2012 Baseline Survey, however, these processing tools and model were only developed to the extent necessary to provide recommendations to GGARCH. They were not sufficiently developed, however, for either BOEM or NPS to actually implement them in an

operational capacity. With this specific goal in mind, a second collaboration was formalized under Intra-Agency Agreement (IAA) M13PG00004 in March, 2013.

To meet this objective, the remaining work was organized within the IAA contract as three separate phases. The first was to merge all the geospatial processing tools used to visualize and assess magnetic data into an automated, custom format compatible with the ArcGIS software package. Many of these processes, however, were derived from the theoretical model proposed by the SRC. When the IAA was formalized, this mathematical modeling algorithm was only developed to the extent that it delivered hypothetical results. Specifically, the quantity used as 'M' value of the modeling equation—the variable representing the magnetic moment, or magnetic field strength of an object—was estimated based upon literature review (see Breiner 1999a, 1999b). Empirical values of magnetic moment were needed for the model to be of any practicable use. To this end, phase 2 tasks of the IAA established the objectives of a field testing protocol (see Bright 2012).

The main objective of the IAA was the development of a customized geospatial processing suite within the *ArcGIS* software package. At the start of the IAA, the model was integrated via spreadsheet, allowing for hypothetical distances, masses, and gamma values to be input and manipulated. Since actual magnetic data could not be processed by the spreadsheet—it only modeled one set of parameters at a time—it offered very little utility for assessing an actual survey. Thus, phase 1 tasks were established to facilitate an advanced development of the modeling algorithm into a custom-programmed *ArcGIS* Python toolbox. This would integrate the mathematics and modeling developed by the SRC with existing GIS processing functions in *ArcToolbox*. The result was a toolbox containing three individual tools that automated the creation of data products necessary to visualize and assess magnetic data.

This report summarizes all of the work conducted under the auspices of IAA M13PG00004. In so doing, this report fulfills a portion of the final task: phase 3 tasks, Reporting Results. This report is accompanied by a completed *ArcGIS* Python Toolbox, and culminates a year's worth of work including theoretical research, field testing, and software programming. In addition to this report, both BOEM OREP and NPS SRC are planning a series of peer-reviewed publications and professional presentations.

Chapter 2 details the theoretical basis for the modeling algorithm and its integration into the geospatial processing tools used in the Python Toolbox. The methodology, results, and conclusions from the field testing operations are discussed in Chapter 3. Chapter 4 provides a comprehensive overview of the Python Toolbox and its components. This includes the parameters of their operation, limitations, assumptions, and applications to the objective of assessing magnetic datasets. Release notes and a user's guide for the toolbox are included as appendices.

CHAPTER 2

THEORY: THE CHALLENGES OF MAGNETIC SURVEY

Magnetic remote sensing for submerged cultural material is an essential tool utilized by underwater archaeologists. Many objects that would be undetectable with conventional acoustic survey equipment—ferrous materials embedded in or below the seabed, or those located on the surface amidst geological formations with high relief—are easily located by a proper magnetic survey. Many maritime cultural objects, furthermore, contain large amounts of ferromagnetic material; items such as iron cannons, naval ordnance, iron fasteners and rigging from sailing ships, and iron or steel hull plating. These materials exhibit a unique induced magnetic field, which distinguishes them, generally, from other forms of natural magnetic anomalies. Specifically, ferromagnetic cultural materials produce a high-intensity, short-duration disturbance in the earth's ambient magnetic field in contrast to relatively long duration geological or solar-induced variations. As a result, magnetic remote sensing is a highly efficient means to detect specific classes of cultural materials with a proper survey design.

Despite the inherent utility of magnetic survey, however, many factors constrain the effectiveness of magnetic systems. Though an object's size—or, more properly, the mass of magnetic material—and magnetic moment remain fairly constant, the distance between the object and the magnetic sensor drastically affects the object's detectability. As these are well defined interactions based on physics, they are quantifiable variables that can be mitigated, at least in theory, through proper survey design and execution. In essence the surveyor accounts for these variables and designs the survey to ensure detectability of targeted objects (see Figure 2-1). Nevertheless, there is little consensus among archaeologists as to what constitutes an effective survey design. After an extensive review of magnetic survey projects, Camidge et al. (2010:23) noted "…it is apparent that certain important aspects of the survey methodologies, particularly fish altitude and run lines spacing, are not always suitably designed for archaeological appraisals."

Another factor to consider is sampling rate, or how often the sensor records a magnetic reading. Commonly used types of magnetic sensors, Overhauser or cesium vapor, are capable of sampling rates up to 10 Hz (10 samples per second), but can be adjusted to sample at lower rates. In combination with vessel speed, sampling rates determine data point density and the spatial distribution of sampling points. At equal sampling rates, faster tow speeds reduce data point density. At equal tow speeds, a lower sampling rate reduces data point density, and vice versa in both cases. Along a given survey line, this density impacts both the degree to which an object is detectable and the smallest possibly detectable object (Camidge et al. 2009:25-27). In practice, operational efficiency tends to favor faster survey speeds (5-10 kts), requiring higher sampling rates to maintain data point density.
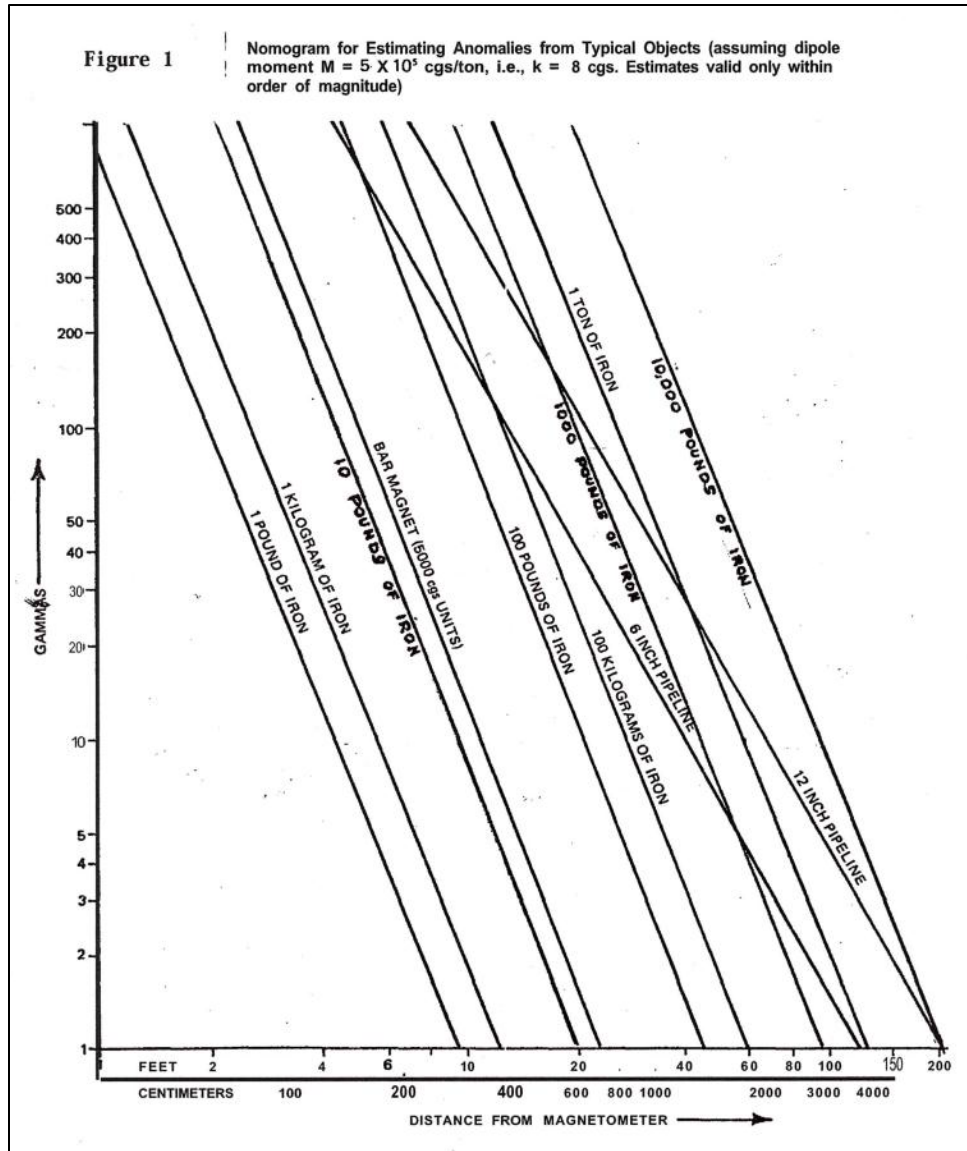
Figure 2-1. Magnetic intensity prediction graph for pure iron (Source: Breiner 1999b:9). The surveyor would use this graph to approximate the amount of distance from a given object necessary to produce the desired magnetic density flux necessary to detect such an object within a survey area.

In terms of the actual spatial distribution of points, consider the following tables (Table 2-1 and Table 2-2) of values for varying survey speeds, sampling rates, and resulting data point density, divided into two types: spatial data point density—measured as meters/point, or the horizontal distance between sequential points—and coverage data point density—the number of samples taken per meter. There is no optimal data point density. Rather, "…data rate and tow speed need to be considered together along with minimum target ferromagnetic mass to be detected to arrive at suitable combination of data rate and tow speed" (Camidge et al. 2009:17). To detect a flux, the sensor must collect multiple samples within the area of an object's magnetic field; otherwise the data will be insufficient to differentiate from the ambient field of the earth. Spatial data point density along a single survey trackline shows the distance between sequential data points, and

thus the minimum distance required to obtain multiple samples; a proxy for the size of the magnetic field a given sampling density could detect.

Table 2-1
Spatial data point density (meters between consecutive points) as a function of sampling rate and survey speed.

Sampling Rate (Hz) Survey Speed (kts):	*10*	*5*	*1*	*.5*
10	.514	1.03	5.14	10.3
7	.360	.720	3.60	7.20
5	.257	.514	2.57	5.14
3	.154	.308	1.54	3.08
1	.051	.103	.514	1.03

The notion that data point density directly impacts the minimum size of the detectable objects only applies directly beneath a survey line, however. In a marine survey block, the space between adjacent survey lines has a data point density of zero. Within these 'no data' areas, information about magnetism is instead determined through interpolation to the nearest sample points. In theory, therefore, data point density will reach a level where increased density adds little to the mathematical validity of interpolation between lines. Surveyors can reduce this effect by decreasing line spacing, but are then faced with time, cost, and efficiency issues. Lacking a specific reference to a mathematically valid limit, the present study recommends using a coverage density of approximately two points per meter; Table 2-2 has highlighted the corresponding parameters in gray.

Table 2-2
Coverage data point density (points/meter) as a function of sampling rate and survey speed. Those highlighted in gray represent parameters yielding approximately 2 data points per meter.

Sampling Rate (Hz) Survey Speed (kts):	*10*	*5*	*1*	*.5*
10	1.94	.973	.195	.097
7	2.78	1.38	.278	.139
5	3.89	1.95	.389	.195
3	6.49	3.25	.649	.325
1	19.5	9.73	1.95	.973

In addition to design parameters and data point density, other factors also impact the effectiveness of a magnetic survey. Weather, ocean currents, water depth, and boat handling influence the position and speed of the magnetic sensor and the survey vessel, resulting in deviations from planned survey parameters. A given survey design, no matter how well planned, is never implemented with complete fidelity. Deviations from planned lines and variations in sensor altitude introduce coverage gaps in the survey area which, if unaccounted for in analysis, negate the ability of the surveyor to assess the efficacy of a given survey operation with confidence.

Beyond operational factors—survey design, sensor altitude, and data point density—the efficacy of magnetic survey is also influenced by the environment of the survey area, specifically the non-archaeological artifacts which appear in the data. These include geological variations, asymmetry in Earth's magnetic field, and constant solar-induced changes. The former can vary greatly, from areas of relatively 'quiet' geology to areas of great heterogeneity (see Hrvoic and Pozza 2004:4-5), which easily obscure the signal produced by small cultural objects. The inherent asymmetry of Earth's magnetic field entails latitude-dependent changes in the strength of the ambient magnetic field. Thus, two identical objects would yield different signatures in different latitudes around the globe (Breiner 1999a:5-6; Hrvoic and Pozza 2004:3). Finally, solar variations in ambient magnetism occur in many forms. The variation of greatest concern is diurnal change, the result of constant aspect changes as Earth orbits the sun, changing the angle at which charged particles emitted by the sun impact Earth's atmosphere (Breiner 1999a:6). This affects a dataset by constantly increasing or decreasing the 'background' magnetic value. Diurnal variation makes visualizing a single large dataset collected over many hours difficult, and it makes coherently merging multiple datasets collected on different days or on a regional level nearly impossible without additional filtering.

2.1 MAGNETIC DATA PROCESSING

Unlike survey design errors, which are mitigated through competent execution of the survey plan and re-acquisition as necessary, non-archaeological ferrous materials affecting the data can only be mitigated through geospatial and/or mathematical processing. Compared to acoustic sensing, magnetic survey is truly *remote* in that magnetic data does not automatically provide an intuitive, visual output of the area being scanned. Rather, magnetic data can only be visualized as the result of a series of processing functions. The most basic of these processes—interpolation and vector contouring—map the sampled values as they are collected and therefore indicate both archaeological and non-archaeological materials within the data. Even where these variations are slight, precise interpretation of discrete magnetic signatures remains challenging. Archaeological sites, furthermore, are often assemblages of items, thus "…the total-magnetic-field anomalies we measure are often complex in shape, even for the simplest point-source dipole" (Hrvoic and Pozza 2004:3). In areas where geological and/or diurnal variation is great, archaeological anomalies may be completely obscured.

Survey design and proper modeling are the precursors of an effective magnetic survey. Once collected, the manner in which the data is processed and visualized is equally important to ensuring maximum coverage of an area, in so much as data acquisition parameters allow. All marine magnetometers have displays in real time. During data acquisition, this typically shows as a graphical trace across a user interface (Figure 2-2), yet it is nearly impossible from this view to visualize the entirety of the survey area. Recorded as discrete sample points (Figure 2-3), several geospatial processing tasks are required to generate a visual output which the user can assess for anomalies potentially associated with archaeological materials.

Figure 2-2. Real time graphical data trace of raw gamma values versus distance along a trackline.

Figure 2-3. Raw magnetic data in a tabular format.

Multiple data processing methodologies exist. The choice of methodology depends mainly on data format and available software, as well as user preference for certain processing operations. Generally, the following workflow applies to magnetic data processing:

1. Data acquisition
2. Filtering (within acquisition program) and exporting tabular data table
3. Input of table into geospatial processing program

4. Conversion of data table to point features
5. Interpolation of continuous surface from sampled magnetic values
6. Generation of isolines based on user-specified interval (contouring)
7. Identification and tagging of anomalies

This workflow does not encompass all possible applications of the numerous commercially available acquisition/processing programs (some do both), or all possible filtering or visualization options. Nevertheless, it captures the essence of magnetic data processing: from a tabular format it must be interpolated into a continuous surface for the user to visualize the data throughout the surveyed area.

2.1.1 DATA INTERPOLATION METHODS

Archaeologists deploy magnetometers through a pre-determined survey sampling matrix with the intention of locating ferromagnetic objects. The goal of the visualization process, therefore, is to represent the data in such a manner as to facilitate this interpretation. The magnetic sampling matrix, however, is not evenly distributed throughout the extent of the survey area. Instead, data collection points are clustered along the axis of parallel survey lines. Space between adjacent lines, therefore, has no actual data. Thus, to visualize a continuous surface throughout the survey area, values for no-data areas must be estimated as a function of the data values along the survey lines. This process is called interpolation, or "…the procedure of predicting the value of attributes at unsampled sites from measurements made at point locations within the same area or region" (Burrough and McDonnell 1998:98).

Many interpolation functions, such as kriging discussed in this section, operate based upon 'gridding' logic. In practice, the entire survey area is parsed into a grid of uniform cell size where the value of each cell is calculated via a geospatial/mathematical relationship to proximate sample points. Generally this results in the production of a raster data product. Though there are several advantages to this approach, the nature of gridding results in a loss of fidelity to the actual data points as the process requires averaging and estimating. Ultimately, the upper and lower extents of the data range are lost. Alternatively, if the magnetic data is treated as elevation values, it can instead be interpolated by building a triangular irregular network, or TIN (Figure 2-4).
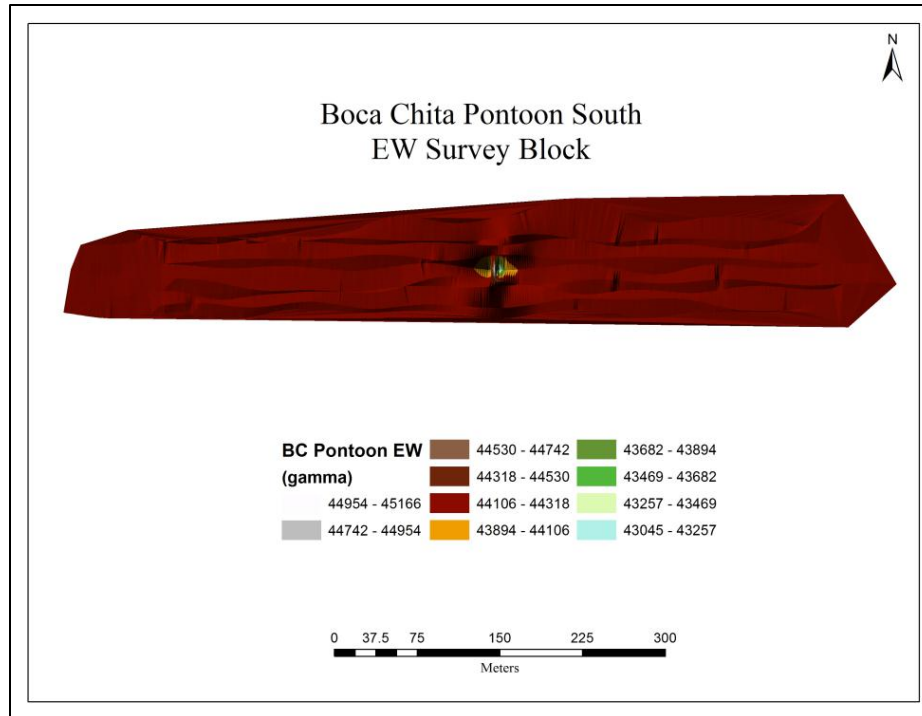
Figure 2-4. A TIN model of raw magnetic data.

As explained by Burrough and McDonnell (1998:124):

> A TIN is a terrain model that uses a sheet of continuous, connected triangular facets based on a Delaunay triangulation of irregularly spaced nodes or observation points [i.e. the magnetic samples]. Unlike altitude matrices, the TIN allows extra information to be gathered in areas of complex relief without the need for huge amounts of redundant data to be gathered from areas of simple relief.

Since the actual sample points are integrated as nodes to the TIN, the value of these points are not diminished through the spatial averaging associated with the gridding functions of kriging. Also, where large areas of similar values are present, they are integrated into larger triangles, reducing processing time and memory requirements (whereas the gridding functions would have to define cells throughout such areas). This reduces data redundancy in uniform areas while allowing the model to "adapt to areas of differing relief complexity" (Burrough and McDonnell 1998:122) where large magnetic flux is present.

For low-noise data—where "noise" is informally defined as false or irrelevant information in the collected data, e.g. fluctuations in the sensor reading caused by variations in the power supply or pseudo cultural factors (noise induced by the boat itself)—TIN modeling is an ideal interpolation method. TIN modeling requires considerably less processing time (during testing a 90,000 data point set took 113 minutes to process via kriging, while a TIN modeling function executed on the same dataset took only 31 seconds) and produces smaller files. Another advantage of TIN modeling is the ability to visualize the data three-dimensionally (Figure 2-5). For these reasons, the present study integrated TIN modeling as the primary visualization method within the set of python tools described in a later section.
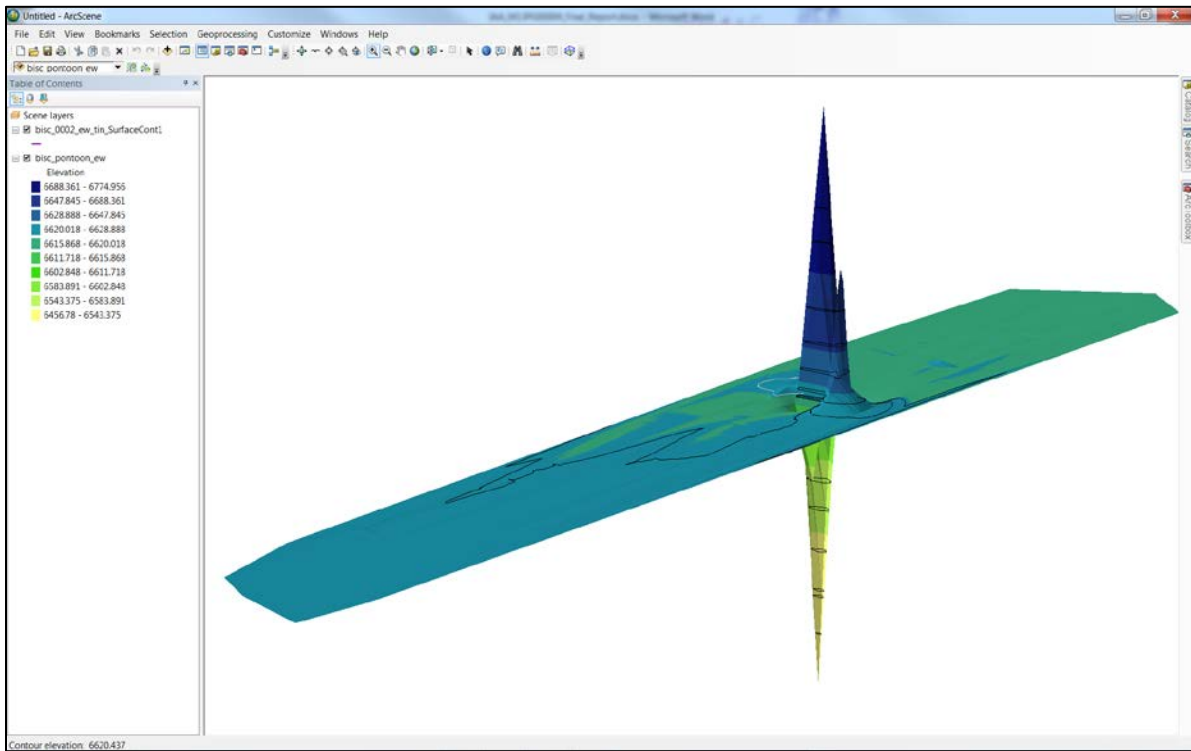
Figure 2-5. An ArcScene 3D rendering of the TIN model from Boca Chita Pontoon South EW survey block.

In certain instances, such as noisy data, TIN modeling might not be the ideal processing method (see Figure 2-6). Instead, to mathematically smooth away noise, a gridding interpolation may be preferable. The method most often employed by archaeologists to visualize magnetic survey data is kriging, a "…variant of the basic linear regression estimator." (Bohling 2005:4). The advantage of kriging over other gridding methods is it "…helps to compensate for the effects of data clustering, assigning individual points within a cluster less weight than isolated data points (or treating clusters more like single points)" (Bohling 2005:3). Thus, estimated values in no-data areas—the space between survey lines—are assigned values as a distance-weighted function of the values recorded in proximate data points. Inherent in this process of averaging data points over distance—which results in an underestimation of high-range values and overestimation of low-range values—is a slight smoothing effect, for example the difference between Figure 2-6 and Figure 2-7. Magnetic anomalies are much more apparent to the user in the latter map.
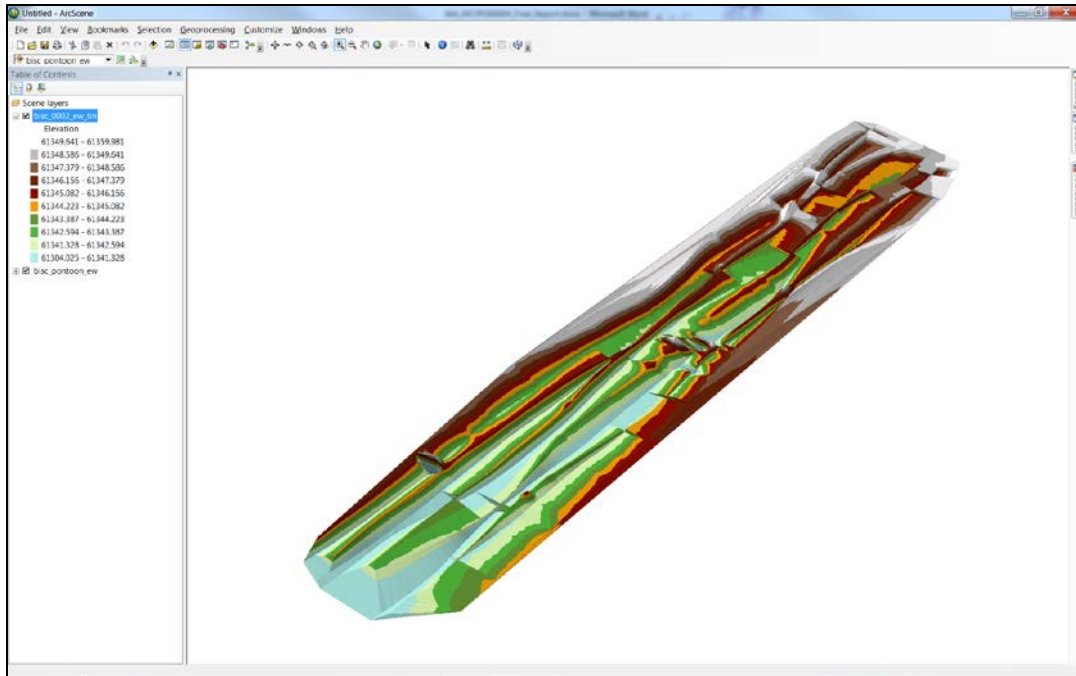
Figure 2-6. TIN model of a dataset containing ~3 γ background noise; any magnetic flux is difficult to identify.
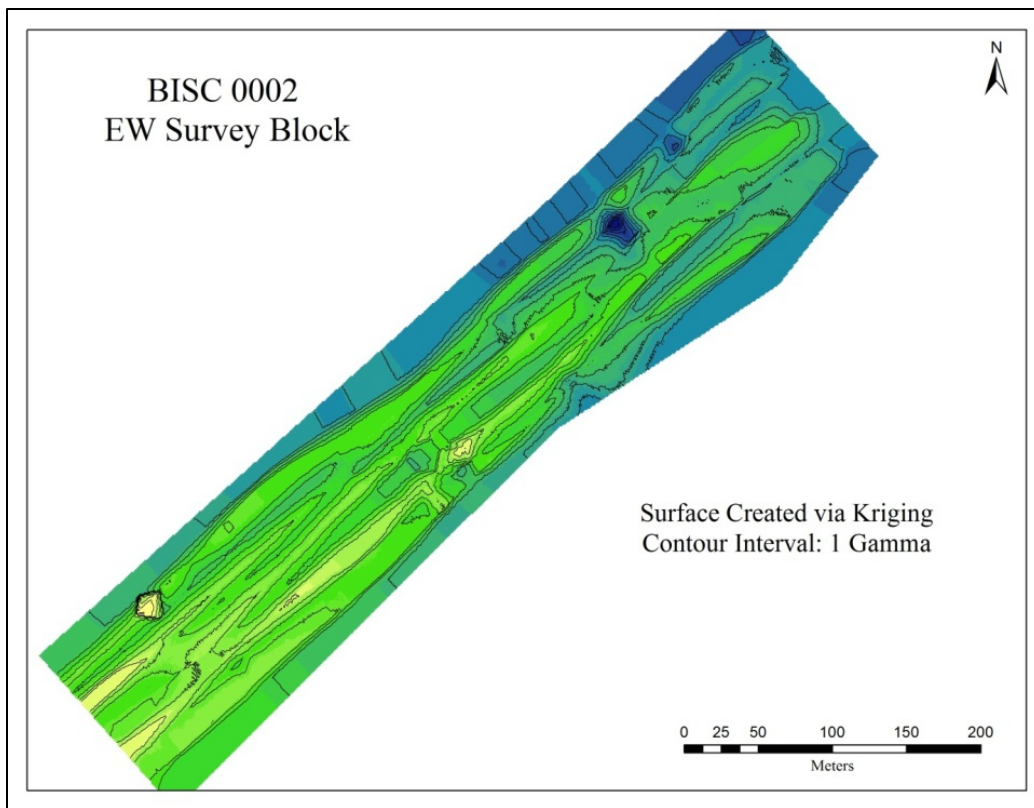
Figure 2-7. Magnetic map generated via kriging.

Both TIN and kriging interpolations display the complete data range of an acquired dataset. As was previously discussed, several sources of noise can affect the data from a survey. Noise, in turn, can obscure the signal of ferromagnetic cultural materials. Thus, archaeologists also employ several filtering methods to reduce the impact of noise on the visualization and interpretation of data. These methods vary, depending upon the type of noise they are intended to cancel. One method is the use of a base-station to record the diurnal changes over the course of a survey project. This entails using two magnetometers, one for survey, and one as a base-station which records the background magnetic field while remaining stationary. Ideally, once a day's survey is complete the data records from each are time-synced and the background diurnal values recorded at the base station are subtracted from the actual survey data, thus eliminating the diurnal variations.

Though this is a fairly straightforward approach to minimize diurnal variability, it does not address the issue of geological variations throughout the extent of a given survey area and the use of a stationary base-station may not be possible in an offshore survey. Perhaps the simplest solution to environmental noise is the use of a gradiometer. Widely available commercially,

> a total-field gradiometer is a specialized type of magnetometer that measures a first spatial derivative, or gradient, of the total magnetic field. This simplest gradiometer consists of two sensors separated by a fixed distance that simultaneously measure the total magnetic field. Difference in intensity is divided by distance between the sensors, giving a linear estimate of the gradient (Hrvoic and Pozza 2004:3).

In essence, this instrument maps the rate of change within the ambient magnetic field as opposed to passively sampling the ambient field strength. This offers several advantages, including the ability to:

> …resolve composite or complex anomalies into their individual constituents and on the same basis automatically remove the regional magnetic gradient [i.e. geological variations] to better define the shallower anomalies assumed to be of interest. Also, the magnetic time variations [i.e. diurnal variations]…are effectively removed (Breiner 1999a:49).

Though the gradiometer may appear to be a panacea for environmental noise, the systems are too complex and cost prohibitive for most operators. Instead, many surveyors elect to use mathematical filtering processes upon data acquired by a single magnetometer, yielding a similar result to data acquired by gradiometer.

2.1.2 MAGNETIC GRADIENT PROCESSING

A technique referred to as gradient processing was developed by the Sandia Research Corporation and NPS SRC in the early 1990s based upon experience gained through years of magnetic surveying within US National Parks. Throughout their surveys, NPS archaeologists observed the physical principle that wherever a magnetic flux changes most dramatically (i.e. where the gradient or rate of change is steepest) is most likely the source of the magnetic field and, therefore, where the physical object responsible for the magnetic anomaly is located. Implementing a mathematical technique to solve for rates of change, therefore, allowed NPS

archaeologists to filter and re-visualize raw magnetic data (Figure 2-8). The resulting data product cancels out nearly every magnetic signal except for short duration, high intensity flux—those most likely associated with cultural objects—which facilitates more effective location, interpretation and allows regional datasets otherwise mired by geological and diurnal variations to be merged and visualized as a whole, even when they were collected days, weeks, or years apart.
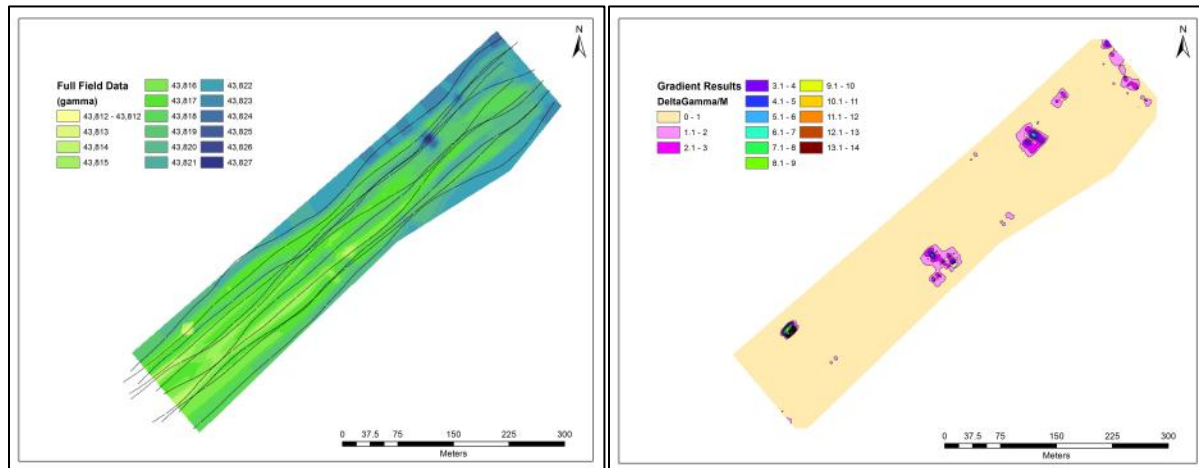
Figure 2-8. One survey block visualized as full-field raw data (left), and visualized following a gradient filter (right).

Gradient processing applies a mathematical function which cancels out long-range spatial and temporal variability within the data set, filtering geological and diurnal variation to an extent that is impossible with basic interpolation. In this way, gradient processing offers an efficient and simple method to filter raw magnetic data. In particular:

> The basis of gradient processing of magnetometer data is to look for changes in the magnetic field over short distances. Because of various geologies, the magnetic field can change significantly over the span of one survey block. Gradient processing can, [therefore], be described as a selective filter (Shope 2011:1).

Mathematically, two types of gradient processes are possible: first- and second-order derivatives of the magnetic field. In a basic form, this relationship is described as follows (Shope 2011:1):

$$Gradient_1 = \frac{\partial H}{\partial r}$$
$$Gradient_2 = \frac{\partial^2 H}{\partial r^2}$$

where ∂H represents the partial derivative of magnetic field intensity (H) with respect to the derivative of distance (∂r). The first-order gradient calculates the rate of magnetic change, i.e. the velocity of change in the measured magnetic intensity versus distance. The second-order gradient uses the second-order derivative to calculate the rate of change in the gradient, i.e., acceleration, as a function of distance (Shope 2011).

Yet, visualizing derivatives as a continuous surface is not mathematically valid. First- and second-order derivatives represent the rates of change between sequential data points; they are linear in nature, a representation of the rate of change over distances, similar to digital signal display. These values are not discrete amounts taken from the wider area, but are instead directionally-dependent linear values. In this way, it is mathematically more similar to time series data than continuous phenomena. Thus, these values cannot be used to estimate values in no-data areas via the spatial averaging utilized by interpolation. To visualize the rate of change, therefore, a more arithmetic approach was conceived. Instead of using derivatives, the NPS used the absolute values derived from a small neighborhood calculation of the rate of change ($\Delta\gamma$) over a given distance (m). With a series of points:

$$N_1 \ \ N_2 \ \ N_3 \ \ N_4 \ \ N_5$$

where N is a sample point containing a geographical position (x,y) and a magnetic field reading (γ), a pseudo-gradient is calculated as follows:

$$\text{Gradient }_{(N1)} = \left| \frac{(N_{2\gamma} - N_{1\gamma})}{\sqrt[2]{(N_{2x} - N_{1x})^2 + (N_{2y} - N_{1y})^2}} \right|$$

where the gradient value for a given point is determined by the absolute value of the change in gamma between the first and second points $(N_{2\gamma} - N_{1\gamma})$ is divided by the change in distance between the two points $\left(\sqrt[2]{(N_{2x} - N_{1x})^2 + (N_{2y} - N_{1y})^2} \right)$, which will be in meters if the X and Y values are UTM coordinates. The resulting value is the change in magnetic intensity per unit distance, generally $\Delta\gamma$/m (change in gamma per meter). Since these values are not linear derivatives, they can be interpolated into a continuous surface.

When dealing with smaller intensity changes, however, this equation becomes problematic. Specifically, if the amount of magnetic change is small relative to the corresponding change in distance (for example, 0.1 γ over 2 m), the process of division yields very slight amounts (in the above case, .05 $\Delta\gamma$/m). As a practical matter, if the measured change in magnetic intensity from one point to another is very slight, there is a risk that the observed change will be less than the instrument signal noise and therefore unusable for analytical purposes.

An alternative mathematical approach, therefore, uses the above equation to solve for $\Delta\gamma$/m, then multiplies all values by the average distance between points, restoring any signal lost by division and converting the units to $\Delta\gamma$. Taken a step further, the process can solve for the rate of change between two points, assigning a new gradient point between two sample points. When executed as such, the gradient process creates a second dataset based upon the raw magnetic values representing the rate of magnetic change throughout the survey area.

All of the processing functions described so far—interpolation with TIN modeling and kriging, as well as gradient processing—are integral to visualizing magnetic data and enabling archaeologists to achieve the primary goal of magnetic survey: location of cultural objects. The efficacy of a survey—the degree to which archaeological materials are actually found—is in part based upon the survey design. Horizontal line spacing, sensor altitude, sampling rate, and vessel speed (or sensor speed, rather) are variables to be manipulated based upon a general level of

desired survey coverage. For example, at the outset of a project a surveyor may reference the nomogram produced by Breiner (1999b:9) for iron detectability. Based upon this information, the surveyor could then determine the appropriate line spacing, altitude, etc.

After the survey is completed, data processed, and anomalies investigated, however, there is no objective means to express the actual coverage or quality of a survey. The survey design parameters are established based upon a hypothetical detection level (itself vague), and therefore cannot be used as a proxy for actual coverage. Operational reality, furthermore, is that no survey is ever executed with 100 percent fidelity to the planning parameters. Thus, surveyors need a means to account for deviations and to assess their data post-acquisition to determine coverage and confidence before making any statement about the efficacy of a given magnetic survey for archaeological resources.

2.2 ASSESSING ACTUAL SURVEY COVERAGE

Coverage, in the sense of magnetic data, is a dualistic term referring to the smallest object which could have been detected, and (more importantly) the largest object which could have been missed. Unlike sonar, where a particular frequency and swath width are set and lines planned to ensure adequate overlap, magnetic systems have no inherent range. Instead, the magnetic sensor passively reads the ambient magnetic field at the time and place of the sample. Ferromagnetic objects create a discrete flux in Earth's ambient field, directly proportional to the mass and make-up of the magnetic material. Thus, if the sensor is too far away from an object's magnetic field, it simply will not be detected.

2.2.1 INDUCED AND REMNANT MAGNETISM

The relationship between mass and detectability is theoretically quantifiable—where such quantification rests upon a series of assumptions about the nature of the objects and their magnetic fields. Ultimately, these relationships are described by physical models which are (necessarily) simplifications of the actual behavior of complex ferromagnetic objects. Generally, objects are magnetized in two distinct ways. To be more precise, small objects manifest two types of magnetism to varying degrees: induced and remnant. Induced magnetization is described as:

> …the combined effect of a magnetic property of the material (permeability), the earth's magnetic field, and the shape and orientation of the object in the earth's magnetic field. If the magnetic permeability (or a related property called magnetic susceptibility) is very high, the material is described as being ferromagnetic….these factors cause the material to act as a magnet in the presence of the earth's magnetic field; [which is] a stronger magnet (Breiner 1999b:3).

A susceptible object, when in the presence of Earth's magnetic field, will take on a magnetic field of its own. The amount of susceptibility varies between materials. Furthermore, "…the shape and orientation of an object also tends to enhance induced magnetism; the longer the object and more nearly parallel to earth's magnetic field, the stronger the magnet" (Breiner 1999b:3).

Remnant, or permanent magnetization, on the other hand, exists independent of any applied magnetic field. Instead, it is a product of the metallurgical history of a material. Mainly this involves the heat of the object's formation and the alignment and intensity of Earth's magnetic field at this exact time, which could be hundreds or thousands of years ago for archaeological materials (for example the casting of an iron cannon). Sufficient heat applied after the formation of a material can also modify its remnant magnetization. The magnitude of remnant magnetization, therefore, is unique for any given substance and very difficult, if not impossible, to predict since many of its determinate factors are simply unknown. Nevertheless, permanent magnetization can exert a magnetic force which will interact with Earth's ambient magnetic field. Depending upon the magnitude of permanent magnetism, and its orientation with respect to Earth's fields, these interactions can neutral, constructive, or destructive.

2.2.2 MATHEMATICAL MODELS OF INDUCED MAGNETISM

Since permanent magnetism cannot adequately be accounted for in unknown objects, the most reliable way to predict magnetic force is to characterize materials based upon their induced magnetic properties. Such a prediction assumes the object is "a concentrated mass of iron [or other ferromagnetic substance], all of whose dimensions are shorter than its distance to the magnetometer [and therefore] behave as a magnetic dipole" (Breiner 1999b:7). The physical relationship is described as follows:

> The magnetic anomaly for such an object would vary <u>inversely</u> as a cube of the distance between the magnetometer and the object, and <u>directly</u> with the weight of the ferromagnetic object, i.e.,

$$T = \frac{M}{r^3}$$

> where T is the anomaly in gauss (1 G = 10^5 gammas), M is the dipole moment [a product of magnetic susceptibility, k, and applied magnetic force, H] in cgs units [the centimeter gram seconds measurement system] and r is the distance in centimeters (Breiner 1999b:7).

To be more specific, Breiner appears to be using the electromagnetic, or emu, version of the cgs system where M is in units of emu. One emu equals 1 gauss per cubic centimeter (G cm^3), or .001 amperes per square meter (A m^2), and represents the magnetic density flux generated when an applied magnetic field induces a field with a mass of susceptible material. Breiner also solved for amplitude of the anomaly, T, in units of gauss; this is somewhat confusing since he uses T, the symbol for tesla (in the International System of Units [SI], not cgs), instead of the correct symbol, G for gauss, or B the generic symbol for magnetic flux density. An alternative format would be: B= $\frac{M}{r^3}$ (where B is magnetic flux density in gauss, M is the dipole moment in a cgs unit that will be derived shortly, and r is distance in centimeters).

A similar modeling algorithm—using SI system variables, not cgs—was proposed by Hall (1966:36) thirty years prior, based upon the same inverse cube relationship, but with the predicted anomaly (ΔM instead of B) determined by incorporating the object's shape, expressed as;

$$\Delta M = 10^4 \left(\frac{a}{b} \frac{w}{d^3} \right)$$

where ΔM is the magnetic flux density in nano-teslas (nT), $\left(\frac{a}{b} \right)$ is the length to width ratio of the object, w is the mass in g, and d is distance in cm. This is fundamentally similar to Breiner's equation in many regards. In fact, if the variables used by Hall were replaced with those used by Breiner, the resulting equation would be: $B = 10^4 \left(\frac{a}{b} \frac{w}{r^3} \right)$. Hall's equation is different, therefore, in that it accounts for an object's shape, the ratio of length to width $\left(\frac{a}{b} \right)$, in such a way that elongated objects have multiplicative effect on the observed magnetic flux density. If one assumes a point or spherical source where $\frac{a}{b} = 1$, however, both modeling equations are nearly identical:

$$\text{Breiner (in cgs units): } B = \frac{M}{r^3}; \text{ and Hall (in SI units): } \Delta M = 10^4 \left(\frac{w}{d^3} \right)$$

where Breiner's 'M' would be the product of Hall's mass (w) times 10^4, demonstrating that even between the different measurement systems (cgs and SI), the actual physical relationship of an induced magnetic field is the same with respect to distance and observed magnetic field strength.

While Hall's equation explicitly accounts for an object's mass, w, it uses a vaguely defined magnetic moment (10^4), whereas Briener's equation does the opposite: it explicitly incorporates the variable M, magnetic moment, with the role of an object's mass vaguely defined. As a result, both Breiner's and Hall's equations are ambiguous in terms of the relationship between an object's mass and magnetic moment. In their extensive review of magnetic modeling techniques, Camidge et al. (2010:36) identified the ambiguity in Hall's equation and proposed an updated version with specified units:

$$\Delta M = 10 \text{ nT } \frac{m^3}{kg} \left(\frac{a}{b} \frac{w}{d^3} \right)$$

In this case, ΔM (magnetic density flux) is in units of nT (1 nT= 1 γ) and is equivalent to gammas. Assuming length/width ration of 1, Hall's updated equation becomes:

$$\Delta M = 10 \text{ nT} \frac{m^3}{kg} \left(\frac{w}{d^3} \right)$$

where mass, w, is in kg and distance is in m. Thus, Camidge et al. derived that Hall's magnetic moment was in units of nano-tesla's per cubic meter per kilogram; when multiplied by distance and mass, these units cancel and the resulting product is simply the nT of magnetic density flux.

The value of '10' used in this equation for magnetic moment is a fixed variable. Thus, by examining Hall's equation, it becomes apparent that it does not incorporate a variable magnetic moment like Breiner's, where the user selects the value input for 'M' based upon the properties of a given material. In other words, although Hall's model captures the inverse cubic nature of signal loss as distance increases, it is not as versatile as Breiner's by virtue of establishing a fixed parameter for magnetic moment. Camidge et al. (2010:37) very succinctly characterized this observation, stating that: "This expression does not allow for variations in material properties but

assumes that all targets are made of the same material and that only their elongation (i.e. the aspect ratio) [A/B] leads to variations in the measured flux density."

As a result, Camidge et al. (2010:37) selected an alternate, volume-based model also derived in the SI system. Using a similar set of assumptions as Breiner—that all targets were a point source by virtue of the distance between the target and sensor being greater than the distance between the target's magnetic poles—they postulated the following equation:

$$B = \mu_0 \frac{m}{d^3}$$

where B is the magnetic flux density in teslas, μ_0 is the magnetic permeability of free space (a constant $4\pi * 10^{-7}$ T m A^{-1} in SI), m is magnetic moment in A m^2, and d is distance in meters. Since μ_0 is a constant, it simply scales the units; the ratio of magnetic moment and the cube of distance drive the equation. In fact, in the cgs system, the magnetic permeability of free space is defined as 1, making Breiner's $B = \frac{M}{r^3}$ the cgs analog to the Camidge et al. SI equation.

Thus, this simple equation is the formula used in both systems to predict magnetic density flux (in the main form used above), magnetic moment, or distance, depending upon its arrangement:

$M = (r^3)B$ for total (mass included) magnetic moment; and $r = \sqrt[3]{\frac{M}{B}}$ for distance in cgs units,

which will be derived shortly. Instead, it is more important to recognize that, thus far, neither equation has explicitly described the role of mass in the derivation of the values used for magnetic moment, 'M,' and therefore cannot be applied to modeling the behavior of magnetic materials based upon size.

2.2.3 COMPONENTS OF MAGNETIC MOMENT 'M'

To define the role of mass, therefore, magnetic moment must be deconstructed into its base units. This requires a theoretical derivation of magnetic moment from its constituent parts, a useful exercise since it will also be part of the procedure used later to derive specific values for survey applications. Both Breiner (1999b:26) and Camidge et al. (2010:37-38) provide this derivation in their work, though Breiner omits explicitly describing its role in later derivations of the cgs inverse cubic function. Thus, for the present study, Camidge et al.'s SI derivation was converted to cgs units. Both define magnetic moment as M = (k B_e V), where M is the product of an object's magnetic susceptibility, the induced magnetic field of Earth (B_e), and the object's volume (V). Susceptibility, k, is unitless in both systems; it is a volumetric proportion of the number of molecules magnetized versus total molecules within a given substance when an external magnetic field is applied. For an object resting on the seabed, this applied magnetic field is the earth's ambient magnetic field, symbolized as B_e, and would be in units of gauss (G) in the cgs system. Volume would be in cubic meters, scaled up or down by applying powers of ten. This basic relationship is defined in terms of an object's volume; a mass-specific value is defined by incorporating the bulk density (ρ, in units of $\frac{g}{cm^3}$) of a material (its mass per unit volume, or $\frac{w}{V}$). Specifically, to convert from volume to mass, the volumetric susceptibility, k, is divided by an object's bulk density (ρ), to calculate a mass-specific susceptibility (χ, in units of $\frac{cm^3}{g}$), and change the mathematical relationship to M = χ B_e w, where the magnetic moment is the product

of an object's mass specific susceptibility (χ), Earth's ambient magnetic field (B_e), and the object's mass (w, in grams). Inserting this articulated magnetic moment expression back into Breiner's original inverse cube equation results in the following expression:

$$B = \frac{\chi \, B_e \, w}{r^3}$$

Reviewing the units within this relationship, the resulting magnetic flux density B, is in gauss, which are also the units of the inducing magnetic field (Earth's ambient field), B_e. The mass-specific susceptibility (χ) is in units of $\frac{cm^3}{g}$; mass (w) is in units of grams; and distance (r) is in units of centimeters. When substituted for their respective variables, the following unit-based equation results:

$$G = \frac{\frac{cm^3}{g} \, G \, g}{cm^3}$$

in which all units but G, gauss, cancel out. Thus, all the base units comprising a mass-specific magnetic moment have been accounted for. Multiplying mass-specific susceptibility, χ by the inducing field, B_e, the induced magnetization per unit mass is determined in units of $\frac{G \, cm^3}{g}$, which simplify to $1 \, \frac{emu}{g}$ (1 emu= 1 G cm^3). This quantity is referred to as the magnetic moment per unit mass (σ), where multiplying by mass (w) in grams will provide the magnetic moment in emu; this is Breiner's 'M' value.

This derivation is important for a number of reasons. First, by knowing the individual components of magnetic moment, the user can account for variation in materials properties (susceptibility and bulk density) and Earth's ambient magnetic field to determine the appropriate M value to use during survey planning. Second, by having the individual components solved, the user can also rearrange this expression in a number of ways to determine mass from a given density flux, magnetic moment per unit mass, and distance; or (of more importance to the present study) to determine mass specific magnetic moment (σ) from known mass, density flux, and distance.

To solve for mass, therefore, the equation is arranged according to w:

$$w = \frac{B \, r^3}{\sigma}$$

and to solve for mass-specific magnetic moment (σ), the equation is rearranged:

$$\sigma = \frac{B \, r^3}{w}$$

The first application, determination of specific magnetic moment per unit mass (σ) values, requires that a material's susceptibility (k), bulk density (ρ), and local ambient Earth magnetic field (B_e) are known. The volumetric susceptibility (k) of pure iron is 5,000, as derived in the SI system. As previously mentioned, the SI derivations are based upon a constant magnetic permeability of free space at 4π, whereas this value is simply 1 in cgs. Thus, to convert k from SI to cgs, the SI value is divided by 4π, making the cgs volumetric susceptibility (k) of pure iron

397.88 (see Jones 2007:1; Camidge et al. 2010:38). Divided by the bulk density of iron, $7.9 \frac{g}{cm^3}$, the result is a mass specific susceptibility (χ) of $50.36 \frac{cm^3}{g}$ or $50.36 *10^{-3} \frac{m^3}{kg}$. The Earth's ambient magnetic field—which induces the field in susceptible objects—generally ranges between .30 and .60 Gauss, depending upon latitude and temporal variations. A common measurement for the southeastern United States is .50 G (50,000 γ). The magnetic moment per unit mass (σ) in this field, therefore, would be $50.36 \frac{cm^3}{g} * 5$ gauss, equal to $25.18 \frac{G\,cm^3}{g}$, or $25.18 \frac{emu}{g}$. According to this susceptibility, the range of magnetic moment per unit mass (σ) of pure iron within the normal range of Earth's magnetic field would be $15.108 \frac{emu}{g}$ to $30.216 \frac{emu}{g}$.

According to Breiner (1999b:7), "…objects made typically of iron or steel, the magnetic moment, M, is between 10 and 100 cgs units per ton." Since all base units used are converted by powers of 10, these components are easily scaled to more useful units such as kg, m, or in Breiner's case, metric tons. In fact, Breiner (1999b:8) worked out many of these conversions for the formula. First, he factored the product of the equation from gauss to the unit of magnetic density flux most commonly used by surveyors, gamma/nanotesla (1 G = 10^5 γ = 10^5 nT). Next, he factored from grams of mass to tons (10 g = 10^{-5} tons), resulting in the following formulas from a 1 ton object 100 ft (3048 cm) distant, at σ = 10 and 100:

$$B= \left[\frac{\left(10\frac{emu}{g}*10^4\right)*\ 1\ ton}{(3048\ cm\ )^3}\right]* \ 10^5 \quad \text{where B = .35}\gamma$$

and

$$B= \left[\frac{\left(100\ \frac{emu}{g}*10^4\right)*\ 1\ ton}{(3048\ cm\ )^3}\right]* \ 10^5 \quad \text{where B = 3.5}\gamma$$

Thereby, Breiner (1999b:8) derived his claim that "a ton of iron is therefore between .35 and 3.5 gammas at 100 feet…." The range of σ values used by Breiner, 10-100, is a very large range which produces vastly different results as mass and distance increase due to the cubic nature of magnetic intensity as a function of distance. The values previously derived for the σ of iron, $15.108 \frac{emu}{g}$ to $30.216 \frac{emu}{g}$, are nested within this range. Knowledge of specific values, therefore, would result in more accurate predictions of various objects.

2.2.4 USING INDUCED MAGNETISM TO MODEL SURVEY COVERAGE

Though Breiner distilled his modeling equation to a fairly useful form, many material culture items of interest to archaeologists are not reported in metric tons. Instead kilograms are often used. Additionally, most surveyors work in units of gamma, not gauss. Scaling the mass variable accordingly, the equation becomes:

$$\Delta\gamma = 10^5* \left[\frac{(m*10^4)*\ kg*10^{-3}}{(cm\ )^3}\right]$$

where magnetic density flux, B, is converted to γ (or, more accurately, change in gamma: Δγ), and tons is substituted with the equivalent kg * 10^{-3}. As the powers of 10 are combined, the resulting simplification is:

$$\Delta\gamma = 10^5 * \left[\frac{(m*10^1)* \text{ kg}}{(\text{cm })^3}\right] \quad \text{or} \quad \Delta\gamma = 10^6 * \left[\frac{(m)* \text{ kg}}{(\text{cm })^3}\right]$$

Over the course of several years of experimentation using the gradient processing methods described previously, the NPS Submerged Resources Center observed an empirical m value of approximately $62 \frac{\text{emu}}{\text{g}}$. This value, higher than theoretical values calculated for pure iron, likely represents the combined effects of permanent magnetism, l_r, and induced magnetism, l_i, for a total magnetization, l. Though merely an observed operational parameter (it has not been explicitly tested) $62 \frac{\text{emu}}{\text{g}}$ proved useful at predicting the anomaly size of ferromagnetic archaeological materials in the coastal areas of the North American continent.

Thus, the resulting equation, adjusted for more common units, is:

$$\Delta\gamma = \left(\frac{w\,m}{r^3}\right) 10^6$$

where magnetic flux density is in Δγ, mass (w) is in kg, and distance (r) is in cm. According to this model, a 1,000 kg iron object 5m (500 cm) from the magnetic sensor, with an M=62, would produce a magnetic anomaly of approximately 490 γ; the same object at 10 m (1000 cm) would produce a 62 γ anomaly. Solving the equation for mass results in:

$$w = \frac{(\Delta\gamma*10^{-6})r^3}{M}$$

where w remains kg. According to this equation, a magnetic flux density of 100 γ (above ambient) observed from a distance of 500 cm would have be caused by a ferromagnetic object of 200 kg, assuming $\sigma = 62 \frac{\text{emu}}{\text{g}}$. This form of the equation is later used for calculation of detection levels based on space (r) throughout the survey area and magnetic flux density.

Extrapolating predicted anomaly amplitudes for various sized objects at varying distances reveals the powerful effect of proximity to strength of observed magnetic shift. Breiner (1999a, 1999b) described this relationship as an inverse cube, meaning that for a single unit change in distance, measured magnetic flux changes by an exponent of three. Table 2-3 shows predicted anomaly sizes for general maritime material culture based upon mass and the distance from the magnetometer sensor, using the M value of $60 \frac{\text{emu}}{\text{g}}$. For this calculation, distance was given as the hypotenuse of sensor altitude and the object's distance from the survey line (see Figure 2-9).

The ability to predict anomalies for different sized objects allows archaeologists to tailor a given survey design to maximize the probability of detection for specific items while minimizing wasted time due to superfluous data collection. For example, an archaeological survey intended to locate a 100 ton (90,718 kg) iron shipwreck would require a line spacing no wider than 150 m, and a sensor altitude no greater than 10 m. A survey intending to locate a small iron canon (572 kg) would require lane spacing no greater than 30 m and a sensor altitude no more than 5 m.

These predictions are based upon the possibility that an object is in the least detectable portion of a survey area, equidistant between two adjacent survey lines. In other words, survey design must account for the likelihood that archaeological material will rest between planned survey lines. To illustrate the importance of this, Table 2-4 shows the difference in predicted anomaly size when a 1,000 kg object rests exactly between two adjacent survey lines versus the sensor passing directly overhead (6m altitude).

Table 2-3
Predicted anomaly sizes for various maritime-related objects; mass is given in pounds and kilograms; distances are calculated from the hypotenuse of a 6 m sensor altitude and 15 m offset from the survey line. Predicted anomaly size given in gamma (Source: Hughes 1917; Graumont and Hensel 1945; Aerodata International 1987; Caruana 1994, 1997; Bowers 1999; Curryer 1999; CFM International 2010).

Object	Mass (kg)	Sensor Alt (m)	Offset (m)	γ
Compound Steam Engine	952	6	15	13.55
Wright R-1820-40 Cyclone Radial Engine	1212	6	15	17.25
18th cent. Iron 4 pounder	1270	6	15	18.07
Small 3x Expansion Engine	1950	6	15	27.75
Wright R-3350 Duplex Cylone Radial Engine	2177	6	15	30.98
Small (4th bower) 17th Cent. Anchor	2511	6	15	35.73
CFM56-3B-2 Jet Engine	2794	6	15	39.76
18th cent. Iron 24 Pounder	4115	6	15	58.55
18th cent. Iron 42 Pounder	4386	6	15	62.41
Large 17th Century Anchor	9652	6	15	137.34
Large Admiralty Bower	14582	6	15	207.49
Large Water Tube Boiler	16561	6	15	235.66
Early Stockless Anchor	18143	6	15	258.17
Large 3x Expansion Engine	36287	6	15	516.35
600 ft. Anchor Chain	16561	6	15	243.19
Modern Stockless Anchor	18143	6	15	266.42
Single-End Scotch Boiler	36287	6	15	532.85
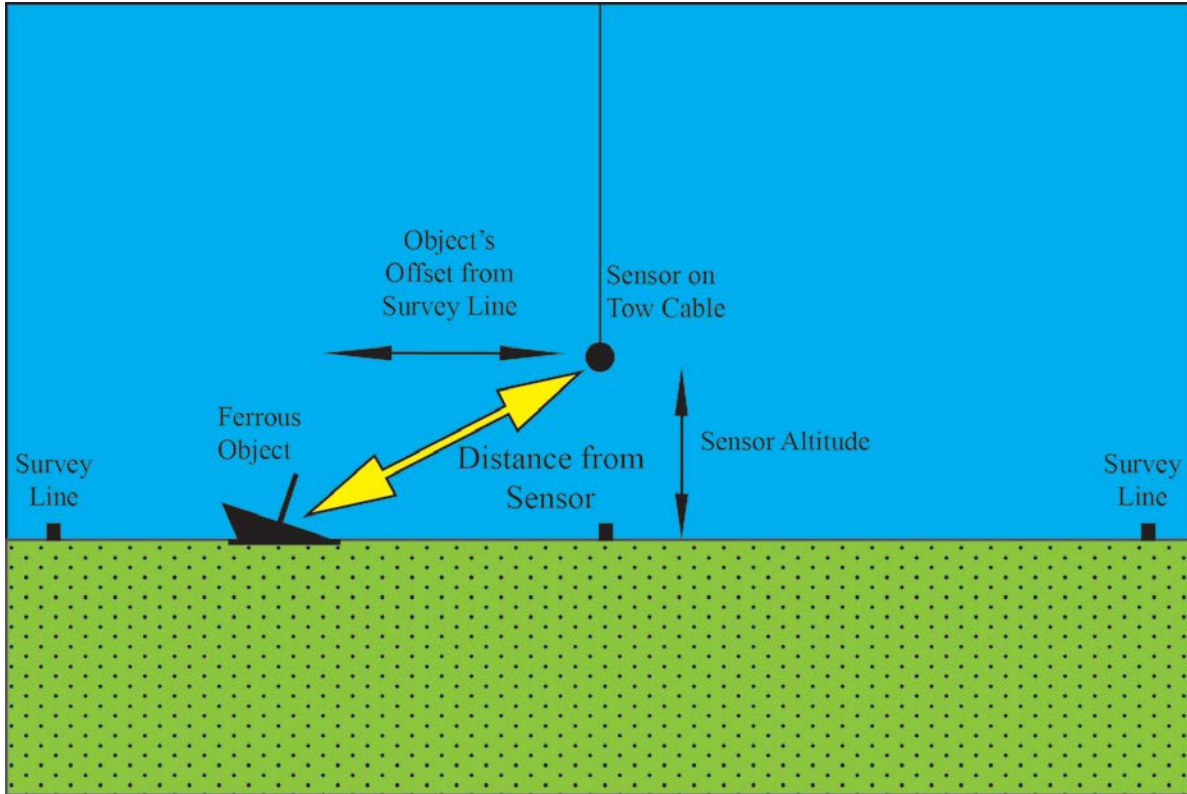
Figure 2-9. Diagram showing the relationship of sensor altitude and object offset from survey line as relates to the object's distance from the magnetometer. Actual distance is hypotenuse of offset and altitude.

Table 2-4
Difference in predicated anomaly size between object resting exactly between two lines and sensor passing directly over the object (1000 kg of iron, M=60).

Survey Line Spacing	50 m		30 m		20 m		15 m	
Object Offset	25 m	0 m	15 m	0 m	10 m	0 m	7.5 m	0 m
Gamma	3.53	277.78	14.23	277.78	37.38	277.78	67.72	277.78

An assumption made when generating survey designs in this manner, however, is that the sensor is moved precisely along the planned survey line. Deviation from planned survey lines, which regularly occurs due to the difficulty of piloting a vessel, currents, winds, and sea state, causes the sensor to deviate from planned lines, thereby changing the actual distances between adjacent track lines. This can work to decrease the distance between object and sensor, or increase the distance beyond the planned maximum. For example, if while driving survey lines spaced at 30 m the operator deviates 5 m to the left of the line, an object 15 m to the right of the line will actually be 20 m from the sensor, as shown in Figure 2-10. Similarly, if on the adjacent line the vessel deviates away from the object and additional space is placed between the sensor and object, the object could potentially escape detection.
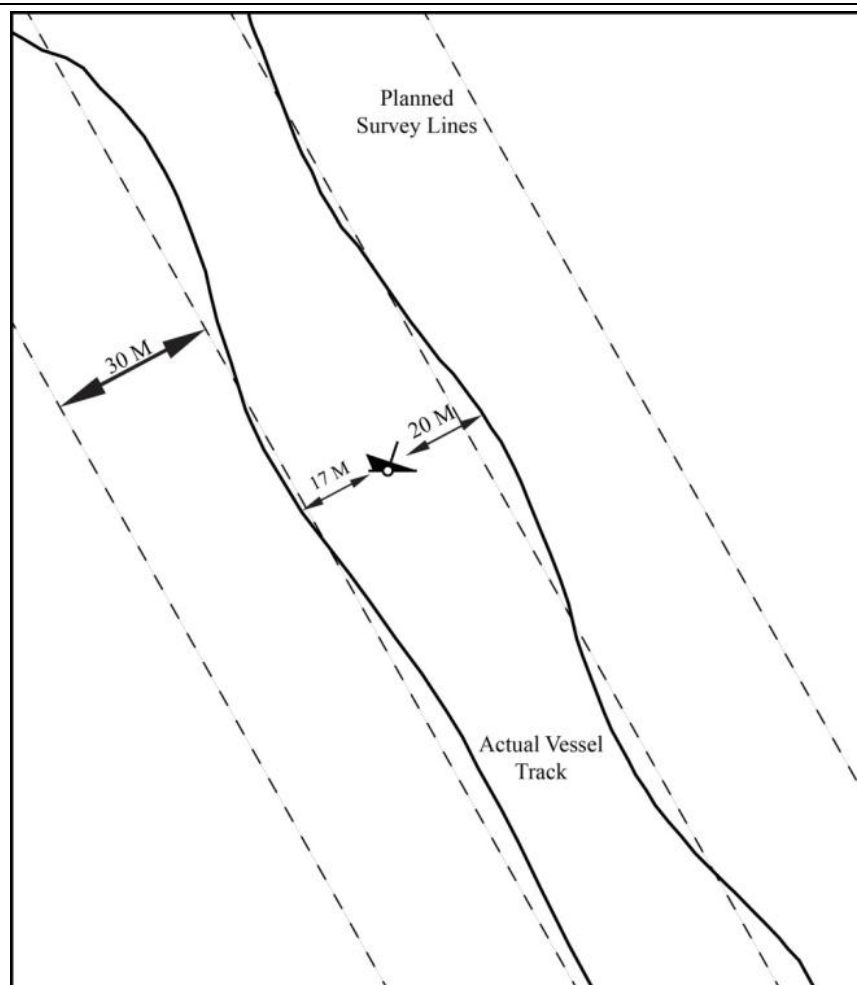
Figure 2-10. Illustration showing how actual vessel course can increase distance between object and magnetometer sensor. (Drawn by John Bright).

It is possible, following a survey, to use the same modeling algorithm to review a dataset in terms of actual coverage. Actual deviations from planned survey lines, represented in the geospatial distribution of raw data points, can be post-processed via spatial buffering to reveal areas where detection thresholds were exceeded and artifacts potentially missed. Such a process, however, would depend upon having accurate values for the magnetic moment of cultural objects. Otherwise, the theoretical range of magnetic moment values put forth by Breiner (10-100 $\frac{emu}{g}$) are too vague for making precise, factual assessments of magnetic surveys. The theoretical value for pure iron supplied by Camidge et al (2010:38) is experimentally unverified and does not likely reflect the magnetization of historical materials composed of iron-alloys. In fact, Camidge et al. report a range of susceptibility values, k, for various iron-based compounds. At the lower end is Ferrite U 60 (k=.55 cgs) up to supermalloy (k=79,580 cgs). Using the bulk density of 7.9 $\frac{g}{cm^3}$, σ values range from .069 $\frac{emu}{g}$ to 10,107 $\frac{emu}{g}$. Thus, while of use as an academic tool, without accurate σ values, this model has a limited ability to produce accurate and scientifically defensible results regarding the assessment of magnetic survey coverage.

For this reason, experimental testing was conducted to better understand the relationship between ferromagnetic mass and observed magnetic moment. In particular, empirical data were collected to determine actual σ-values for various ferromagnetic cultural materials. The inverse cube modeling equation applied to pre-and post-survey assessment proved an effective tool that provided valuable results regarding data coverage, information that is vital to appropriate submerged cultural resource management, especially when such areas are under consideration for bottom-disturbing activities and development. These data are presented in the Results and Conclusions section of the Field Testing Operations chapter of the report.

2.3 BASELINE MODELING: INDUCED MAGNETIZATION OF IRON

By its nature, underwater cultural heritage consists of archaeological materials submerged in aqueous environments for long periods of time and in various states of chemical modification. Depending upon the archaeological site, these items could include wood, ceramics, or ferromagnetic objects. When inundated in an aqueous environment, especially a marine environment, ferromagnetic materials oxidize at varying rates. As the chemical composition of the object changes, its magnetic properties are altered as well. Thus, depending upon the chemical environment, the properties of the material, and the time of submergence, a ferromagnetic object's magnetic properties could change significantly.

The previous discussion of modeling magnetism for archaeological materials in terms of an object's detectability assumes the object's magnetic moment—the strength by unit volume and/or mass of its induced magnetic field—is known. Though this study presents data collected over a range of submerged archaeological materials, this information cannot encompass the entire range of underwater material culture items at varying states of chemical modification across the globe. Though several recommendations are put forth in the results and conclusions section to incorporate the results gained from the field testing operations, not all scenarios can be modeled precisely. Where local information is unknown, the magnetic properties of pure iron are recommended for modeling applications. As an idealized theoretical baseline, the modeling results provided by using the σ value of pure iron can be scaled accordingly to capture the local environment and material culture array where the survey is taking place.

Most historical ferromagnetic materials (such as cannon, anchors, etc.) were composed of some impure form of iron, however using pure iron provides an idealized approximation of the object's magnetism. Also, given that the magnetic properties of iron compounds vary greatly (see Camidge et al. 2010:38), modeling based upon pure iron provides a more universal standard. This might be especially useful for survey planning, when the disposition of submerged archaeological materials and their corresponding σ values are simply unknown.

The magnetic moment of pure iron was previously derived by calculating the induced field strength as a result of exposure to the larger, ambient field of Earth (B_e). The strength of Earth's magnetic field varies geographically and temporally, thus a unique B_e value would be derived for any given time/place. This data is collected and made publically available by the US National Oceanic and Atmospheric Administration's (NOAA) National Geophysical Data Center (NGDC) at http://www.ngdc.noaa.gov/geomag-web/#igrfwmm. For the sake of review, this derivation is repeated with these specific values.

During the month of June 2013, when the present study was conducted, the ambient magnetic field near Miami, FL, was approximately 44,377 nT (1 nT=1 γ). This value will be used for the following example. The magnetic susceptibility, k, of 99.8 percent pure iron is 5,000 in SI units (Camidge et al. 2010:38). Though k is a dimensionless value, it is derived differently in the SI and cgs systems. Thus, the conversion from SI to cgs is $k_{(SI)}=4\pi\, k_{(cgs)}$; for pure iron, this converts to 397.88 cgs (see Jones 2007). This value can be converted to a mass-based variable by dividing k by the bulk density of iron, $7.9\ \frac{g}{cm^3}$, arriving at $50.3\ \frac{cm^3}{g}$. Multiplied by the strength of Earth's magnetic field in Miami in June of 2013, 0.44377 G, a mass-specific moment of $22.35\ \frac{G\,cm^3}{g}$, or $22.35\ \frac{emu}{g}$ is determined. Extrapolated to tons of material, this multiplier changes to $22.35 * 10^5$ emu per ton of material.

Since the induced field of iron is variable depending upon the force of the applied field, the observed flux density for such an object will vary geographically and temporally. Thus, the data recorded by NOAA's NGDC should be referenced when modeling based upon the magnetic moment of iron. For example, at the same time the present study was taking place off Miami, Florida, June of 2013, the ambient field in New Orleans, LA was approximately 47,698.7 nT (0.476987 G), the ambient field in Boston, MA was approximately 52,462.5 nT (0.524625 G), and the ambient field in Honolulu, Hawaii, was approximately 35,066.2 nT (0.350662 G). In each of these locations, the magnetic moment per unit mass of an identical mass of pure iron would vary slightly. Since this data is freely available to the public, it is recommended that geographically and temporally specific values for σ be derived for modeling individual surveys.

In addition to changes in the inducing magnetic field, the permanent magnetism of an object may also increase or decrease this amount. In fact, according to Breiner (1999b:3), "…the perm [permanent magnetism] sometimes represents the predominate magnetic property useful in a search for such an object." The effect of permanent magnetism explain why NPS SRC archaeologists observe an approximate σ = 62 during their survey operations. Depending upon local conditions and the individual properties of archaeological objects, estimation of their σ values can be scaled up or down accordingly. The derived σ values for cultural materials calculated in Biscayne National Park, and their applicability to the modeling system are described in detail in the following section.

CHAPTER 3

FIELD TESTING OPERATIONS

Field testing operations were required to determine the validity of the inverse-cube model of induced magnetism and to derive empirical values for the magnetic moment of cultural materials. These tasks were outlined in the phase 2 tasks section of the IAA. As per this agreement, the NPS SRC facilitated all field operations and supplied both a survey platform and survey system. NPS SRC selected Biscayne National Park (BISC) as the location for testing. The basic methodology involved conducting a systematic magnetic survey over known sites and assessing the acquired data to determine if it conformed to the inverse cube model, and then solving for the object's magnetic, or dipole, moment. Integral to this methodology was selecting sites of a quantifiable mass. The park has a very diverse cultural resource inventory (maintained within the NPS Archaeological Sites Management Information System [ASMIS] database0 with several suitable sites, and just beyond the park's offshore boundary is an extensive system of artificial reefs offering additional suitable survey targets. In addition to multiple suitable sites, the park also offered excellent logistical support.

Of a potential 124 ASMIS sites, 2 non-archaeological sites within park boundaries, and 37 artificial reef sites along the park's boundary, 27 were determined suitable for survey. BISC Cultural Resource Manager Charles Lawson and park volunteer Terry Helmers assisted in the site selection process, providing invaluable first-hand knowledge and information. Of the 27 sites designated for survey, time and weather permitted for 15 to be sampled. Of these sites, one was an historical cannon, four were historical anchors, four were consolidated modern debris (large pieces of steel), and three were wooden shipwrecks with various ferromagnetic elements. The remaining three sites were large steel-hulled shipwrecks, artificial reefs within the Florida Keys National Marine Sanctuary. Survey operations on these sites were conducted with permission of FKNMS (see Appendix III). Field testing was conducted between 18 June and 6 July, and again on 12, 13, and 17 July, and 5 August, 2014. The core research team consisted of four NPS and two BOEM staff.

Data acquisition occurred on NPS SRC vessel *Cal Cummings*, Figure 3-1. This vessel was the optimal survey platform for working in BISC. *Cal Cummings* is a 27 foot Boston Whaler Challenger model outfitted with dual Honda 225 hp outboard motors and an enclosed cabin. The vessel's shallow draft (~24 inches) made it suitable for navigation through most portions of BISC, while the closed cabin and dual engines make it safe for moderate offshore operations. The survey tools described below have been built into the vessel, and are powered by a dedicated inverter which transforms the boat's direct current power (generated by the engines) into 120 V alternating current power. The vessel also has a dedicated computer and navigation system to run the data acquisition software.

Figure 3-1. NPS SRC Survey Vessel *Cal Cummings*.

The SRC utilized a Geometrics G-882 marine magnetometer for this survey. This system combines a highly-sensitive cesium vapor sensor with an echosounder/altimeter arranged on a portable towfish. The towfish is rigged for two tow positions—nose tow for shallow water and center-of-gravity tow for deeper water—making it ideal for the variable survey areas in and around BISC. The sensor's operating range is 20,000 to 100,000 nT (1 nT equals 1 γ), with a sensitivity of 0.004 nT, and can operate at sampling rates up to 10 Hz. The towfish's maximum operating depth is 9,000 ft (2,750 M), more than sufficient for the survey areas off BISC (Geometrics 2003). SRC's additional sensors were present as backups, but were not used.

The magnetic sensor and other survey instruments were interfaced with Hypack 2012, the SRC's data acquisition software. Hypack combines magnetic data with navigation information provided by the system's GPS system: a Hemisphere Power Max differential GPS (DGPS) receiver with sub-meter accuracy, linked to the differential broadcast beacon in Miami. Navigation data were collected in the NAD83 datum and projected, processed, and reported using the NAD83 UTM Zone 17N projection system. Exact sensor position was calculated via measured offsets between the GPS receiver and a 3PS Instrumented Sheave System (cable counter), as shown in Figure 3-2. The cable counter automatically measured layback, relaying the information to Hypack in real-time. The most accurate layback positions were attained with a 'surface tow' configuration.
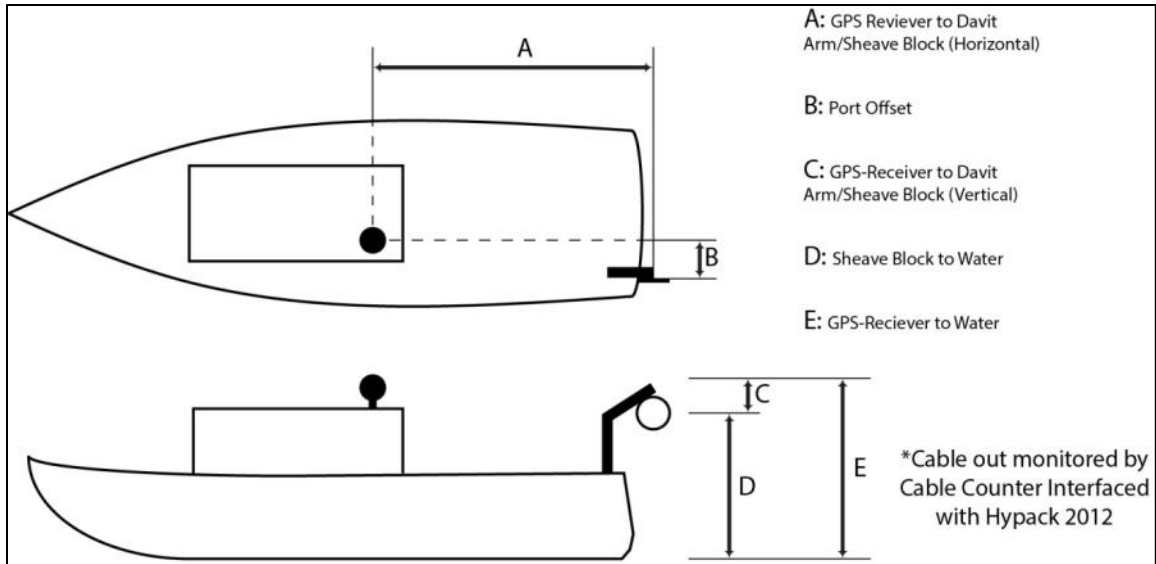
Figure 3-2. Schematic of GPS and instrument cable offset measurements. (Drawing by John C. Bright).

Data were acquired over each target according to the methodology described below. Once collected, a basic processing function was run prior to the data being exported from the acquisition program. Once exported, the data were migrated into ArcGIS where most remaining processing took place. In addition to testing the validity of the algorithm upon which the geospatial tools were based, the tools themselves were tested. All data acquired were processed using the *Generate Survey Boundary* tool, the *Visualization* tool, and later through the *Confidence Model* tool (the *Input Tool* was developed afterwards) to evaluate their application within an actual survey operation (see Appendices A and B for tool notes and instructions). Afterwards, tabular data were exported from *ArcGIS* and copied into a spreadsheet where the magnetic moment for a given target was determined. The next section details the sampling methodology and specific data processing steps used, followed by a description of each sampling site. A logistical overview of these testing operations is included at the end of this section, as the bulk of IAA funding was used to cover the travel and expenses of field testing.

3.1 SAMPLING METHODOLOGY AND DATA PROCESSING

The basis of the experimental design involved deploying a magnetometer along a survey grid designed to detect an object of known mass, then processing the data to calculate the object's magnetic moment as a function of distance and recorded anomaly amplitude. This procedure allowed the inverse cube function to be tested. Since the magnetometer passed the object at varying distances, the model predicted a specific change in the observed anomaly amount. If this relationship is indeed characterized by an inverse cube function of distance and magnetic field strength, the quantity derived for magnetic moment should be consistent at varying distances.

Using Breiner's equation presented in the previous section, with the additional derivation of magnetic moment into mass-specific units, the equation was solved for σ, changing from the original as follows:

$$\text{Breiner's original equation:} \qquad B = \frac{M}{r^3}$$

Equation with base M units: $\qquad$ $B = \dfrac{\chi\, B_e\, W}{r^3}$

Equation with σ $\left(\dfrac{\text{emu}}{\text{g}}\right)$: $\qquad$ $B = \dfrac{\sigma\, w}{r^3}$

As discussed in the previous section, the standard units are converted such that mass (w) is in kilograms, distance (r) is in centimeters, and magnetic density flux (B) is in gammas. The utility of deriving the base units of M is the ability of the user to manipulate the equation to solve for magnetic density flux (B), mass (w), or magnetic moment per unit mass (σ), when all other variables are known. In this way, the experimental design was established to provide the information necessary to solve for magnetic moment (σ), based upon the equation as follows:

$$\sigma = \frac{(B * 10^{-6}) * (r^3)}{w}$$

where magnetic density flux (B) is in γ, distance (r) is in centimeters, and mass (w) is in kg. During data processing, this equation was built into a spreadsheet where mass, distance, and gamma values (derived from GIS analysis of the acquired data) were input for each sampling site. If the model was accurate, the σ value for a given substance should be fairly consistent throughout the range of experimental conditions.

Ideally, testing magnetic survey equipment would occur under laboratory conditions, where exact masses of precisely known metals (iron and steel alloys) would be systematically sampled in an otherwise magnetically 'sterile' environment. Sampling materials representing the full range of material culture items encountered in the field, including comparable masses to a large iron-hulled shipwreck, would require enormous amounts of ferromagnetic material which, under laboratory conditions, would need to be measured in precise quantities. Such a procedure, however, was neither practical nor possible. Facilities (a magnetically neutral laboratory containing hundreds of thousands of kilograms of iron and steel) simply do not exist, nor were the required amounts of metallic materials available for the project. Instead, the most practical – and the most realistic – way to conduct magnetic experimentation was to sample known archaeological resources *in situ.* Thus, the readily accessible resources at BISC were chosen.

Several challenges present themselves while sampling resources *in situ*. The first is obtaining accurate position information for the target object. In cases where the position of a resource was uncertain divers were deployed to locate and mark the exact location of a given object, with a tethered buoy, which also served as a visual aid for the boat driver during survey. In most cases, additional ground-truthing was necessary to determine the extent and composition of archaeological remains, with divers using measuring tapes to record relevant measurements to aid in the determination of a target's mass and ensuring that other ferrous materials that might contaminate the quality of the data were not in the study area.

The next challenge to *in situ* sampling was to properly fix the position of the magnetic sensor during survey operations. Layback calculations—determination of the sensor by measured offsets from a GPS receiver and control of tow-cable length—are a standard procedure for any marine survey. Obtaining precise offset measurements from the GPS receiver to tow point is

fairly straightforward; estimating length of cable out, however, has the potential to introduce error into the navigation data. To mitigate this error, the SRC employed a 3PS Instrumented Sheave System, basically an electric cable counter. This device operates by measuring the length of cabled paid through a calibrated sheave block, and relaying this information into the navigation feed of the data acquisition software so that a more precise sensor location was recorded.

Another difficulty inherent in the research methodology was fidelity to the survey design. Parallel lanes, spaced 10 M apart for smaller objects and 30 M for larger objects, were developed around a given target object. It is impossible, however, for any vessel to remain exactly along planned survey lines during sampling and ultimately, the collected data points deviated from planned lines. Knowing the exact distance between the data points and the target object, however, was critical to this study. Post-processing easily determined this distance. The primary magnetometer, a Geometrics G-882, is equipped with an altimeter, and records towfish altitude during data sampling. Thus, the distance between the sample and target can be derived from the hypotenuse of the triangle bounded by vertical distance from the bottom (altitude) and horizontal distance from the object (offset), calculated in ArcGIS. While minor deviation from planned lines can be accounted for, close adherence to planned lines was still necessary to ensure a systematic sampling interval.

Accounting for all of these factors, the following methodology was implemented:

1. Test all survey components at dock prior to departure.

2. Transit to site.

3. Arrive at site; commence ground-truthing operations

    a. Maneuver vessel over recorded position

    b. Deploy tethered marker buoy.

    c. Deploy divers on buoy.

    d. Divers reposition buoy over site as necessary, marking the center of extant remains.

    e. Divers conduct circle search to check adjacent area for any addition ferromagnetic materials (magnetism is determined by observing the behavior of an underwater compass when placed over the material).

    f. Divers collect any necessary measurements.

4. Using marker buoy as reference, boat operator takes updated GPS position of center of site.

5. Using this reference, a survey grid is developed in the data acquisition software. Target locations, exported from the project's GIS, are imported into Hypack 2012 as individual point locations. Once ground-truthed, the Hypack software then programs a series of parallel survey lines, as well as perpendicular tie lines, centered on an

individual target object, as shown in Figure 3.3. Once drawn, these survey lines become the navigational reference for the boat operator to drive. The line number and survey block, furthermore, become the nomenclature of the individual files, and are also written into the data record for each sampled point.

Figure 3-3. Hypack 2012 display of parallel and perpendicular survey lines.

6. The magnetometer is powered on.

7. While approaching the first line, the magnetometer is deployed, with cable paying out through the calibrated sheave block.

8. The instrument cable is secured for towing once the desired layback is achieved.

9. Data logging is turned on/ off as lines are driven, these events being recorded in a survey logbook.

10. Once the first lines plan is completed, it is deactivated and the second, perpendicular lines plan is displayed on the screen.

11. Using steps 7-9, this second lines plan is surveyed.

12. Once the second lines plan is completed, the survey equipment is powered down and retrieved onboard the vessel.

13. The marker buoy is retrieved.

14. Transit to next site, and repeat 2-13.

Once acquired, the remainder of data processing was done through Hypack, ArcGIS, and an Excel spreadsheet. Hypack 2012 was used for initial processing via the software's Single Beam

Editor tool. This tool allows the surveyor to individually inspect data files for irregularities and noisy data, and provides the ability to clip (remove) these areas prior to visualization. Noise can be introduced in a number of ways, including power supply spikes, the sensor passing close to a fixed object such as a navigation buoy, or another boat driving too close to the sensor (a common occurrence in the high-traffic waters of South Florida). If necessary, the software will average the values preceding and succeeding the clipped data and apply them to the clipped area. In most cases, however, the sampling sites were so small that there was no noise introduced into the data. Rather, importing the raw files into Single Beam Editor simply allowed the surveyor to verify that the data acquisition procedures had produced useable information.

After going through the Single Beam Editor, Hypack 2012 converts the line files from a .raw format to an .edt format. In this way, Hypack always preserves the raw data in an original, unprocessed format. Once converted to .edt, these files can be compressed into a single table and exported in a number of user defined formats. For this survey, 'X' and 'Y' geographical information, measured magnetic intensity, sensor altitude, and line file name were needed and were therefore selected for export into a comma-delimited format. Output as a .csv file, the data was directly loaded into *ArcGIS*. In a normal survey, the surveyor would begin using the scripted tools to process, visualize, and assess the dataset. To determine magnetic moment, however, the data needed to be migrated into a spreadsheet where horizontal and vertical distance and change in gamma could be calculated. An additional processing step in *ArcGIS*, however, was required to determine the horizontal distance from each sample point to the target object.

A spatial join allows the user to assign the attributes of one feature class to another based on their spatial relationship (Figure 3-4). A feature class representing the survey target was created from GPS positions collected in the field. When this target feature class is spatially joined to the raw data feature class a third feature class is created which joins the attribute tables and calculates the distance from each raw data point to the survey target. The distance is calculated in the horizontal unit of the data frame. The project used the NAD 1983 UTM zone 17 projection so all of the calculated distances were in meters. Values from the 'Distance' field of the output feature class (Figure 3-5) were then copied into the calculation spreadsheet.

Not all data points within the survey grid were needed for the magnetic moment calculation. Instead, only those taken within the influence of the object's magnetic field represented the strength of that field. To retrieve these specific points, the data points within the target object's magnetic field were identified and selected using the *Polygon Select* tool. Figure 3-6 shows an example of the selected raw magnetic data points around a survey target. Once selected, they can be viewed in the attribute table by pushing the *Show Selected Records* button. To determine the background ambient field strength—each survey block was collected in such a short amount of time that diurnal variation was ignored—the selected records were switched (Figure 3-7), and statistics calculated on the remaining data points (Figure 3-8). The mean value represented the strength of the ambient field in that location.
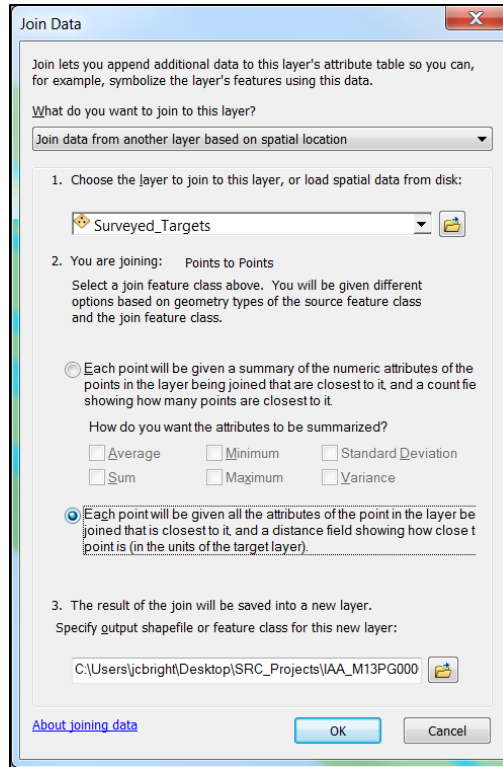
Figure 3-4. ArcGIS Spatial Join Interface.

Figure 3-5. Attribute table after Spatial Join, distance from sample site (BISC_0122) are calculated in meters.
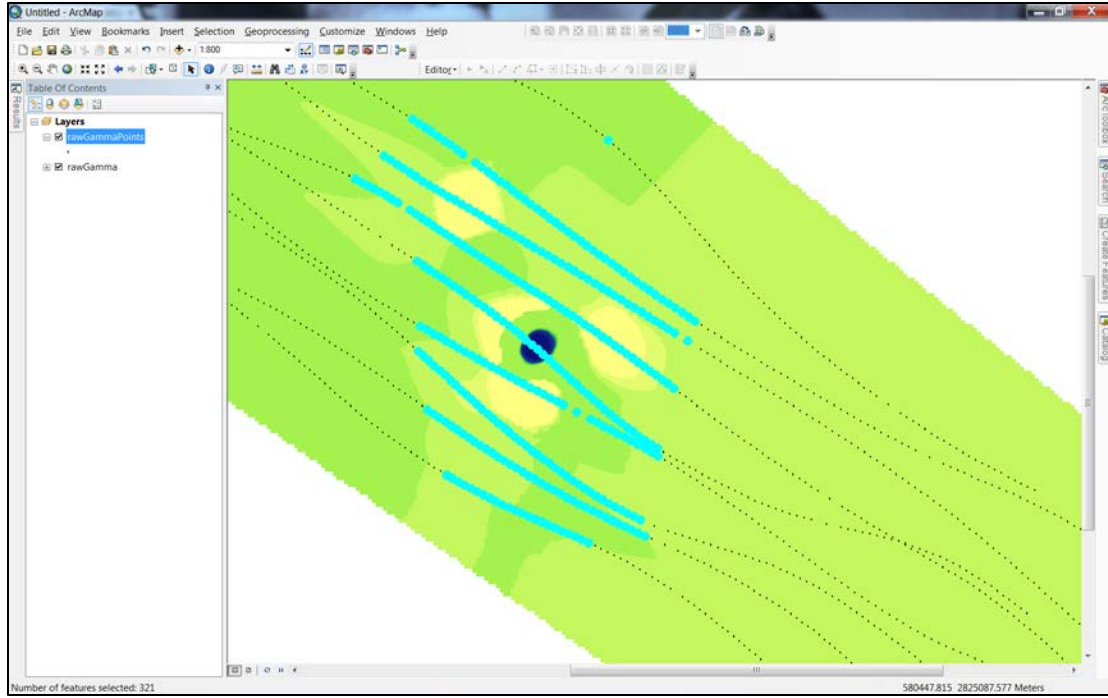
Figure 3-6. Selection of points (in blue) within the object's magnetic field.
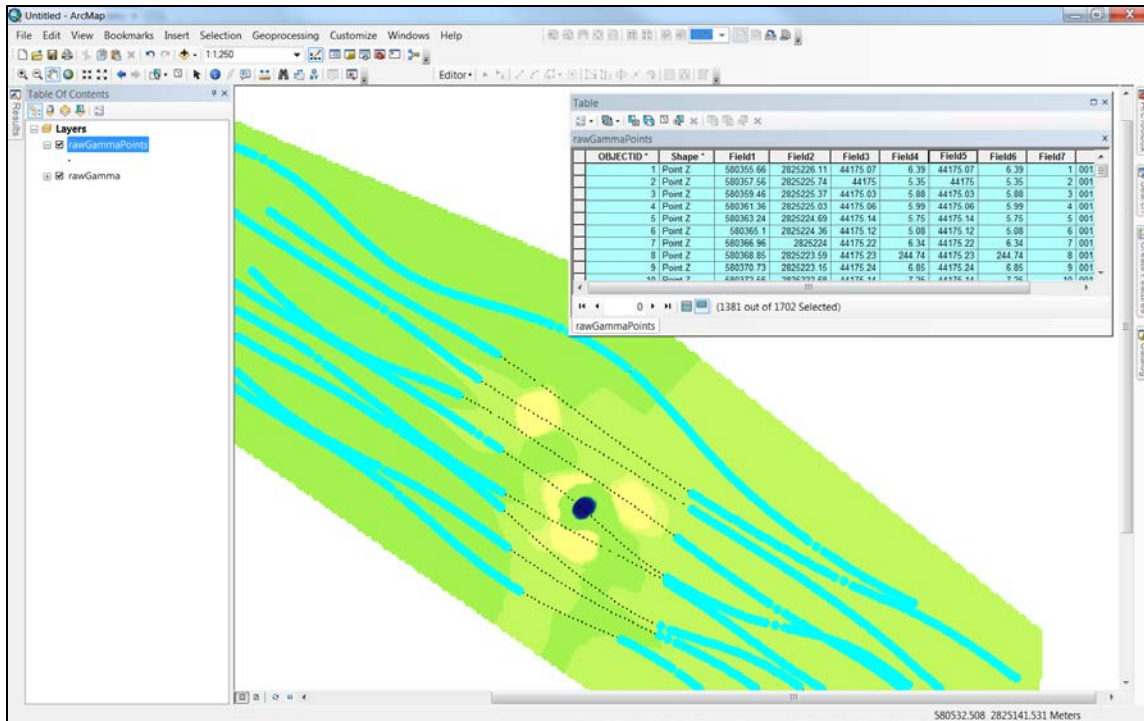
Figure 3-7. Reverse selection of points outside of magnetic field representing ambient magnetism.
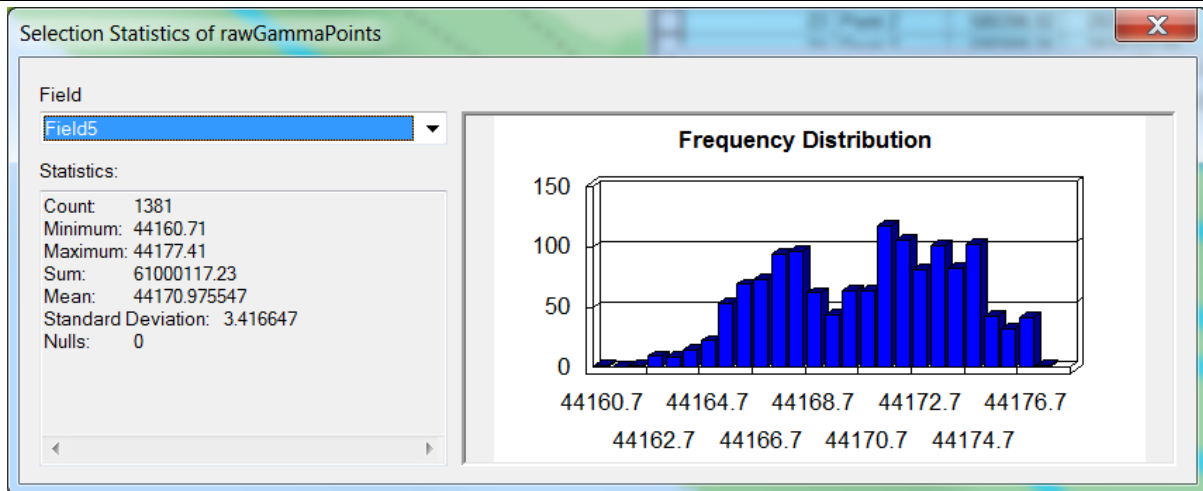
Figure 3-8. Statistical summary of background points, including the mean.

With horizontal distance and background magnetism solved for, all the variables needed to calculate magnetic moment were available. Data was moved into the Excel spreadsheet simply by cutting and pasting fields out of the attribute table and into Excel. The first computation determined the amplitude of magnetic force change ($\Delta\gamma$) as the absolute value of the difference between the background γ value and raw γ. Absolute value is used since positive and negative shifts are the result of vector addition/subtraction between the object's induced field and Earth's. In other words, magnetic force is symmetrically distributed between the object's poles and the positive or negative shift is observed as a result of either constructive or destructive interference with the force vector of Earth's magnetic field; thus, the amount of variance, be it positive or negative, is a function of magnetic field strength and can therefore be expressed absolutely (Figure 3-9). Next, total distance was solved as the hypotenuse of the sensor offset and altitude from the object. Finally, the spreadsheet calculated magnetic moment as a function of distance and $\Delta\gamma$. An example of this process via spreadsheet integration is shown in Table 3-1.
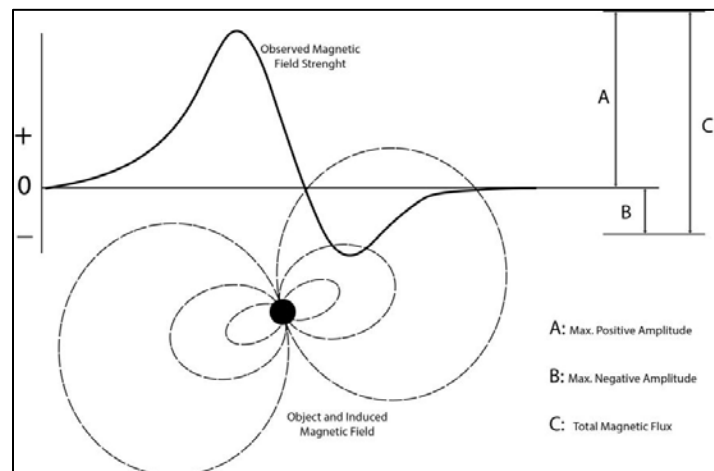
Figure 3-9. Characteristics of observed magnetic field strength trace. (Source: Weymouth 1976, modified by John C. Bright).

Table 3-1
Arrangement and computation of magnetic moment.

Object	Mass (kg)	Survey Line	Background γ	Raw γ	Δ γ	Alt. (M)	Offset (M)	Distance (cm)	Magnetic Moment (emu/g)
	1270	13-3-001	42100	42115	15	4.4	10.8	1166.190	12.551
	1270	13-3-001	42100	42145	45	4.5	10.6	1151.56	53.938
Anchor Target 1	1270	13-3-001	42100	42155	55	4.5	10.5	1142.36	14.511
	1270	13-3-001	42100	42072	28	4.4	10.2	1110.85	12.469
	1270	13-3-001	42100	42085	15	4.5	11.1	1197.74	20.235

All selected sampling points were processed in this manner, usually a few hundred points per calculation. The actual magnetic moment per unit mass, therefore, was determined from a statistical summary of all results. This included determination of the mean, median, and standard deviation for each sample set, at each estimated mass, to determine the level of consistency with which the model calculated dipole moment. Some variation was expected, given that "…magnetometer surveys are conducted on relatively horizontal planes that slice through the [three-dimensional] fields we wish to detect" (Hrvoic and Pozza 2004:3). The result is samples taken in areas of varying magnetic force within a single field. Other anticipated sources of variation were the potential effects of the objects' permanent magnetization, which could add and subtract vectors with the force of the induced magnetic field in ways not accounted for in the model. Finally, another source of potential variation was the necessary mathematical simplification of the object's geometry into a single point without physical dimensions. The results of these calculations are presented and analyzed following a description of each sample target.

3.2 SAMPLING SITES

Objects used for sampling were quantifiable masses of magnetic material composed mainly of iron or steel. All objects were accessible by boat, in and around BISC. Accessibility and quantifiable size were the most important factors for sampling site determination. Two sets of resources were used for testing: items within the BISC ASMIS inventory and Florida artificial reef sits adjacent to BISC within NOAA's FKNMS. To protect sensitive sites from looting or destruction, information regarding site location of BISC archaeological sites is not included in this report. Locations for sampled artificial reef sites can be found at http://myfwc.com/conservation/ saltwater/artificial-reefs/.

At the time of this study, BISC had 124 cultural resource sites logged in the NPS ASMIS Database. Forty-seven of these sites were of interest to the present study due to the documented presence of metallic cultural material. These ranged from individual iron or steel shipwrecks, assemblages of various-sized metallic objects, or wooden shipwrecks containing metallic fasteners and other assorted hardware. The main utility of these sites was known location and years of collective knowledge regarding site disposition resulting from systematic monitoring by NPS archaeologists. Quantification of the actual mass of ferrous material, however, was difficult in most instances, requiring divers to ground-truth the sites prior to sampling.

In addition to the 47 BISC archaeological sites, the state of Florida manages an extensive network of artificial reef sites, including 361 locations in Monroe, Dade, and Broward Counties. Of these, over 200 were reported to contain ferrous materials, ranging from large individual shipwrecks to piles of construction materials (for example, steel pipes and cable spools). The complete list of sites, including materials information, and descriptions, is available through the URL provided at the start of this section. Due to distance, however, many of the northern Broward and southern Monroe County sites were not easily accessible. Operating from the docks at BISC, the only artificial reef sites considered were those in Dade County, with some consideration given to northern Monroe county sites.

Unlike many of the BISC sites, which were comprised of smaller archaeological materials, the artificial reef sites were generally very large structures, such as entire sunken vessels. Sampling these sites along with BISC resources allowed for magnetic sampling across an entire range of material culture items with a great degree of variance in both type and size (including ferromagnetic mass versus item volume). The Florida Fish and Wildlife Conservation Commission (FWCC) is the governmental organization tasked with managing artificial reef permitting and placement, and maintains a comprehensive (and publically available) database of all Florida artificial reef sites. Included are locations, names, and descriptions (materials, approximate size, ect…), which were imported into *ArcGIS*. More specific physical dimensions of these resources, however, were needed to accurately assess the mass of magnetic material at a given site.

Jon Dodrill, Environmental Administrator for the Florida Division of Marine Fisheries Artificial Reef Program, was contacted for assistance in obtaining more detailed information regarding the artificial reef sites in Dade County. Dodrill (pers. comm.) provided the following response:

> Nearly all of these Miami-Dade artificial reef shipwrecks which you requested information for were from the early days of Miami-Dade's artificial reef program (1975-1985) and predated a regularly funded state artificial reef program where a dedicated position and funding was instituted in 1986 and prior to which there was no formal artificial reef activity record keeping at the state level. As a result we have no grant or contract related records on these shipwrecks that may provide more in depth historical and technical spec information on these older sites.

Dodrill did provide reference to a recent publication (Barnette 2010) which is a compilation of popular dive-site histories, including several of the Miami-Dade artificial reef sites. Barnette's (2010) book included information for 21 of the 37 sites identified in the artificial reef database, several of which were sampled.

Many of these listings are quite vague and would require research efforts beyond the scope of the present study to find records with more specific physical dimensions. Nevertheless, several of the artificial reefs are well documented and were ultimately chosen as sampling targets. Specifically, vessels with prior service in either the American or British navies are recorded in a number of sources, including the online NavSource Naval History website (navsource.org). These records contain displacement tonnages which directly correspond to the mass of the vessel. Otherwise, the tonnages listed are fairly ambiguous. In numerous places, Barnette (2010) refers to 'gross tonnage displaced', 'displaced gross tons,' or 'gross tons burden.' Despite this

ambiguity, approximate tonnages were calculated from length and beam proportions, but these were not as accurate as those obtained from vessels with documented naval service.

It is important to note, however, that listings of merchant vessels describe the *gross* tonnage of a vessel, which is a measure of the internal cargo capacity. The actual mass of a vessel is determined via displacement tonnage; the volume of water the vessel displaces. According to Naval Architect Charles H. Hughes (1917:168) if a vessel is "…floating in equilibrium in still water, the weight of water she displaces equals the weight of the vessel herself with everything on board." Hughes (1917:169) provides a calculation to determine displacement based upon carrying capacity: "…displacement = dead weight X 1.64 (approximately)," where dead weight is defined as "…the carrying capacity and includes the tons of cargo and generally the coal." Thus, each individual vessel was handled differently. Where displacement tonnage was available, it was used. Otherwise, an estimation was made from available information and observations during ground-truthing.

The mass of disarticulated or partial vessel remains was determined as the sum of individual components at the site, such as hull sections and machinery. Hughes (1917:122-125) provides the weights per square-foot for various thickness of plate steel and plate iron used in forming hull sections. The weight per-foot of structural shapes—such as shipbuilding channels, equal angle beams, unequal angle beams, I-beams, bulb beams, H-beams, bulb angles, equal tees, unequal tees, and so on—are also provided (Hughes 1917:129-154). Thus, the approximate mass of a section of iron or steel hull was determined by finding the area of plating and linear feet of framing materials and solving for their corresponding weights. Figure 3-10 and Figure 3-11 show commonly used structural shapes, as well as some common structural configurations. The tables for plate and structural shape weights are provided in the appendices of the research design (Bright 2012).
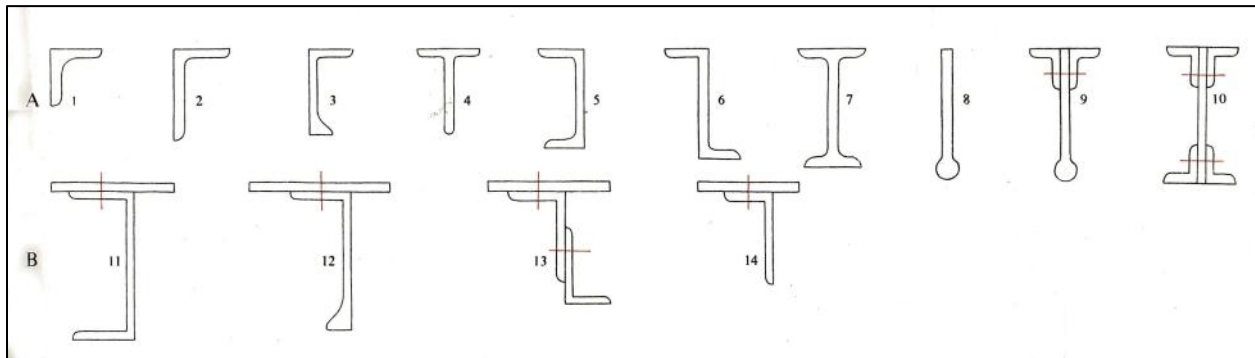
Figure 3-10. Assorted Cross-Sections of Iron and Steel Sections. (Source Engelbrektson 1975:39).
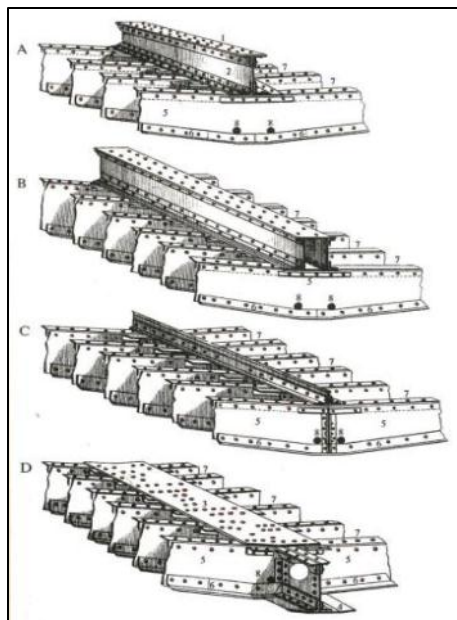
Figure 3-11. Representative Iron and Steel Framing Configurations. (Source Engelbrektson 1975:38).

The remaining archaeological sites of interest in the BISC ASMIS database were small individual artifacts. Specifically, these sites contained anchors or iron cannons. Anchors and iron cannon were ideal objects for magnetic modeling since the weights of each are historically recorded in great detail. In fact, anchor weights and designs were standardized by the mid-1600s, as were sizes and designs of naval ordnance. Thus, by reviewing the appropriate historical records, a fairly precise mass for each object, prior to introduction into the corrosive sea environment, was determined.

British naval historian Brian Lavery (1987:30) noted that "The proportions of anchors changed very little between 1600 and 1815." In fact, this holds true for most northern European varieties of anchor. With slight, but distinctive variations, the English, Dutch, French, and Spanish—those being European nations representing the bulk of historical maritime travel in the area of BISC—generally followed the same guidelines for anchor design. These guidelines are based upon the proportions of the parts of the anchor to one-another. For example, the stock was approximately equal in length to the shank, the shank was approximately three-times the length of the arm, and length of the arm twice the length of the fluke, and the breadth of the fluke equal to the diameter of the anchor ring (Tinniswood 1945:84-86; Lavery 1987:30; Curryer 1990:41-61).

Prior the 1600's, these proportions are not as well defined (see Tinniswood 1945), though afterwards they became explicitly specified through contracts between the navies and anchor manufacturers. English anchors fairly accurately follow the proportions listed above, and set the arms—which were straight—at a 60º angle to the shank. Dutch and French anchors, on the other hand, commonly featured an articulated arm, meaning an additional angle in the arm, where the fluke was welded. Figure 3-12 (courtesy of Dr. Fred Hocker, pers. comm.) shows this design characteristic of a Dutch anchor circa early 1600's. Figure 3-13 shows this design also present in French anchors. Spanish anchors were distinguished during this time period by slightly rounded arms and crown (Curryer 1990:41-48).
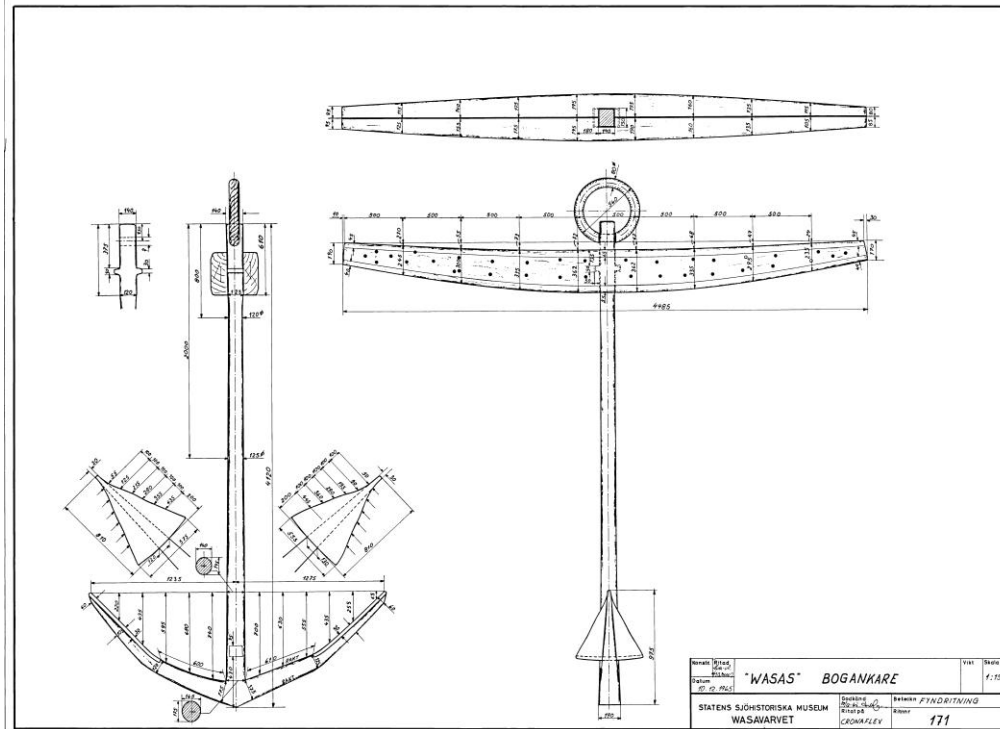
Figure 3-12. Bower anchor from Swedish ship Vasa. (Source Eva Marie Stolt, Vasa Museum; Dr. Fred Hocker pers. comm. 2012).
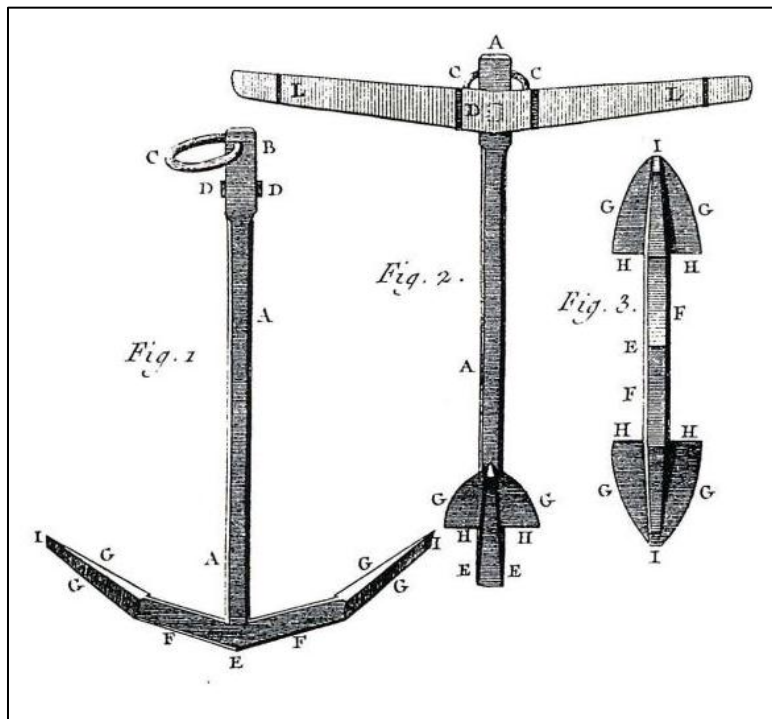
Figure 3-13. Example of French anchor design. (Source Curryer 1990:46).

Review of the ASMIS data for the 13 anchor sites showed that most are believed to be English-style longshank anchors. It should be noted, though, that at least one of the anchors, BISC00124 is improperly identified. Described as a 'stockless' anchor from the 19th-20th century, it actually appears to be an English-pattern longshank anchor from the 17th to 19th century. All sampled anchors were verified by actual field observation, measured, and compared to historical records to determine proper dating and corresponding weight.

One site which was sampled, BISC00062 consisted of an isolated cannon. The size and material, however, were unknown and were ascertained by ground-truthing. Like anchors, sizes and weights of cannon were thoroughly documented. Retrieval of diagnostic measurements from each will allow for cross-referencing with historical tables (see Caruana 1994, 1997).

Many of the shipwreck sites in BISC are wooden vessels containing iron fastenings, rigging, hardware, or other metallic machinery. The identity of the vessels wrecked at most of these sites is not presently known and therefore could not be used to retrieve historical information regarding the vessels' sizes. Were the identity known, furthermore, there is no convention to determine the mass of ferromagnetic material *within* a wooden vessel based upon its size. Though this will not assist in the main thrust of this study (to determine the magnetic moment of known quantities of magnetic materials), these sites offered another unique and valuable opportunity.

Wooden shipwrecks are ubiquitous submerged cultural resources throughout the world. They are commonly encountered within National Parks, as evident in the preponderance of wooden shipwrecks to iron or steel vessels in the BISC ASMIS alone. Understanding the magnetic signature of these vessels, therefore, is of obvious utility. More specifically, magnetic sampling of these sites can aid in the quantification of the amount of ferrous material within the total mass of a wooden vessel.

Historically, the use of metal within wooden vessels varied greatly. Composite ships substituted iron in the place of wood for certain structural members such as beams and knees, as well as for fasteners, and therefore contained large amounts of magnetic materials. Older wooden vessels, those dating prior to the 18th century, used iron much more sparsely. The proportion of ferrous material to non-ferrous materials in a ship's structure varied with known historical construction methodologies. Magnetically sampling these wooden vessels provided a better understanding of how much magnetic material they contained and therefore the corresponding magnitude of anomaly generated.

The necessity of such data is rooted in the process of quantitative data quality assessment. The magnetic modeling algorithm determines thresholds of coverage as the composite of dissolved spatial buffers extending from each magnetic sampling point. Throughout an entire survey area, this process reveals areas of greater or less coverage, expressed in terms of the detectable masses of ferrous material. The purpose of this type of assessment is to determine types of archaeological material that may have gone undetected during a given survey. Cultural items not composed entirely of magnetic material, therefore, must somehow be accounted for.

Analysis of a magnetic survey block might reveal it covered an area to such a degree that in 95 percent of the space a ferromagnetic mass of 3,000 kg would have been detected. In terms of material culture, this could equate to a piece of naval ordnance, iron or steel machinery

(windlass, steam engine components, etc.), or any other entirely ferromagnetic item of 3,000 kg or greater. Yet, the meaning of this figure to items not composed entirely of ferromagnetic material is less clear. For example, a 50 ton (45,360 kg) wooden sloop containing 2.5 tons (2,268 kg) of ferrous material—5 percent of the vessel's total mass—would have potentially been missed during the survey. Even though the total mass of the sloop was greater than that defined as the detection threshold, only the proportion of magnetic material can be used to express its detectability, thus some determination of the amount of ferrous material typically found in wooden shipwrecks is necessary.

Several historic shipbuilding treaties (see Murray 1745, Chapman 1786, and Desmond 1919) give dimensional information relating scantling sizes and vessel proportions to overall tonnages. Desmond (1919:19) describes the general formula used to determine tonnage—defined as the sum of internal space of the vessel—by the following formula:

$$\text{Tonnage} = \frac{L*W*D*.75}{100}$$

This tonnage formula does not relate to the weight, or displacement, of the vessel, but instead to its internal capacity. Thus, additional calculation is necessary to determine the total mass of the vessel. Given that the present study only needs to understand the ratio of ferrous material to non-ferrous material, gross tonnage can be used as the 'total' tonnage of the vessel. Assuming that displacement tonnage and gross tonnage are directly linked, then the ratio of ferrous material to non-ferrous material can be expressed as the gross tonnage of the vessel divided by the calculated mass of iron based on magnetic sampling. In this way, empirical data can provide a means to quantify the expected magnetic anomaly produced by wooden shipwrecks.

3.2.1 BISC 0002 ENGLISH CHINA WRECK

This site consisted of the remains of a wrecked wooden-sailing vessel. Brocken ceramics are apparent throughout the area, indicating the vessel was most likely a merchant ship. Large iron fasteners were observed along the vessel's keel, and heavily concreted iron remains were intermittently dispersed around the main artifact scatter. In all, there was a very small total mass of ferromagnetic material on the site, relative to the extent of remains. The area, therefore, manifested a very small magnetic signature. The utility of this location was to collect data and observe the magnetic signature of a magnetically small, but otherwise moderately sized archaeological site similar to other historical wooden vessels BOEM or NPS may encounter in federally managed areas. Sampling on this site was limited to a single survey block at 10 m line spacing.

3.2.2 BISC 00020 HMS *FOWEY*

This site was the remains of 18th century British warship HMS *Fowey* (see Skowronek and Fischer 2009). During the 2013 field season, NPS SRC led an excavation and mapping project at BISC 0020, concurrent with the IAA phase 2 task field operations. As a result, an extensive

magnetometer survey of the shipwreck site and surrounding areas was planned and executed to the mutual benefit of both projects. Data was collected and processed using the Python toolbox, which assisted the excavation and mapping of the ship's remains, and portions of the dataset were isolated for analysis of magnetic moment. Specifically, the area around the main site extent (Figure 3-14 and Figure 3-15) was processed. This map represents the magnetic signature of several ferromagnetic objects present: three cannon, large piles of cannon balls, iron rigging, and numerous iron fasteners through the wooden remains. Much like BISC 0002, this will provide information regarding the detectability of partially ferromagnetic sites, particularly historic wooden vessels, in this case a naval vessel.
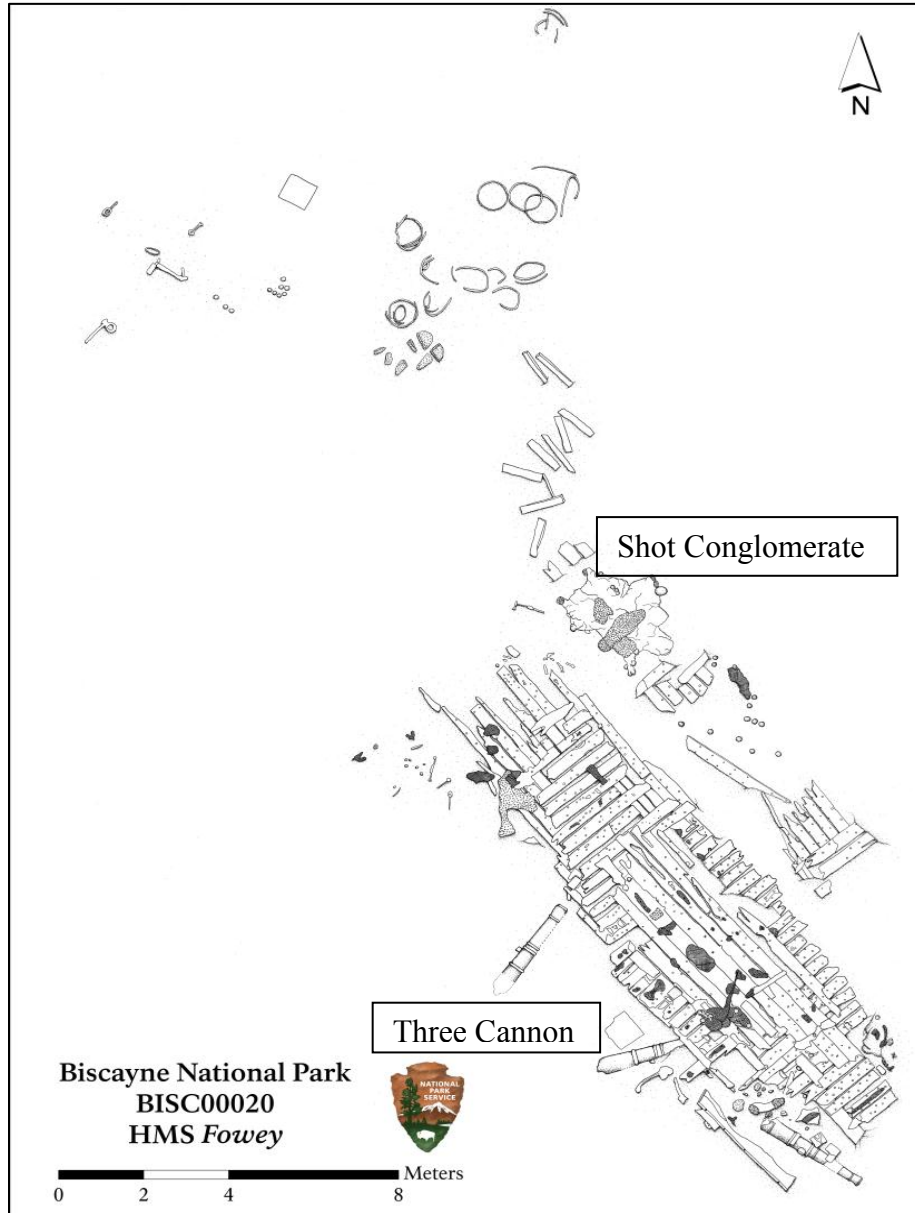
Figure 3-14. Site plan of BISC 00020 highlight cannon and shot conglomerate.

Though there were metallic fasteners and small metallic artifacts dispersed throughout the site area (such as rigging parts, and barrel hoops), the main site component had a consolidated concentration of ferromagnetic elements. Surveyed at sufficient distance to consider these items a single point source, their magnetic signal was isolated and used to determine the magnetic moment of the objects detected. Specifically, this area contained three cannon (18 pounders), estimated at 2032 kg each, plus a large pile of 18 lb (8.1 kg) shot. Using estimates of between 50 (405 kg) and 100 (810 kg) individual shot pieces, a high and low mass estimate of 6906 kg and 6501 kg were derived (for cannon and shot specifications, see Caruana 1994,1997).

An additional component to the site was discovered during survey efforts. A very large anomaly was located approximately 90 meters to the south and east of the main area of wreckage (Figure 3-16). When investigated, divers located the remains of a very large anchor buried in the seabed (Figure 3-17). Historical research indicated the anchor could have weighed 38-40 hundredweights (cwts), equating to 1930-2,032 kg (Curryer 1990:53-61). Additional investigation of the area yielded no additional finds, so the data points surrounding the anchor were isolated and used to determine its magnetic moment. Since the data were acquired during an exploratory survey, however, the survey lines were only run in a single direction unlike the standard survey protocol used at other sampling targets. Nevertheless, these data were a useful addition to that collected at all other sampling sites.
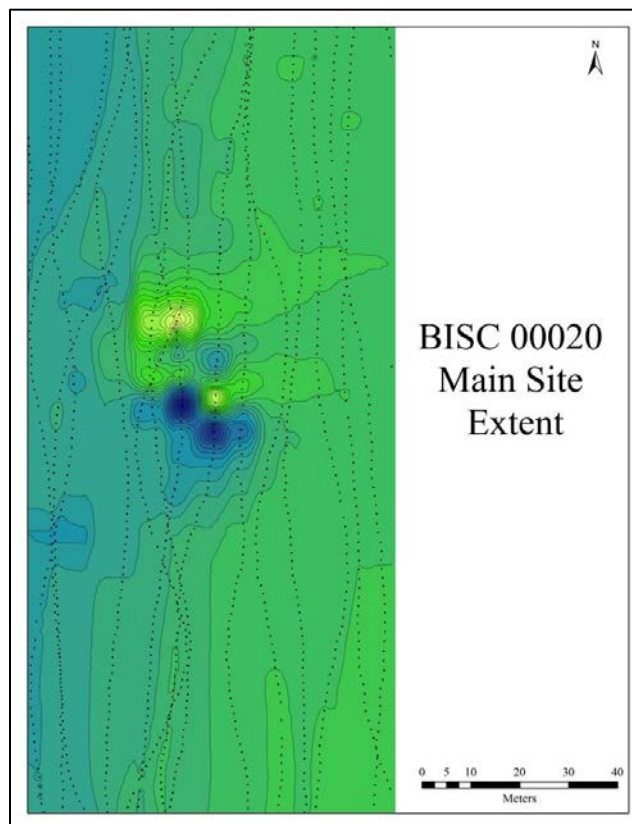
Figure 3-15. Main site extent for remains of HMS *Fowey*.
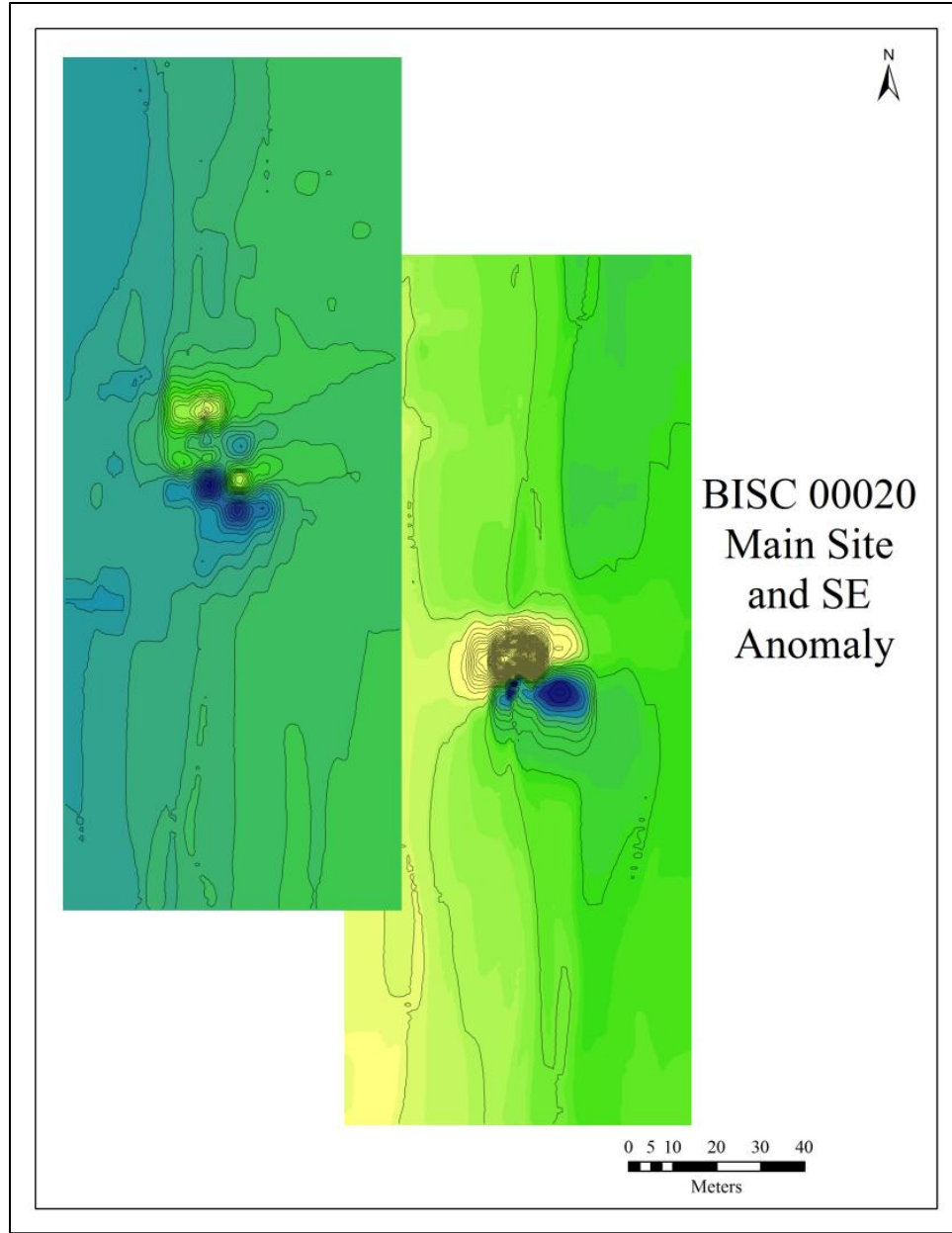
Figure 3-16. Main site area (left) and large anomaly (right) approximately 90 meters to the south and east.

Figure 3-17. Diver investigating magnetic anomaly. (Source: NPS SRC).

3.2.3 BISC 00062 LONG REEF CANNON

This location contained a single, isolated cannon (Figure 3-18). Though the ASMIS entry for the site did not specify the material used to make the cannon, the presence of iron was confirmed by divers prior to survey. After measurements were collected by divers, an approximate mass was determined for the cannon. Historical records, however, yielded a wide range of possible weights, depending upon the design of the piece. Though general measurements were taken, concretion and biofouling on the artifact obscured the details necessary to make a more determinate assessment of the artifacts age, thus, all the possible sizes were used in determining the objects mass, 16 cwts (813 kg), 18 cwts (914 kg), 20.5 cwts (1,041 kg), 24.5 cwts (1,244 kg), 26 cwts (1320 kg), and 29.5 cwts (1,498 kg) (Caruana 1994:106, 1997:14-66). Each of the masses was also used to determine respective magnetic moments. The site was sampled from east-west and north-south orientations, at 10 m line spacing. One line was run directly over the remains, with an additional four to each side, totaling nine lines.

Figure 3-18. Single iron cannon at BISC 00062. (Source: BISC Photo).

3.2.4 BISC 00008 KEEL SHOWING WRECK

BISC 00008 was the third and final wooden vessel sampled during the survey. Located in the inner-reef area of the park, and flanked on it northern and southern boundaries, the site was only sampled in an east-to-west orientation (Figure 3-19). The archaeological remains consisted of two distinct ballast piles connected by an area of wooden framing elements containing several iron fasteners. Small, metallic artifacts were also present in and around the ballast piles. Much like BISC 00002, the majority of material remains at the site were non-magnetic materials. Thus, analysis of the magnetic signal produced by the site will inform the detectability of historic wooden vessels. Site was sampled with 10 m line spacing.
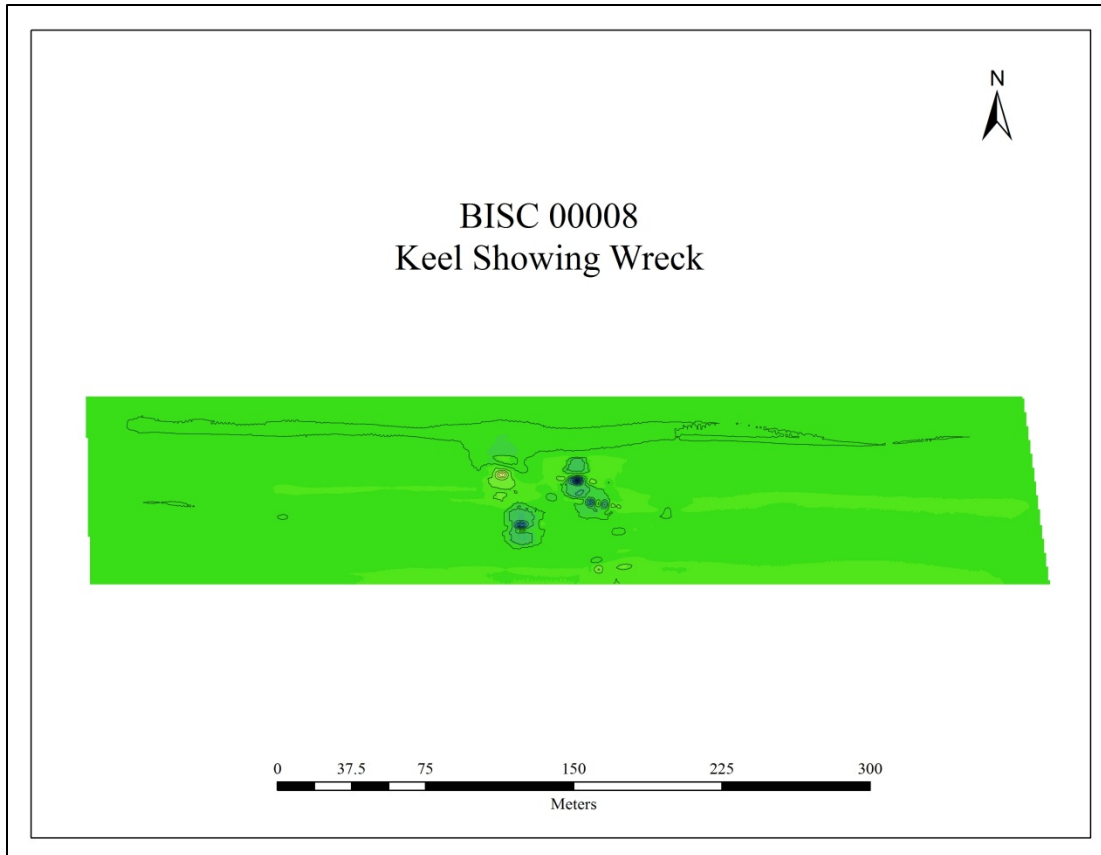
Figure 3-19. Full field map, contoured at 7 gammas, of BISC 00008.

3.2.5 BISC 00089 SUNKEN BELL BUOY

This was a small site in the northern area of the park. It contains the remains of a former navigation buoy, including riveted steel frames and a large brass bell. These remains structurally resembled a small tower, with a steel base, steel frames extending upward towards the bell's mount. In addition, a 5.4 meter length of steel chain is situated next to these remains. Using the dimensions and thickness of the steel elements present, the mass of the materials was calculated as the sum of the weight per foot or area of the various components (see Hughes 1917:122-124; Graumont and Hensel 1994). Based upon these calculations, it was determined that the site contained between 1,051 and 2,823 kg of ferromagnetic material; everything but the brass bell. The site was sampled from east-west and north-south orientations, at 10M line spacing. One line was run directly over the remains, with an additional four to each side, totaling nine lines.

3.2.6 BISC 00114 BOCA CHITA NORTH PONTOON

BISC 00114 consists of the remains of a fairly modern steel pontoon (Figure 3-20). In the same way the mass of BISC 00089 was determined as the sum of the lengths and areas of its

constituent parts, divers also collected similar information. Using the materials data in Hughes (1917:122-142), the mass of each individual component was determined. The area of the body was determined as a cylinder, but was scaled down 80 percent to account for the missing material along the top. The range of estimated masses was between 2,707 and 3,007 kg. The site was sampled from east-west and north-south orientations, at 10 m line spacing. One line was run directly over the remains, with an additional four to each side, totaling nine lines.

Figure 3-20. NPS SRC Diver ground-truthing BISC 00114. (Source NPS SRC).

3.2.7 BOCA CHITA PONTOON SOUTH

Though this site was not in the BISC ASMIS database at the time of the study, it was the counterpart to the remains at BISC 00114. The object was a nearly identical modern steel pontoon, completely intact, approximately 500 meters from BISC 00114. The same calculation used to determine the mass of BISC 00114 was used to determine the mass without using the 80 percent cylinder reduction. Thus, it was determined the site contained between 3,007 and 3,300 kg of ferromagnetic material. The site was sampled from east-west and north-south orientations, at 10 m line spacing. One line was run directly over the remains, with an additional four to each side, totaling nine lines.

3.2.8 BISC 00122, BISC 00123, BISC 00124: HISTORICAL ANCHORS

This site was discovered by the SRC during a regional-level exploratory survey. The remains consisted of an isolated anchor partially embedded in the seabed. No additional archaeological materials were found in the immediate vicinity. Using numerous historical sources (Tinniswood 1945:84-86; Lavery 1987:30; Curryer 1990:41-61), the sizes of these anchors were determined:

BISC 00122: 10 cwt (508 kg)/ 12 cwt (609 kg)

BISC 00123: 9 cwt (457 kg)/ 15 cwt (762 kg)

BISC 00124: 8 cwt (406 kg)/ 11cwt (559 kg)

Each was sampled in both a north-south and east-west orientation, with a line spacing of 10 m. One line was run directly over the target, and four were run on each side. Thus, for each block nine lines were run.

3.2.9 DREDGE FLOAT

This sample location was not an archaeological resource, but a consolidated piece of modern debris within BISC waters. It was a single float used to support dredge piping. Essentially it was two large steel barrels set parallel to each other, attached at the ends with angle iron to form a structure similar to a raft. Using materials information from Hughes (1917:122-142), a high and low mass was calculated for the object: 1,730 kg and 1,999 kg. The site was sampled from east-west and north-south orientations, at 10 m line spacing. One line was run directly over the remains, with an additional four to each side, totaling nine lines.

3.2.10 *ALMIRANTE*

This was an older artificial reef established in April of 1975, according to Florida Fish and Wildlife records. The site consists of the remains of a former Royal Navy ship HMS *Gillstone*, an *Isles* Class trawler (see Figure 3-21). Following the end of the Second World War, the vessel was decommissioned from the Royal Navy, converted to a cargo vessel, and traded among various owners. A Miami-based company bought the vessel in 1970, changing the name to *Almirante*, only to abandon the ship several years later on the Miami River. In response, the city of Miami had the vessel's superstructure removed (so as to minimize the risk to offshore navigation) and sank the ship to form an artificial reef. Though the vessel remains generally intact, decades underwater—including several major hurricanes—have caused some deterioration along the vessel's structure (Barnette 2010).

Since the vessel was constructed for the Royal Navy and commissioned for service, it was well-documented in the historical record (see Bishop 1998:512). This included information on size, speed, propulsion, armament, and fighting capabilities. In addition to recording basic physical dimensions such as length and width, the displacement tonnages—the weight of water displaced by the vessel—is commonly recorded for all naval vessels. Thus, HMS *Gillstone*, as per the *Isles* class standards, displaced 545 tons , or 553,746 kg. The vessel underwent modification when converted from a naval vessel to a freighter; however, much of the modification was superficial: re-configuring internal spaces to hold cargo and modifying the superstructure. The bulk of the vessel's hull, therefore, would have remained the same. The removal of the superstructure prior to deployment as an artificial reef, in addition to the site formation process once underwater, all resulted in a reduction of total mass. Thus, the ferromagnetic mass remaining is less than 553,746 kg. Assuming a reduction in mass from 545 to 500 tons, a mass of 453,592 kg was used to determine the object's magnetic moment. The site was surveyed using 30 m line spacing, with a single line directly over the site, and four on either side, a total of nine. Additionally, to keep

the magnetometer far enough away from the object for its signal to resolve into a point source, a surface tow was used despite the depth of water being nearly 150 feet.

Figure 3-21. Image of HMS *Gillstone*, later *Almirante*. (Source: Imperial War Museums, Online Collections).

3.2.11 BLUE FIRE

According to Florida FWCC records, this artificial reef was established in January of 1983. The vessel was a freighter seized by the United States Coast Guard while transporting Cuban refugees. Following the seizure, the vessel was removed from service and transferred to the artificial reef program. A decade after its sinking, the waves generated by Hurricane Andrew nearly broke the vessel in half, bending the vessel amidships into an L-shaped configuration (Barnette 2010). Barnette also reported the vessel was originally 183 feet long, making it slightly larger than the 164-foot *Isles* class *HMS* Gillstone. Since a mass of 500 tons was used for *Almirante*, as slightly larger mass of 525 tons, or 476,272 kg, was used to calculate the magnetic moment of *Blue Fire*. The site was surveyed using 30 m line spacing, with a single line directly over the site, and four on either side, a total of nine. Additionally, to keep the magnetometer far enough away from the object for its signal to resolve into a point source, a surface tow was used despite the depth of water being nearly 150 feet.

3.2.13 *ST. ANNE D'AURAY*

Florida FWCC records state that 110 ft steel vessel *St. Anne D'Aury* was established as an artificial reef in March 1986. Otherwise, there was little additional historical information. Bartnette (2010) reiterates the data in the FWCC database, noting that the site remained upright and intact following Hurricane Andrew. During ground-truthing, divers confirmed the vessel's location and observed that it was arranged like a large fishing trawler. Based upon these observations and the vessel's size, several estimated masses were used to calculate the object's magnetic moment: 400 tons (362,874 kg), 350 tons (317,515 kg), and 300 tons (272,155 kg). The site was surveyed using 30 m line spacing, with a single line directly over the site, and four on either side, a total of nine. Additionally, to keep the magnetometer far enough away from the object for is signal to resolve into a point source, a surface tow was used despite the depth of water being nearly 90 feet.

3.3 RESULTS AND CONCLUSIONS

With the exception of BISC 00002, BISC 00008, and BISC 00020, each target was sampled twice with perpendicular survey plans. Thus, twenty-six individual survey blocks were completed over the fifteen targets. For each target, a range of masses was determined based upon historical research (Table 3-2). Using the methodology previously described, where the inverse cube equation was solved for magnetic moment per unit mass in units of $\frac{emu}{g} x10^4$:

$$\sigma = \frac{B\,r^3}{w}$$

with magnetic density flux (B) in units of gamma, distance (r) in units of centimeters, and mass (w) in kilograms. All data points influenced by the object's magnetic field were isolated and moved into a calculation spreadsheet where numerous potential magnetic moments were calculated for each site for every survey block and mass combination (Table 3-3).

Inferences and interpretations regarding the inverse cube model and the strength of an object's magnetic field, therefore, were determined by statistical evaluation of this empirical data. Based upon this model, it was found that the inverse cube model adequately characterized the magnetic fields of ferromagnetic cultural materials. Trends emerged in the strength of an object's magnetic field emerged according to the age (time of submergence) of the object, orientation to the sensor, and materials used. Additionally, observations were made regarding the detectability of historical wooden vessels with ferromagnetic components.

Table 3-2
Ferromagnetic masses determined for sample sites. Type codes are as follows: C/S is cannon and shot; A is anchor; C is cannon; MD is modern steel debris; SS is a steel ship.

Site	Type	Estimates of Ferromagnetic Mass (kg)					
		Min(kg)					Max(kg)
BISC 00020	C/S	3,453	3,250	6,501		6,906	
BISC 00020	A	1,930		1,981		2,032	
BISC 00062	C	513	914	1,041	1,244	1,320	1,498
BISC 00089	MD	1,051		1,684		2,823	
BISC 00114	MD	2,707.10		2,970.20		3,007.90	
BISC 00122	A	508				609	
BISC 00123	A	457				762	
BISC 00124	A	406				559	
Almirante	SS	226,796		453,592		553,746	
Blue Fire	SS	272,155		362,874		453,592	
Dredge Float	MD	1,730				1,999	
BC Pontoon South	MD	3,007.90				3,300.27	
St Anne D'Auray	SS	272,155		317,515		362,874	

The statistical overview of all the datasets is contained in Appendix IV, and includes 65 individual magnetic moment calculation datasets excluding the two additional non-calculated datasets from the wooden shipwreck remains sampled at BISC 00002 and BISC 00008 (where a quantifiable mass of ferromagnetic material could not be determined). Each overview includes a frequency distribution for the dataset as well as a report of the mean, median, standard deviation, and range of the derived magnetic moment values. From these statistical overviews several observations were made.

First, all of the frequency distributions for the calculated magnetic moments—derived from datasets ranging from N=46 to N=2009 sample points—were positively skewed, with nearly all of the values for each data set within two standard deviations of the mean value. In most cases, the relative standard deviation (ratio of mean to standard deviation, RSD) of a given dataset was approximately 100 percent (Table 3-4), meaning that though the values clustered around a mean value, the positive outlying values skewed the mean away from the median values derived (Table 3-5). In most cases, these high positive values were few, but substantial, indicating there were areas of an object's magnetic field which were significantly stronger than the remaining field. Presumably, these areas are proximate to the object's magnetic poles. Thus, as a result of this skewing, the median values presented in Table 3-5 more accurately characterize the predominate magnetic field strength for a given object. For the present study, the median values were used as the designated modeling parameter for a given object based upon the following rationale: though discrete areas of higher density flux were observed, the majority of the magnetic field's spatial extent was much weaker. Thus, to model an object's detectability, the predominate (i.e. most likely to be sampled) magnetic field strength was selected.

Table 3-3
Mean of values derived for the dipole moments of each target by survey block and calculated mass. All magnetic moments in $\frac{emu}{g}$.

	Estimated Mass (kg)					
	Higher	**Med/High**	**Med.**	**Med/Low**	**Low**	**Lowest**
Site						
BISC 00020 Main	17.496				18.586	
BISC 00020 Anom	108.935		111.667		114.69	
BISC 00062 NS	4.139	4.697	4.984	5.956	6.784	7.627
BISC 00062 EW	1.837	2.085	2.212	2.643	3.011	3.385
BISC 00089 NS	10.276		17.223		27.603	
BISC 00089 EW	8.535		14.307		22.925	
BISC 00114 NS	63.547		64.261		70.506	
BISC 00114 EW	67.502		68.359		75.003	
BISC 00122 NS	82.939				99.429	
BISC 00122 EW	72.039				86.362	
BISC 00123 NS	29.225				48.73	
BISC 00123 EW	112.736				187.976	
BISC 00124 NS	52.148				71.8	
BISC 00124 EW	24.112				33.045	
Almirante NS	61.186				74.696	
Almirante EW	64.853				79.173	
Blue Fire NS	53.548				56.225	
Blue Fire EW	61.929				65.026	
Dredge Float NS	59.806				69.105	
Dredge Float EW	54.537				63.261	
BC Pontoon S. NS	124.317				136.4	
BC Pontoon S. EW	85.201				93.482	
St Anne D'A NS (EW)	21.787		24.9		29.05	
St. Anne D'A EW	21.005		24.063		28.074	

Table 3-4
Relative standard deviations for each survey block; these are reported at percent of mean and therefore do not have units.

BISC 0020 A	BISC 0020 M	BISC 0062 NS	BISC 0062 EW	BISC 0089 NS	BISC 0089 EW
151.329	88.899	96.041	74.604	76.141	84.612
BISC 0114 NS	**BISC 0114 EW**	**BISC 0122 NS**	**BISC 0122 EW**	**BISC 0123 NS**	**BISC 0123 EW**
426.130	424.390	86.151	140.157	96.286	139.256
BISC 0124 NS	**BISC 0124 EW**	*Almirante* **NS**	*Almirante* **EW**	*Blue Fire* **NS**	*Blue Fire* **EW**
124.793	102.245	80.681	79.237	83.313	80.561
Dredge NS	**Dredge EW**	**Pontoon NS**	**Pontoon EW**	*St. Anne D*. **NS**	*St. Anne D*. **EW**
119.017	80.161	197.384	237.357	76.809	107.656

Table 3-5
Median of values derived for the dipole moments of each target by survey block and calculated mass. All magnetic moments in $10^4 \frac{emu}{g}$.

Site	Mass (kg)					
	Higher	**Med/Higher**	**Med.**	**Med/Lower**	**Low**	**Lowest**
BISC 00020 Main	11.782				12.516	
BISC 00020 Anom	31.852		31.884		33.535	
BISC 00062 NS	2.751	3.122	3.312	3.959	4.509	5.069
BISC 00062 EW	1.633	1.853	1.966	2.351	2.677	3.001
BISC 00089 NS	8.122		13.615		21.816	
BISC 00089 EW	6.565		11.005		17.634	
BISC 00114 NS	23.838		24.141		26.487	
BISC 00114 EW	25.243		25.563		28.047	
BISC 00122 NS	48.506				58.15	
BISC 00122 EW	22.997				27.569	
BISC 00123 NS	29.225				37.433	
BISC 00123 EW	50.249				84.228	
BISC 00124 NS	22.123				30.46	
BISC 00124 EW	14.346				19.54	
Almirante NS	51.562				63.32	
Almirante EW	56.562				69.052	
Blue Fire NS	40.266				42.279	
Blue Fire EW	47.933				50.329	
Dredge Float NS	59.279				48.132	
Dredge Float EW	42.921				50.042	
BC Pontoon S. NS	58.293				63.959	
BC Pontoon S. EW	59.101				64.845	
St Anne D'A NS	17.452		19.946		23.27(	
St. Anne D' A EW	14.984		17.125		19.979	

The grouping of most values within the first and second positive standard deviations of their respective frequency distributions illustrates that most values derived for magnetic moment were

fairly consistent. Only within discreet areas of the object's magnetic field were there large asymmetries. Though these variations were observed, especially within the objects made predominately of iron, several predictable (theoretical) factors explain the differences. Every magnetic sensor has an inherent amount of 'noise,' or innate variation. In other words, were a given sensor placed in a magnetically neutral space, it would nevertheless produce varied readings. Sensor noise is exacerbated by environmental parameters such as imperfections in the survey package hardware, the towfish hitting the bottom, or external interference (geological anomalies and solar activity). Thus, a 1-2 gamma variation would reasonably be expected in a normal survey dataset (see Camidge et al. 2010). At increased distances, however, adding 1-2 gammas of sensor noise on top of the object's measured magnetic density flux would result in differing calculated magnetic moments.

Another factor introducing variation into the datasets was the geometry of an object's magnetic field (at this point excluding discussion about the geometry of the object itself). This field extends three-dimensionally into space and, like Earth's magnetic field, is characterized by asymmetries in magnetic field strength. While using a magnetometer, however, this three dimensional field is sampled along a flat, two-dimensional plane (see Hrvoic and Pozza 2004), meaning the sensor will encounter these slight asymmetries as it moves through an object's magnetic field (Figure 3-22). Though the field strength predictably changes between positive and negative poles, the rate of change throughout its geometric extent is not consistent. Thus, the magnetic field is measured as stronger in certain locations of the field relative to others. As a result, these variations manifest when using acquired sample points to calculate an object's overall magnetic field strength: a range of values will result from the range of strengths.

When combined, sensor noise and field asymmetries inevitably introduced the variability observed throughout the sampled datasets. Another factor introducing variability is the geometry of the object itself. Hall's equation, introduced during the theory section, included a parameter whereby the length and width ration of a given object $\left(\frac{a}{b}\right)$ had a multiplicative effect on the object's potential magnetic density flux. The inverse cube function integrated into the present study's modeling algorithm, however, assumes a dimensional ratio of 1 consistent with a sphere or point source. At sufficient distance, in fact, the magnetic signal of all ferromagnetic materials resolves into a single point source. Yet, during operational testing the magnetometer passed directly over many of the targets. Thus, though they were mathematically treated as point-source signals, they were sampled at proximity where the increased magnetic field strength characteristic of elongated objects was recorded in the data record, resulting in the high relative standard deviations in the calculated magnetic moment values.

Perhaps the most significant factor influencing the derived magnetic moment values was the effect of the object's permanent magnetism. As discussed in the theory section, this form of magnetism may significantly impact an object's detectability and observed flux, but is also too complex and object-specific to be effectively modeled. Thus, for the present study it was excluded from the modeling algorithm, which instead incorporated only the properties of the object's induced magnetism. The range of derived magnetic moment values, especially those beyond the theoretical values determined for the induced magnetic field of pure iron, were likely due to the interaction of the object's remnant magnetism with its induced field.
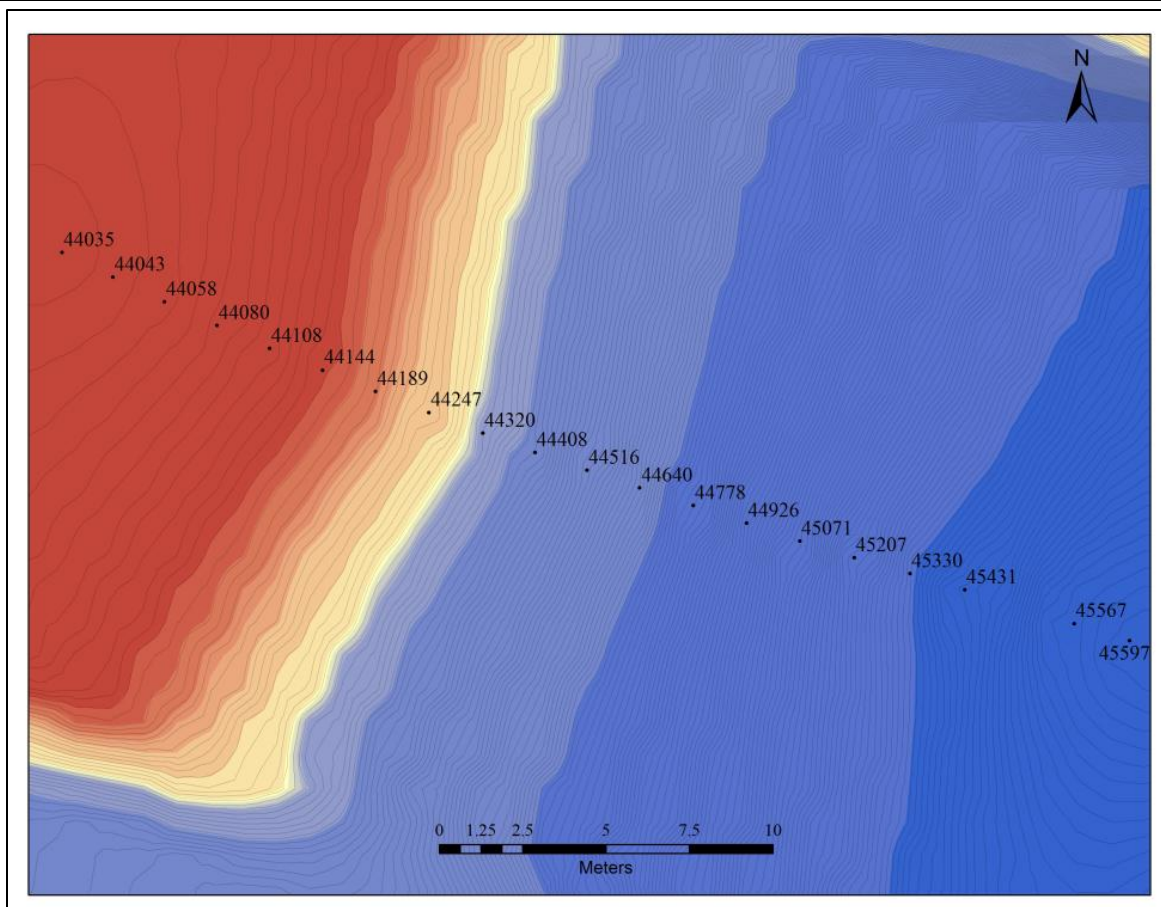
Figure 3-22. Individual sample points within a large magnetic anomaly (*St. Anne D'Auray*) demonstrating minor asymmetries in the field change, i.e. the rate of positive and negative flux is not uniform throughout the field.

In certain sites, this effect was clearly evident. For example, the BISC Pontoon, BISC 00122, and BISC 00020 Anomaly sites had magnetic moment values greater than the theoretical threshold established by Briener; that is, greater than $100 \frac{emu}{g}$. In these instances, the simplest explanation for why the observed the magnetic field strength exceeded the maximum theoretical value was that the object's permanent magnetism was acting in addition to the induced magnetic field, the sum of which was actually being observed.

Conversely, the very low magnetic moment values derived for BISC 00062, BISC 00089, and BISC 00020 Main could also be the effect of permanent magnetism, in this case interacting negatively with the induced field—however their weakened magnetic fields could have also been the result of site formation processes (such as exposure to heat during the deposition process; in other words, the object was in a ship that burned and sank). It is also possible that these lower magnetic fields resulted from the chemical composition of the individual materials; they were iron alloys with inherently lower magnetic susceptibilities.

Based on our measurements, in most cases permanent magnetism appeared to enhance the magnetic field strength of an object beyond the theoretical range for an induced magnetic field

for pure iron. Assuming that the presence of permanent magnetism increases the predicted magnetic density flux, the mitigation for survey modeling would be to simply use low magnetic moment values. This would ensure that objects without appreciable permanent magnetism will be accounted for, and those with permanent magnetism will exceed the predicted thresholds of detection.

Interestingly, the older historical materials (BISC 00020 Anomaly, BISC 00122) tended to have stronger magnetic fields than the larger, more structurally complex artificial reef sites (*Almirante, Blue Fire, St. Anne D'Auray*). The primary difference between the two would be chemical composition. Historical artifacts were made mostly of iron, whereas the modern ships were built from varying steel alloys; alloys with (presumably) inherently weaker induced magnetic fields. This could be attributed to the internal structural orientation of the large ships resulting in a more homogenous magnetic field.

More puzzling, perhaps, was the variability of relative standard deviations (RSDs) between two survey blocks acquired over the same sampling site. Table 3-4 reported these values, where the NS and EW survey blocks over a target had noticeably different values. When the means of the RSD from north-south oriented blocks and east-west oriented blocks were compared there was little difference. The variation, therefore, was produced by the individual object. In other words, there was no statistically significant variability in the derived values when an object was sampled north-south versus east-west overall.

Each object, however, was oriented differently with respect to earth's magnetic field. Thus, sampling the object in one general direction encountered a more complex 'slice' (to borrow from Hrvoic and Pozza 2004:3) than that experienced at a perpendicular orientation. Sampling the more complex field, therefore, produced one dataset with more variable values. Thus, the trend emerged where the frequency distribution of magnetic moment values was affected by the orientation of the object to the Earth's magnetic field; though the median calculated magnetic moments remained fairly constant (see Table 3-5). The orientation of the sampled objects, therefore, influenced the range of observed values, though the measured magnetic field strength remained the same. Since the magnetic moment values were consistent regardless, the theoretical detectability of an object remained the same. The mathematical complexities of doing so aside, this observation argued against an attempt to incorporate potential object orientation into the modeling system.

Numerous types of materials were sampled during field testing. Inquiry into the specific material properties of the sampled objects was deemed impractical, so sample targets were structurally classified as either iron or steel. The sites, furthermore, spanned a large temporal range. This included historical materials which have been inundated in marine environment for nearly 400 years (BISC 000020), to artificial reef sites inundated less than 40 years (*Almirante, Blue Fire,* and *St Anne D'Auray*). The age of the sampled material impacted the observed strength of its magnetic field. From these observations, the inference is that electrochemical changes to the material as a result of submersion in a marine environment also degraded the material's magnetic properties. Though metallurgic or chemical analysis of materials was beyond the scope of this study, it was generally assumed that if ferromagnetic materials degraded, the magnetic properties of the object would likewise degrade.

As a counter-point to chemical degradation reducing magnetic field strength, however, the aforementioned effects of permanent magnetism can be sufficient to maintain a very strong magnetic field, especially if favorably oriented with Earth's ambient field. Referring to Table 3-5, the magnetic moments derived for modern materials (Dredge Float, *Almirante, Blue Fire,* and *St. Anne D'Auray*) were lower than those derived for historical materials (BISC 00020, BISC 00062, BISC 00089, BISC 00122, BISC 00123, and BISC 00124); materials which had undergone significantly more chemical alteration during centuries of submergence in the marine environment. These historical structures, however, would have been made entirely of iron (though not 100 percent pure iron), conforming to historical patterns of metallurgy and material properties. The greater percentage of iron in these materials increased the probability that the remnant magnetism would enhance the overall magnetic field strength when combined with the induced field. Though more thorough testing would be needed to definitively substantiate and quantify the permanent magnetism of these objects, and the relative magnetic field strength of varying steel alloys compared to iron, a trend emerged where historical materials, on average, had a higher magnetic moment compared to more modern materials.

Compared to the value representing the magnetic moment of a consolidated amount of pure iron derived in the Theory section (10-100, Breiner; 15-31, Camidge) the sites sampled had highly variable magnetic field strengths. Non-magnetic elements within these metals (such as carbon) could diminish the magnetic field strength, as would chemical changes resulting from site formation processes during or following inundation. The latter effect most likely impacts the magnetic signal of archaeological materials, especially in a warm marine environment such as BISC. Conversely, the remnant magnetism of the object could significantly increase the magnetic field strength beyond the limits of the material's induced susceptibility. Though the modeling algorithm cannot account for the effects of materials composition, permanent magnetism, object orientation, and metallurgic factors (such as heating), the user can simply select lower magnetic moment values to account for the worst-case scenario of materials within their survey having lower magnetic field strengths. In areas where material types are unknown, a conservative magnetic moment value will account for more objects and yield higher detection types but also risks higher false positives.

3.4 OPERATIONAL MAGNETIC MOMENT (Σ) VALUE SELECTION

The results of field testing underscore the complexity of marine magnetic survey for archaeological resources. Operational field testing sought to determine what empirically derived magnetic moment value(s) for ferromagnetic archaeological materials is appropriate for modeling purposes. In the theory section, the magnetic moment for pure iron was calculated as the product of several variables:

$$M = \chi\, B_e\, w$$

such that magnetic moment (M) was the product of an object's mass specific susceptibility (χ), Earth's ambient magnetic field (B_e), and the object's mass (w) in grams. For iron, χ is a constant $50.36\,\frac{cm^3}{g}$, based upon iron's volumetric susceptibility and bulk density. The applied magnetic field (B_e) was the strength of Earth's ambient field—taken for a given time and location based

upon data collected by NOAA's NGDC at http://www.ngdc.noaa.gov/geomag-web/#igrfwmm. Expressed in metric units, mass (w) was converted from grams to kilograms by factoring in powers of ten when necessary.

Thus, with this simple formula, the theoretical magnetic moment of iron for any given location at earth at a given time can be obtained. These values, range between 15 and 31 $\frac{emu}{g}$ depending upon the strength of Earth's field. Yet, the derived magnetic moment values for archaeological materials in BISC ranged from 1.63 to 69.05 $\frac{emu}{g}$, well above and below this limit. In fact, the data were evenly distributed above, within and below this limit (see Table 3-6). It is important to note that 12 of the 20 values below 15 $\frac{emu}{g}$ were from a single site, BISC 00062, calculated at 6 different potential masses. Thus, in reality, the derived σ values were within or above the range of theoretical values for pure iron.

Table 3-6
Distribution of σ values below, within, and above theoretical range of pure iron based upon k=398 (cgs).

σ values below 15 $\frac{emu}{g}$	σ values between 15-31 $\frac{emu}{g}$	σ values above 31 $\frac{emu}{g}$
20 (12 BISC 00062)	21	22

The result of field testing, therefore, seemed to exacerbate the dilemma of selecting the appropriate magnetic moment to model archaeological resources as it greatly extended the range of values determined by the theoretical study. Perhaps the most poignant observation resulting from field testing is that there was not one single magnetic moment value that encompassed all archaeological materials. Instead numerous variables, including material properties, permanent magnetism, orientation to the Earth's magnetic and the sensor's path, and the object's geometrical complexity result in a range of magnetic field strengths. Thus, it is incumbent upon the user to assess a given dataset in light of these observations, and to choose assessment parameters accordingly.

The fact that these variables produced a large range of magnetic moment values, however, does not negate the systematic application of the approach used throughout the present study: model survey coverage based upon the magnetic properties of pure iron and adjust modeling parameters according to local conditions. Instead, it simply requires additional planning to identify the correct values to derive the magnetic moment for iron for the time and location of the survey, then to scale these values according to the material culture items the survey intends to find. Determination of the magnetic moment for pure iron in a given time and location is fairly straightforward given the availability of this data via NOAA. Table 3-7 provides a general ambient magnetic field for several geographical regions, based upon NOAA data.

Scaling these pure iron values, however, is not as straightforward. All of the magnetic moments determined during the present study were based upon data collected with a short time period in June of 2013 off Miami, Florida. These values, therefore, were dependent upon Earth's magnetic field strength at that time and place. To make them more applicable, therefore, they were converted to a ratio representing the difference between the derived magnetic moment of that object and the theoretical value of pure iron at that given time and location. These values (Table

3-8) provide the scaling factor to adjust the geographical/temporal pure iron magnetic moment
into an archaeologically relevant value.

Table 3-7
Approximations of the magnetic moment per unit mass (σ) in various locations in the United States based upon the local magnetic field; note: these values are approximations. Exact values should be derived for the time and place of a given survey.

Location	~Ambient Field (+/- .01 G)	σ in $\frac{emu}{g}$
New Orleans, LA	.48	24.17
Norfolk, VA	.51	25.68
Boston, MA	.53	26.69
Seattle, WA	.53	26.69
San Francisco, CA	.49	24.67
Honolulu, HI	.35	17.62
Miami, FL	.45	22.66

As was shown in Table 3-6, most of the empirically derived magnetic moment values were within or greater than the values derived for pure iron (when the 12 values from BISC 00062 are excluded). The ratios of these values to the derived pure iron magnetic moment for Miami, Florida, were generally close to 1 or greater, as reported in Table 3-8. Given that some of the historical materials (BISC 00020 Main Site, BISC 00062, and BISC 00089) had lower ratios, conservative modeling would require the user to account for the probability that their survey area also contained ferromagnetic historical materials with weak magnetic fields. For such situations, a scaling factor of .5 should be applied to the derived pure iron amount. For more modern materials, or larger sites such as entire shipwrecks, the empirical data showed these items had values greater than the derived magnetic moment of pure iron. To model these items, a scaling factor of 1 to 1.5 would be more practical

Table 3-8
Ratio of median magnetic moments to theoretical magnetic moment per unit mass of pure iron (i.e. scaling factor for archaeological materials) determined for Miami, Florida, in June of 2013 (22.35 emu/g).

Site	Estimated Mass (kg)					
	Higher	**Med/Higher**	**Med.**	**Med/Lower**	**Low**	**Lowest**
BISC_0002						
BISC_00020_Main	0.53				0.56	
BISC_00020_Anom	1.43		1.43		1.50	
BISC_00062_NS	0.12	0.14	.15	0.18	0.20	0.23
BISC_00062 EW	0.07	0.08	0.09	0.11	0.12	0.13
BISC_00089_NS	0.36		0.61		0.98	
BISC_00089_EW	0.29		0.49		0.79	
BISC_00114_NS	1.07		1.08		1.19	
BISC_00114_EW	1.13		1.14		1.25	
BISC_00122_NS	2.17				2.60	
BISC_00122_EW	1.03				1.23	
BISC_00123_NS	1.31				1.67	
BISC_0023_EW	2.26				3.77	
BISC_00124_NS	0.99				1.36	
BISC_00124_EW	.64				.87	
*Almirante*_NS	2.32				2.83	
*Almirante*_EW	2.53				3.09	
*Blue_Fire*_NS	1.80				1.89	
*Blue_Fire*_EW	2.14				2.25	
Dredge_Float_NS	2.65				2.15	
Dredge_Float EW	1.92				2.24	
BC_Pontoon_S_NS	2.61				2.86	
BC_Pontoon_S_EW	2.64				2.90	
*St_Anne_D'A*_NS	0.78		0.89		1.04	
St_Anne_D'A EW	.67		.77		.89	

3.5 DISCUSSION OF WOODEN SHIPWRECK SITES WITH FERROMAGNETIC ELEMENTS

Three of the sites sampled during field operations were wooden shipwrecks with iron and/or steel components: BISC 0002, BISC 00020, and BISC 0008. Ferromagnetic elements at BISC 00020 (anchor, cannon, shot) were significant enough that they were isolated and used to calculate a magnetic moment for their respective objects. In terms of the detectability of wooden ships with ferrous components, BISC 00020 represented an extreme example. Namely, the vessel was a naval ship and was therefore outfitted with substantial amounts of ferrous materials: ordinance, shot, iron ballast and weapons. Though not arrayed in a single, continuous mass, these elements were nonetheless easily detected during exploratory magnetic survey around the site. In this regard, the detectability of a single (or multiple) piece of material culture associated with a

wooden warship—iron cannon, shot conglomerate, anchors—could serve as a proxy for the detectability of the vessel itself.

On the other hand, BISC 0002 and BISC 0008 were not naval vessels. Instead, both were presumed to be un-armed merchant vessels. As such, neither had large ferromagnetic elements; they only contained small, diffuse metallic elements such as rigging hardware, individual fasteners, and small personal items (metal hardware from chests, locks, etc.). Not surprisingly, neither site produced the high intensity magnetic fluxes observed on BISC 00020: the anchor at HMS *Fowey* generated a 199 γ anomaly; the main site area of BISC 0002 barely produced a 5 γ anomaly; the main site area at BISC 0008 produced a maximum 80 γ anomaly, but several 20-40 γ hits around this area. It is also important to remember that these sites were located in shallow water (less than 10 feet) and were sampled at 10 meter line spacing with at least one line passing directly over the main site area. Thus, the small anomaly observed at both sites might not have been produced at all under 'normal' survey parameters of 30 meter line spacing. Additionally, the shallow water of all of these wreck sites leads to the supposition that ferrous materials could have been removed from them as either historic salvage or more recent looting, thus our statements about the magnetic signature of a sailing vessel, while representing the actual current condition of an historic vessel in South Florida, should be tempered with the knowledge that an intact (i.e. un-salvaged vessel) would likely have a larger magnetic signature.

Though not a primary focus of the present study, the observations made while surveying these wooden shipwrecks offered some potentially useful recommendations regarding survey assessment and confidence. First, as was outlined in the previous sections, the modeling algorithm used assumes a single, consolidated mass of ferromagnetic material. As a result, the only way such a model could be applied to a scattered wooden shipwreck site would be to model the detectability of individual artifacts within the site. For example, though HMS *Fowey* was a large warship, its magnetic detectability is the product of the individual ferromagnetic elements associated with the ship. Using historical documentation, archaeologists could determine the potential detectability of the types of artifacts associated with the ship (cannon or anchor), and assuming they were spatially isolated, use these parameters to plan and/or assess a magnetic survey.

Similarly, this type of approach could be used with a non-naval vessel where the ferromagnetic elements would be considerably smaller than those associated with a warship. Obviously, these types of wooden shipwrecks would be more difficult to detect. Any such modeling using this approach, however, would also have to explicitly declare a major assumption: that the associated objects used to model detectability and confidence are actually present at the site. It would not be uncommon for these artifacts to have been removed following the wrecking process. Nevertheless, though not a planned function of the GIS modeling tools, this approach could be employed to estimate coverage or detectability of wooden shipwreck sites within a given survey area.

3.6 FIELD OPERATIONS OVERVIEW

Field operations took place during simultaneously occurring SRC work in BISC, between 18 June and 5 August, 2013, under archival collection number SRC-00165. SRC Archaeologist Andres Diaz was the Principal Investigator (PI) for SRC-00165. SRC Archaeologist John Bright

supervised magnetic sampling operations and served as PI for phase 2 task operations and all other IAA-related work. SRC personnel requirements were minimal, requiring three individuals for survey and diving operations.

Field operations employed three core SRC personnel, two core BOEM personnel, and an additional NPS GIS specialist, with support from BISC staff. All of the NPS personnel were magnetic survey specialists, NPS-qualified boat operators, and NPS divers. BOEM staff provided additional survey and operational expertise. Each participant was assigned one of the flowing roles:

> PI/ Operational Supervisor: Responsible for overall operations leadership, target site selection, data acquisition parameters, data processing, and report writing.

> Dive Leader: Diving operations were conducted in conformity with the BISC Safe Practices Manual (SPM) and Emergency Operations Plan (EOP), at discretion of Dive Leader. Responsible for adherence to this policy, including management of project dive plan, daily dive logging, and diving logistical support.

> Boat Support: Responsible for daily boat maintenance, fueling, logging boat usage. Must file daily float plan as per BISC SPM policy, and responsible for acquiring and operating park radio..

> Ops Support: GIS and geospatial processing expertise, dive support for ground-truthing and site documentation, survey support to assist deploying magnetic instrumentation, data logging, and data acquisition.

Operations were divided into four phases: Mobilization and Testing, Priority 1 Sampling, Priority 2 Sampling, and Demobilization. The mobilization process took four days, during which time SRC personnel retrieved the SRC survey vessel and equipment from storage at Everglades National Park (left by SRC staff at conclusion of previous project at Gulf Islands National Seashore). After transit, SRC vessel *Cal Cummings* was launched at BISC, and the complete survey system was assembled, calibrated, and dry-tested. Mobilization also entailed in-water testing to verify proper function of survey system prior to the start of field testing. Furthermore, a meeting was scheduled with BISC personnel on 24 June, prior the start of sampling, to discuss sampling targets and site dispositions, drawing upon the local expertise of BISC resource managers and divers.

The next phase of the project was Priority 1 sampling: the magnetic survey of targets deemed first priority by project staff after consultation with BISC archaeologists and divers. During this phase, numerous Ops Support roles were necessary. The first was fulfilled by NPS Natural Resources Division GIS specialist Sage Wall. Wall provided expertise in the mathematic and geospatial aspects of magnetic modeling, assisting in the establishment of the data processing methodology, and real-time evaluation and development of the python-scripted tools. Ops support for in-water diving and magnetic survey efforts was provided by BOEM personnel Brandi Carrier and William Hoffman. Carrier and Hoffman participated as divers/dive supervision for ground-truthing operations, under a diving reciprocity agreement between

BOEM and NPS, allowing the project to utilize dive teams to more efficiently while conducting in-water assessment of sampling sites. Carrier and Hoffman also assisted with the operation of the survey systems.

The initial project plan allotted time to sample all of the first priority sites selected by the research team before moving on to lower priority targets. Priority was based upon the ability to determine an accurate ferromagnetic mass for a given archaeological site, thus the first priority targets were those for which the research team felt certain that, based upon historical data, a mass could be determined. Lower priority sites were those for which determination of ferromagnetic mass was more ambiguous, such a wooden shipwrecks with iron components. As it turned out, weather kept the sampling team from operating during most of the two weeks initially planned for field operations. On days where weather was marginal, the team was not able to reach some of the priority 1 sites and had to instead settle for lower priority sites.

To compensate for poor weather during the planned project dates, the SRC opportunistically surveyed additional targets during the on-going field activities at BISC. The operational support of BOEM, however, was not available during this time so the research team depended heavily upon BISC personnel to complete the diving and survey operations. Nevertheless, by the conclusion of field testing operations, the SRC had sampled 15 sites—described in the previous sections—of varying size, age, and material composition. Most sites were sample from a north-south and east-west direction, providing information on object orientation as it related to observed magnetic field strength.

CHAPTER 4

GIS SCRIPT DEVELOPMENT

The primary objective of the study was to extend the theoretical research begun during the MA WEA Baseline Survey into a field-testing program with the objective of creating customized and experimentally verified geospatial processing tools. Though the IAA mandate was to produce a toolset to assist BOEM archaeologists in the evaluation of data submitted to the agency, in actuality these tools are of great benefit to both agencies. When completed, the development process resulted in the creation of a single utility consisting of four component tools. These tools operate upon a single, continuous magnetic dataset (i.e. a discrete area of magnetic data, not multiple non-contiguous datasets, Figure 4-1). The resulting products allow the user to visualize the raw and filtered data and determine thresholds of detection, survey coverage and data quality. Contiguous, complex data geographies (Figure 4-2) can be processed, but may require additional boundary refinements.
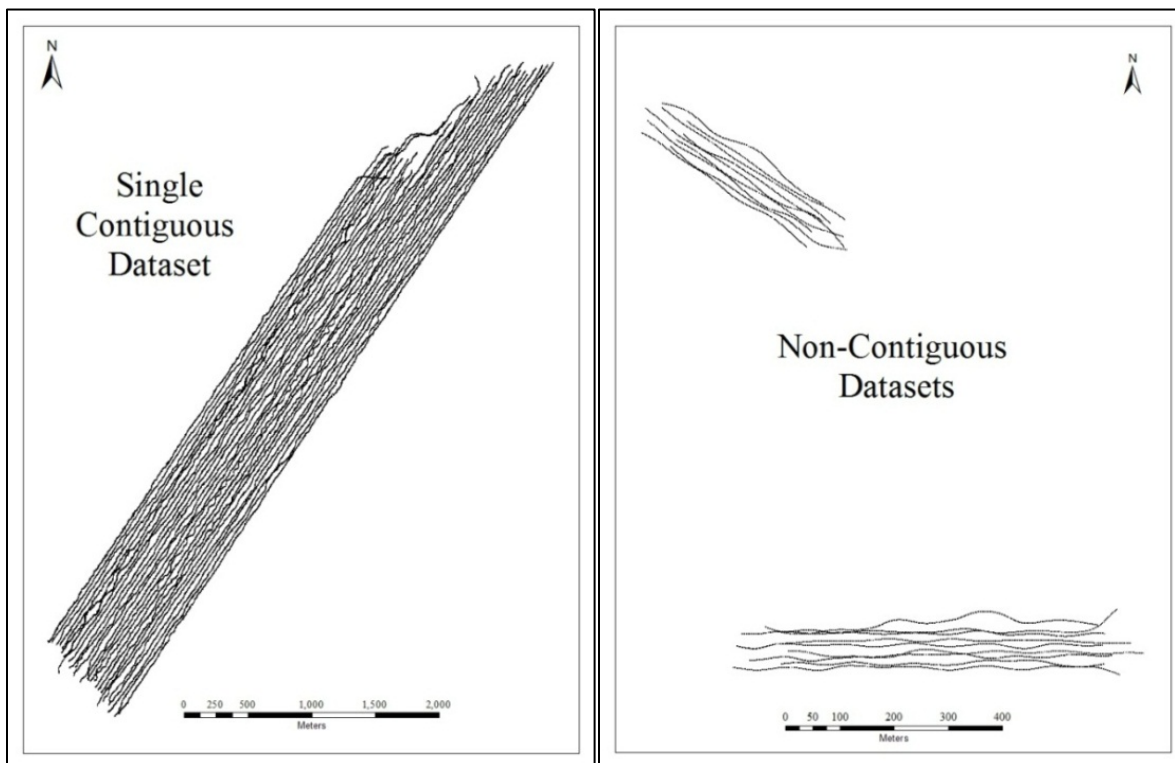
Figure 4-1. Single dataset acceptable for processing with the tools (left) and a non-continuous dataset that cannot be processed by the tools (right).
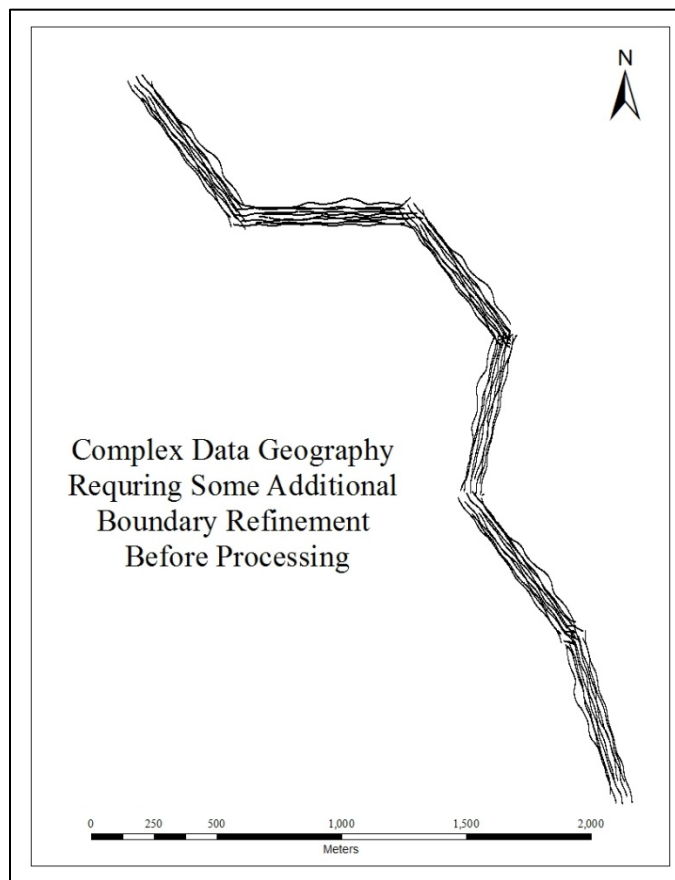
Figure 4-2. Data distribution which can be processed after additional boundary refinements.

The first component tool, the *Input Tool*, converts a magnetic dataset into a standardized schema that the remaining tools are coded to recognize. A 'magnetic dataset' encompasses any tabular data formant containing position information, magnetic readings, and a line or file name. A standard data format economizes downstream processing since the user only has to identify the requisite data inputs once. The three remaining component tools automatically recognize the necessary data fields for the respective processing functions. In other words, the user only has to specify position information, magnetic readings, altitude, and file name in the *Input Tool*; afterwards, the data schema automatically feeds these inputs into the remaining tools.

Next, the *Generate Survey Boundary* tool produces a polygon feature class representing the perimeter of the survey area which is used as an analysis mask in the next two processing functions. This is an optional function; the user can alternatively opt to create their own feature class for a given survey area. The third tool (*Visualization*) generates data products that allow the user to visualize the raw and filtered magnetic readings as a continuous surface. In addition, the *Visualization* tool also produces a series of contour lines for each surface (raw and filtered data) at user-specified intervals.

The most basic form of visualization, a full field map, is not a simple process. Though the steps involved—export of data from acquisition program, input into GIS program, conversion to point-feature class, and interpolation of a continuous surface—are time-intensive, they are basically the

same for any magnetic dataset. Automating these functions greatly expedites the process. Inherent in the NPS SRC's recommendation that BOEM independently verify submitted magnetic survey datasets is the need to visualize raw data and verify the identification and interpretation of suspected anomalies, thus the Visualization tool is a significant asset to the agency.

Rather than producing only full-field maps from magnetometer surveys, however, the NPS SRC integrated an additional spatial processing function into this utility. Starting in the late 1990s, SRC began development of a mathematical filtering algorithm called gradient processing. Given the possible masking of smaller magnetic anomalies among geological, secular, and diurnal variations, gradient processing serves as a selective spatial filter that mathematically eliminates any noise characterized by gradual changes over long distances—geological and diurnal variation—leaving only the short duration, high intensity fluxes induced by man-made objects. Gradient processing, therefore, is an extremely effective means to identify anomalies within a magnetic survey dataset. By eliminating environmental noise, furthermore, gradient processing also facilities the merging of temporally isolated, geographically proximate datasets into a single visualized product; datasets which would otherwise have vastly different data ranges.

The fourth and final tool is the most complex utility in the toolbox and was the main objective of the IAA. The *Confidence Model* combines the modeling algorithms proposed in 2012, described in the Theory Section, with the testing results from 2013 IAA field experimentation into a unique GIS package designed to produce data on survey area coverage. Additionally, the *Confidence Model* calculates the potential mass of detected anomalies as a function of flux intensity and distance from the sensor. Thus, instead of simply identifying anomalies in a dataset, this utility enables the user to identify areas of reduced coverage and estimate the size of the objects producing any observed anomalies. Prior to the development of this tool for the IAA, no such program existed to supply quantitative information about coverage levels based upon data distribution; this tool is the first of its kind.

From these data outputs, furthermore, the user can then determine the extent of area covered within a survey block at one or multiple detection thresholds. For example, the user could determine in what percentage of the survey a 1,000 kg or larger object would have been detected. They could also calculate the percentages of the survey area encompassing a range of coverage levels, such as for 100, 500, and 1,000 kg objects. These statistics then inform quantitative assessments regarding the efficacy of a given survey effort, allowing the user to determine if the survey was successful at achieving an appropriate level of coverage.

Throughout this study, NPS SRC and BOEM OREP utilized ESRI's *ArcGIS 10.2.1*. In addition to *ArcGIS* being the most widely used GIS software platform in the United States, *ArcGIS* also offers its users the ability to custom-build toolboxes—individual or groups of related processing functions—using the Python programming language. Employing this feature, the mathematic formulas developed during the theoretical research and field experimentation were coded into generic geospatial processing functions (such as kriging and raster calculations) with the necessary data processing parameters either hard-coded or user-selectable. Since March, 2013, the IAA team has moved through 14 separate prototypes of the toolbox, each adding to and refining the previous version.

These Python toolboxes integrate into the *ArcToolbox* library of geoprocessing functions
included in the *ArcGIS* software package, and also with *ArcCatalog* to organize and store data
products. The scripts themselves are Python code sequences that function like a recipe or
roadmap. They direct existing function of *ArcGIS* in a defined way to generate specific products.
Thus, these tools themselves are fairly small, less than 1 megabyte combined, and are therefore
easily transferred. Nearly any form of tabular data can be input into the script—such as .csv, .txt,
.shp, .dbf, etc.—and the tools produce results stored in a small file geodatabase.

The following sections provide a comprehensive explanation of each tool. Along with this
description, release notes and instructional documents were written to accompany the tools
(Appendix I and II). Those documents detail the operation of each function on a step-by-step
basis, guiding the user through each keystroke and button push. They contain important technical
information, such as file nomenclature, integral to the actual function of the tools but which is
not thematically related to the topic of this chapter: how these tools process data and provide
meaningful outputs. In other words, the user guides and release notes do not detail how or why a
function executes a certain way, but instead just explain the operation of the tools. The
descriptions of individual processing functions, operating parameters, and the rationale behind
their use are presented in this chapter.

4.1 *INPUT TOOL*

The first tool in the *Magnetometer Survey* toolbox converts the incoming dataset into a
standardized format required by the other toolbox functions. This tool integrates only the
necessary data items—position information, raw magnetic readings, altitude, line name/file
name, and the spatial reference system into a standardized schema (Figure 4-3). The three other
tools are programmed to recognize this schema, thus maximizing the economy of the
downstream workflow. In other words, this tool prevents the user from having to define the basic
data input for each operation and eliminates the creation of redundant data products.
Additionally, the *Input Tool* converts altitude data into centimeters, the required unit of the
modeling algorithm.

The tool operates via the standard *ArcGIS* interface (Figure 4-4). Any number of formats can be
input for the data table. These include .csv, .txt, .dbf, and .shp files, essentially any tabular data
format recognized by *ArcGIS*. The user then specifies all relevant data fields, including easting
(longitude) data, northing (latitude) data. Though the words 'easting' and 'northing' are used in
the interface, any form of spatial reference data will work as long as each number is contained in
a single cell of the data table (such as decimal degrees). Next, the user defines which field in the
data table contains the raw magnetic readings—the required units are γ or nT. If the dataset
contains altitude readings, the user must then specify the field in which it is contained, and the
format of the measurement (feet or meters). If altitude data is not present, an offset value must be
entered. Incorporation of sensor altitude (real or estimated) is necessary for the *Confidence
Model* since all mass calculations are a function of distance throughout the survey area. The
distribution of distance relative to the magnetic sensor is three dimensional, with sensor altitude
comprising the vertical, or 'Z' component.

OBJECTID *	Shape *	recordedGamma	lineNumber	altitude
1	Point	44135.98	005_1122.EDT	149
2	Point	44136.01	005_1122.EDT	151
3	Point	44136.02	005_1122.EDT	155
4	Point	44136.04	005_1122.EDT	157
5	Point	44136.03	005_1122.EDT	137
6	Point	44135.96	005_1122.EDT	470
7	Point	44135.91	005_1122.EDT	157
8	Point	44135.9	005_1122.EDT	143
9	Point	44135.87	005_1122.EDT	131
10	Point	44135.79	005_1122.EDT	115
11	Point	44135.76	005_1122.EDT	123
12	Point	44135.67	005_1122.EDT	95
13	Point	44135.61	005_1122.EDT	163
14	Point	44135.54	005_1122.EDT	139
15	Point	44135.51	005_1122.EDT	111
16	Point	44135.44	005_1122.EDT	131
17	Point	44135.39	005_1122.EDT	117
18	Point	44135.41	005_1122.EDT	131
19	Point	44135.38	005_1122.EDT	197
20	Point	44135.31	005_1122.EDT	187
21	Point	44135.23	005_1122.EDT	165
22	Point	44135.2	005_1122.EDT	125
23	Point	44135.1	005_1122.EDT	125
24	Point	44135.07	005_1122.EDT	109
25	Point	44135.01	005_1122.EDT	67
26	Point	44134.95	005_1122.EDT	76
27	Point	44134.9	005_1122.EDT	83
28	Point	44134.85	005_1122.EDT	61
29	Point	44134.89	005_1122.EDT	77
30	Point	44134.93	005_1122.EDT	97
31	Point	44134.97	005_1122.EDT	83
32	Point	44135	005_1122.EDT	87
33	Point	44135.01	005_1122.EDT	81
34	Point	44135.01	005_1122.EDT	91

1 ▶ ▶| (0 out of 2987 Selected)

rawGamma

Figure 4-3. Attribute table of point feature class created by *Input Tool*.

Not all magnetometers have altimeters, however, so the user must designate a single input representing the estimated average sensor altitude during the survey. Since accurate mathematical modeling of this space requires a vertical dimension, doing so without an altitude input would be the mathematical equivalent of modeling along on a perfectly flat plane, where any resulting data would be useless in terms of assessing a three-dimensional survey area. Obviously, having actual altitude data is ideal since this will capture changes in bathymetry and sensor position. In the absence of altitude data, the user must instead set a default vertical offset. The resulting data is inherently less accurate, especially in survey areas with variable bathymetry, but this is only way for the model to proceed without real altitude data.

The next input is for the user to define the field in the data table containing a line or file name. A unique designator is needed for each line of collected data. Both the *Visualization* and *Confidence Model* execute linear data filtering functions that have to know where one line ends and the next begns to properly compute their respective products. Without this input, neither tool will execute. To verify that the data is arrayed within individual lines, the tool also produces a

line feature class where all points of a given line name are converted to a single line feature. If a line file has been properly designated, this feature class should appear as the individual tracks taken by the survey vessel.

Next, the user defines the spatial reference system of the dataset. Expanding this input will take the user to *ArcMap's* library of projected and geographical reference systems. The final prompt launches an *ArcCatalog* window where the user navigates to the desired work space to create a file geodatabase where all data products will be stored. Selecting an existing file geodatabase will completely overwrite its contents (unless locked by *ArcGIS*). When the user selects 'Ok,' the tool will create a point feature class called *rawGamma* and a line feature class called *surveyLines* in the specified file geodatabase.
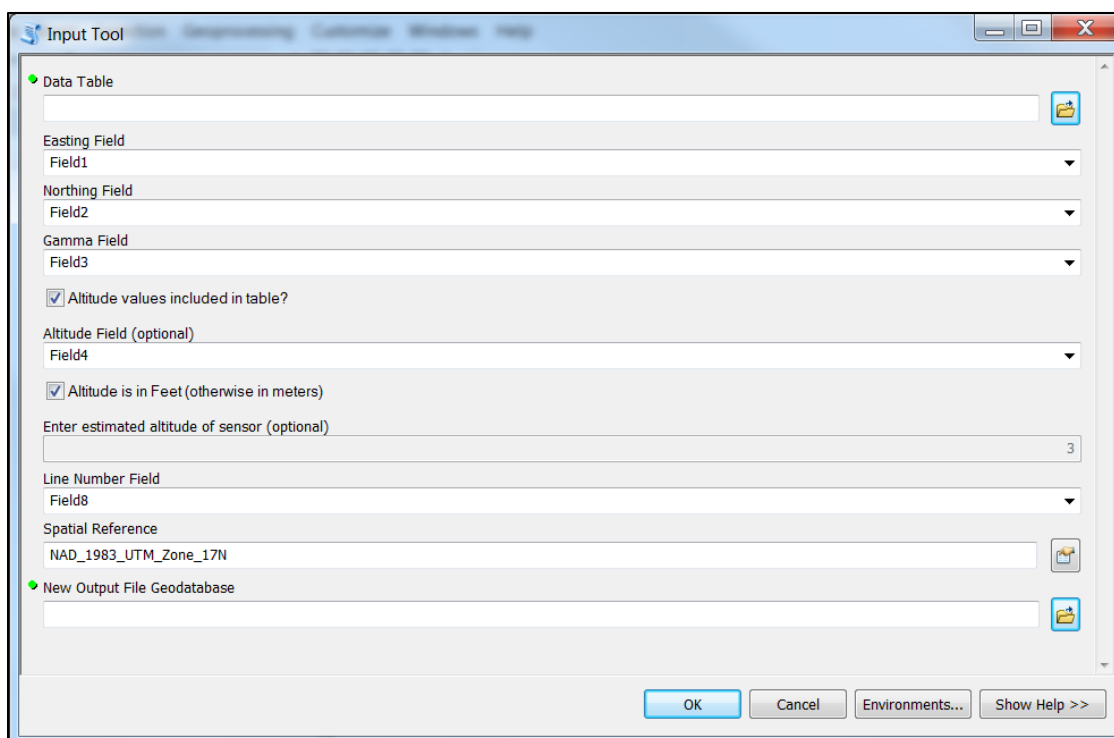
Figure 4-4. *Input Tool* **interface.**

4.2 GENERATE SURVEY BOUNDARY

The second tool in the *Magnetometer Survey* toolbox develops three polygon feature classes around the extents of an input feature class; either the points in the *rawGamma* feature class, or the lines in the *surveyLines* feature class. To develop the first polygon, a convex hull shape is generated around the input features using the minimum bounding geometry logic which is then extended by a user-defined buffer. The two resulting polygon shapes—one snapped to the extents of the points, the convex hull, and another extending out to the specified buffer distance—are shown in Figure 4-5. The third boundary polygon is developed by buffering each individual feature, then dissolving these buffers into a single polygon shape, and removing an

internal voids (Figure 4-6). The dissolved survey area boundary is particularly good at bounding datasets with complex geometries.

This function was developed as an optional tool to simplify the process of creating a defined boundary, which is necessary for all subsequent processing functions. The boundary serves as an analysis mask to limit the extent of all the processing functions and data outputs that would otherwise extend well beyond the area actually surveyed, especially the raster data products. The user can manually create their own survey area as well, so use of this tool is not required to complete visualization or confidence modeling.
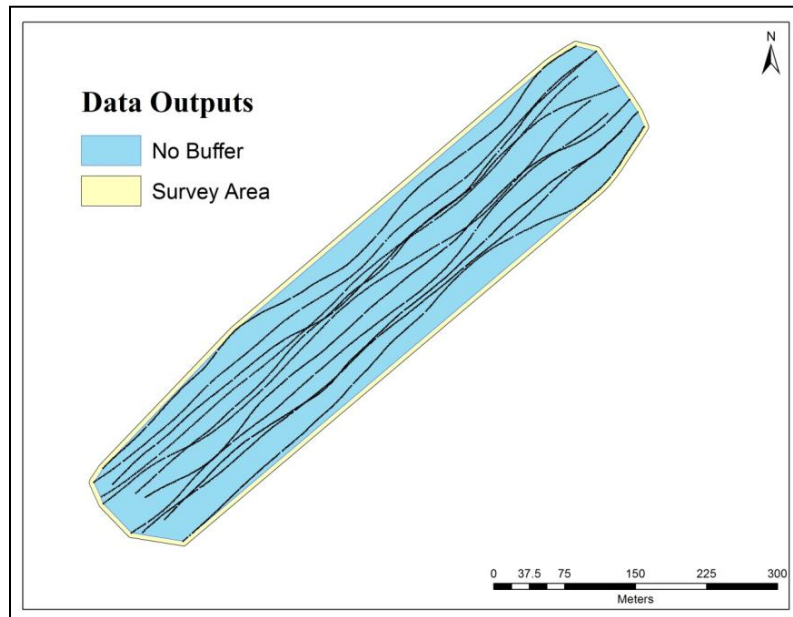
Figure 4-5. *ConvexHull* and *surveyArea* **Outputs from the** *Generate Survey Boundary* **tool.**
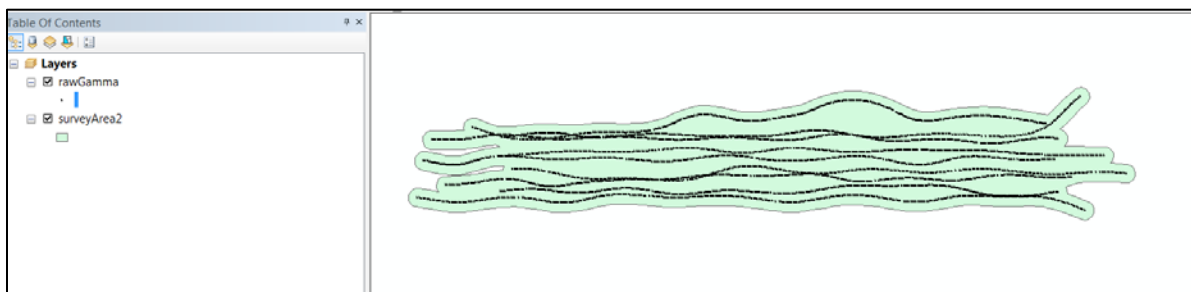
Figure 4-6. *surveyArea2* **output from** *Generate Survey Boundary* **tool.**

Although a boundary is required for subsequent processing, one generated via this tool might not always be the best option. Since the tool creates a boundary around all data points that comprise the dataset, it operates on the assumption that all acquired points represent the entirety of the survey area. Though this is true in some cases, there are several operational situations that result in data points acquired outside of a given survey area. Often, surveyors collect data beyond the extent of a pre-planned survey area to ensure full coverage (Figure 4-7), thus the portion of the data requiring processing is actually a subset of the total data collected. In many cases, therefore,

the user would need to manually create a survey area instead of using the survey boundary creation tool. Nevertheless, when appropriate this tool significantly expedites the process.
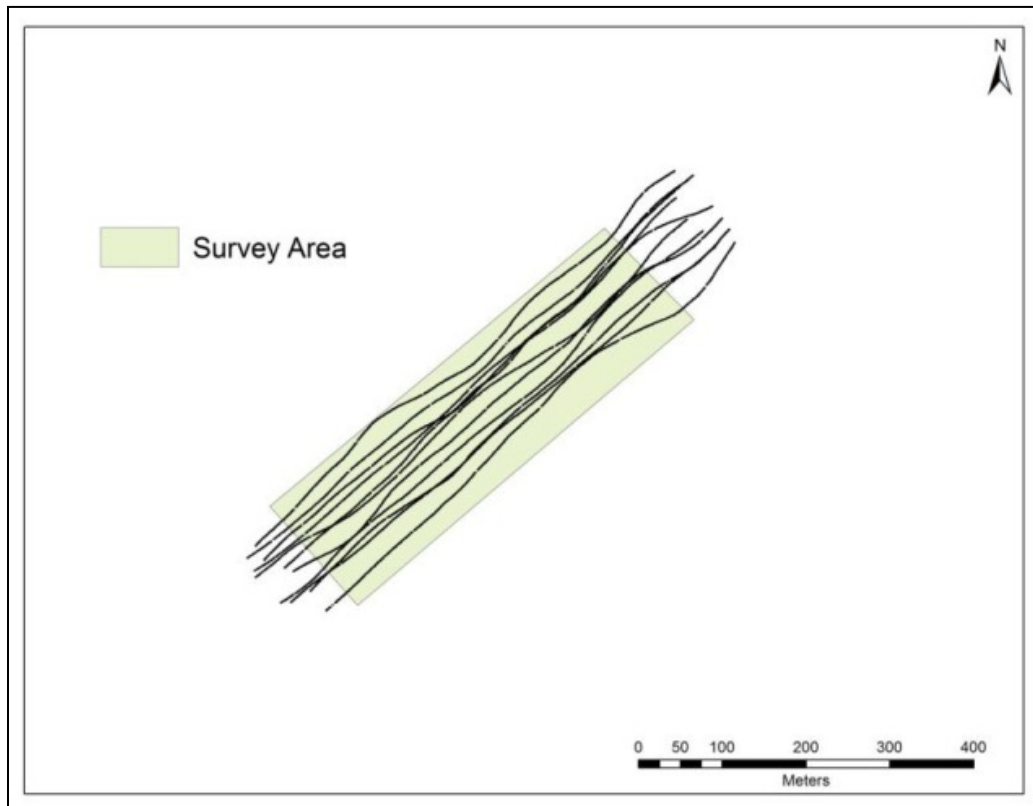
Figure 4-7. Example of survey area where data is acquired beyond the extents of the intended survey block.

It operates via a simple user interface (Figure 4-8), requiring the user to simply reference the *rawGamma* or *surveyLines* layer generated with the *Input Tool* and define a desired buffer distance. By default, the three data products will save to the geodatabase created by the *Input Tool*. If desired, however, the user can un-check this option and create a new geodatabase. The buffer distance (measured in meters) is a distance at which the tool will expand the perimeter of the convex hull polygon away from the initial polygon for the first boundary polygon, and the distance away from the data points or survey lines it will buffer for the second boundary polygon. As shown in Figure 4-5, the tool first creates a layer whose perimeter is snapped to the outermost data points. From this layer, it then uses the buffer distance to expand this perimeter in all directions. The appropriate amount will vary among datasets, but generally half of the planned line spacing is sufficient. Since the interpolation functions run during the visualization and confidence modeling calculate a continuous surface between adjacent lines, it is equally mathematically valid to interpolate a surface in a proportionate amount away from lines on the extents of a survey area. In other words, since the interpolation function assumes the magnetometer 'covers' half the distance between adjacent survey lines, then this logic would also allow the interpolation to include an equal amount of distance around the perimeter of the acquired points. A log file is created once the function is complete to store the operation's parameters should they be needed later.
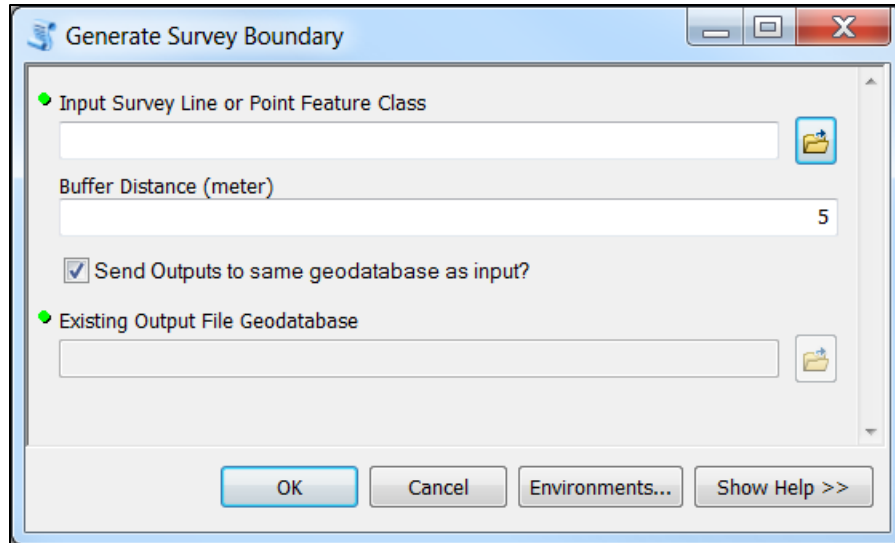
Figure 4-8. User interface for the Survey Area Boundary Tool.

If the user wants to manually create a survey area, several tools exist in *ArcGIS* for the user to create and edit polygon feature classes. The user may even be able to transfer the survey areas developed in the data acquisition program into *ArcGIS*.

It is important to note that, whether using the generate survey area tool or not, the boundaries of the analysis mask have a profound impact upon the confidence modeling process. Specifically, the *Confidence Model* will calculate data throughout the entire analysis mask area, detection thresholds decrease dramatically as distance from the data points increases. If the boundaries of the analysis mask do not accurately reflect the actual survey area, the derived statistics will likewise be inaccurate. In other words, there is a difference between poor coverage of a survey area, revealed by low detection thresholds, and low detection thresholds calculated as a result of improper survey area boundary creation. The user must, therefore, determine the applicability of the *Generate Survey Boundary* tool to each individual dataset. Regardless, a survey area boundary is required for all remaining processing functions.

Another drawback to this tool is the limitation of the convex hull creation method. This operation builds the simplest polygon around the extent of the input points. The method, therefore, is incapable of conforming to concavities within the geography of the data points, instead, it bridges them by connecting their two outermost vertices (Figure 4-9). To correct the survey area, the user would have to manually adjust the vertices of the polygon feature class to the true extents of the data points—a basic editing function within *ArcMap*, or rely upon the second boundary creation methodology. This method was developed to mitigate the shortcomings of the convex hull geography. Instead of bounding the extent of all points, it individually buffers each point or survey line, and then dissolves these individual buffers into a single polygon feature (Figure 4-10).
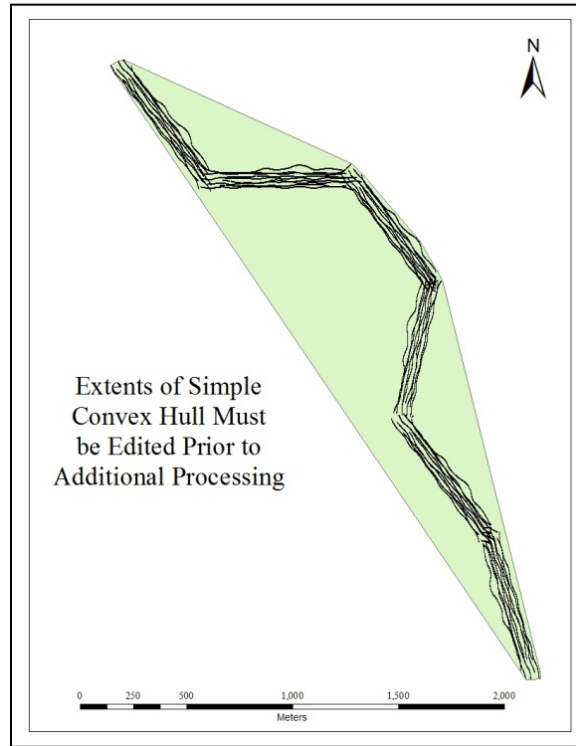
Figure 4-9. Concavities in the data geography resulting in an inaccurate survey boundary.
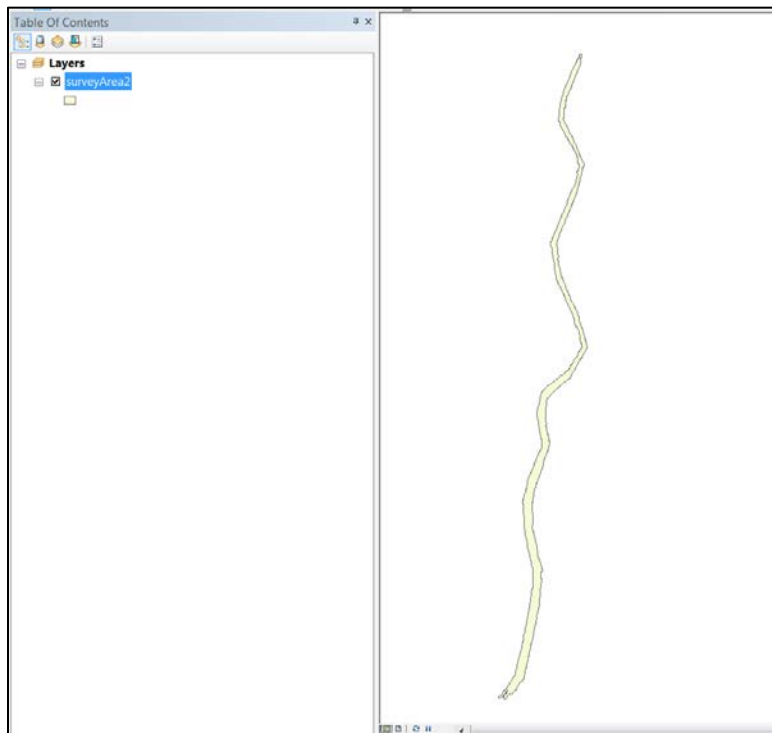
Figure 4-10. Dissolved-buffer boundary creation product.

This function is particularly useful at capturing complex data geometries, such as that shown in Figure 4-9, where the magnetic data were collected along a river. The method, however, is not without its drawbacks. Namely, if the user-specified buffer is too small, internal 'gaps' will develop between adjacent lines which are greater than twice the buffer distance apart (Figure 4-11). In this instance, the user must either re-create a survey area with a greater buffer distance (Figure 4-12), or manually remove the internal gaps. If the defined buffer interval is below a minimum threshold, where there is not sufficient overlap between adjacent buffers, the tool cannot merge them into a single polygon. Thus, when executing the tool, it is recommended that half of the survey line spacing is used for the buffer amount to ensure adequate overlap.
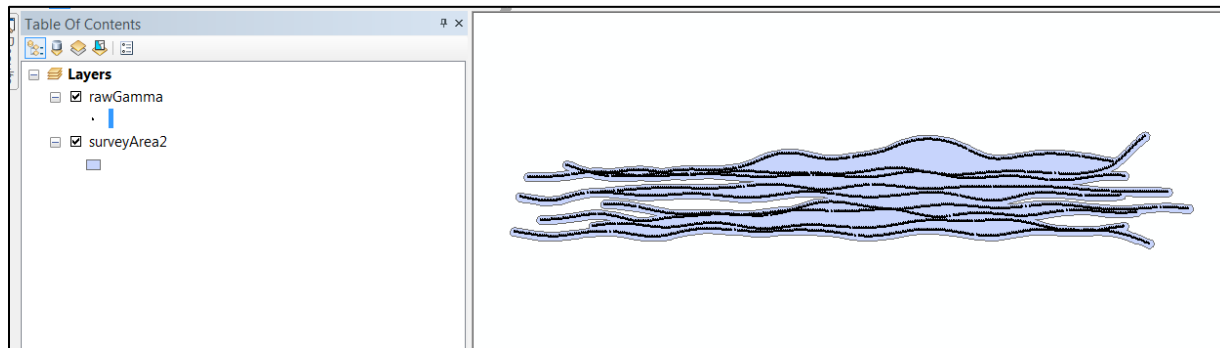
Figure 4-11. Survey area polygon generated by dissolved-point buffer where buffering distance was less than space between adjacent lines.
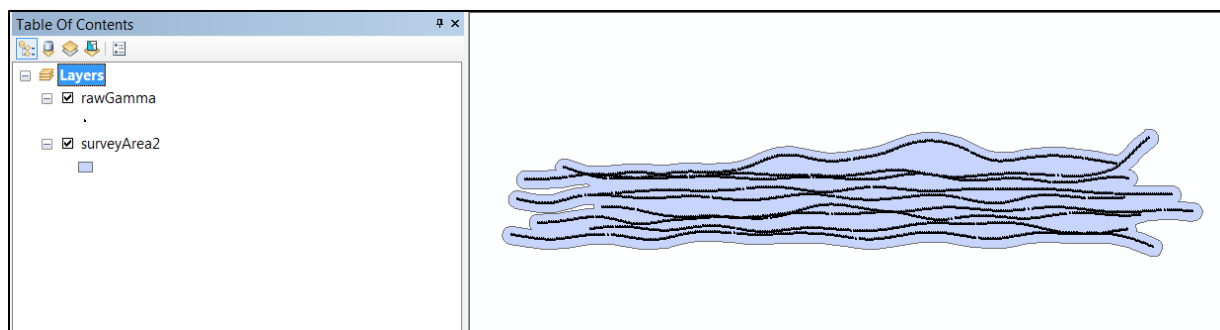
Figure 4-12. Polygon generated at an increased buffer amount to remove internal gaps.

4.3 *VISUALIZATION TOOL*

The next tool in the toolbox executes a visualization and selective spatial filtering function. This user interface (Figure 4-13) requires only a few basic input parameters. First, the user must reference the data table (the *rawGamma* layer created by the *Input Tool*) and survey area. Next, the user selects the interpolation function executed on the data products: kriging or TIN. The method chosen will be used to create two continuous surfaces, one for the raw readings, and another for the gradient values. If TIN is selected, the Survey Line Spacing (meter) is greyed out. This quantity, provided in meters, affects the mathematical search radius used by the kriging

interpolation function, which is set to be 1.5 multiplied by the line spacing. In this way, the scope of the interpolation function varies depending upon data point density to supply more accurate results. If using the TIN mode, the user must ensure that the *3D Analyst* and *Spatial Analyst* extensions are turned on in the extension selection menu (see Figure 4-14).

Next the user defines the contour intervals of the isolines which are produced with the full field and gradient maps. These are separate inputs since the raw and filtered datasets have different ranges, with gradient values usually much smaller than the raw readings. It is important to remember that the contour interval selected by the user has a direct impact on the 'detectability' of magnetic anomalies. If too large an interval is selected then, though the sensor may have recorded a magnetic density flux, it will not be visually apparent to the user (i.e. contour at 15 γ and miss a 7 γ 'hit'). It is recommended that the user start contouring at the same value used for sensor noise to ensure that smaller flux anomalies are apparent in the data. Next, the user defines the desired cell size for the two rasters which will be created, and either accepts the default output location (the same geodatabase created by the *Input Tool*) or defines a new file geodatabase where the outputs will be stored.
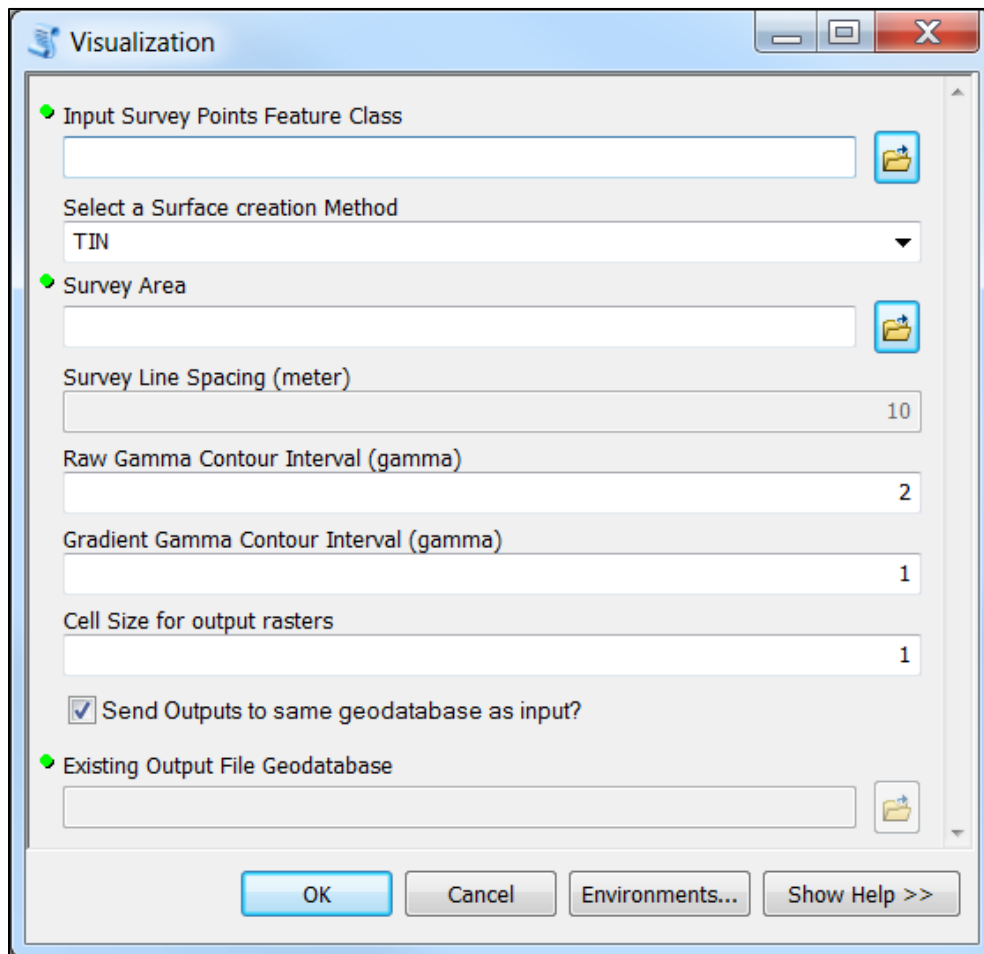
Figure 4-13. User interface for the *Visualization* tool.
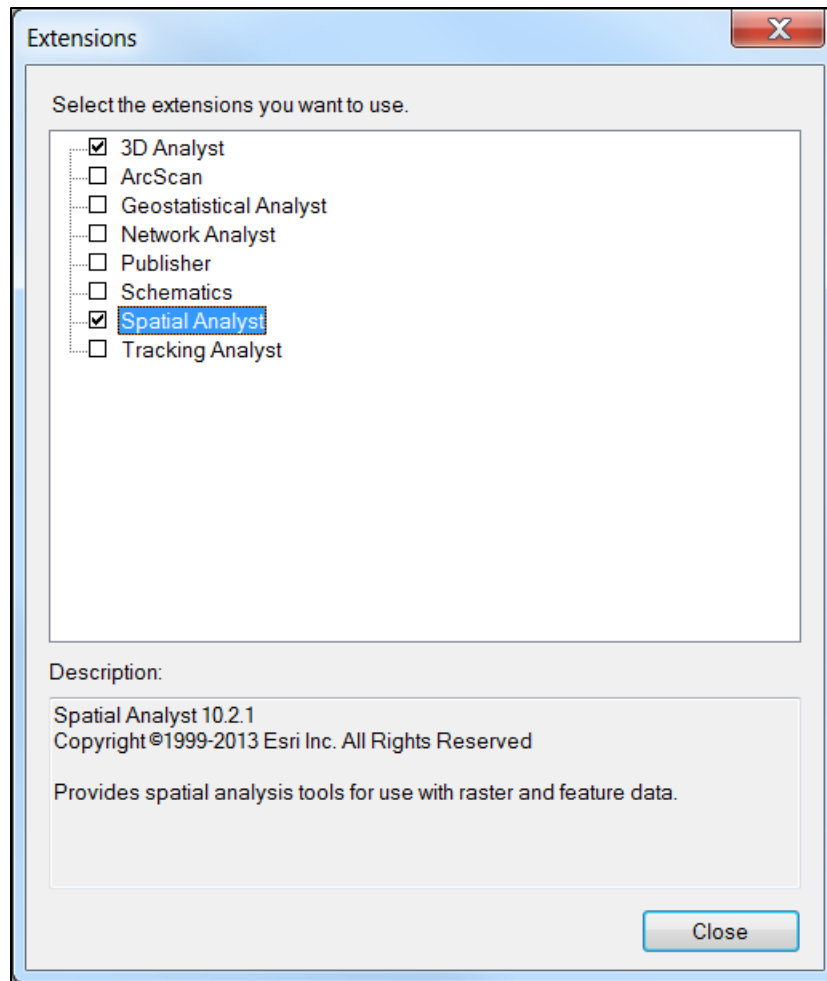
Figure 4-14. The extension selection window.

Once the *Visualization* tool begins, it first computes the gradient values from the raw magnetic readings. These new values are stored as a point feature class called *gradientGamma*. Next, the survey area boundary is designated as an analysis mask to limit the extent of the remaining processing. The tool then executes the selected interpolation function to generate a continuous full-field magnetic floating-point raster (Figure 4-15). A raster-to-polyline conversion generates a layer of isolines at the user-specified gamma contour interval (Figure 4-16). When using the TIN method, an actual TIN is created in a scratch workplace, then flattened into a raster which is saved in the geodatabase (Figure 4-17).
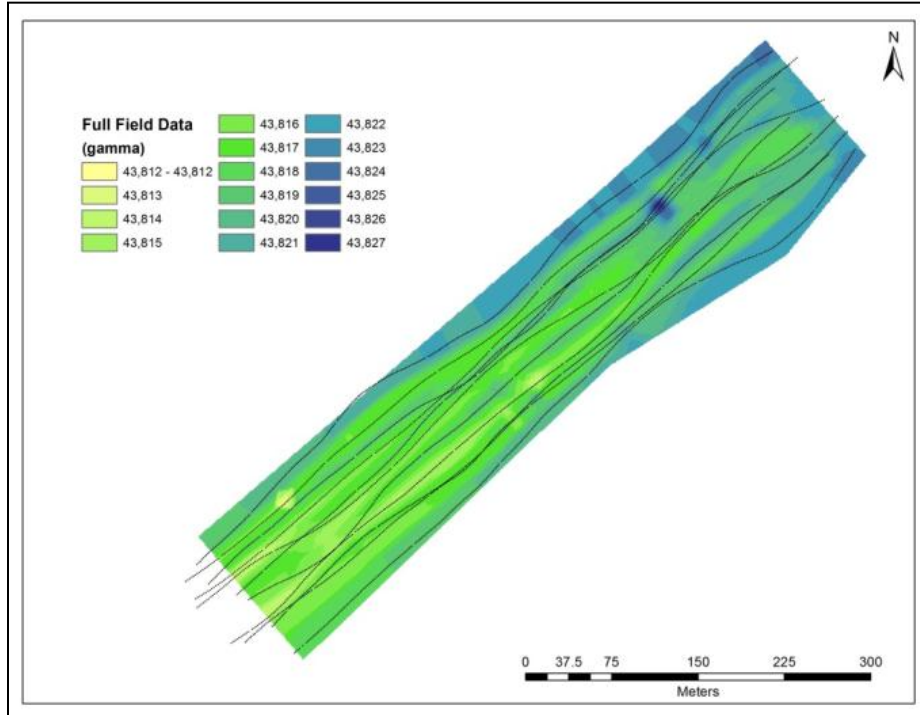
Figure 4-15. Floating-point raster of full field magnetic data overlaid with data points.
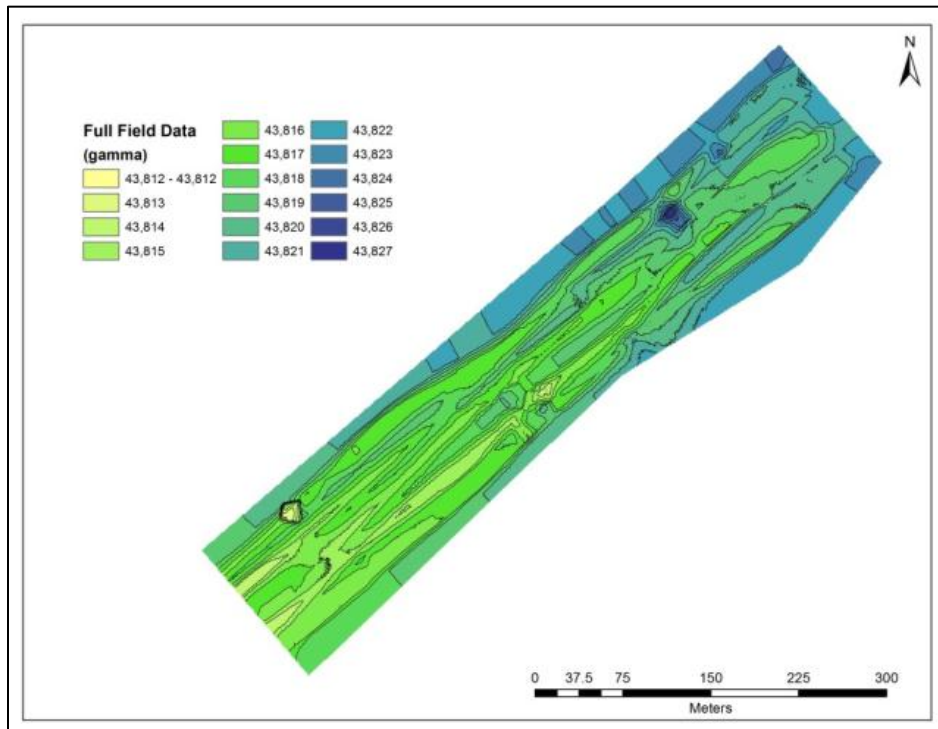
Figure 4-16. 1-gamma contour isolines overlaid on raster surface.
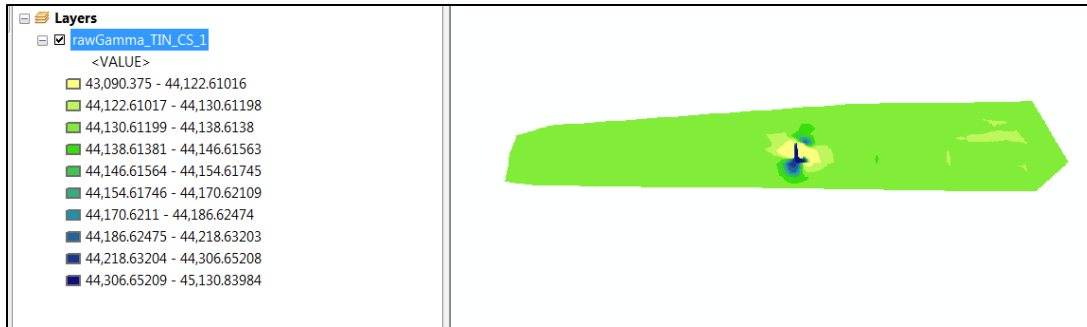
Figure 4-17. Raster created by converted TIN model.

After generating the components of the full field map, the *Visualization* tool then interpolates as second surface based upon the calculated gradient values. When the tool starts to execute, it locates the raw gamma values from the *rawGamma* attribute data and calculates the gradient as the $\Delta\gamma$ from 1 point behind, divided by the corresponding distance. The resulting $\Delta\gamma$ values are then multiplied by the average point-to-point distance to restore any signal loss due to division. These values are interpolated via the same method used on the raw data (Figure 4-18). Though this function is not a true mathematical gradient, which would be the derivative of magnetic intensity along the survey line, the gradient processing simulates the effect of a derivative process while maintaining gammas as the working units. The map in Figure 4-18 shows how the gradient processing eliminates nearly all of the low-intensity magnetic changes apparent in the full field data. In the resulting map, only the short-duration anomalies remains, those most likely associated with cultural materials.
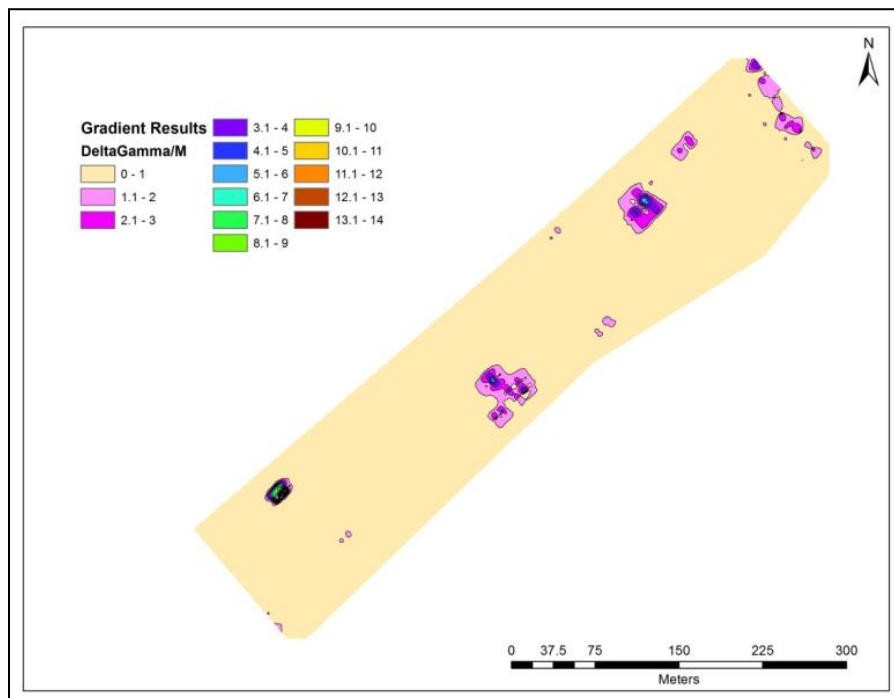
Figure 4-18. Gradient output raster with 1 $\Delta\gamma$ isolines overlaid.

When used in combination, the full field and gradient maps form an extremely effective tool to identify magnetic anomalies within a survey area. Under BOEM's current guidelines, developers are required to submit a full field magnetic map and corresponding list of anomalies. As such, BOEM is relying upon the developer's data processing and visualization methods to ensure that all anomalies in the dataset were actually identified. Utilizing this *Visualization* tool, the agency can re-process the raw data and independently verify the list of anomalies submitted. With the addition of the gradient processing feature, the agency will have an enhanced capability to ensure that the data set was thoroughly evaluated, and that no additional anomalies were obscured by geological, secular, and diurnal variations.

The inclusion of the gradient processing function within this toolbox, furthermore, constitutes the first time this selective spatial filtering process will be available to the wider public. Since the late 1990s, it has been a magnetic data processing methodology utilized internally – and developed over decades of field experimentation – by the NPS SRC. Gradient processing has the potential to enhance any archaeological program that regularly utilized marine magnetic surveys.

Each of the individual data outputs is shown as they appear in *ArcCatalog* in Figure 4-19. The recommended resolution of the raw gamma raster is one meter, though the user can specify greater or lesser resolution depending upon survey area size, sample point distribution and data storage requirements. A one meter resolution—meaning that each raster cell is one square meter—makes later confidence model calculations much easier since there is a one-to-one ratio between the raster cell count and area in square meters; every cell represents 1 square meter, so 1,000 cells equals 1,000 square meters. As a floating point, furthermore, this layer can be symbolized a number of ways by the user in the *ArcMap* interface.
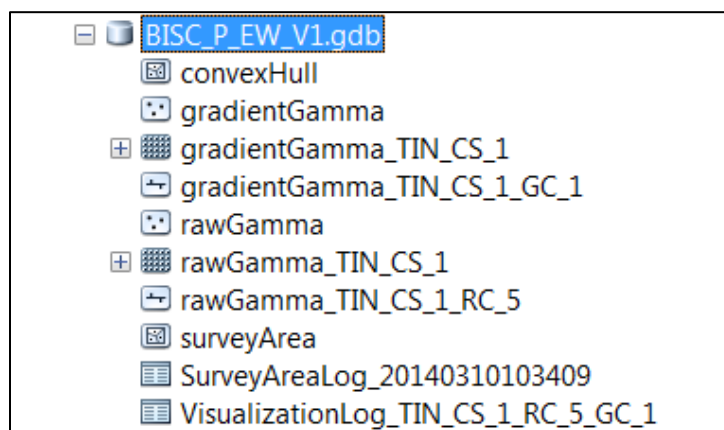
Figure 4-19. Data outputs from *Input Tool*, *Generate Survey Boundary*, and *Visualization* tool.

A system of abbreviated nomenclature was developed to imprint each output file with its basic construction parameters. Each suffix is unique and is intended to allow the user to distinguish between data products resulting from multiple executions of the tools. For example, the user may elect to visualize their data using both interpolation methods for comparison, or would use varied contour intervals. In each case, the parameters are coded into the file names so they may be differentiated for final map preparation. The following table (Table 4-1) contains the list of these abbreviations.

Table 4-1
Key to abbreviations used to code file names from *Visualziation* tool.

Abbreviation	Meaning
TIN	TIN interpolation used
Kriging	Kriging interpolation used
LS	Line Spacing
CS	Raster Cell Size
RC	Raw gamma Contour interval
GC	Gradient Contour interval

Since the *Visulaization* tool will not overwrite data, the user can continue running a given dataset at varied parameters without any data overwriting. In the event the user selects identical parameters, the tool will replace the old data with the most recently created data. In addition to the data products, a *Visualization log file* is produced for each run, storing all input parameters. This file is also name coded. An image of multiple processing runs stored in *ArcCatalog* is shown in Figure 4-20. It is highly recommended the user familiarize themselves with the nomenclature so as to avoid later confusion.
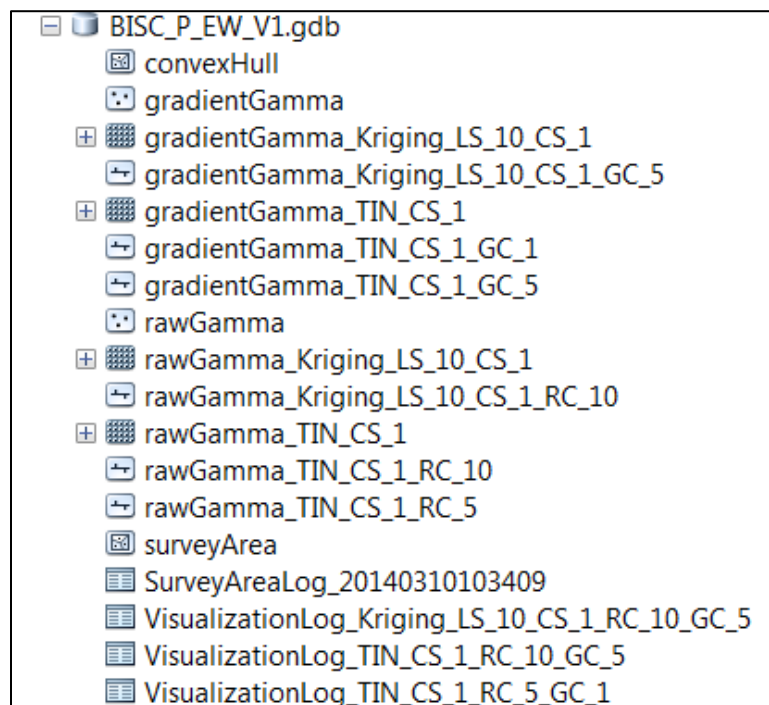
Figure 4-20. *ArcCatalog* view of numerous data products from *Visualization* tool.

4.4 *CONFIDENCE MODELING*

The final tool in the toolbox produces the data outputs needed to assess actual survey coverage. Though the term 'coverage' is often used in the context of data acquisition to describe the completeness of data gathering in an intended area, it is here meant to describe the degree to

which data point density and sensor altitude correspond to the detectability of ferromagnetic objects. Coverage in this sense means the extent to which data acquisition resulted in the likely detection of objects of given masses as this varies throughout an area. With small objects more detectable closer to the position of the sensor during sampling, coverage is therefore expressed in terms of thresholds of detection. These thresholds are delineated by varying theoretical masses, selected by the user according to whatever criteria they use to evaluate a given dataset.

The data products used to generate this information are created by calculating potential detectable/non-detectable masses around acquired data points via the inverse cube model of induced magnetic behavior. Using a series of sequential raster calculations, the tool solves for the total sampling distance throughout the survey area as the hypotenuse of the horizontal distance from the nearest data point and the sensor altitude, and assigns this value to each cell in the resulting raster layer. Next, another raster is produced by solving for the largest mass that could have gone undetected (largest object that could have been missed) at that location using the total sampling distance, a user-defined magnetic moment (m), and the noise level of the instrumentation, using the equation derived for mass in the Theory section:

$$w = \frac{(\Delta\gamma * 10^{-6})r^3}{m}$$

Here, w is the mass in kg, $\Delta\gamma$ is the sensor noise amount (the amount of flux that would not result in a noticeable anomaly), and r is the total distance in cm. It is from this raster, the *potentialMassMissed* layer, that thresholds of detection are derived.

The *Confidence Model* also executes a second operation, also utilizing the inverse cube function, to determine the smallest potential mass of anomalies detected (or smallest object that could have been located). This would be the 'idealized' case where the object responsible for the magnetic flux lies directly beneath (i.e. as close as possible) to the sensor. In this function, the amplitude of a given magnetic flux is input as $\Delta\gamma$ to determine the mass of an object capable of inducing such a flux given the sensor distance and user-defined magnetic moment.

The large user interface for the *Confidence Model* tool is a result of the specificity required to establish appropriate parameters for the processing (Figure 4-21). As with the *Generate Survey Boundary* and *Visualization* tools, the first inputs are the *rawGamma* layer and the survey area boundary. The next input parameters apply to data sets with altitude data present.

During field testing operations, especially in shallow water areas, the research team observed the propensity for bottom strikes—an event where the sensor grazes the seabed—at slower survey speeds (Figure 4-22). Though bottom strikes do not necessarily affect the magnetic readings, they do introduce erroneous altitude data into the record. An altimeter on a magnetometer is an acoustic transducer which measures distance between itself and the bottom via the time delay between a transmitted sound wave leaving and returning. When resting against the bottom, this function is disrupted since the sound wave has no room to propagate. As a result, the transducer interprets an erroneous altitude, which it writes to the data record. These erroneous readings—the NPS SRC G-882 defaulted to a value of 244.9 feet—dramatically affect the detection threshold calculations as they erroneously represent pockets of significantly dissimilar distances than the remainder of the survey area.
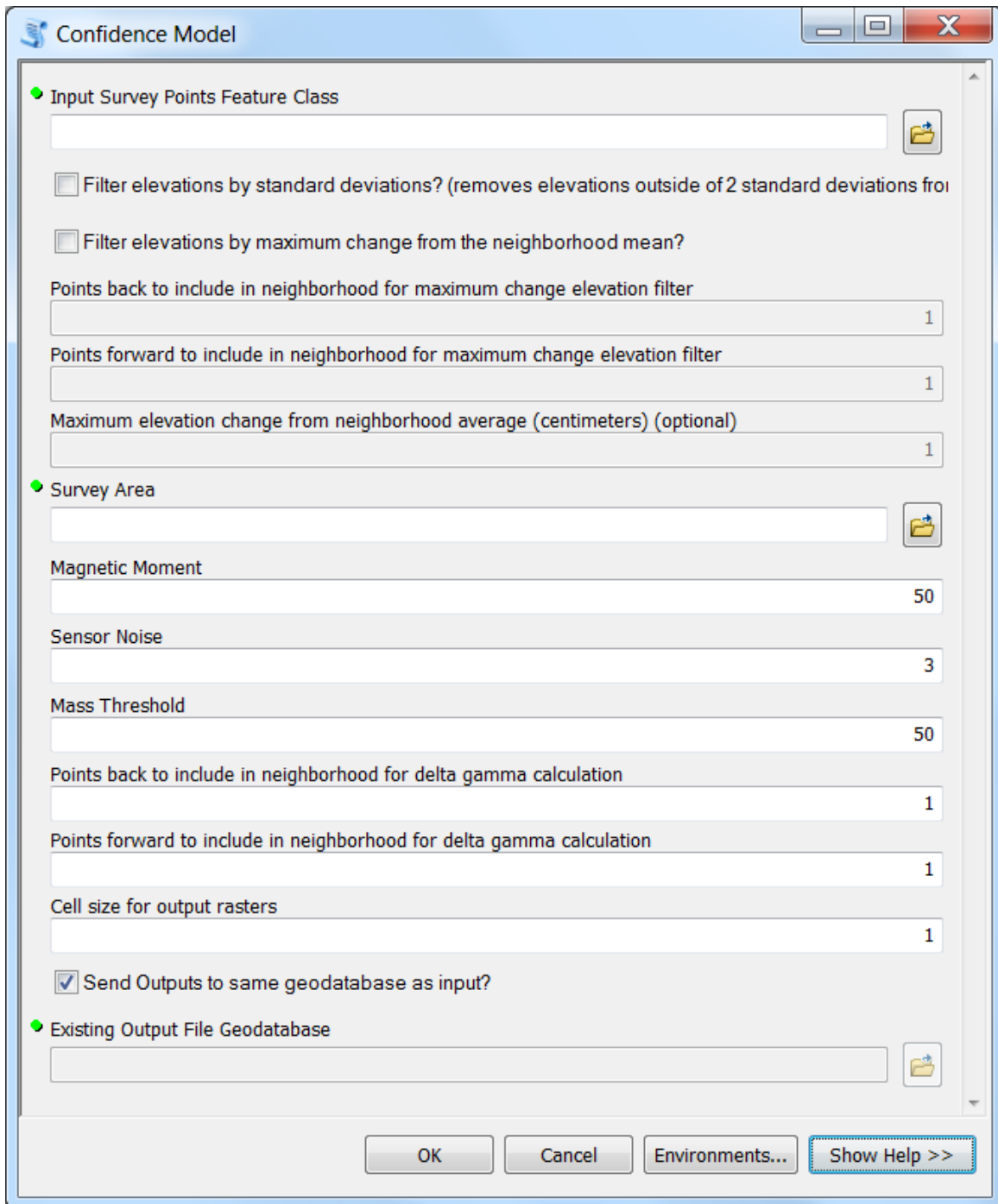
Figure 4-21. *Confidence Model* **user interface.**
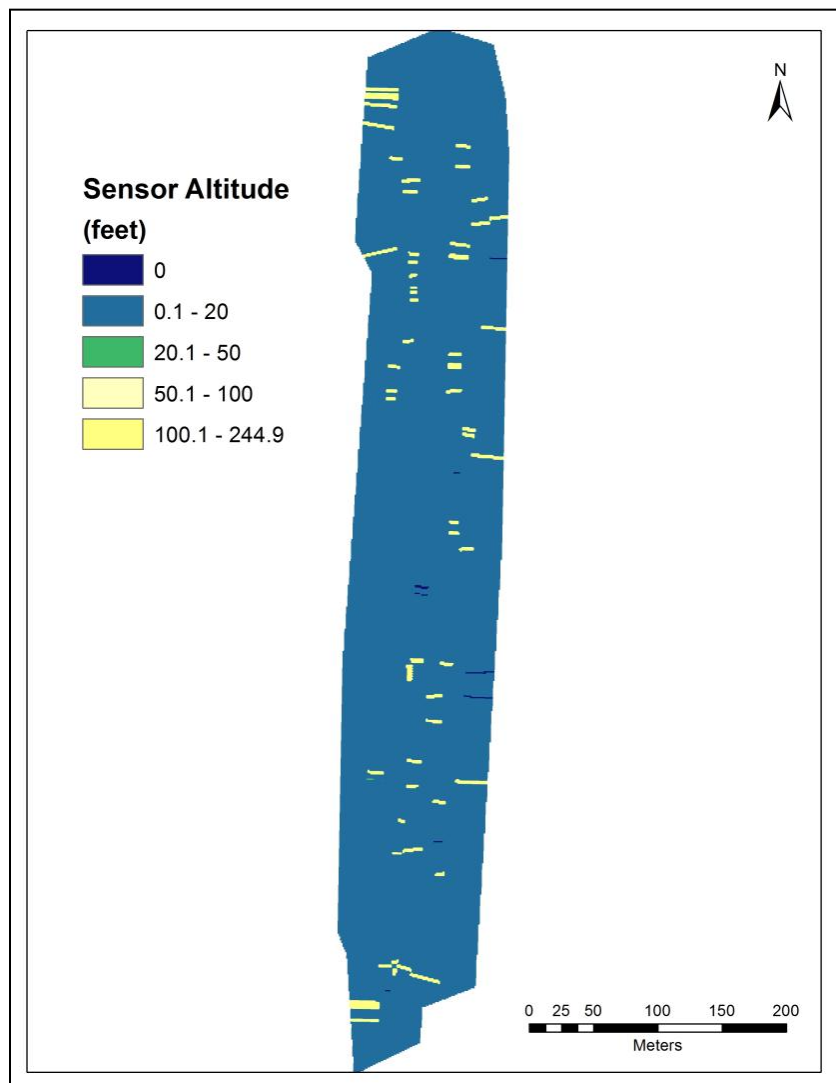
Figure 4-22. Map of sensor altitudes from survey block where water depth did not exceed 20 ft. All values greater than 20 ft were the result of bottom strikes and are erroneous.

Similar disruptions in altitude data logging were also observed in deeper surveys, where the sensor passed over large concentrations of schooling fish. The fish communities were dense enough that they reflected the sound waves emitted by the transducer, which interpreted them as shallow areas in an otherwise deep-water survey area. As was the case with bottom strikes, the erroneous altitude values skewed the detection threshold calculations.

The simplest way to deal with erroneous altitude data is to manually edit it within the data acquisition software. For example, the data acquisition program used by the NPS SRC during the IAA has an editing function called *Single Beam Editor*, where the user can scroll through the data trace and smooth out bad altitudes. This solution, however, is not practical for a user like BOEM OREP, where data is transferred in a generic format that cannot be re-loaded in its native acquisition software (unless BOEM OREP wanted to maintain user licenses for all commercially available remote sensing software programs). Instead, an alternative solution was developed

specifically for BOEM to clean and filter altitude data. These functions were built into the *Confidence Model* and offer the user several options to handle bad altitude data.

The first option is a simple statistical exclusion. Here, the altitude data is statistically summarized and any values beyond two standard deviations are excluded from later processing. This is a very quick and simple function, though it is not a perfect solution. Depending on the nature of errors in altitude data, this function could remove values that are legitimate, but beyond two standard deviations of the mean. It could also fail to filter all of the erroneous altitude data in instances where there are many bad values.

To minimize good data loss and/or bad data retention, another option was also coded. This function is a smoothing operation that queries sequential data points against a user-defined Δalt value. Basically, if a point varies more than the Δalt value from the average value of the surrounding points, the value is excluded. This method is especially effective for bottom strikes, where the recorded value during sensor grounding is usually an order of magnitude greater than the points surrounding it. For example, if the sensor is recording altitudes of approximately .5 meters when it is close to the bottom, then it grounds on the seabed, recording a value of 33.3 meters, before rising back off the bottom and recording values of .5 meters, these differences are easily identified and smoothed.

In some instance, however, the sensor may drag for a period of seconds across the bottom resulting in sequential bad data points. These multiple erroneous values in a row would pass a simple Δalt query, where the query only looked at one point preceding. To handle this condition, the user can program the tool to query any number of points ahead and/or behind the altitude values. When executed, this system will identify erroneous points in a series and exclude them from processing. This solution, however, can also potentially affect good data. A survey area characterized by highly variable bathymetry, such large coral reefs, could produce highly variable sequential altitudes when the sensor passed over these features. If the user-specified Δalt was less than theses variations, the tool would unnecessarily smooth this altitude data.

To summarize, each of these altitude filtering methods has the potential to alter viable data, and to leave erroneous data in the table. Since none are capable of entirely removing only bad altitude values in all datasets, the optimal solution is to prevent the sensor from striking the bottom during data acquisition. Nevertheless, since BOEM must accept data submitted to the agency, and therefore has little control over the acquisition process, it is likely they will encounter data sets with erroneous altitude data. For very large datasets where processing times will be large, statistical exclusion would be ideal. For datasets acquired over fairly consistent bathymetry, a simple Δalt exclusion, executed by setting the points-back to '1' and forward to '0,' would be ideal, and those with numerous groundings would benefit from the multi-point Δalt query. Each of these methods excludes values identified as bad in lieu of trying to replace them with another value. The primary reason for this is the drastically reduced processing time offered by exclusion. Additionally, very few values with regards to the totality of the dataset (for example, 10 values out of 10,000) are removed, resulting in a negligible impact on the overall statistics.

Once these inputs and parameters are established in the interface, the user must complete the additional inputs shown in Figure 4-21. The next two inputs establish the remaining parameters

for the inverse cubic algorithm. The first, magnetic moment, represents the intensity of the magnetic field of ferromagnetic materials. A range of values were derived during field testing, generally trending in terms of an object's age; older ferromagnetic items had weaker magnetic fields. Thus, depending upon the target of the survey, the user and increase or decrease this amount accordingly. Based upon the results of the present study's empirical testing, 0.5 of the σ value for pure iron is recommended for historical materials and 1-1.5 the σ value of pure iron for modern ferromagnetic materials.

The next input is sensor noise. This established the minimum magnetic flux which can be distinguished from the ambient noise of the sensor. Though most manufacturers report their sensors have less than 1 γ of noise, several operational factors, such as power supply, tend to slightly increase this amount. For this reason, the default value in the tool is 3 gammas. Additional information regarding operational noise levels is provided by Camidge et al. (2009:16), "in practice a minimum detectable anomaly of 5 nT [equal to 5 γ] may be a little on the conservative side; where the data are relatively noise-free 3 or even 2 nT may be practical. In practice, targets smaller than 5 nT deflection are sometimes selected."

The next input is a theoretical mass that will be used to calculate a quick detection threshold level. This is intended as a quick check on the data set, and is not the entire detection threshold output. Instead, by providing a single mass parameter the tool can automatically generate a layer that determines in which portions of the survey area the input mass would have been detected (Figure 4-23). Using this mass, the tool will generate a raster layer with two values. The '0' values are cells where that mass could have been missed, and the '1' values are cells where that mass could have been detected. An example, calculated for a 150 kg mass, is shown in Figure 4-23. In this survey area 2,154 cells are designated '0' where an object less than 150 kg would have gone undetected, and 82,784 cells are designated '1' where an object of 150 kg or greater would have been detected. Thus, 98 percent of the survey area was covered to such an extent that a 150 kg object would have been detected. These results are also displayed in the geoprocessing results window when the tool completes (Figure 4-24).

The next two inputs are mathematical parameters for the *Confidence Tool's* internal gradient processing. As in the *Visualization* tool, the *Confidence Model* determines Δγ, but instead of generating a continuous surface from the derived values, it instead uses them to determine masses of objects that could have induced them. These parameters define the number of points forward and backward from a given data point that the tool will use to determine the Δγ for a given space. The more points included, the more changes will be averaged and changes in gamma values smoothed out. At the ends of lines, furthermore, the function will simply ignore any values that are not present; since the function is programmed to search for a neighborhood of points, it would not be able to cope with the ends of lines without such programing.
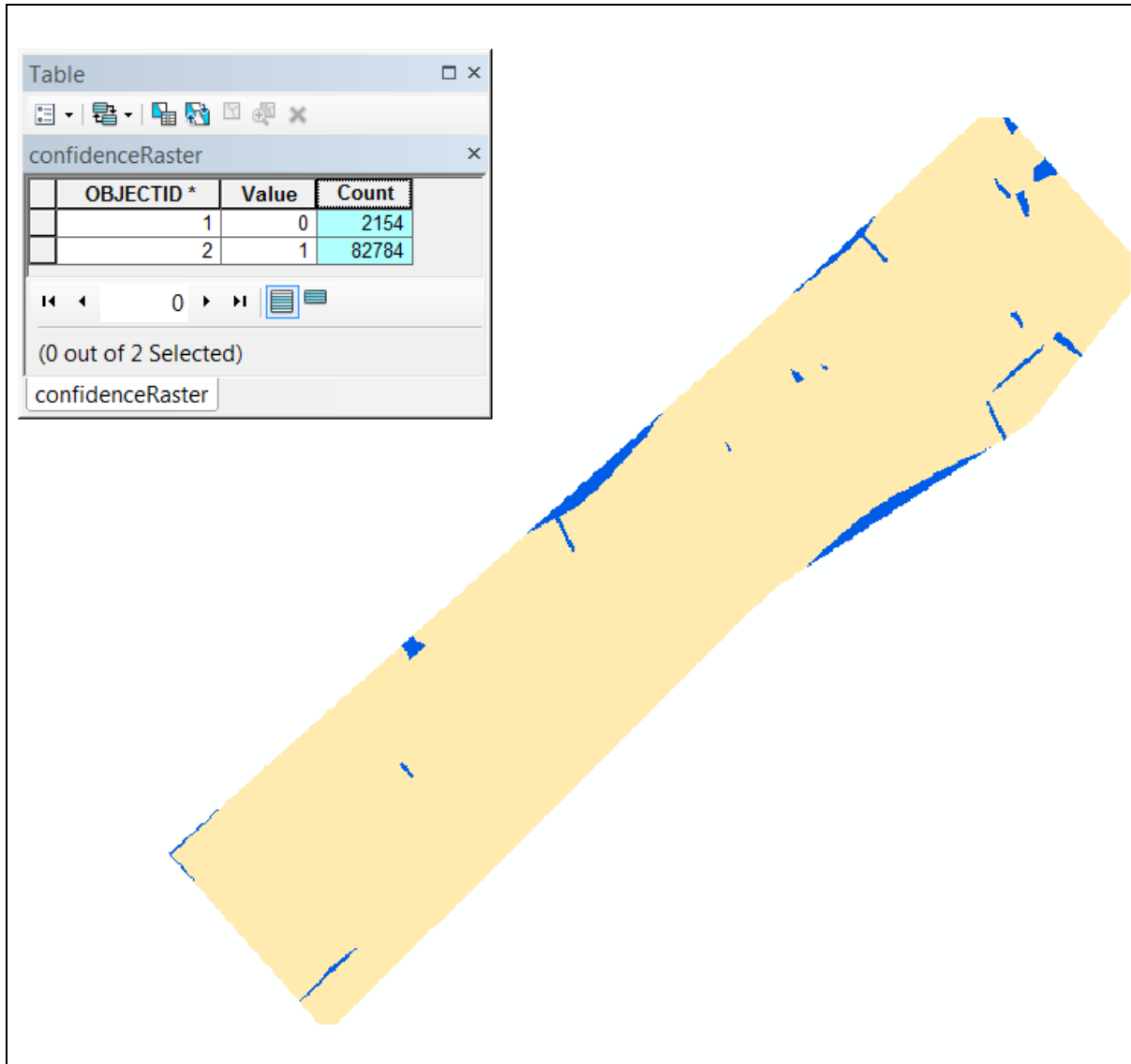
Figure 4-23. The *confidenceRaster* layer calculated from a mass input of 150 kg.

The next input is the cell resolution for all the rasters the tool will create. Again, the recommended value is 1, however, larger datasets may require less resolution to decrease processing time and file sizes. The final input is the designation of a file geodatabase (the default being the *Input Tool* geodatabase) where all the data products will be stored (Figure 4-25). As with the *Visualization* tool, a coded suffix is written into the name (see Table 4-2 for codes)
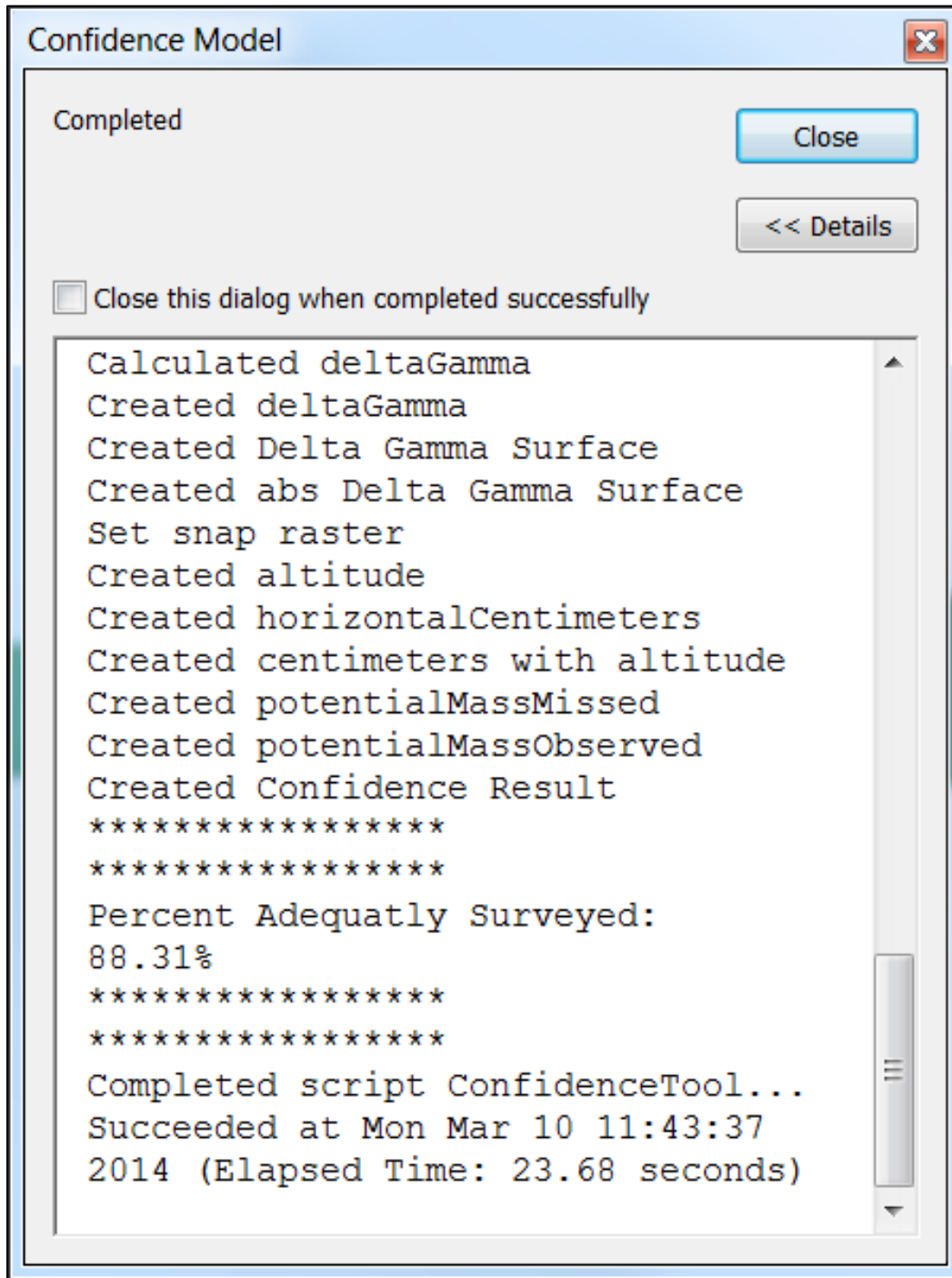
Figure 4-24. The mass threshold calculation result displayed in the geoprocessing results window.
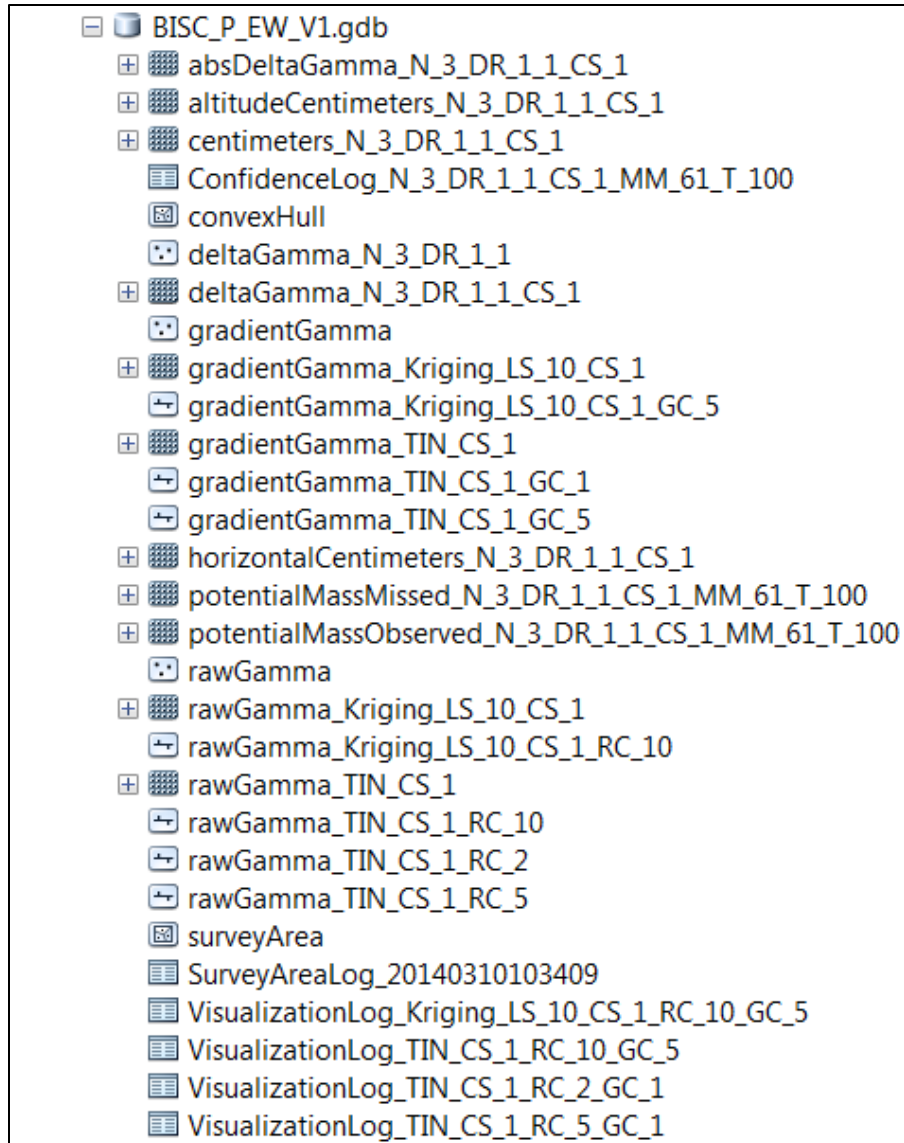
Figure 4-25. *Confidence Model* **outputs in** *ArcCatalog* **along with** *Input, Survey Area***, and** *Visualization* **results.**

Table 4-2
Key to abbreviations used to code file names from *Confidence Model* **tool.**

Abbreviation	Meaning
N	Noise
DR	Delta gamma Raster (points back/forward)
CS	Cell Size (raster)
MM	Magnetic Moment
T	Mass Threshold (kg)
FSD	Altitude Filtered (Standard Deviations)
FMC	Altitude Filtered (Maximum Change) points back, forward, and max Δalt

Once the *Confidence Model* starts running, it uses the survey boundary area to set an analysis
mask. The data table is read and the appropriate altitude filtering and delta gamma calculations
are performed. The delta gamma values are used to create the *deltaGamma* point feature class
and are then allocated into a raster with all areas in the raster assigned the value of the closest
point's delta gamma value. Next, it begins building two distance rasters used to calculated total
survey distance. The first raster, *horizontalCentimeters*, is created from a point density analysis
which determines the horizontal spacing from the nearest data point for each cell in the raster
(Figure 4-26). The next layer formed transfers sensor altitude readings into a vertical distance
raster. A Thiessen polygon function allocates all the space around the data points according to
distance, and then assigns the point's altitude value to all raster cells within the boundaries of
that point's Thiessen polygon. This vertical distance values are automatically rounded to the
nearest whole value to streamline processing (Figure 4-27).
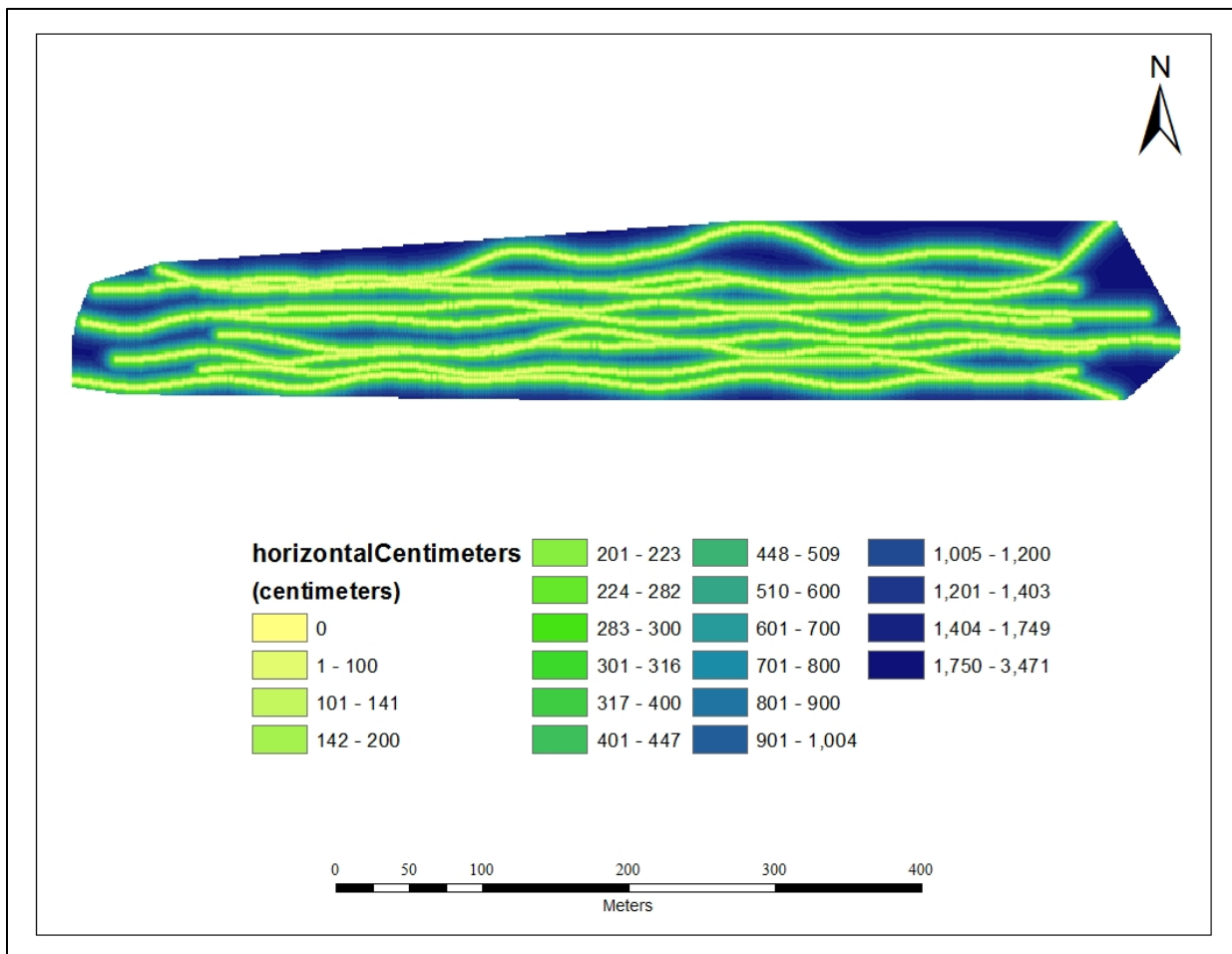
Figure 4-26. The *horizontalDistance* raster layer.
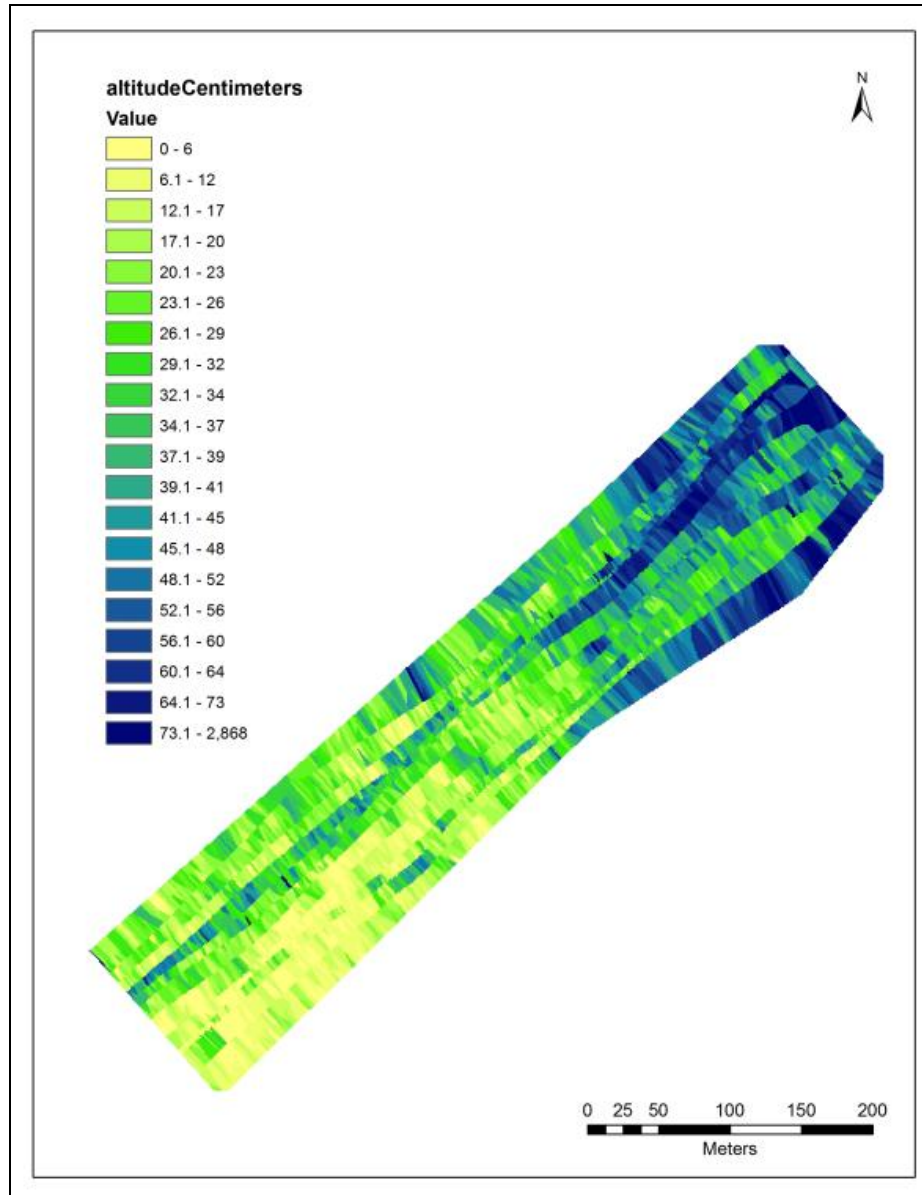
Figure 4-27. The vertical distance raster layer called *altitudeCentimeters*.

Once rasters for vertical and horizontal distance are finished, the tool then uses the Pythagorean Theorem to calculate the hypotenuse, or total distance, to produce a fourth raster layer called centimeters (Figure 4-28). Every cell in this raster represents the total distance from the seabed and adjacent data collection points, rounded to the nearest whole number. Using these distances, the user-input magnetic moment amount, and the sensor noise level, the tool then calculates the largest theoretical mass for each raster cell that could have gone undetected. This layer is called *potentialMassMissed*. These values are also rounded to the nearest whole kilogram value. Using integers throughout this process greatly speeds the processing time and reduces file size without any significant loss of accuracy. The 'blank' spots in the layer were filtered altitude values which were excluded from calculation; these are essentially no data areas.
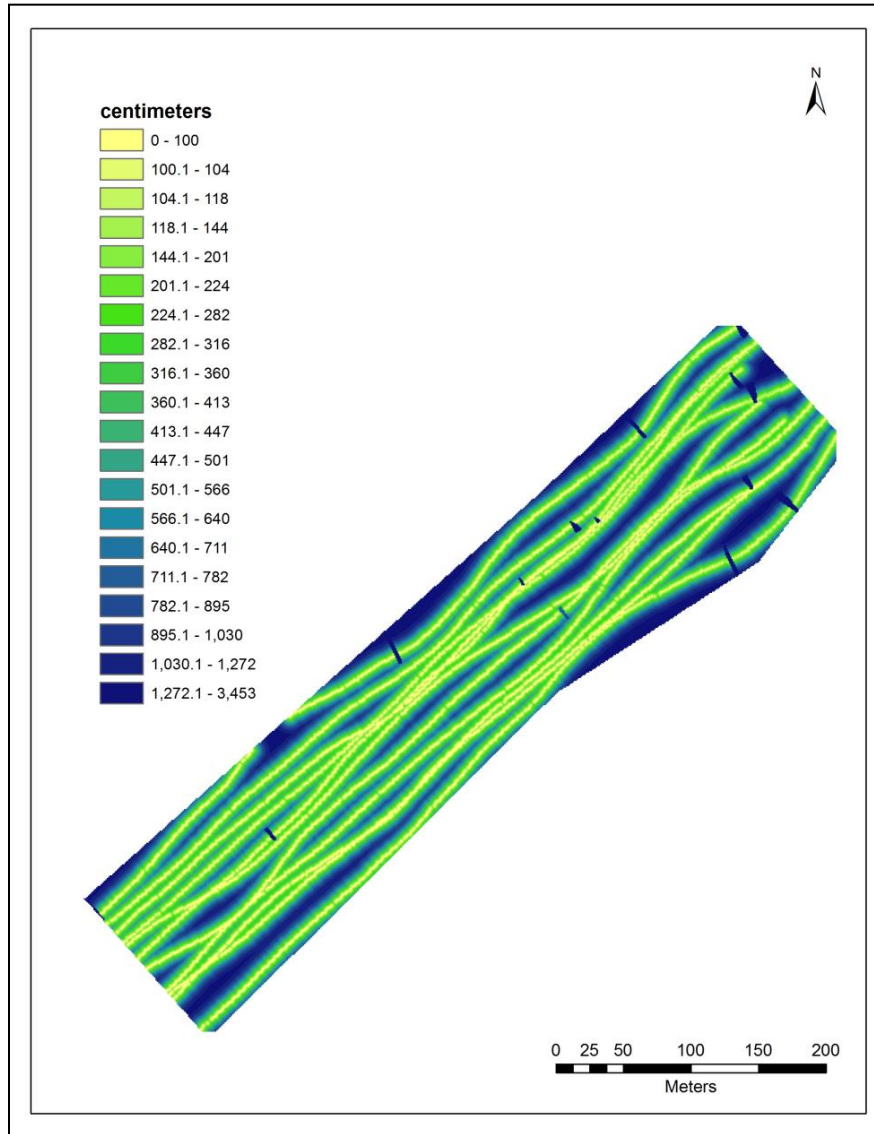
Figure 4-28. The total distance raster in centimeter units.

The resulting raster, labeled *potentialMassMissed* is a signed integer raster with an attribute table of cell values and counts (Figure 4-29 and Figure 4-30). The values are the potential masses, in kilograms, that were calculated by the tool; the count is the number of cells in the raster layer corresponding to that value. For example if the value is 500, i.e. 500 kg, and the count is 25, then in 25 cells of the raster layer, a 500 kg object or smaller could have been missed. If the raster cell resolution is set to 1 meter, then this equates to 25 square meters within the survey area (25 cells at 1 x 1 meter). This is essentially how thresholds of detection are calculated; except that the particular mass threshold includes that mass and every mass that is smaller. Using the 500 kg example, to determine the threshold of detection for a 500 kg object, total the cell count for 500, and then the cell counts for every mass smaller (499 kg, 498 kg, etc.), all the way to 0. The total of those cells, when multiplied by the cell resolution, is the area within the survey block where a 500 kg object or small could have gone undetected.

Based upon the information in the attribute table, the user can select the varying levels of coverage to be assessed in terms of ranges of masses, then add up the number of raster cells within each range, which are found in the *Count* column of the attribute table. If the raster cell resolution is 1, then this total of cells is also the area in square meters, otherwise the count must be multiplied by the cell resolution. These can also be expressed as percentages by dividing the number of cells in a range by the total number of cells in the raster and multiplying by 100. These ranges can also be expressed graphically, such as the bar graph in Figure 4-31. It is very important to remember that a given threshold includes the specific values (such as 500 kg in the example above), and every smaller mass. Though it seems onerous to repetitively add and divide these values in the attribute table, the *Select* and *show selected records* features of *ArcMap* makes summarizing these cell counts fairly easy. Once selected, the user can right click on the *Count* field and select *Statistics*. Here, *ArcGIS* will provide the sum of all the counts. Deselecting all records and re-launching the *Statistics* function on the *Count* field will provide the total number of cells in the raster.
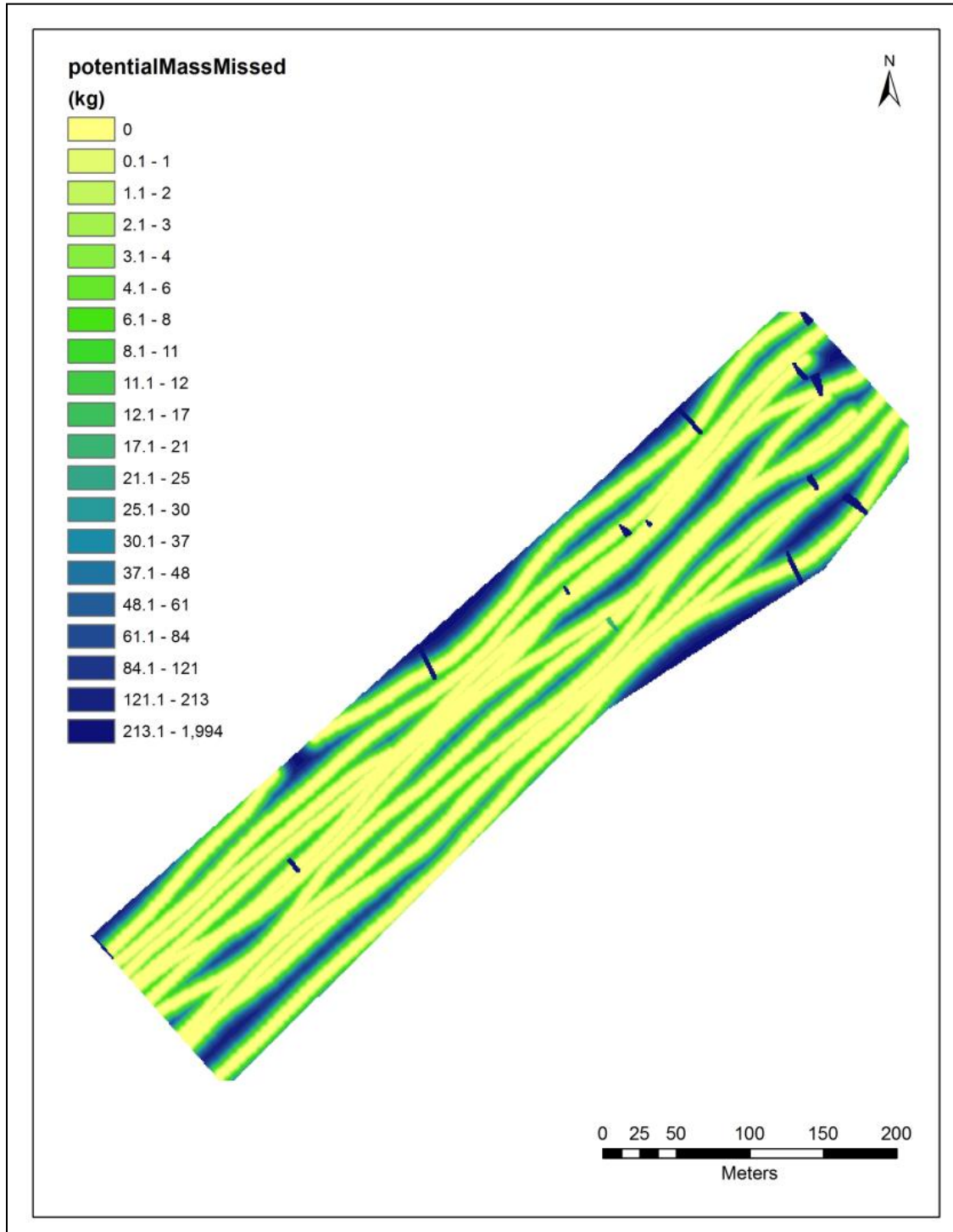
Figure 4-29. *potentialMassMissed* **raster, values in kilograms; voids are filtered altitude readings.**

OBJECTID *	Value	Count
1	0	30885
2	1	8410
3	2	5220
4	3	4438
5	4	2369
6	6	4239
7	7	1500
8	8	2003
9	9	1899
10	10	64
11	11	13
12	12	3236
13	13	9
14	14	1188
15	15	1
16	16	14
17	17	1578
18	18	1478
19	19	10
20	20	3
21	21	771
22	22	1
23	23	1628
24	24	9
25	25	878
26	26	4
27	27	41
28	28	1
29	29	1015
30	30	936
31	31	87
32	33	2
33	34	527

(0 out of 336 Selected)

potentialMassMissed

Figure 4-30. *potentialMassMissed* **attribute table.**
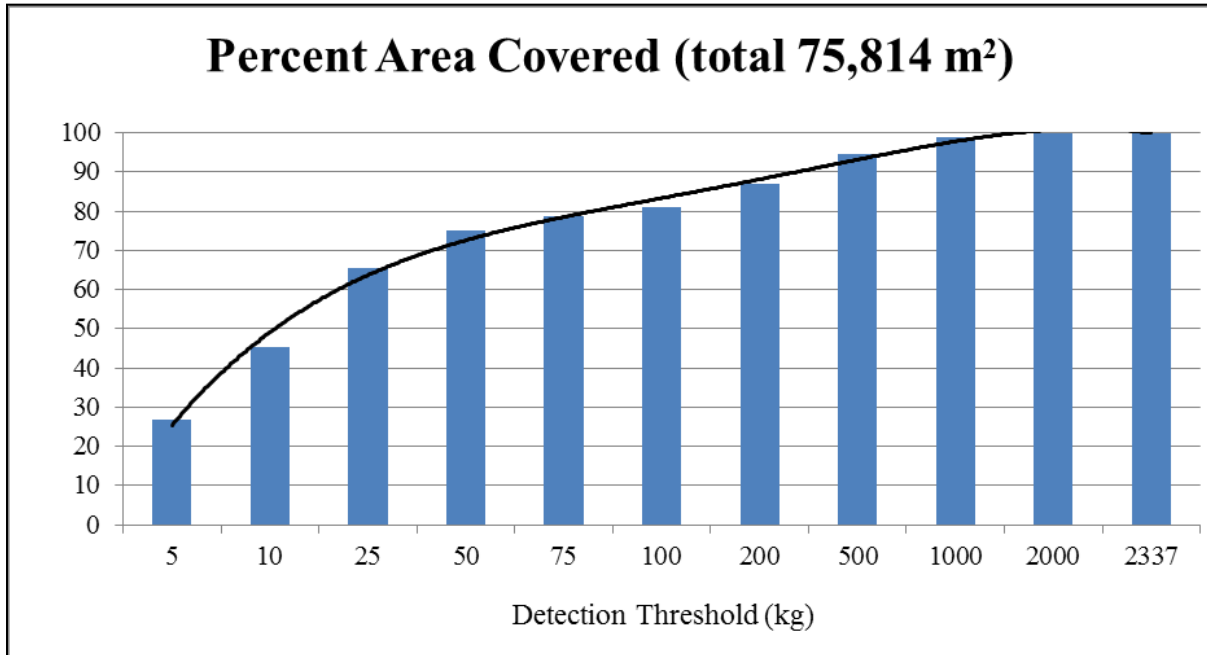
Figure 4-31. Bar graph depicting detection thresholds as percentages of total survey area.

Once finished producing the *potentialMassMissed* information, the tool then begins a separate set of processes. These are intended to provide the user with information about actual anomalies detected. Specifically, the potential mass which could have induced the observed magnetic flux given its distance from the sensor is determined. An initial raster layer, called *deltaGamma*, is produced based upon the parameters established in the user interface (Figure 4-32). Next, the tool uses the absolute value of these changes to produce a second raster, called *absDeltaGamma*. From this layer, and using the magnetic moment amount provided in the user interface, the tool produces a final raster which calculates the mass of objects which could have produced the observed anomaly amounts, called *potentialMassObserved* (Figure 4-33). This data can greatly assist archaeologists in the investigation of anomalies since the estimated mass can be compared with actual finds to determine if additional investigation is necessary at a given site. For example, if a potential mass of 1,000 kg was determined for a given anomaly but archaeologists only accounted for approximately 250 kg of ferromagnetic mass, this information may compel them to search for additional mass (though it may also be the case that the object had a higher magnetic moment than was used for modeling and therefore was the entirety of ferromagnetic mass in the area).
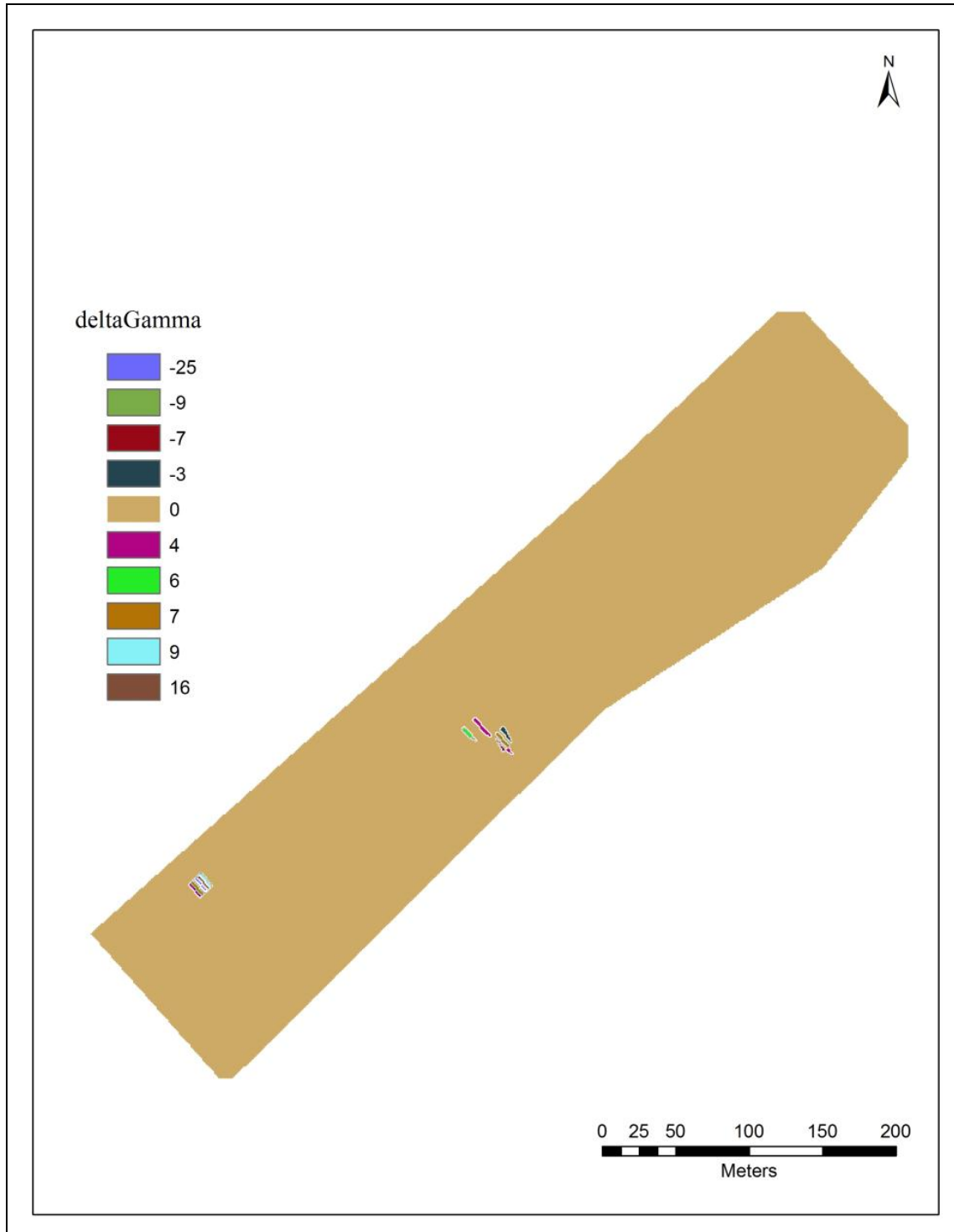
Figure 4-32. The *deltaGamma* raster layer.
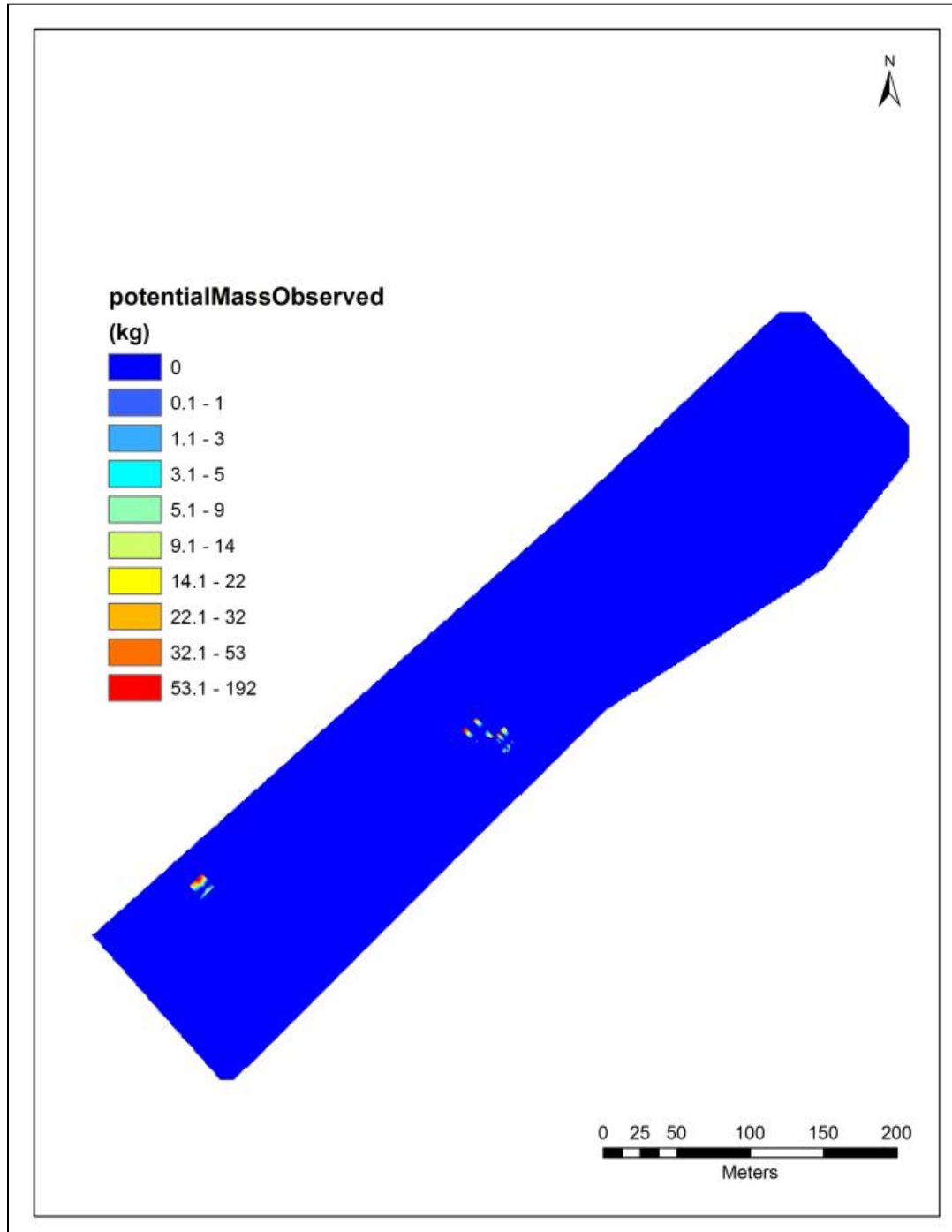
Figure 4-33. *potentialMassObserved* **raster layer.**

By providing quantitative information on actual survey area coverage, the *Confidence Model*
allows archaeologists to report survey area coverage assessment at a level not previously
possible. Prior to the development of this tool, archaeologists estimated survey coverage as a
proxy to the hypothetical coverage levels established during survey planning. For example, using
the diagram created by Breiner (see Figure 2-1) a survey could be planned such that a 1,000 kg

object would be detected; in this case at a maximum range of 30 m, producing a 5 gamma anomaly. If the 30 m maximum range was split into an offset and altitude, the survey plan would require 29 m lines with a sensor altitude of no more than 5 m, or 30 m line spacing with an altitude of ~ 1 to 2 m.

The algorithm used by Breiner, however, incorporates a mass-specific magnetic moment that varies by an order of magnitude—10 to 100 $\frac{\text{emu}}{\text{g}}$, thus the results derived from his planning tool are not very accurate. Considering that survey data acquisition entails an inherent amount of deviation from planning parameters, using planning parameters to describe actual coverage is very problematic. Instead, the inverse cubic function needs to be applied to the actual distribution of acquired data points, with a single magnetic moment used to make the assessment calculations. Though the *Confidence Model* and Breiner's planning graphic are based upon the same physical relationship—the inverse cubic function of induced magnetic fields—the *Confidence Model* applies it to actual data and provides the user the ability to manipulate the calculation parameters. Additionally, the user can query the resulting data products to whatever degree is necessary to articulate coverage of a given survey area via single or multiple coverage thresholds at user-defined intervals.

In fact, this tool can be run at varying parameters, creating numerous subsets of coverage information for varying amounts of sensor noise, magnetic moment, and mass thresholds. Though the other tools within the *Magnetometer Survey Toolbox* are powerful additions to archaeological magnetic survey and data assessment protocols, they are essentially just refinements and enhances of previously existing methods (even the gradient processing, which existed for over a decade within the SRC). The *Confidence Model*, on the other hand, is a new utility for magnetic data assessment, one which will hopefully become of mainstay of magnetic remote sensing for submerged archaeological materials.

BIBLIOGRAPHY

Aerodata International. 1987. *U.S. Navy Carrier Fighters of World War II.* Squadron/Signal Publishers, Carrollton, TX.

Barnette, Michael C. 2010. *Encyclopedia of Florida Shipwrecks, Volume I: Atlantic Coast.* Association of Underwater Explorers, FL.

Bohling, Geoff. 2005. Kriging. Kansas Geological Survey, Lawrence, KS. <http://people.ku.edu/~gbohling/cp e940/Kriging.pdf>. Accessed 20 Sept. 2012.

Bishop, Chris (ed). 1998. *The Encyclopedia of Weapons of World War II: The Comprehensive Guide to over 1,500 Weapons Systems, including Tanks, Small Arms, Warplanes, Artillery, Ships, and Submarines*. Metro Books, New York, NY.

Blum, Peter. 1997. *Physical Properties Handbook: A Guide to the Shipboard Measurement of Physical Properties of Deep-Sea Cores by the Ocean Drilling Program.* Texas A&M University Press, College Station.

Bowers, Peter M. 1999. *Boeing B-29 Superfortress*. Specialty Press Publishers and Wholesalers, North Branch, NM.

Breiner, Sheldon. 1999a. Applications Manual for Portable Magnetometer. Geometrics, San Jose, CA < ftp:// geom.geometrics.com/pub/mag/Literature/AMPM-OPT.PDF>. Accessed 10 Sept. 2012.

Breiner, Sheldon. 1999b. Magnetic Search in the Marine Environment. Geometrics, San Jose, CA < ftp://geom.geometrics.com/pub/mag/Literature/MarineSearch.pdf>. Accessed 10 Sept. 2012.

Bright, John C. 2012. NPS SRC Marine Magnetic Modeling: Research Design for Operational Testing; Phase 2 Task Operations Purusant to BOEM/NPS IAA M13PG0004. Manuscript on file. BISC-00168. Submerged Resources Center, Intermountain Regional Office, National Park Service, US Department of the Interior, Denver, CO.

Bureau of Ocean Energy Management (BOEM). 2012. Guidelines for Providing Geological and Geophysical, Hazards, and Archaeological Information Pursuant to 30 CFR Part 585. Office of Alternative Energy Programs, Bureau of Ocean Energy Management, Regulation and Enforcement, US Department of the Interior.

Bureau of Ocean Energy Management (BOEM). 2013. Collaborative Archaeological Investigations and Sound Source Verifications within the Massachusetts Wind Energy Area. Manuscript on file. Office of Renewable Energy Programs, Bureau of Ocean Energy Management, US Department of the Interior, Herndon, VA.

Burrough, Peter A., and Rachael A. McDonnell. 1998. *Principles of Geographical Information Systems.* Oxford University Press, New York, NY.

Camidge, Kevin, Peter Holt, Charles Johns, Luke Randall, and Armin Schmidt. 2010. *Developing Magnetometer Techniques to Identify Submerged Archaeological Sites: Theoretical Study Report*. Historic Environment, Environment, Planning & Economy, Cornwall Council, Cornwall, United Kingdom.

Caruana, Adrian B. 1994. *The History of English Sea Ordnance 1523-1875, Volume I: 1523-1715 The Age of Evolution.* Jean Boudriot Publications, East Sussex, England.

Caruana, Adrian B.1997. *The History of English Sea Ordnance 1523-1875, Volume II: 1715-1815 The Age of the System.* Jean Boudriot Publications, East Sussex, England.

CFM International. 2010. CFM56-3 Technology. CFM International website. <http://www.cfmaeroengines.com/ engines/cfm56-3>. Accessed 22 Oct. 2012.

Chapman, Fredrik Henrik Af. 2006. *Architectur Navalis Mercatoria*: *The Classic of Eighteenth-Century Naval Architecture.* Dover Publications, Mineola, NY (originally published 1768).

Curryer, Betty Nelson. 1999. *Anchors: An Illustrated History*. Naval Institute Press, Annapolis, MD.

Dalan, Rinita A. 2006. Magnetic Susceptibility. In *Remote Sensing in Archaeology: An Explicitly North American Perspective*, Jay K. Johnson, editor, pp. 161-204, University of Alabama, Tuscaloosa.

Desmond, Charles. 1919. *Wooden Ship-Building.* The Rudder Publishing Company, New York, NY.

Engelbrektson, Einar (ed). 1975. *The Lore of Ships.* AB Nordbok, Gothenburg, Sweden.

Geometrics. 2003. G-882 Marine Magnetometer. Product Brochure. <ftp://geom.geometrics.com/pub/mag/DataSheets/G-882_DataSheet.pdf>. Accessed 12 March 2013.

Graumont, Raoul and John Hensel. 1994. *Splicing Wire & Fiber Rope.* Cornell Maritime Press, Centreville, MD.

Hall, E.T. 1966. The Use of the Proton Magnetometer in Underwater Archeology. *Archaeometry*, Vol. 9:32-44.

Hrvoic, Doug and Matthew Pozza. 2004. High-Resolution Magnetic Target Survey: Harnessing the power of three-axis total-field magnetic gradient. *Hydro Journal.* 8.6: 2-5.

Hughes, Charles H. 1917. *Handbook of Ship Calculations, Construction and Operation.* D. Appleton and Company, New York, NY.

Lavery, Brian. 1987. *The Arming and Fitting of English Ships of War: 1600-1815.* Conway Maritime Press, London.

Murray, Mungo.1754. *A Treatise on Ship-building and Navigation.* D. Henry and R. Cave, London, UK.

Shope, S.M. 2011. *Magnetic Gradient Processing*. Report to National Park Service Submerged Resources Center, Lakewood, CO, from Sandia Research Corporation, Mesa, AZ.

Skowronek, Russell K., and George R. Fischer. 2009. *HMS* Fowey *Lost and Found.* University Press of Florida, Gainesville.

Tinniswood, J. T. 1945. Anchors and Accessories, 1340-1640. *The Mariner's Mirror* Vol 31(2):84-105.

Jones, F. 2007. Magnetic susceptibility of geological materials. University of British Columbia (UBC) Department of Earth, Ocean and Atmospheric Sciences. Vancouver, BC. <http://www.eos.ubc.ca/ubcgif/iag/foundations/properties/magsuscept.htm>. Accessed 25 February 2014.

Weymouth, John W. 1976. A Magnetic Survey of the Walth Bay Site (39WW203). Manuscript, National Park Service, Midwest Archeological Center, Lincoln, NE.

APPENDIX I

MAGNETOMETER SURVEY PYTHON TOOLBOX V 1.0:

RELEASE NOTES

INTRODUCTION:

The following release notes describe the function and operation of the individual tools within the Magnetometer Survey Python Toolbox, V 1.0. This toolbox was developed under the auspices of Interagency Agreement (IAA) M13PG00004 between the Bureau of Ocean Energy Management's Office of Renewable Energy Programs (BOEM OREP) and the National Park Service's Submerged Resources Center (NPS SRC). This IAA, initiated in March of 2013, was established for the NPS SRC to provide scientific and technical services to BOEM OREP via the development of an analytical tool for assessing confidence and coverage of marine magnetic surveys for archaeological resources.

Specifically, NPS SRC and BOEM OREP collaborated to create a custom-scripted python toolbox to automate magnetic data processing and generate the data outputs necessary to quantify the coverage of a given magnetic survey. In this way, these tools actually perform two functions: visualize the data for anomaly detection and provide a post-acquisition coverage assessment. Though the term 'coverage' is often used in the context of data acquisition to describe the completeness of data gathering in a survey area, it is here meant to describe the degree to which data point density (a composite of sampling rate and survey vessel speed) and sensor altitude correspond to the detectability of ferromagnetic objects. In other words, coverage refers to the extent to which the data acquisition parameters resulted in the probable detection of ferromagnetic objects of varying masses.

Since this varies throughout an area, modeled as an inverse function of distance between an object of a certain mass and the location of the sampling instrument (i.e. the magnetometer), coverage is therefore expressed by thresholds of detection. These thresholds are determined by the largest theoretical mass which could have gone undetected in a given space, corresponding to changes in horizontal line spacing and sensor altitude. As these parameters increase, distance between the sensor and the object increases, thus detection thresholds likewise increase, meaning that relatively larger objects could have gone undetected within the survey area. These delineations are made at the discretion of the user, corresponding to the objectives of each individual survey. For example, these thresholds could be expressed in terms of 100, 200, and 300 kg masses, or 1,000 and 500 kg masses. Thus, in its simplest form, confidence in a magnetic survey is a determination of its success or failure to achieve a given survey's objectives.

SCOPE:

These tools carry out a series of geospatial processing functions which provide the data products necessary to visualize and assess a given dataset. The first tool, the *Input Tool*, converts magnetic data from a tabular format into a standardized point feature class. This data schema is hard coded into the remaining tool (in other words it is the only format they will recognize), thus all data must first be loaded through the *Input Tool*. Any tabular data format recognized by ArcGIS can be loaded into the *Input Tool*. The result is a single point feature class called *rawGamma* containing raw magnetic readings, altitude data (if collected), and survey line number in its attribute table; in addition to a line feature class called *surveyLines*, where the points are converted into lines based upon line file name.

Next, a *Generate Survey Boundary* tool develops two buffered polygon feature classes encompassing the extent of all input data points. This is an optional tool for the user to automate boundary creation around the extent of all acquired data points. Otherwise, the user will need to manually construct a polygon feature class representing the survey area. A boundary is needed to function as an analysis mask for all remaining processing functions. This analysis mask limits the extent of data processing and all layers created by the toolbox which would otherwise extend well beyond the boundaries of the survey area.

This tool is programmed to accept either the point or line feature class generated by the *Input Tool;* the boundary creation methods slightly vary. The first polygon created by this tool is built as a convex hull around a minimum bounding geography. In other words, it will draw the simplest shape encompassing all points/lines. When the magnetic data is arrayed in a large, continuous block this tool functions very well. Datasets with complex geometries (especially those with any concavities) are better bounded by the second polygon feature class which is developed as a series of dissolved buffers merged into a single polygon. In either case, these feature classes may require additional editing to adjust the vertices of the created boundaries to the actual data; the tool creates both automatically.

A third tool, called the *Visualization* tool, carries out the basic data processing functions of interpolating a full-field raster map with polyline iso-lines at a user-defined contour interval. In addition to generating a full field map, this tool also executes a selective spatial filtering algorithm, referred to as gradient processing, to eliminate most geological, secular, and diurnal variations from the data. This gradient data is also interpolated into a continuous surface with contour lines. When visualized, gradient processed data reveals discreet areas of high intensity magnetic flux, those most likely to correspond with man-made ferromagnetic objects, making the interpretation and identification of anomalies much easier.

The fourth tool in the toolbox generates the coverage/confidence assessment data and is therefore called the *Confidence Model* tool. This tool uses a series of sequential raster calculations, a density analysis, and spatial allocation to determine the distribution of survey distance—the hypotenuse of sensor altitude and horizontal distance between points—throughout the survey area. The result is a total distance raster which is a three-dimensional representation of distance from the magnetic sensor to the seabed throughout the survey area. Next, using an inverse-cube model of induced magnetic fields, the largest undetectable mass is determined for each raster

cell. This raster, and its accompanying attribute table, is used to calculate detection thresholds. The equation used to solve for mass is as follows:

$$W=\frac{(\Delta\gamma*10^{-6})r^3}{M}$$

where w is mass (kg), $\Delta\gamma$ is amount of magnetic density flux at which an anomaly would not be detected (i.e. equal to sensor noise), r is distance (cm), and M is the magnetic moment ($\times 10^4$ $\frac{emu}{g}$). Here, sensor noise is the maximum amount of magnetic density flux that would not result in an observed anomaly. Thus, an object inducing this amount or less would not be detected. It is important to note that detection of a ferromagnetic object by the sensor does not necessarily mean that the survey will detect the object, since the design of a survey in advance of data collection entails the establishment of multiple parameters such as contour interval and data representation that may selectively mask or highlight the measurements of the instrument (see *confidenceResult* below).

Nested within this process is a simplified coverage calculation referred to as the *confidenceResult*. Based upon a user-specified mass (referred to in the interface as the *mass threshold*), the tool will calculate the percentage of the survey area in which that mass would have been detected at a given set of modeling parameters. This is intended to function as a quick-check of a given dataset, where the user can begin to develop more articulated statistics based upon the data products.

Additionally, the *Confidence Model* also evaluates magnetic anomalies within the dataset. Using the same inverse-cube algorithm, the tool determines the mass of an object responsible for a given magnetic flux as a function of total distance from the sensor in an idealized situation (one in which the object responsible for the anomaly sits at a minimum distance from the sensor). Thus, in addition to categorizing anomalies in terms of the amplitude of magnetic flux, the user may also be able to determine the approximate mass of the individual object.

Collectively, the *Magnetometer Survey* toolbox is an effective tool for archaeologists to evaluate the efficacy of a given survey. As detection thresholds are expressed in terms of theoretical masses, archaeologists can use mass as a proxy for various cultural materials. For example, if the intent of a survey was to locate a historical anchor, detection thresholds would be expressed in terms of the historically reported masses of various anchor sizes. Evaluating their survey dataset as such, the user could determine in what percent of their survey area they would have detected an anchor of a given size. Based upon this percent of coverage, they can determine if their survey thoroughly examined the area for the targeted objects.

Inherent in this modeling process, however, are certain assumptions based upon the theoretical behavior of ferromagnetic objects. Primarily, this algorithm describes the magnetic field induced in an object by the Earth's ambient magnetic field (ignoring any remnant magnetism an object may have). As Earth's field changes geographically and temporally, it is incumbent upon the user to account for these variations and their subsequent effect upon an object's induced field when deciding upon values to input for magnetic moment. As described in the field testing section of the IAA report, historical materials exhibit a range of magnetic moments. The field strength of a given item can only be determined after it is found; thus, it is recommended the user

select conservative (i.e. lower) M values to account for the possibility that archaeological materials within the survey area have weaker magnetic fields. Likewise, the chemical environment and site formation processes acting upon submerged cultural materials affect the physical structure of an object and may change its magnetic properties. In many cases, these factors cannot be accounted for systematically. In other words, one cannot know the magnetic properties of objects that have not yet been found and should therefore model upon a worst-case scenario.

Specifically, it is recommend initial modeling of a survey area be completed based upon the magnetic properties of pure iron, calibrated for local conditions. Some literature ascribes magnetic moments of 10 to 100 $\frac{\text{emu}}{\text{g}}$, while others a more specific range: 15-35 $\frac{\text{emu}}{\text{g}}$, approximately. Ferrous compounds range significantly from these baseline values, sometimes multiple orders of magnitude up or down. A more detailed discussion of selecting magnetic moment values is contained in the full IAA report. For practical applications, it is recommended that the user access the NOAA NGDC online database to determine the ambient magnetism for the time and location of their survey. Enter this value into the *Magnetic Moment Calculation Spreadsheet* accompanying this document. Combined with an Archaeological Scaling Factor (the use of archaeological material-to-pure iron ratios is outlined in the IAA report), this magnetic moment value can be adjusted for local conditions.

SYSTEM REQUIREMENTS:

The Magnetometer Survey toolbox was developed on ESRI's ArcGIS 10.2.1 platform. **This tool is not backwards compatible with older versions of ArcGIS, with the exception of ArcGIS 10.1.** In addition to the basic platform, the user must also have licensed **Spatial Analyst and 3D Analyst** extensions. The toolbox is a Python toolbox (.pyt) that the user can upload into ArcToolbox (via ArcCatalog) once it is saved on their hard drive. The attached User Instructions detail the uploading process.

Once loaded, the tool can accept any tabular data formats recognized by ArcGIS, including:

> Comma separated value (.csv)—recommended
> Text file (.txt)
> Database (.dbf)
> Shapefile (.shp)

Within the data table, furthermore, the following items are required. Each of these components must occupy a single field within the table. For example, easting or longitude data must be within a single column in the data table. This would include a column for an easting amount, or longitude in decimal degrees, not a table with separate columns for degrees and another for decimal minutes.

Input Data Requirements:

> Easting/Longitude

> Northing/Latitude
> Raw Magnetic Readings
> Altitude (optional, but recommended)
> Survey Line Number/Name

As previously mentioned, the tool also requires a polygon feature class representing the survey area. This is needed as an analysis mask for the *Visualization* and *Confidence Model* tools. One can be selected from the *Generate Survey Boundary* tool outputs, or manually constructed by the user.

As the tools operate, all products are saved to a user-designated file geodatabase (.gdb) which, depending upon the dimensions of the survey area—and resulting number of data points—will vary in size. All tools were tested using a one-million point survey dataset. The resulting geodatabase totaled 235 MB, and the tools took the following approximate times to execute:

Input Tool:	2 min
Generate Survey Boundary:	30 min
Visualization (Kriging):	180 min
Visualization (TIN):	10 min
Confidence Model:	10 min

*Note: depending upon the platform and computer used processing times may vary.

Each tool writes data products to a designated geodatabase. The default settings enable to user to create a single file geodatabase using the *Input Tool*, and then all remaining data products from that survey area will save to the same geodatabase. A unique nomenclature is derived for each file, so multiple processing runs at varying settings will save to the same geodatabase and be distinguishable from other, similar products.

During execution, the tools will navigate to inputs, such as the data table and survey area, through their accompanying file structure. **As the tools execute, however, they cannot locate files if there are any spaces in the file structure leading to them**. Thus, it is necessary for users to be vigilant about file nomenclature within the entire file structure used for GIS data management. This includes individual file names and also folders. It is recommended the user substitute underscores for spaces, such as Mag_Data.

MAGNETOMETER SURVEY TOOLBOX OPERATION:

This section outlines the basic function of each tool, including the user interface, processing operations, and data outputs. This consists of descriptions of each input and user-selected parameter, as well as the format and nomenclature of data outputs. Specific step-by-step instructions on the use of each tool are contained in the instructions document accompanying these release notes. This overview is intended as a quick-reference regarding each tool's function and outputs. A more detailed theoretical overview is contained in the IAA report.

INPUT TOOL

This tool converts a tabular magnetic dataset into a standardized data schema that is recognized
by the other Magnetometer Survey Toolbox processing tools. This is accomplished by
converting the tabular dataset into a point feature class with accompanying attribute table. Input
data must, for every sample point, contain 1) easting/longitude, 2) northing/latitude, 3) magnetic
readings, and 4) a line/file name. Altitude is highly recommended.

User Interface:
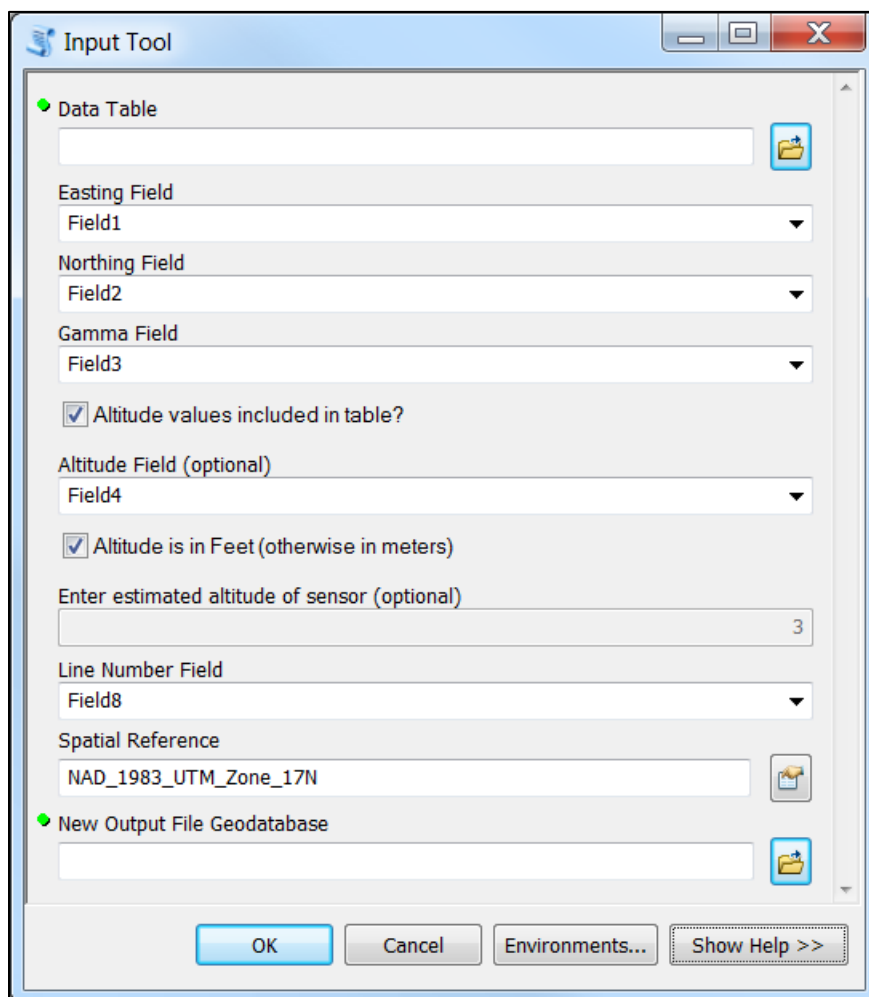
Inputs:

1. <u>Data Table</u>: tabular data exported from data acquisition program.
2. <u>Easting Field</u>: Define the title of the data table field containing
   easting/longitude information. Though the default is "Field1," the interface
   will auto-populate with the names once the data table is defined.

3. <u>Northing Field</u>: Define the title of the data table field containing northing/latitude information. Though the default is "Field2," the interface will auto-populate with the names once the data table is defined.

4. <u>Gamma Field</u>: Define the title of the data table field containing magnetic readings. Though the default is "Field3," the interface will auto-populate with the names once the data table is defined.

5. <u>Altitude values included in table</u>?: This is a yes/no check box. If checked yes, then user must define the field in the table (see step 6). If not, user must enter a default values (see step 8).

6. <u>Altitude Field</u>: Define the title of the data table field containing sensor altitude values. Though the default is "Field4," the interface will auto-populate with the names once the data table is defined.

7. <u>Altitude is in Feet (otherwise Meters)</u>: This is a yes/no check box. If checked yes, the tool assumes the altitude values are in feet; if unselected it assumes they are in meters. Tool will convert these into units of centimeters when it creates the new feature class.

8. <u>Enter estimated altitude of sensor</u>: This remains inaccessible unless the *Altitude values included in table* input is de-selected. **If the data table contains no altitude information, a default value must be entered for this tool to operate**. This value represents the estimated average sensor altitude throughout the entire survey area.

9. <u>Line Number Field</u>: Define the title of the data table field containing the line file name. Though the default is "Field8," the interface will auto-populate with the names once the data table is defined.

10. <u>Spatial Reference</u>: Define the spatial reference system (datum and/or projection system) used in the data table.

11. <u>New Output File Geodatabase</u>: Once open, navigate to desired work space and enter the name that the tool will assign to the geodatabase it creates to store the data products. This will become the default geodatabase which all subsequent data products are created in.

Operations:

12. Uses position information to create a point feature for each sample point, then attaches the magnetic value into an attribute table under the heading recordedGamma, the line name/number under the heading lineNumber, and converts the altitude values from either feet or meters to centimeters. When no altitude value is present, the tool writes the user-input estimated altitude to each point in units of centimeters.

13. All data points are converted into a series of line corresponding to the survey line file name. This line feature class represents that actual lines driven by the survey vessel.

Outputs:
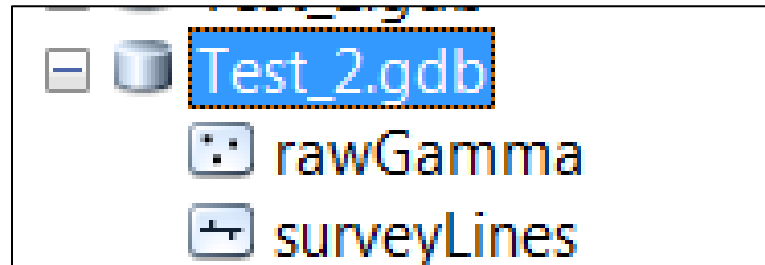
14. rawGamma (Point Feature Class): points and attribute data including ObjectID, Shape, recordedGamma, lineNumber, and altitude in centimeters, as converted from its original units.

15. surveyLine (Line Feature Class): A line corresponding to each unique line file name in the attribute data. The feature class represents the actual lines travelled by the survey vessel. This feature class provides a visual output which can be used to determine line spacing and to verify that the correct line file parameter was established in the tool.

GENERATE SURVEY AREA TOOL

This tool creates two buffered polygon feature classes around the perimeter of all input data points or survey lines. The first perimeter is generated as buffered convex hull around the extent of the input feature class. The second is created as a dissolved buffer around each individual feature class item (either data points or survey lines). Once produced by the tool, these polygon features can be easily edited by the user if adjustments are necessary.

User Interface:
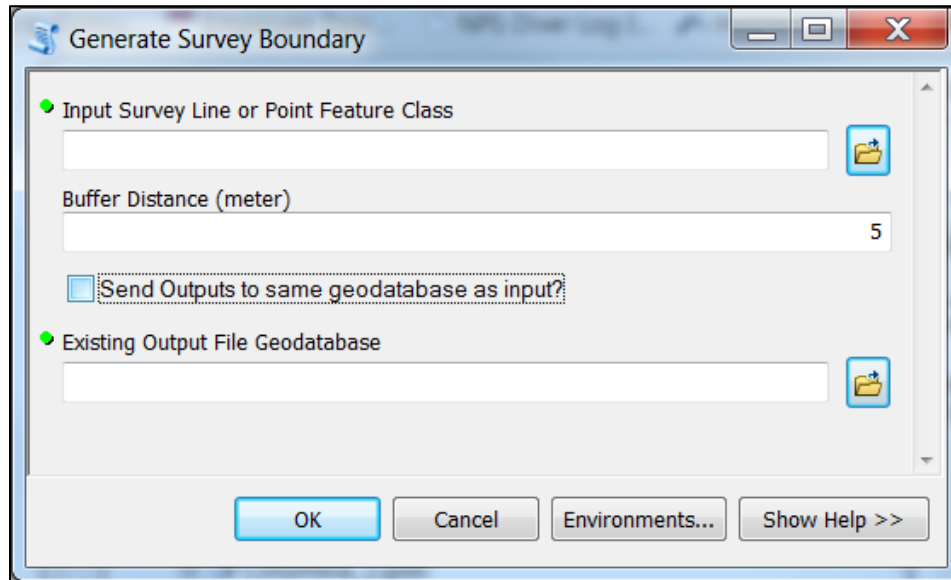
Inputs:

16. Input Survey Line or Point Feature Class: link to either the *rawGamma* feature class or *surveyLines* feature class created by the *Input Tool*. If point are used, the individual data points will be buffered; if the lines are used the survey lines will be buffered. Generally, they produce the similar boundary geometries, but since there are fewer lines than points, inputting the survey lines features will result in much quicker processing times.
17. Buffer Distance: The distance in meters the tool will extend the boundary of the convex hull polygon away from the input features, and the distance buffered from each individual data point or line. Recommend using half of planned line spacing (i.e. 15 m for 30 m line spacing). Buffering at less than this distance can create issues when the tool is merging the individual buffer into a single polygon boundary; if there is not sufficient overlap (buffer distance), the process cannot complete.
18. Send Outputs to same geodatabase as input?: This is a yes/no selection. By default, the tool will save the products to the same geodatabase created by the

Input Tool. If unselected, the user can create a new file geodatabase via the last input window.

Operations:

19. Creates *convexHull* polygon around input features using the minimum bounding geometry logic—the smallest polygon to encompass all input points or lines.
20. Expands geometry of *convexHull* based upon user-specified buffer distance to create *surveyArea* polygon.
21. Buffers individual data points or lines at user-specified buffer distance.
22. Dissolves individual buffers into single polygon and then removes internal voids to produce a feature class called *surveyArea2*.

Outputs:
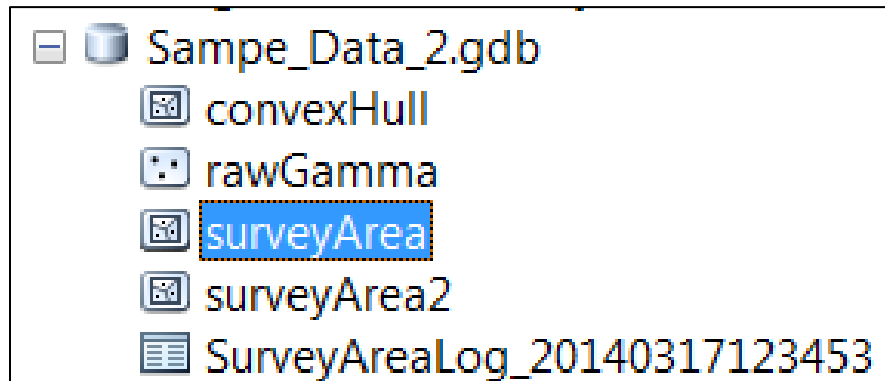
23. convexHull (Polygon Feature Class): convex polygon generated around the extent of data points.
24. surveyArea (Polygon Feature Class): polygon shapefile generated at user-defined buffer distance based upon geometry of *convexHull* polygon.
25. surveyArea2 (Polygon Feature Class): polygon shapefile generated at user-defined buffer distance around each point, dissolved into a single polygon.
26. SurveyAreaLog_YYYYMMDDHHMMSS (table): A record of all input parameters for later reference. File name is date/time coded.

*Note, the user may wish to make minor adjustments to the survey area polygons. This can be done via the Editor toolbar in ArcMap at the discretion of the user. Depending upon data geometry, using the *rawGamma* feature class versus the *surveyLine* may produce slightly different boundary geometries; the user should experiment with both to achieve the appropriate survey area boundary.

VISUALIZATION TOOL

This tool produces a series of continuous surfaces and contour lines based upon the raw magnetic values in the input data table. These include a raster surfaces and iso-lines at a user-specific contour interval from the raw magnetic values and the calculated gradient values. In ArcMap these products can be symbolized and used to identify magnetic anomalies associated with potential archaeological material.

User Interface:
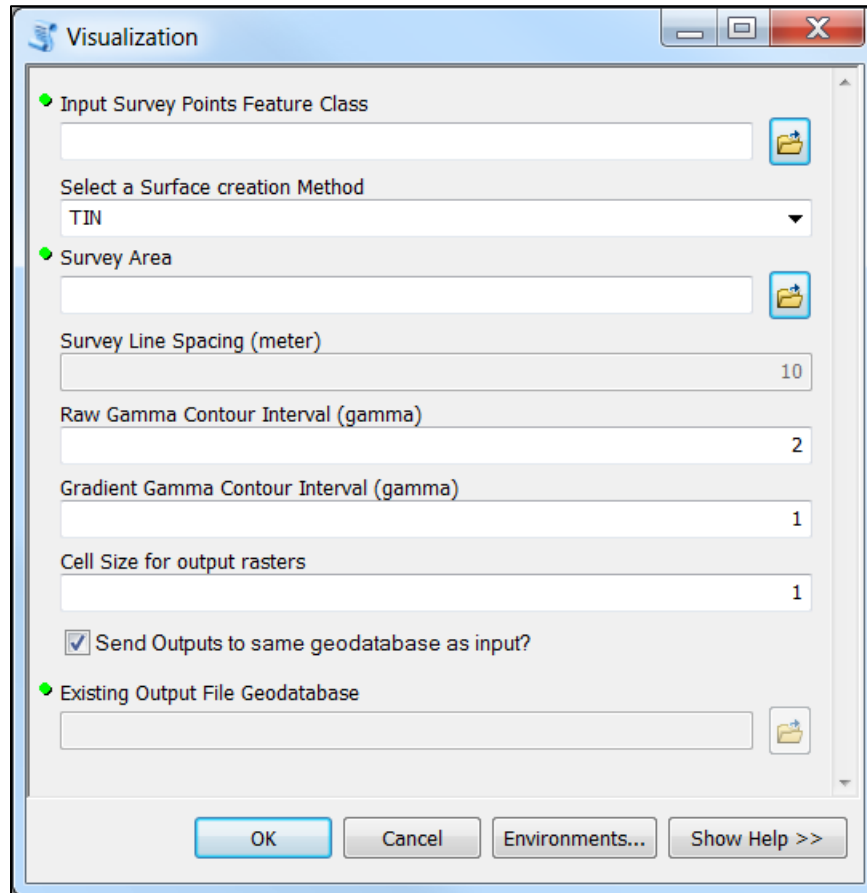
Inputs:

1. <u>Data Table:</u> link to the *rawGamma* feature class created in the *Input Tool*.
2. <u>Survey Area:</u> Input a polygon feature class representing the survey area. The default will open to the input geodatabase where the *surveyArea* and *surveyArea2* feature classes created by the *Generate Survey Boundary* tool are located.
3. <u>Kriging/TIN selection:</u> User chooses which interpolation method will be applied to generate continuous surfaces from the raw and gradient points.

4. Survey Line Spacing: This remains inaccessible unless the user selects the Kriging interpolation method. Enter the average horizontal spacing between survey lines based upon survey design. This amount will influence the distance at which the mathematical function averages magnetic values.

5. Raw Gamma Contour Interval: Input the desired contour interval for the polyline iso-lines representing gamma values, extrapolated from the full field raster surface.

6. Gradient Gamma Contour Interval: Input the desired contour interval for the polyline iso-lines representing gamma values, extrapolated from the gradient raster surface. Note that the gradient processing function, because it only measures differences between consecutive points, results in a surface with much less variation than the full-field surface so a contour interval smaller than the full-field contour interval is highly recommended.

7. Cell Size for output rasters: Define the resolution of output raster cells. Since all raster cells are square, this amount will be the resulting length and width of all the cells, in meters. A value of 1 is recommended to maintain a 1-to-1 ratio between raster cell counts and area in square meters.

8. Send Outputs to same geodatabase as input?: This is a yes/no selection. By default, the tool will save the products to the same geodatabase created by the *Input Tool*. If unselected, the user can create a new file geodatabase via the last input window.

Operations:

1. Gradient values are calculated from raw magnetic readings.
2. Input survey area boundary is used to set an analysis mask.
3. Raw gamma readings used to interpolate a continuous surface, produced as a floating-point raster.
4. A raster to polyline conversion is used to generate iso-lines at the user-specified contour interval.
5. A continuous surface is interpolated from gradient values, saved as a floating-point raster.
6. A raster to polyline conversion is used to generate iso-lines at the user-specified contour interval.

Outputs:
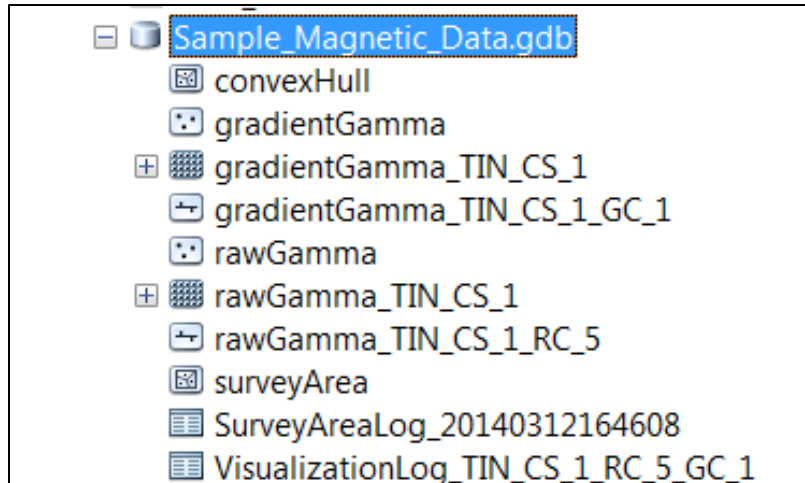
1. gradientGamma (Point Feature Class): Points created during gradient calculation. New feature class has attribute data containing the gradient values (gradientGamma field) and line number.
2. gradientGamma_code (Floating-Point Raster): continuous surface interpolated from gradient point values. Code is Interpolation Method (TIN or Krig), Cell Size(CS).
3. gradientGamma_code (Polyline Feature Class): Isolines drawn at user-specified contour interval. Code is Interpolation Method (TIN or Krig), Cell Size (CS), and Gradient Contour interval (GC).
4. rawGamma_code (Floating-Point Raster): continuous surface interpolated from *rawGamma* point values. Code is Interpolation Method (TIN or Krig), Cell Size(CS).
5. rawGamma_code (Polyline Feature Class): Isolines drawn at user-specified contour interval. Code is Interpolation Method (TIN or Krig), Cell Size (CS), and RawGamma Contour interval (RC).
6. VisualizationLog_code (Table): The log where all run parameters are saved. Each table is coded by abbreviated run parameters: Interpolation Method_Cell Size_value_RawGamma Contour interval_value_Gradient Contour interval_value.

CONFIDENCE MODEL TOOL

This tool provides the data outputs necessary to determine thresholds of detection within a survey area. Using data point density, sensor altitude, and an inverse-cube model of induced magnetic fields, the tool calculates the largest potential mass that could have gone undetected in a given location inside the survey area, and also the masses of objects required to produce any anomalies observed with the area.

User Interface:
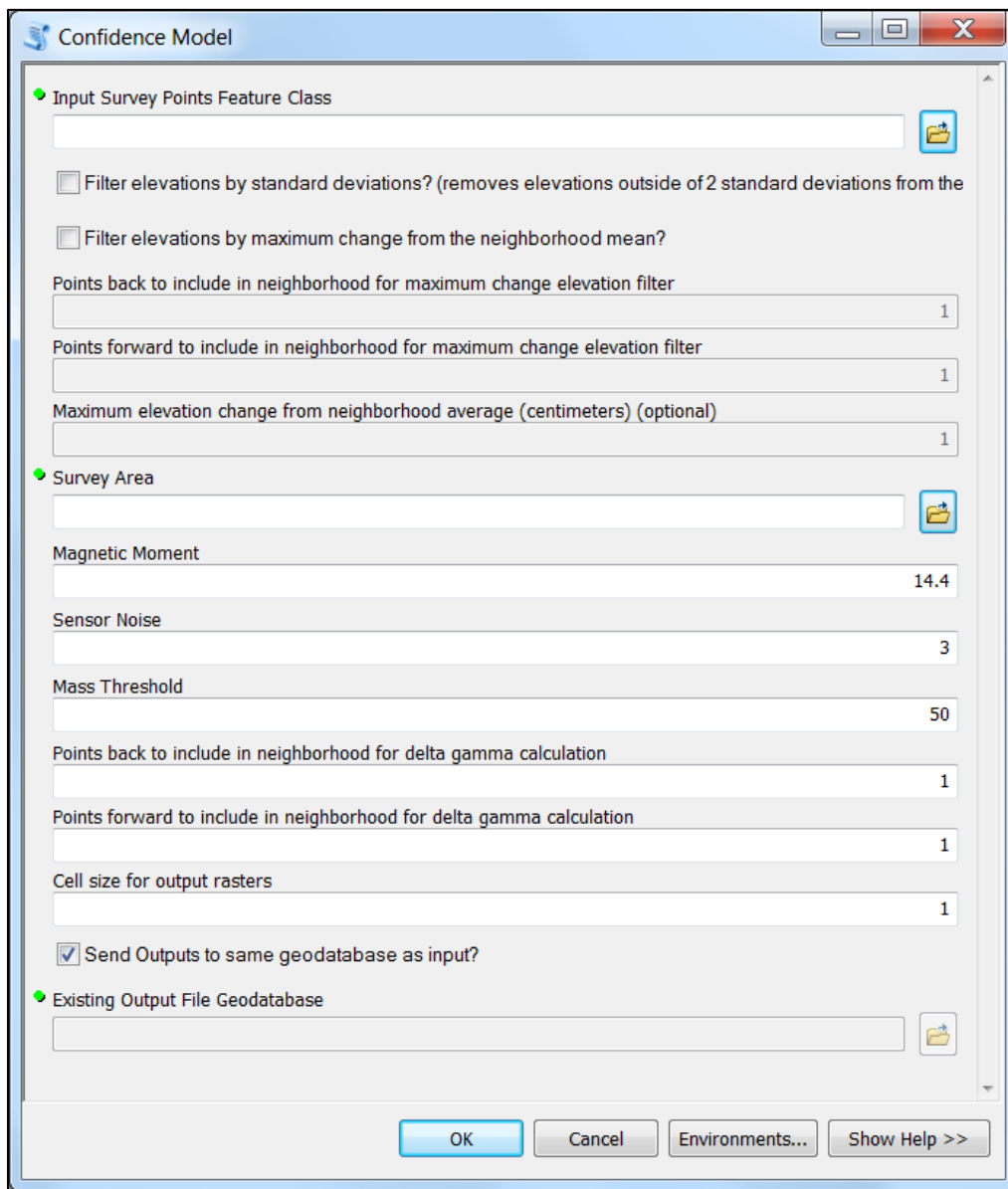
Inputs:

1. Data Table: link to the *rawGamma* feature class created in the *Input Tool*.
2. Filter elevations by standard deviations: Select the check box to statistically exclude any altitude values beyond two standard deviations of the mean altitude value. For use in datasets were erroneous values were introduced via bottom strikes or sensor malfunctions. Recommended for very large datasets.
3. Filter elevations by maximum change from the neighborhood mean: Select the check box to exclude altitude values that fail an averaging query established by neighboring points. This targets only erroneous altitude values introduced into the data by bottom strikes or sensor malfunction unlike statistical exclusion which may leave bad values in, or exclude good values, depending upon the statistical breakdown of the data.
4. Points back to include in neighborhood for maximum change elevation filter: If using the filtering method described above in item 3, enter the number of points preceding the data point to average for the filter query.
5. Points forward to include in neighborhood for maximum change elevation filter: If using the filtering method described above in item 3, enter the number of points succeeding the data point to average for the filter query.
6. Maximum elevation change from neighborhood average (optional): Another altitude filtering method. This sets a maximum allowable change, Δalt (in cm), from the calculated neighborhood average. Use with datasets acquired over varying topography to avoid excluding altitude values generate by rapid changes in bathymetry or sensor position.
7. Survey Area: Define the location of the survey area polygon feature class.
8. Magnetic Moment: Input the value for the strength of the magnetic field used to calculate potential masses in the survey area. General values for pure iron are between 10 and 100; see the full IAA report for a discussion of selecting appropriate magnetic moment values.
9. Sensor Noise: Enter the observed amount of sensor noise. This establishes the minimum amount of magnetic flux necessary to be distinguished from background noise. Though sensor manufacturers report low levels of noise, several operational parameters tend to increase noise level. **A value twice the reported noise level is recommended**. The default is 3 γ.
10. Mass Threshold: User input mass (kg) which will result in a raster layer that represents all portions of the survey area where the entered mass would have been detected.
11. Points back to include in neighborhood for delta gamma calculation: User selects how many data points proceeding (in combination with points succeeding) a given point will be used to determine the average Δγ.

12. Points forward to include in neighborhood for delta gamma calculation: User
    selects how many data points succeeding (in combination with points
    preceding) a given point will be used to determine the average Δγ.

13. Cell Size for output rasters: Define the resolution of output raster cells. Since
    all raster cells are square, this amount will be the resulting length and width of
    all the cells, in meters. A value of 1 is recommended to maintain a 1-to-1 ratio
    between raster cell counts and area in square meters.

14. Send Outputs to same geodatabase as input?: This is a yes/no selection. By
    default, the tool will save the products to the same geodatabase created by the
    Input Tool. If unselected, the user can create a new file geodatabase via the
    last input window.

Operations:

1. Input survey area boundary is used to set an analysis mask.
2. Points from the data table are converted into a point shapefile with all
   information migrated into the shapefile's attribute table.
3. A Thiessen Polygon operation allocates all space within the survey area
   according to the nearest data collection point for the sensor.
4. The data point's altitude value is assigned to the corresponding Thiessen
   Polygon
5. Thiessen Polygons are converted into a raster with each cell containing an
   altitude value, converted to centimeters.
6. Density analysis of survey area generates raster representing horizontal
   distance from the nearest data point to each raster cell throughout survey area.
7. Total survey distance, in centimeters, is calculated as the hypotenuse between
   vertical (altitude) and horizontal distance.
8. Using the inverse-cube model of induced magnetic fields, the largest potential
   mass that could have gone undetected is calculated for each raster cell,
   producing the potentialMassMissed layer and attribute table.
9. The potentialMassMissed raster is queried with respect to the user-defined
   mass threshold value to in which cells of the raster that mass would have been
   detected.
10. A confidenceRaster is created to represent where in the survey area this mass
    could have been detected.
11. From the point data, Δγ is calculated in accordance with the user-defined
    neighborhood search parameters.
12. These values are allocated via the Thiessen polygon geometry into a
    continuous surface.
13. This surface is then converted such that only the absolute values of the Δγ
    results are retained.

14. Using the inverse-cube model of induced magnetic fields, the mass responsible for inducing the observed magnetic flux is determined and recorded in the potentialMassObserved layer.

15. A processing log is generated in the form of a data table that records the initial inputs and parameters along with run time and date.

Outputs:

```
□ 🗄 Sample_Magnetic_Data.gdb
   ⊞ ▦ absDeltaGamma_N_3_DR_1_1_CS_1
   ⊞ ▦ altitudeCentimeters_N_3_DR_1_1_CS_1
   ⊞ ▦ centimeters_N_3_DR_1_1_CS_1
      ▦ ConfidenceLog_N_3_DR_1_1_CS_1_MM_50_T_150
      ▦ convexHull
      ▦ deltaGamma_N_3_DR_1_1
   ⊞ ▦ deltaGamma_N_3_DR_1_1_CS_1
      ▦ gradientGamma
   ⊞ ▦ gradientGamma_TIN_CS_1
      ▦ gradientGamma_TIN_CS_1_GC_1
   ⊞ ▦ horizontalCentimeters_N_3_DR_1_1_CS_1
   ⊞ ▦ potentialMassMissed_N_3_DR_1_1_CS_1_MM_50_T_150
   ⊞ ▦ potentialMassObserved_N_3_DR_1_1_CS_1_MM_50_T_150
      ▦ rawGamma
   ⊞ ▦ rawGamma_TIN_CS_1
      ▦ rawGamma_TIN_CS_1_RC_5
      ▦ surveyArea
      ▦ SurveyAreaLog_20140312164608
      ▦ VisualizationLog_TIN_CS_1_RC_5_GC_1
```

*(see table at end of section for file name abbreviation meanings)

1. absDeltaGamma (signed integer raster): Layer generated by recording the absolute value of the cell values in the deltaGamma raster.

2. altitudeCentimeters (unsigned integer raster): Continuous surface produced by allocating each data point's altitude value to areas delineated by Thiessen Polygons, then converting it into a raster, then changing the units from either feet or meters to centimeters.

3. confidenceLog (data table): A metadata file which records all of the parameters and inputs established prior to the execution of the tool.

4. centimeters (signed integer raster): A continuous surface produced by a raster calculation determining the smallest total survey distance from each raster cell as the hypotenuse of vertical distance (altitude) and horizontal distance, in centimeters, to the sensor. The resulting raster represents the three-dimensional coverage of the magnetic sensor within the survey area.

5. confidenceRaster (unsigned integer raster): A raster layer generated to by querying each cell in the potentialMassMissed layer. Based upon the user-input mass (in the Mass Threshold interface), if a cell in the

potentialMassMissed layer contains a value greater than or equal to the mass threshold, the cell is designated '0' for undetected. If the cell value is less than or equal to the mass threshold, the cell is designated '1' for detected. The resulting layer represents which portions of the area an object of a user-input mass would have been detected.

6. deltaGamma (signed integer raster): A continuous surface produced by spatial allocation via the Thiessen polygon geometry of the Δγ values calculated for each sampling point according to the neighborhood parameters established in the user interface.

7. horizontalCentimeters (signed integer raster): Layer generated by converting the horizontalDistance raster from meters to centimeters.

8. potentialMassMissed (signed integer raster): A layer generated by calculating the largest potential mass that could have gone undetected in each cell of the centimeters distance raster. Calculation of mass is based upon the inverse-cube model of an induced magnetic field via parameters set in the user interface (magnetic moment and sensor noise). Using this raster's attribute table, the user can calculate thresholds of detection.

9. potentialMassObserved (signed integer raster): A layer generated by calculating the required mass to produce the magnetic fluxes observed in the dataset, as represented in the absDeltaGamma layer. Calculation of mass is based upon the inverse-cube model of an induced magnetic field via parameters set in the user interface (magnetic moment and sensor noise) in the 'best case' scenario where the sensor passes directly above the object responsible for the observed magnetic density flux.

Abbreviation	Meaning
N	Noise
DR	Delta gamma Raster (points back/forward)
CS	Cell Size (raster)
MM	Magnetic Moment
T	Mass Threshold (kg)
FSD	Altitude Filtered (Standard Deviations)
FMC	Altitude Filtered (Maximum Change) points back, forward, and max Δalt

Confidence Tool File Name Abbreviation Explanations

APPENDIX II

OPERATING INSTRUCTIONS FOR MAGNETOMETER SURVEY PYTHON TOOLBOX V.1.0

Important: Prior to use, please refer to the Magnetometer Survey Toolbox Release Notes accompanying this instructional document. This document contains stepwise guidance for the use of each tool. More information about data products, system requirements, etc. is contained in the Release Notes. This set of instructions assumes a basic functional knowledge of ArcGIS 10.2.1. If unsure, seek the assistance of a proficient ArcGIS user.

LOADING THE MAGNETOMETER SURVEY TOOLBOX IN ArcCatalog

1. Save the MagnetometerSurveyToolbox files to the desired GIS workspace on your computer.
2. Locate the toolbox files in your file directory. In windows explorer it may appear as six separate files. These files can be copied and pasted to any location on your hard drive before being uploaded into ArcGIS.

Name	Date modified	Type	Size
Magnetometer Survey.ConfidenceTool.py...	3/17/2014 1:09 PM	XML Document	12 KB
Magnetometer Survey.InputTool.pyt.xml	3/17/2014 12:33 PM	XML Document	8 KB
Magnetometer Survey.pyt	3/17/2014 11:23 A...	ArcGIS Python Too...	69 KB
Magnetometer Survey.pyt.xml	3/17/2014 1:12 PM	XML Document	1 KB
Magnetometer Survey.SurveyAreaTool.py...	3/17/2014 12:53 PM	XML Document	4 KB
Magnetometer Survey.VisualizationTool....	3/17/2014 1:00 PM	XML Document	8 KB

3. Launch ArcCatalog. Using the *Connect to Folder* icon, navigate to the directory where the toolbox was saved.
4. Connect to that folder and then expand it in the Folder Connections interface. You should see the *MagnetometerSurveyToolbox.pyt* icon in this folder. When expanded, the four individual tools will appear. They can be launched and used from here, but it is recommended to copy the script into your Toolbox library so that you can disconnect from the file folder.
5. To do this, expand the *Toolboxes* folder, then *My Toolboxes*. Drag and drop the *Magnetometer Survey Toolbox* from the folder connection into *My Toolboxes*.
6. Once transferred, right click on the connected folder and select *Disconnect Folder*.
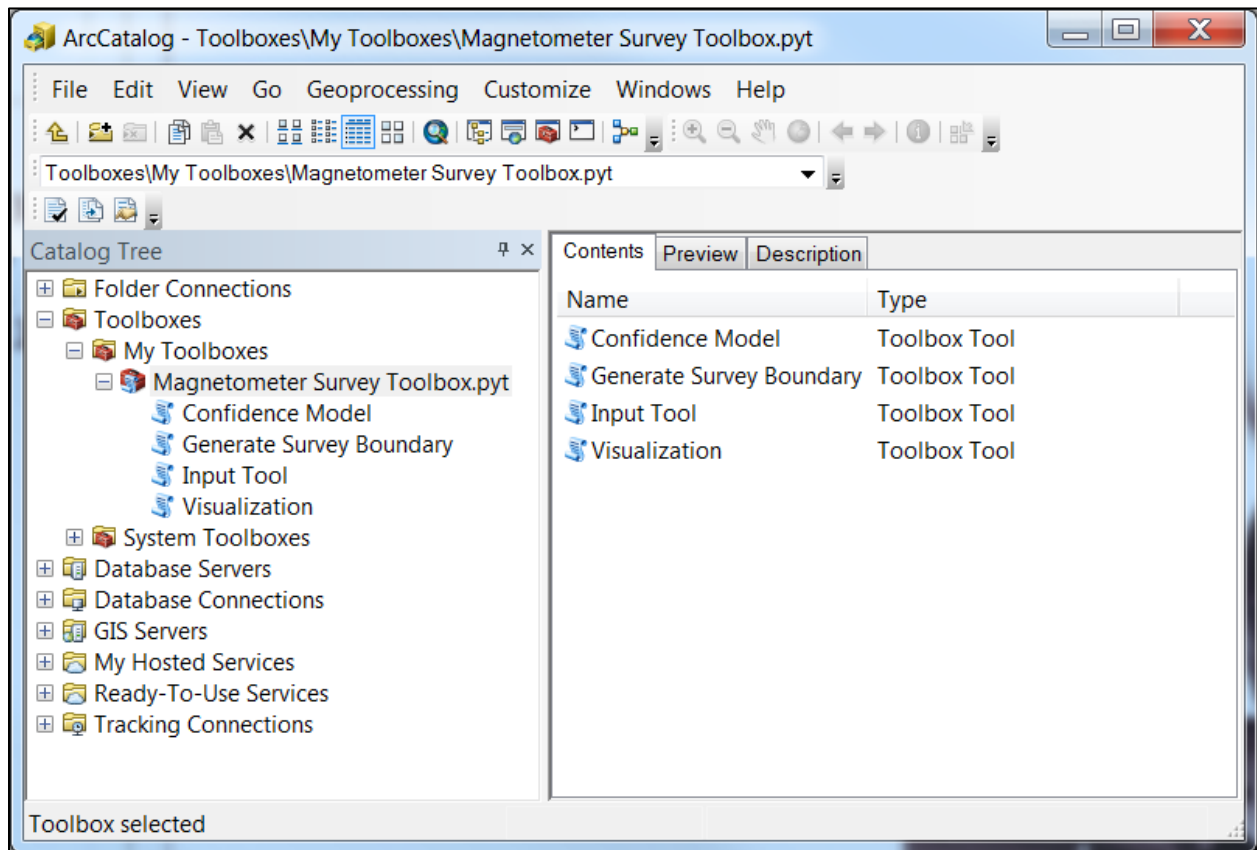
INPUT TOOL

This tool must be used since its output is required for all other processing tools.

1. Open the unprocessed magnetic data table and confirm the presence of easting (longitude), northing (latitude), raw magnetic, altitude (if present), and line number data. Note their respective field names/positions. In the example below, a comma delimited data table, fields 1 and 2 are easting and northing coordinates, field 3 is raw magnetic data, field 4 is altitude, and field 7 is the line file name.
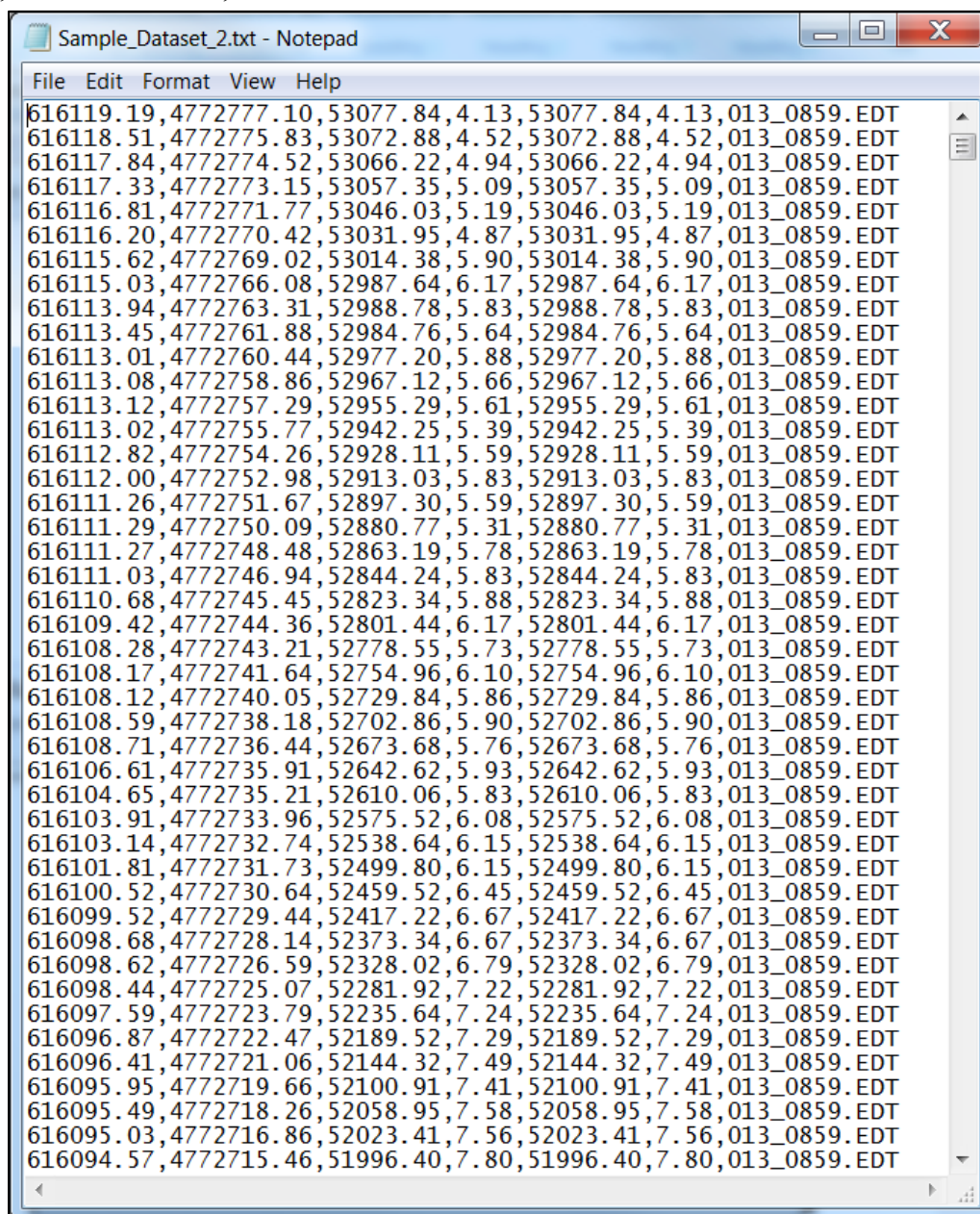
```
Sample_Dataset_2.txt - Notepad
File  Edit  Format  View  Help
616119.19,4772777.10,53077.84,4.13,53077.84,4.13,013_0859.EDT
616118.51,4772775.83,53072.88,4.52,53072.88,4.52,013_0859.EDT
616117.84,4772774.52,53066.22,4.94,53066.22,4.94,013_0859.EDT
616117.33,4772773.15,53057.35,5.09,53057.35,5.09,013_0859.EDT
616116.81,4772771.77,53046.03,5.19,53046.03,5.19,013_0859.EDT
616116.20,4772770.42,53031.95,4.87,53031.95,4.87,013_0859.EDT
616115.62,4772769.02,53014.38,5.90,53014.38,5.90,013_0859.EDT
616115.03,4772766.08,52987.64,6.17,52987.64,6.17,013_0859.EDT
616113.94,4772763.31,52988.78,5.83,52988.78,5.83,013_0859.EDT
616113.45,4772761.88,52984.76,5.64,52984.76,5.64,013_0859.EDT
616113.01,4772760.44,52977.20,5.88,52977.20,5.88,013_0859.EDT
616113.08,4772758.86,52967.12,5.66,52967.12,5.66,013_0859.EDT
616113.12,4772757.29,52955.29,5.61,52955.29,5.61,013_0859.EDT
616113.02,4772755.77,52942.25,5.39,52942.25,5.39,013_0859.EDT
616112.82,4772754.26,52928.11,5.59,52928.11,5.59,013_0859.EDT
616112.00,4772752.98,52913.03,5.83,52913.03,5.83,013_0859.EDT
616111.26,4772751.67,52897.30,5.59,52897.30,5.59,013_0859.EDT
616111.29,4772750.09,52880.77,5.31,52880.77,5.31,013_0859.EDT
616111.27,4772748.48,52863.19,5.78,52863.19,5.78,013_0859.EDT
616111.03,4772746.94,52844.24,5.83,52844.24,5.83,013_0859.EDT
616110.68,4772745.45,52823.34,5.88,52823.34,5.88,013_0859.EDT
616109.42,4772744.36,52801.44,6.17,52801.44,6.17,013_0859.EDT
616108.28,4772743.21,52778.55,5.73,52778.55,5.73,013_0859.EDT
616108.17,4772741.64,52754.96,6.10,52754.96,6.10,013_0859.EDT
616108.12,4772740.05,52729.84,5.86,52729.84,5.86,013_0859.EDT
616108.59,4772738.18,52702.86,5.90,52702.86,5.90,013_0859.EDT
616108.71,4772736.44,52673.68,5.76,52673.68,5.76,013_0859.EDT
616106.61,4772735.91,52642.62,5.93,52642.62,5.93,013_0859.EDT
616104.65,4772735.21,52610.06,5.83,52610.06,5.83,013_0859.EDT
616103.91,4772733.96,52575.52,6.08,52575.52,6.08,013_0859.EDT
616103.14,4772732.74,52538.64,6.15,52538.64,6.15,013_0859.EDT
616101.81,4772731.73,52499.80,6.15,52499.80,6.15,013_0859.EDT
616100.52,4772730.64,52459.52,6.45,52459.52,6.45,013_0859.EDT
616099.52,4772729.44,52417.22,6.67,52417.22,6.67,013_0859.EDT
616098.68,4772728.14,52373.34,6.67,52373.34,6.67,013_0859.EDT
616098.62,4772726.59,52328.02,6.79,52328.02,6.79,013_0859.EDT
616098.44,4772725.07,52281.92,7.22,52281.92,7.22,013_0859.EDT
616097.59,4772723.79,52235.64,7.24,52235.64,7.24,013_0859.EDT
616096.87,4772722.47,52189.52,7.29,52189.52,7.29,013_0859.EDT
616096.41,4772721.06,52144.32,7.49,52144.32,7.49,013_0859.EDT
616095.95,4772719.66,52100.91,7.41,52100.91,7.41,013_0859.EDT
616095.49,4772718.26,52058.95,7.58,52058.95,7.58,013_0859.EDT
616095.03,4772716.86,52023.41,7.56,52023.41,7.56,013_0859.EDT
616094.57,4772715.46,51996.40,7.80,51996.40,7.80,013_0859.EDT
```

2. From ArcCatalog or ArcMap, expand the Magnetometer Survey Toolbox.
3. Launch the *Input Tool* by double clicking. This will bring up the user interface.
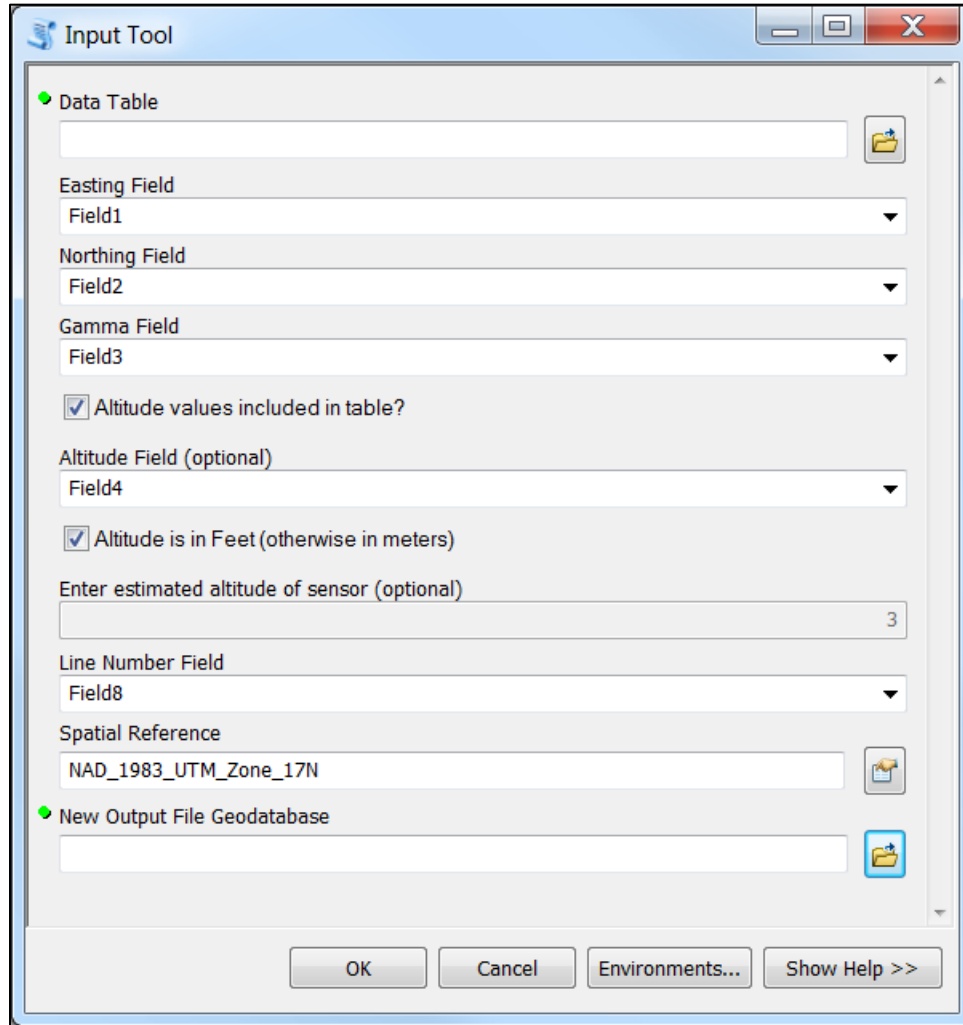
4. Enter all fields in the interface. First, upload the data table containing the magnetic survey data. Click the folder icon at the right and use ArcCatalog to navigate to the data table. You may have to use the *connect to folder* function and link to the file folder in which the magnetic data table is stored, as per the instructions from the Tool Uploading section.
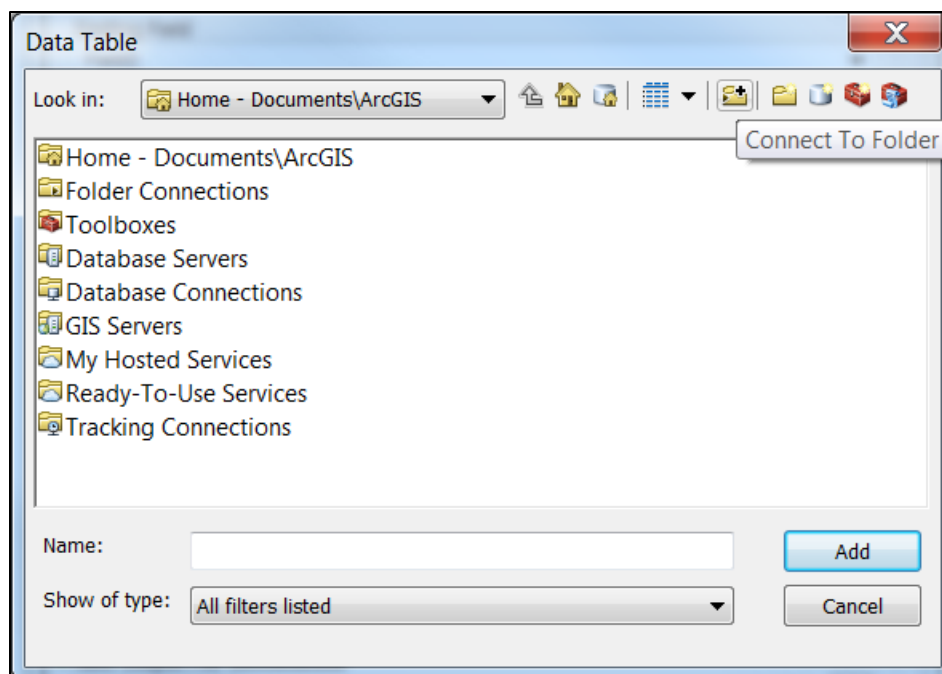
5. Once the data is selected, click *Add* to load it into the interface.
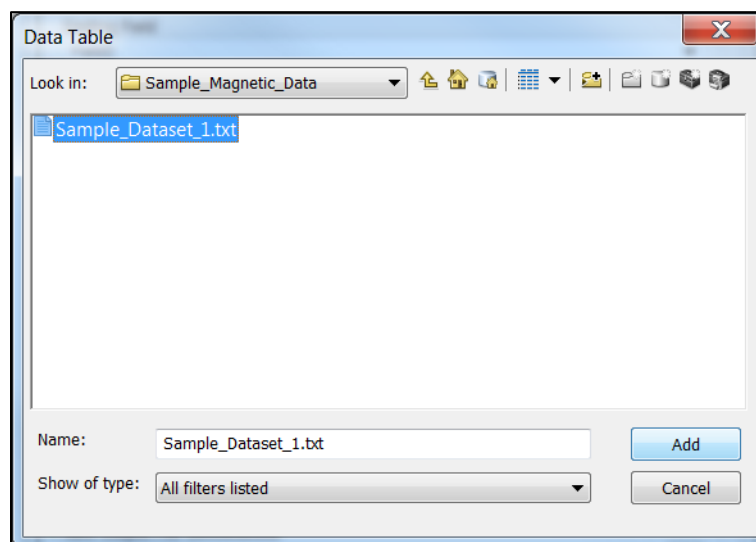
6. Once loaded, the next three fields of the interface will auto-populate with the field names in the data table. Define which field contains the Easting (or longitude) data, which contains the Northing (or latitude) data, and which contains the raw magnetic readings.

7. There is a check/uncheck option to indicate the presence/absence of sensor altitude data. If checked yes, define the field in the data table containing altitude information, then its units of measurement (either feet or meters).

8. If the data table does not contain sensor altitude information, uncheck the box. In the *Enter estimated altitude of sensor* field, input the estimated average towfish altitude in units of meters.

9. Next, define the field in the data table containing the line number or file name for each survey line.

10. Define the spatial reference system for position information. Expanding this field will call up ArcGIS's library of geographic and projected coordinate systems to choose from.
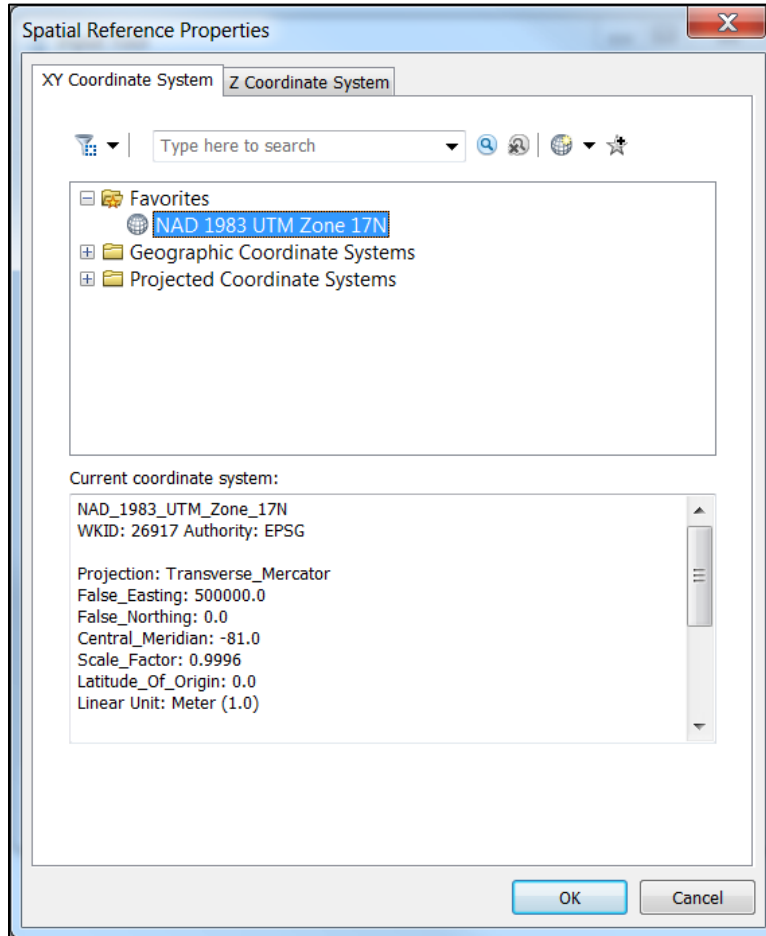
11. Select/define a geodatabase for data products to be saved. A default workspace and file name will appear in the interface, depending upon the location of input table. To input a different name and location, click the folder to launch ArcCatalog; navigate to the desired workspace and either enter the name of the new geodatabase to be created by the tool, or select an existing geodatabase.

12. Note, selecting an existing file geodatabase will overwrite all contents; all files in the geodatabase will be erased and replaced with the tool's data product.
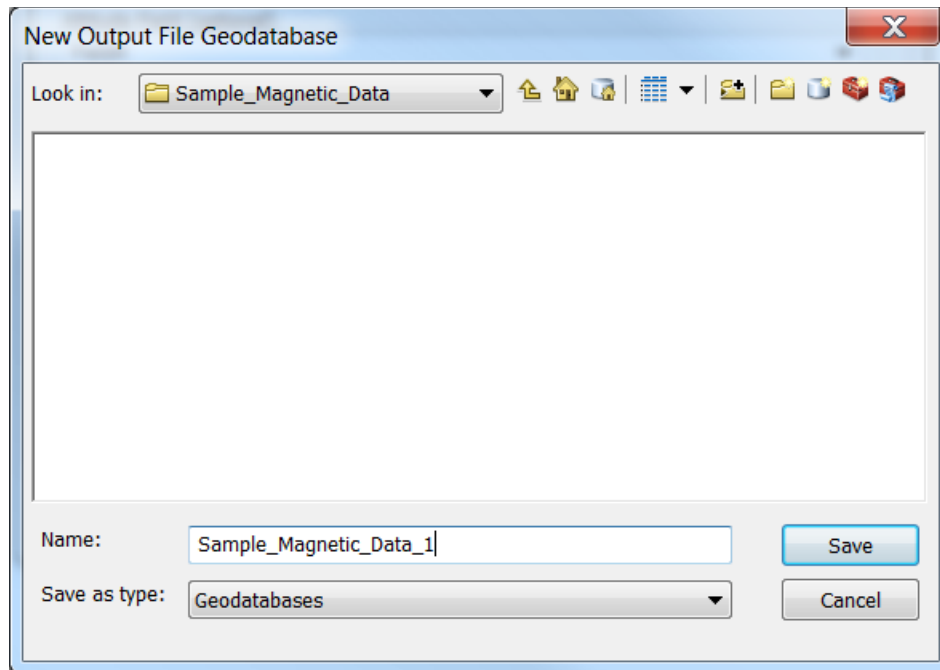
13. If a file geodatabase containing data is selected, the following warning will appear to alert the user of a potential overwrite. A lock on a file (such as having it open in ArcMap) will prevent the tool from overwriting and terminate its operation prematurely.
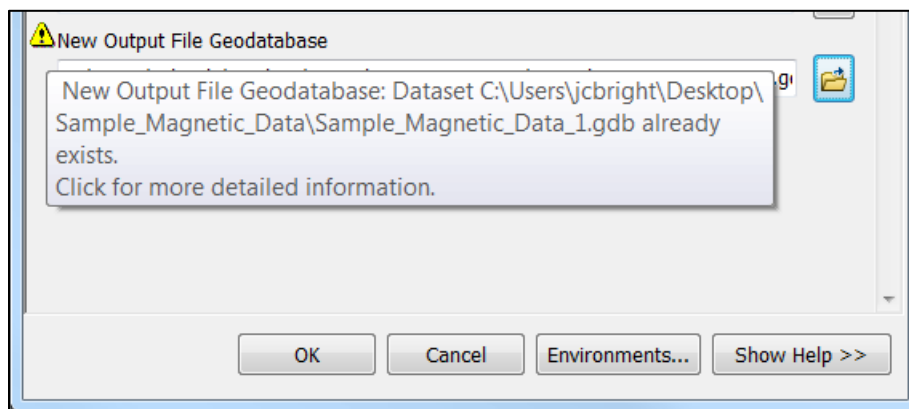
14. Once all inputs are defined, select *Ok* for the tool to execute. The following data products will result.
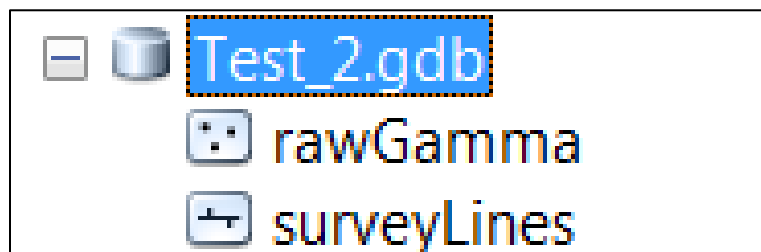
15. Open the *rawGamma* feature class attribute table and verify the recorded magnetic values (recordedGamma), line number, and altitude values were properly transcribed, with altitude values in centimeters.
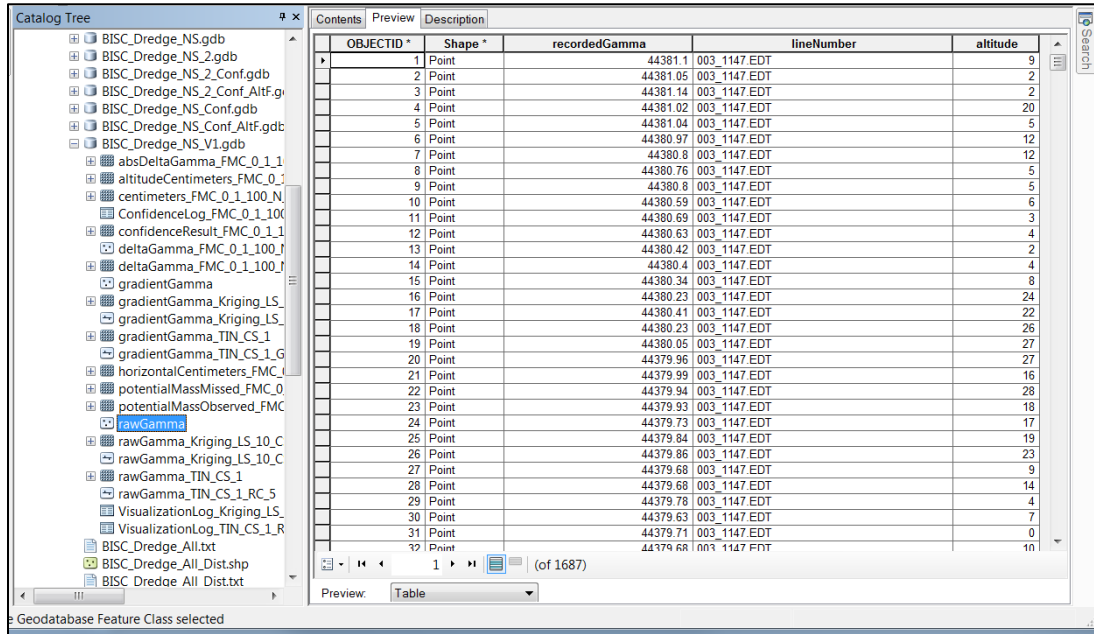
16. Next, preview the *surveyLines* feature class to verify the conversion of individual data points to line features. Since data-to line organization is crucial for the execution of many of the subsequent processing functions, verifying the data is correctly arrayed within lines is crucial to preventing subsequent errors in the processing work flow. A common mistake is to define a field in the data table other the line name during the *Input Tool*.
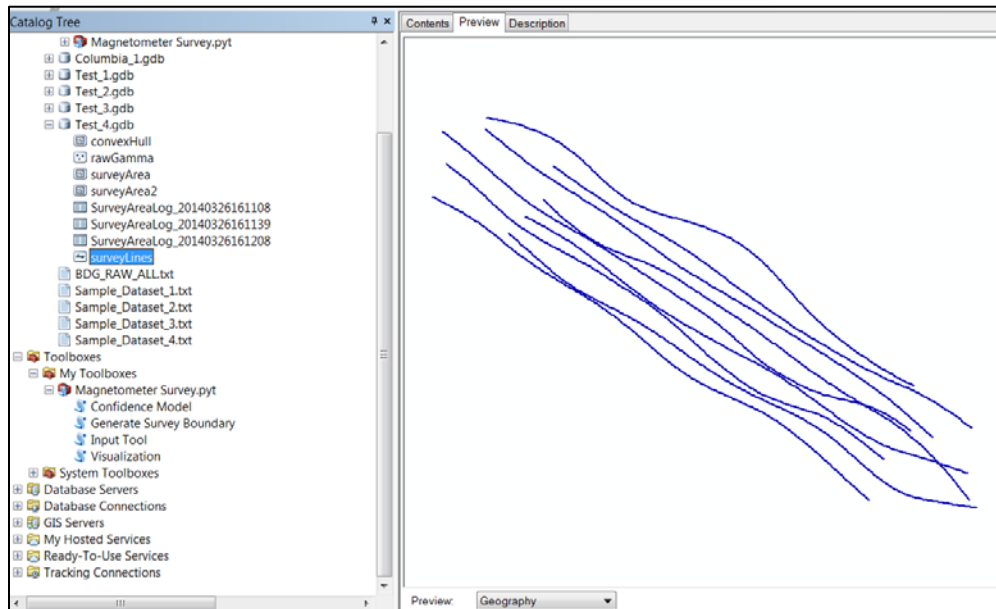
GENERATE SURVEY BOUNDARY TOOL

This is an optional tool; a survey boundary polygon is required for Visualization and Confidence Modeling, but not necessarily one developed by this tool. The user may elect to transfer the survey boundary from their data acquisition system, manually create a boundary polygon, or use this tool. Additionally, the user may need to edit the outputs of this tool to adjust the boundary geometry as necessary. A basic editing procedure is outlined after the function of the tool is explained.

1. Expand the Magnetometer Survey Toolbox.
2. Launch the *Generate Survey Boundary* tool by double clicking. This will bring up the user interface.
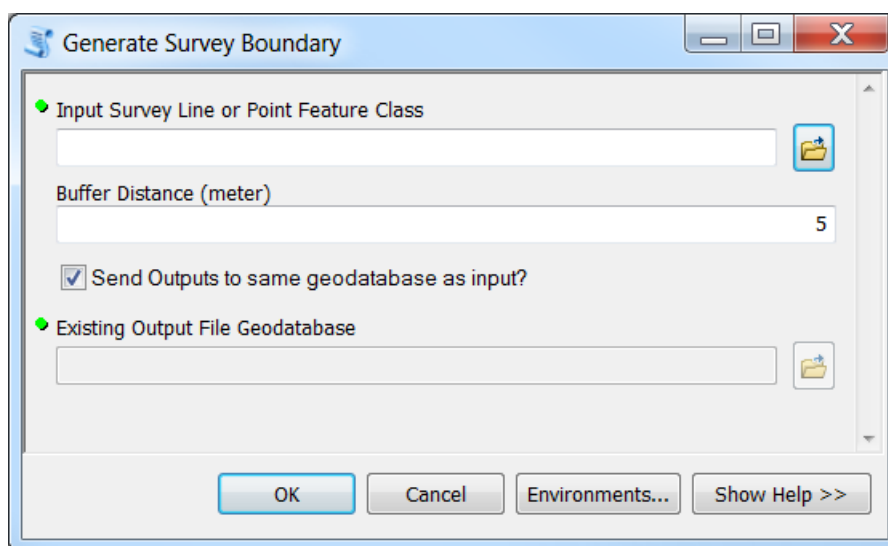
3. Enter all fields in the interface. First, load the points or line feature class created by the *Input Tool* by navigating into the previously created file geodatabase.

*NOTE: For block data sets—those arrayed as squares or rectangles, there is very little difference between selecting point or line features to create the boundary polygon. Since there are few lines than points, buffering lines requires much less processing time. With complex data geometries—such as data collected along a winding river—variation will exist between the point-based boundary and the line-based boundary. The user should experiment with both to choose the one most appropriate for the dataset.

4. Input the desired buffer distance for expansion of the *convexHull*, recommend half of the planned line spacing.

NOTE: If there was no information on planned line spacing in the survey notes or metadata and the user is unsure what the planned line spacing was, visualize the surveyLines feature class in ArcMap and estimate line spacing based upon data distribution.

5. The default settings will save the data products to the same file geodatabase created by the *Input Tool*. If a different destination is desired, un-select and create new as per step 10 of the *Input Tool* instructions.
6. Click *Ok* to execute the tool.
7. Once the geoprocessing is complete, navigate to the output file geodatabase in ArcCatalog.
8. Depending on the lapsed time, you may need to refresh the destination folder. If you do not see the data outputs in the geodatabase, right click it and select *Refresh*.
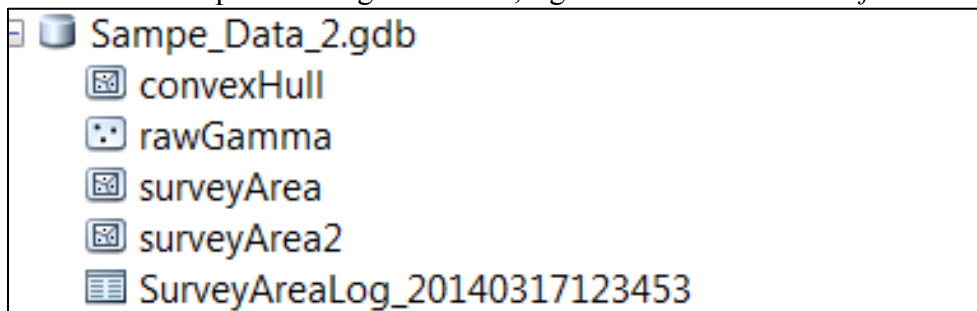
9. The data outputs should appear, along with a log file which saves the run parameters and a YYYY/MM/DD/HHMMSS date/time stamp. These can be visualized by selecting the *Preview* tab in ArcCatalog. Otherwise, drag and drop into ArcMap and symbolize accordingly.
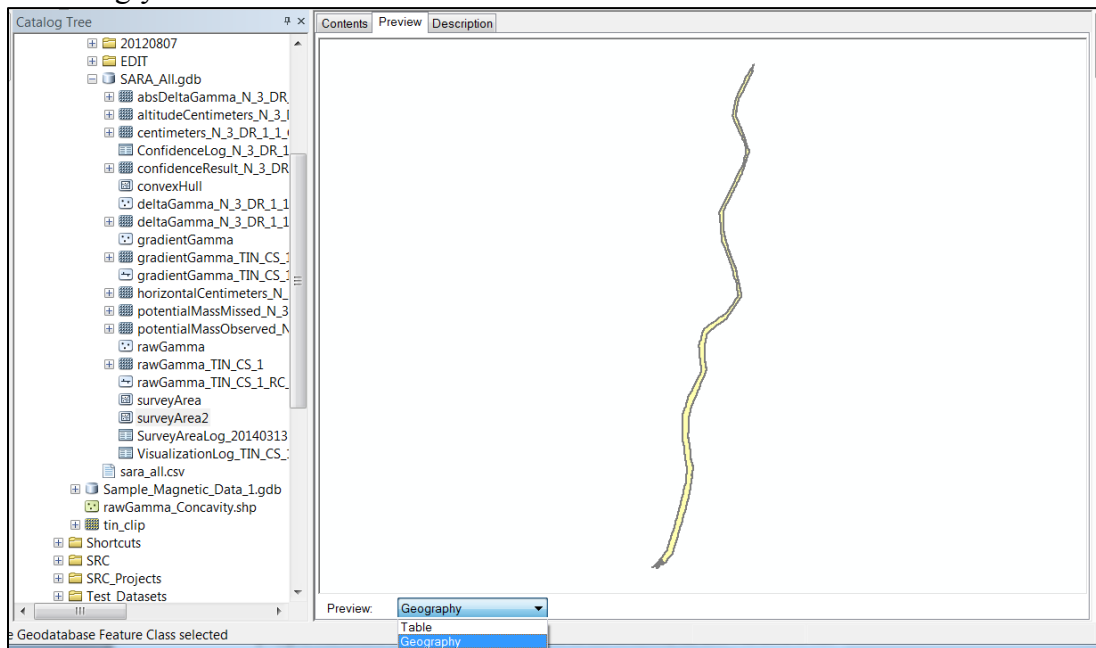
Editing the Survey Boundary for Concave Data Geometry/or Boundary Adjustments.

Steps 10-20 describe editing features of the convex hull boundary polygon (surveyArea). Steps 21-32 describe editing features of the dissolved point/line buffer polygon (surveyArea2). Preview both survey area boundaries to determine which boundary best encapsulates the survey area and which will require the least amount of editing to encompass the actual survey area.

10. If there are concavities in the geometry of the data points, the convex hull boundary polygon will form a convex shape around them. In this situation, the user will need to edit the feature class produced by the tool prior to any additional processing.
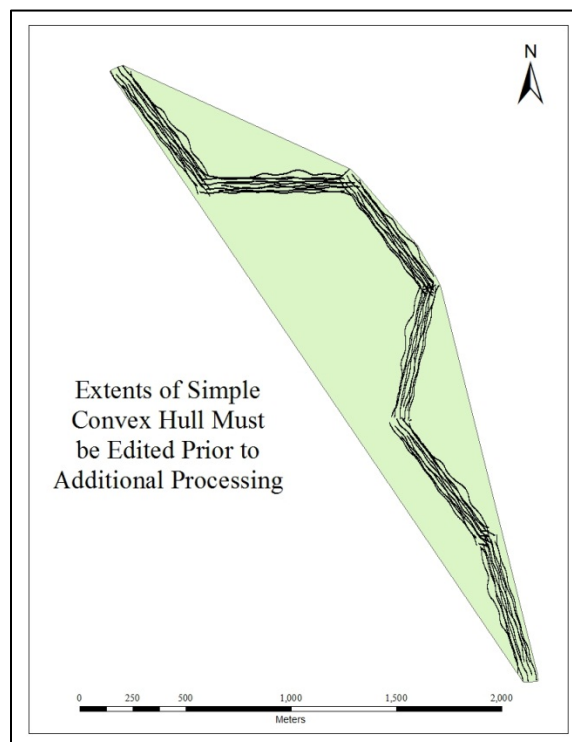
11. Thus, if the tool produced a boundary polygon like that pictured above, the user can quickly edit this feature class in ArcMap.
12. Drag and drop the *surveyArea* layer from ArcCatalog into the layer manager in ArcMap.
13. Right-click on the layer, scroll down to *Edit Features*, then select *Start Editing*.
14. Right-click on the layer again, scroll down to *Selection*, then click *Select All*. The survey area boundary polygon should turn bright blue.
15. This should bring up the *Editor* toolbar. Click the *Edit Vertices* function, which will bring up a second, small *Edit Vertices* toolbar
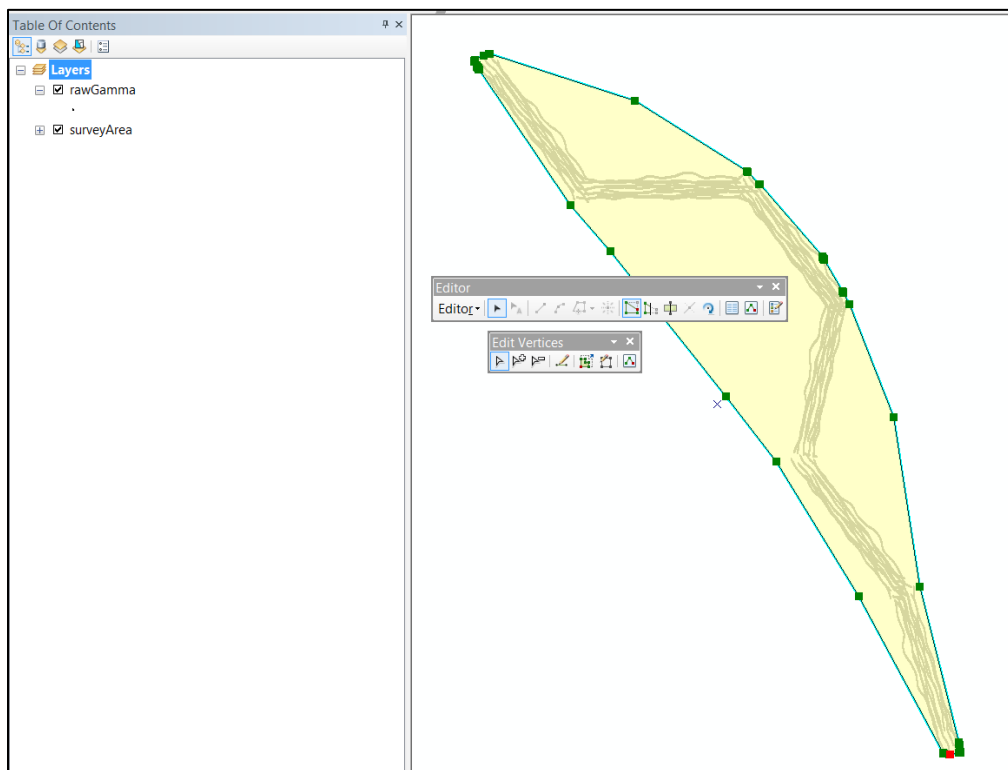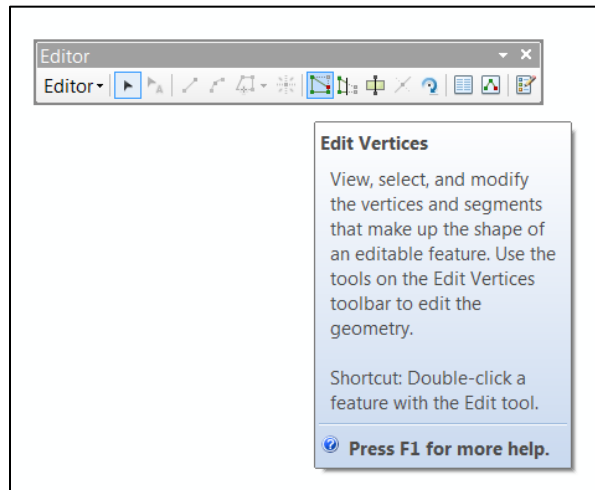
16. Once the *Edit Vertices* feature is active, the survey boundary polygon will become transparent and all vertices will appear as small red boxes.

17. Vertices can be added, deleted, and dragged-around to fit the geometry of the points.

18. Once all vertices have been adjusted, return to the *Editor* toolbar.
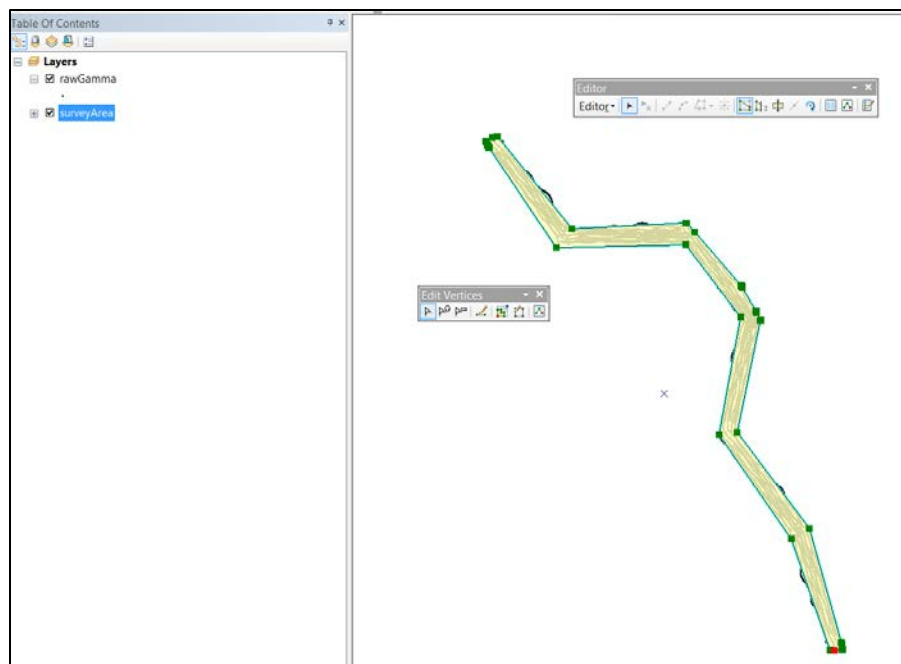
19. Click the *Editing* menu on the far left of the *Editor* toolbar, scroll down and select *Save Edits*. Repeat, and select *Stop Editing*.
20. Modifying the convex hull survey area features class is complete.

Dissolved-Point-Buffer Polygon

21. In most instances, the dissolved-point-buffered polygon feature class will produce a sufficient boundary file. In some areas, however, the buffer distance may have been insufficient to fill in the gaps between adjacent lines.
22. One of two options is possible:
    a. Re-run the *Generate Survey Boundary* Tool at an increased buffer distance to 'fill' the gaps.
    b. Manually delete the vertices of the gaps within the polygon to create a solid, contiguous polygon.
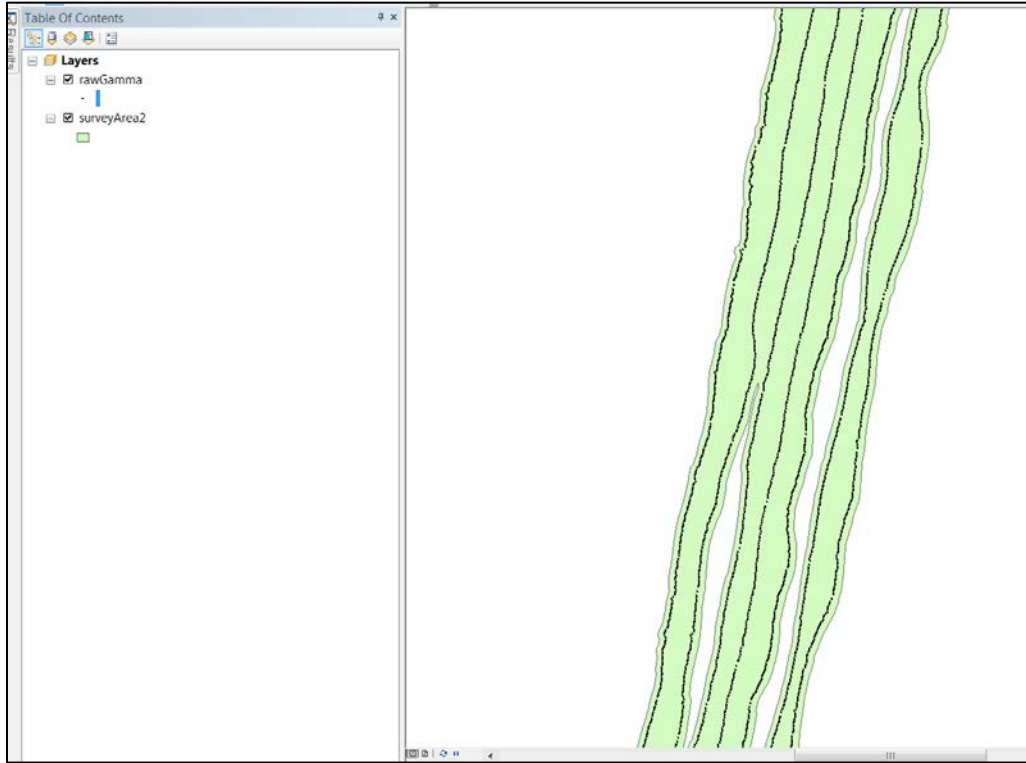
23. Thus, if the tool produced a boundary polygon like that pictured above, the user will need to edit this feature class in ArcMap.

24. Drag and drop the *surveyArea2* layer from ArcCatalog into the layer manager in ArcMap.

25. Right-click on the layer, scroll down to *Edit Features*, then select *Start Editing*.

26. Right-click on the layer again, scroll down to *Selection*, then click *Select All*. The survey area boundary polygon should turn bright blue.

27. This should bring up the *Editor* toolbar. Click the *Edit Vertices* function, which will bring up a second, small *Edit Vertices* toolbar
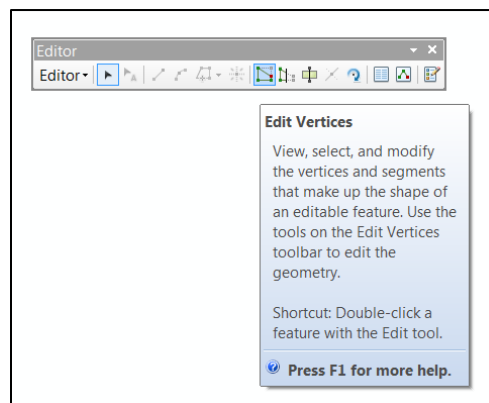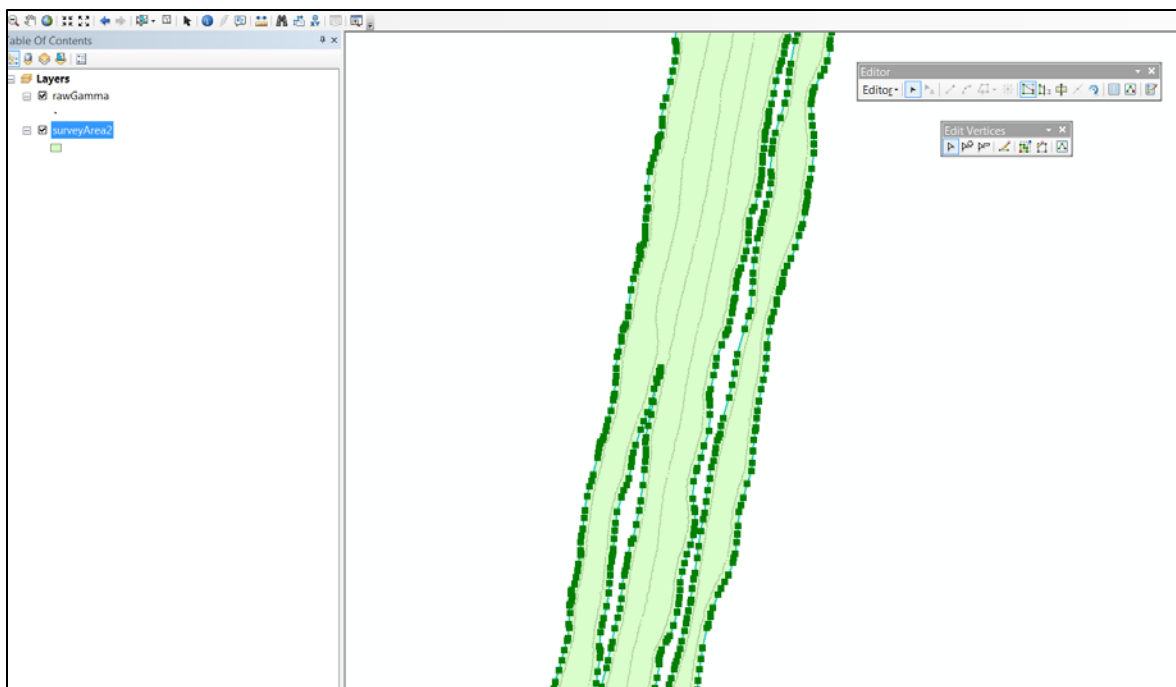
28. Once the *Edit Vertices* feature is active, the survey boundary polygon will become transparent and all vertices will appear as small boxes.
29. Vertices can be added, deleted, and dragged around as necessary. To remove the gaps, use the *Delete Vertices* tool; click and form a box over the vertices, release the mouse to remove the encompassed points. Repeat until all internal vertices are eliminated.
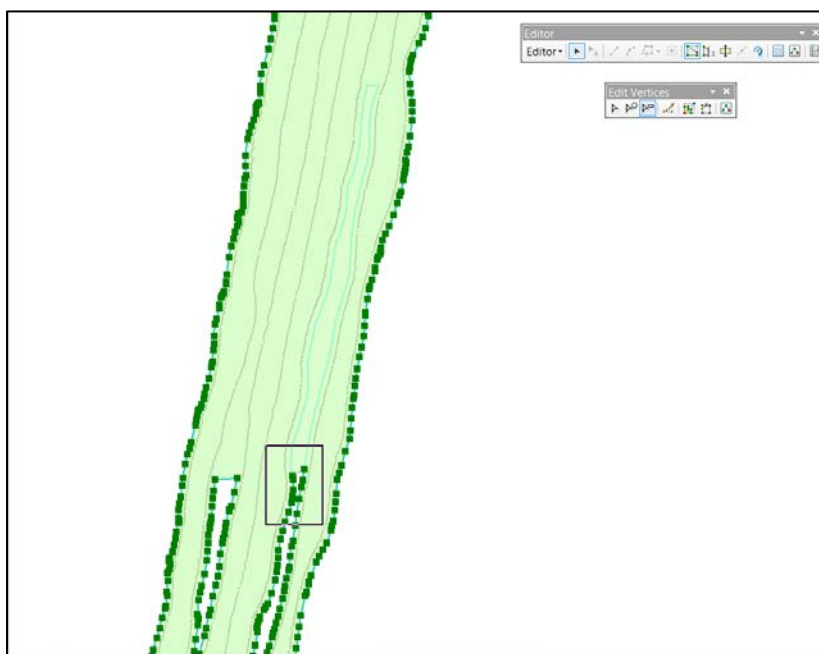
30. Once all vertices have been adjusted, return to the *Editor* toolbar.

31. Click the *Editing* menu on the far left of the *Editor* toolbar, scroll down and select *Save Edits.* Repeat, and select *Stop Editing.*

32. Modifying the dissolved-point-buffer survey area features class is complete.

MANUALLY CREATE SURVEY BOUNDARY

This section provides instructions for the user to manually create a survey boundary polygon. If the user is satisfied with the outputs of the Generate Survey Boundary tool, disregard this section and proceed to the Visualization tool instructions.

1. Choose a file folder or file geodatabase where the intended survey area boundary feature class will be created and connect to that folder in ArcCatalog.

File Folder

2. If working in a file folder: right click on the folder, scroll down to *New*, then to *Shapefile*.
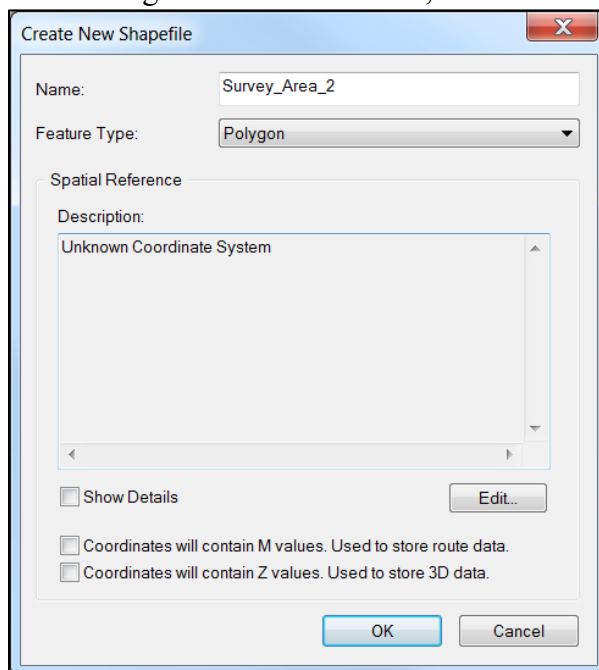
3. In this interface, enter the name of the area, **being careful not to use spaces in the title.** Next, select *Polygon* as the feature type.
4. Using the *Edit* button, select the appropriate spatial reference system.
5. Click *Ok*.

Geodatabase:

6. If working in a file geodatabase, right click, scroll down to *New*, then to *Feature Class*.
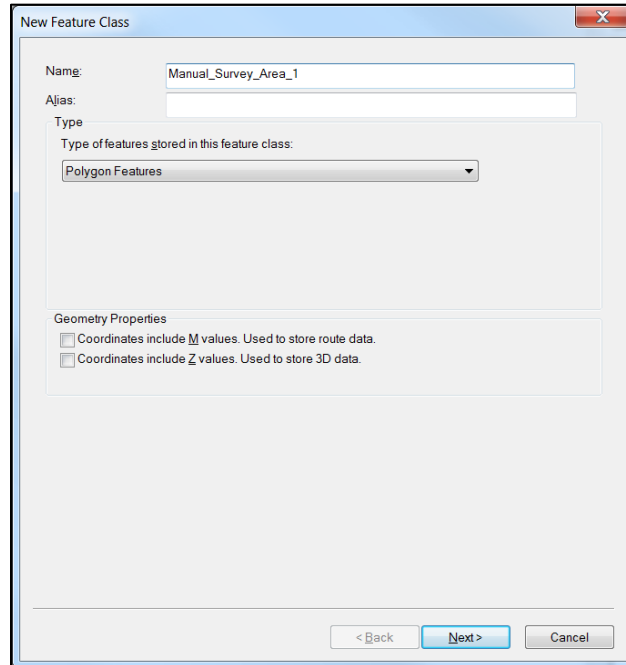
7. Type the name of the new survey area and verify that *Polygon Features* is selected in the drop down menu for feature type.
8. Click *Next,* select the appropriate spatial reference system, advance to *Next*, and accept the default values for XY tolerance, database storage configuration, attribute table properties, and select *Finish*.

9. The new shapefile/feature class will appear in ArcCatalog and should also automatically load in to ArcMap.
10. Before editing the feature class, it is helpful to visualize the data points to better capture the extent of the survey area. The simplest way is view the *rawGamma* feature class from the *Input Tool* in ArcMap.
11. In the Layer manager of ArcMap, right click the survey area feature class. Scroll down to *Edit Features*, then *Start Editing*.
12. Dismiss any warnings by clicking *Continue* or *Ok*.
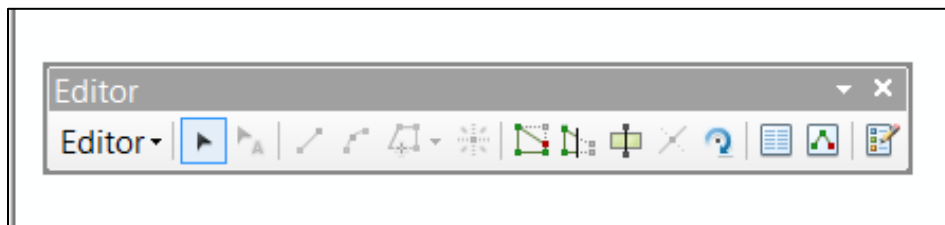
13. Once editing is initiated, an *Editor Toolbar* will appear.
14. Click the *Create Features* icon on the far right of the *Editor Toolbar*.
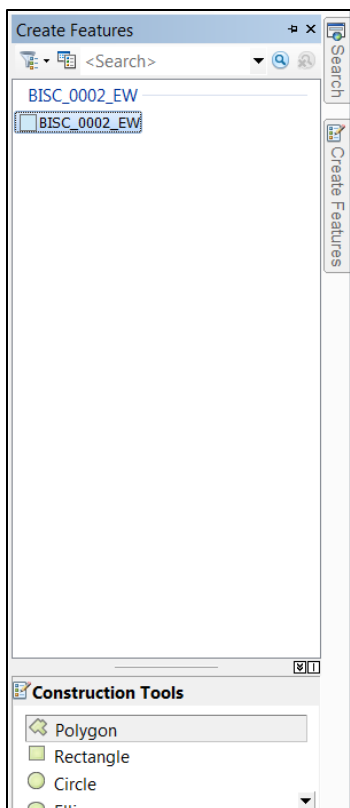
15. This will launch the *Create Features* tab on the right of the ArcMap program. At the top of the interface, click on the feature class you are editing (anything in the layer manager will appear, so there could be multiple feature classes to choose from). Once selected, a number of construction tools will appear at the bottom of the tab.
16. Select the *Polygon* construction tool.
17. When the cursor is moved back into the ArcMap data surface, it will appear as a set of cross-hairs. By clicking the left button of the mouse, a polygon vertex is placed.
18. Continue placing vertices until the entire survey area is drawn. Close the polygon by double clicking on the original vertex.
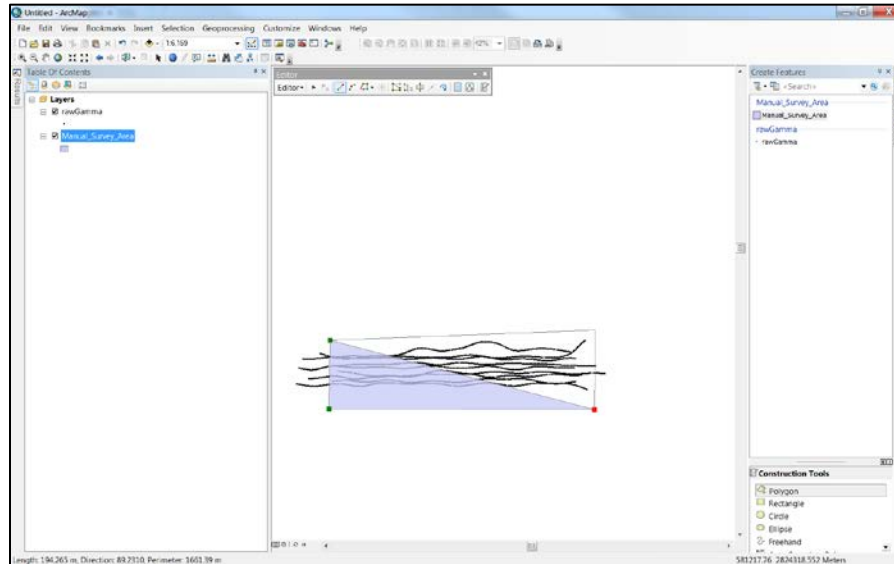
19. The perimeter of the resulting polygon will be a bright blue color, indicating the newly formed polygon is 'selected.' While selected, the vertices can be adjusted using the edit vertices function, accessed through the icon on the *Editor Toolbar*.

20. When in *Edit Vertices* mode, the cursor will change from a crosshair to arrow, which will transform into a four-directional arrow when moved over a vertex. Click and drag the vertex to make any necessary adjustments.

21. Once the polygon is complete, click the word *Editor* on the *Editor Toolbar*. Scroll down and select *Save Edits*. Repeat, and select *Stop Editing*.

22. The survey area boundary feature class is created.

VISUALIZATION TOOL

This tool produces continuous surfaces based upon the full field and gradient values, as well as magnetic iso-lines at user-specified contour intervals. For this tool to function, the user must have the Spatial Analyst extension activated. To activate, click the Customize *menu option from ArcMap or ArcCatalog, scroll down and select* Extensions. *Within the* Extensions *window, check the box next to 3D Analyst and Spatial Analyst.*
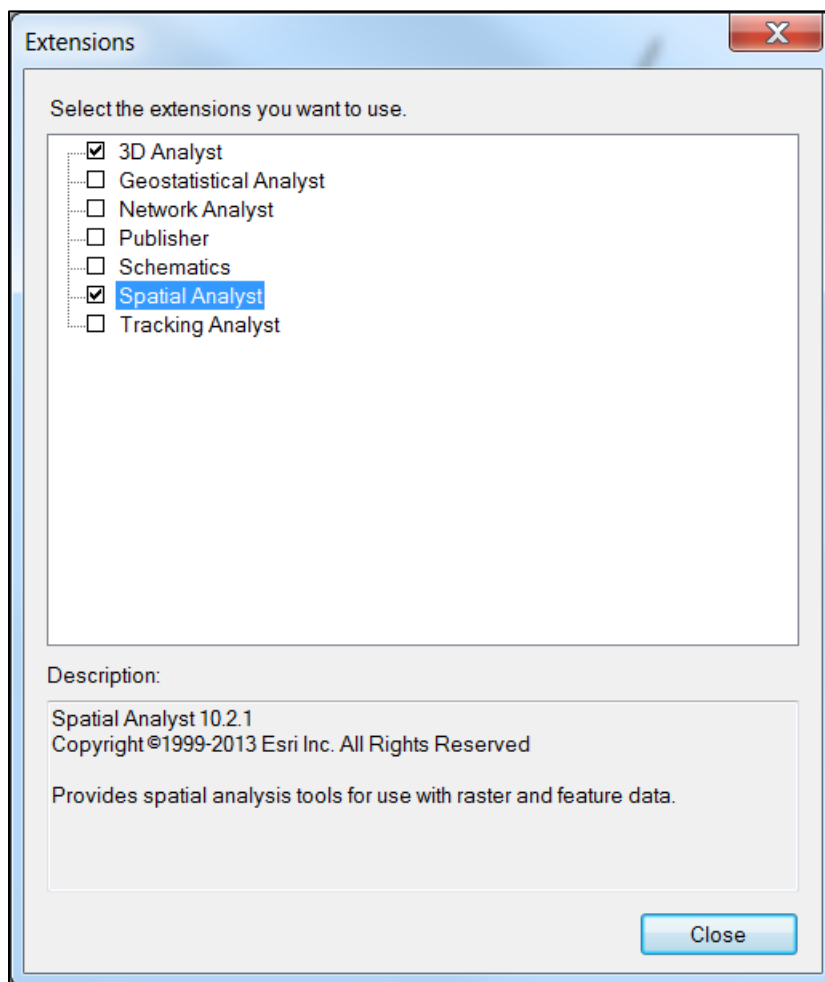
1. Expand the Magnetometer Survey Toolbox.
2. Launch the *Visualization* tool by double clicking. This will bring up the user interface.
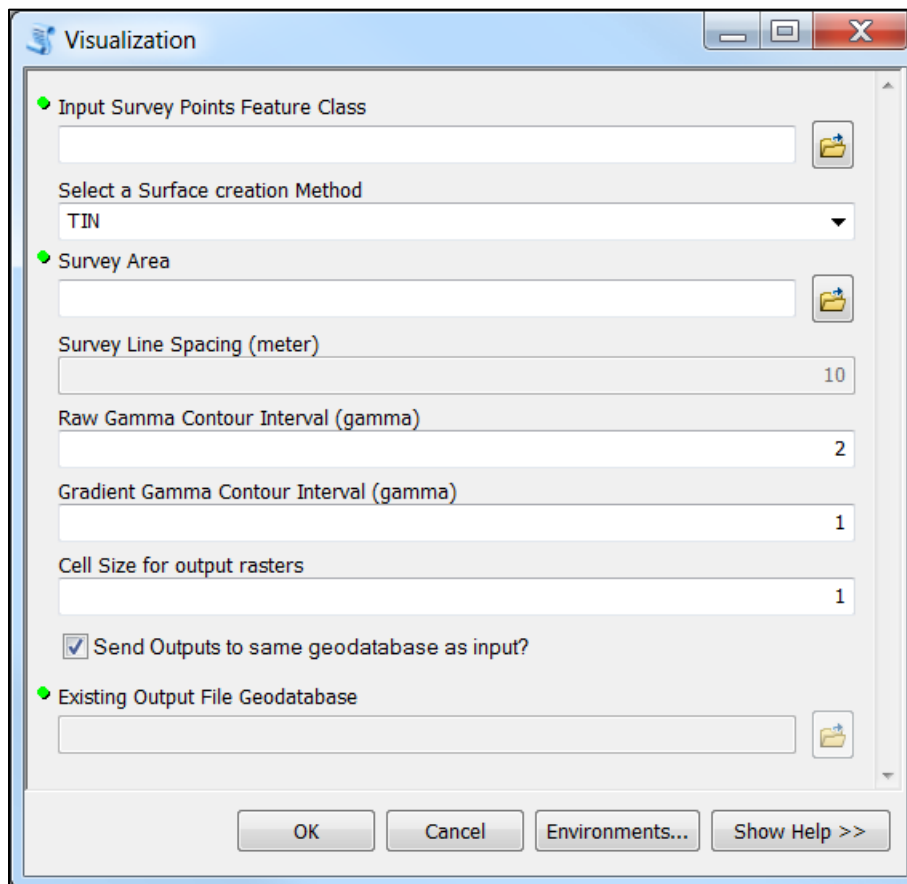
3. Enter all fields in the interface. First, load the *rawGamma* feature class from the *Input Tool*.
4. Input the survey area boundary by navigating to its folder/geodatabase and selecting.
5. Select the desired interpolation method (*Kriging* or *TIN*). If *Kriging* is selected, the *Survey Line Spacing* input will activate. Here, input the planned line spacing for the survey; this affects the range of interpolation math.
6. Input the desired contour interval for the polyline feature class that will be created from the raw magnetic surface (contour lines).
7. Input the desired contour interval for the polyline feature class that will be created from the gradient surface (contour lines). Note that the gradient processing function, because it only measures differences between consecutive points, results in a surface with much less variation than the full-field surface so a contour interval smaller than the full-field contour interval is highly recommended.
8. Input cell size for the rasters generated during processing. Recommend a cell size of 1.
9. The default settings will save the data products to the same file geodatabase created by the *Input Tool*. If a different destination is desired, un-select and create new as per step 10 of the *Input Tool* instructions.
10. Once all inputs are entered, click *Ok* at the bottom of the user interface window and the tool will execute.
11. Once the geoprocessing is complete, navigate to the output file geodatabase in ArcCatalog.

12. Depending on the lapsed time, you may need to refresh the destination folder. If you do not see the data outputs in the geodatabase, right click it and select *Refresh*.

```
☐ 🗄 Sample_Magnetic_Data_1.gdb
    ⊞ convexHull
    ⊡ gradientGamma
  ⊞ ▦ gradientGamma_TIN_CS_1
    ⊡ gradientGamma_TIN_CS_1_GC_2
    ⊞ Manual_Survey_Area
    ⊡ rawGamma
  ⊞ ▦ rawGamma_TIN_CS_1
    ⊡ rawGamma_TIN_CS_1_RC_10
    ⊞ surveyArea
    ▤ SurveyAreaLog_20140311131149
    ▤ VisualizationLog_TIN_CS_1_RC_10_GC_2
```
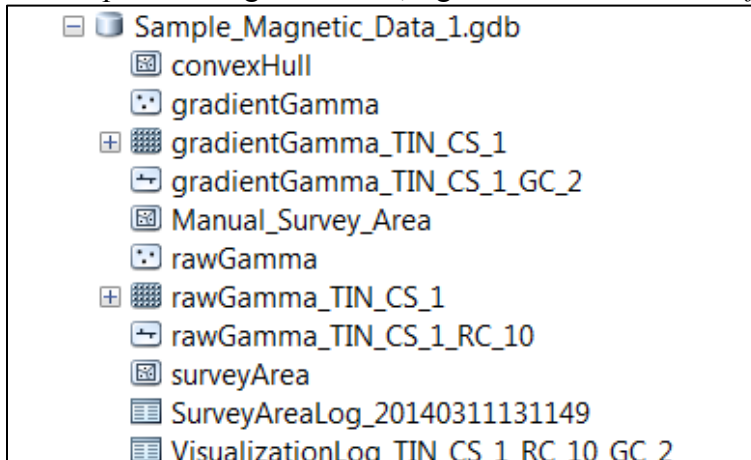
13. The data outputs will appear, along with a log file that records the run parameters and is coded accordingly. Refer to Release Notes for code definitions. Since each file receives a unique suffix multiple processing runs can be saved in the same file geodatabase.
14. Drag and drop into ArcMap and symbolize accordingly.

Visualizing Processed Data

15. Drag and drop *rawGamma* into ArcMap. If not visible, right click on file name and select *Zoom to Layer* to bring map to extent of data points
16. From ArcCatalog, drag and drop *rawGamma* raster into ArcMap layer manager
17. From ArcCatalog, drag and drop *rawGamma* polyline feature class into ArcMap layer manager. Pay attention to the order of layers in the layer manager: they will be represented in the order of their listing. If the raster image is on top, layers underneath it will not be visible.

A range of symbology options are available and a beyond the scope of this document. Instead, a short list of recommendations is provided.

18. If used, reduce the size of the points in the *rawGamma* layer to .5.
19. Likewise, change the isolines in the *rawGamma* contour layer to color black and thickness to .5. Right click on the file in the layer manager and go to *Properties*. On the top of this window, select the *Display* tab. Enter *'25'* for *Transparency*.
20. Right click on the *rawGamma* raster layer and select Properties.
    a. In the *Display* tab, change the resampling method from *Nearest Neighbor* to *Bilinear Interpolation*, which smoothes the display of the data.
    b. Under the *Symbology* tab, select appropriate method of symbology.
    c. For large datasets (those with a large data range), use *Stretched* symbology and for stretch type, use *Histogram Equalize* and turn on hillshade effect and determine an appropriate Z value.

    d. For smaller datasets, or less noisy datasets, use a *Classified* symbology with a *Defined Interval* corresponding to the desired gamma contour interval. If the data range is beyond 100 gammas, a quantile or geometric classification may be more appropriate.

    e. Select colors as necessary.
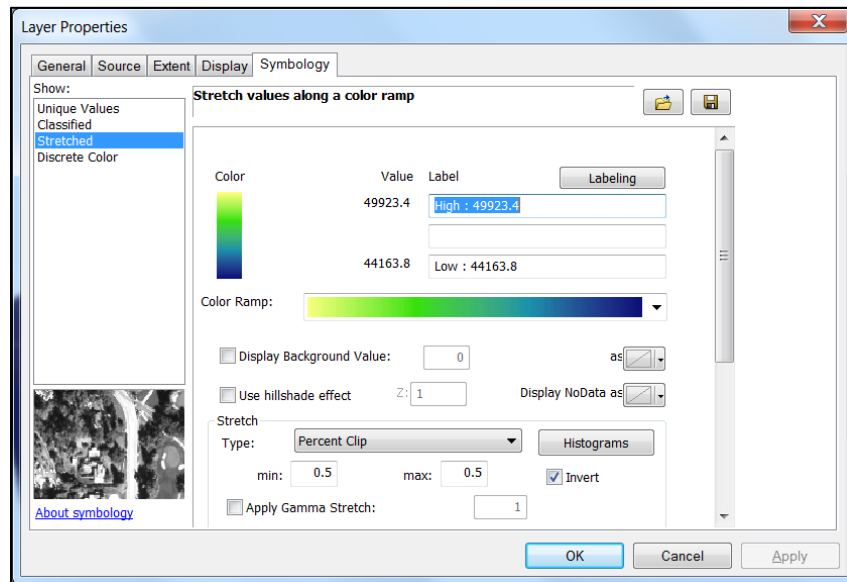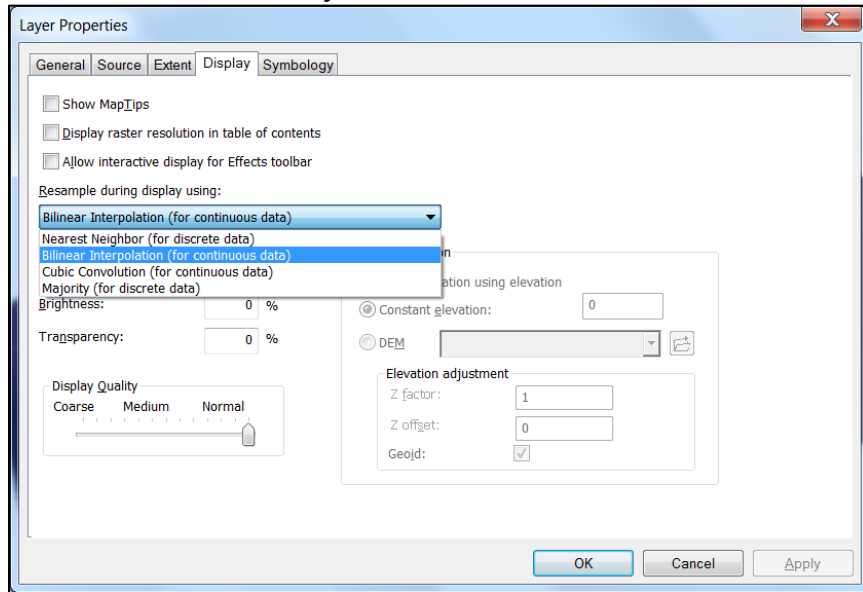
21. This group of layers represents the raw magnetic surface. A similar process is used for visualizing the gradient data.

22. Likewise, put the raster and contour lines into ArcMap making sure the contour lines layer is situated above the raster image.

23. Change the symbology of the gradient contour lines as per the above procedure.

24. Change the symbology of the gradient raster surface as per the above producer, but using a geometric interval classified symbology.

NOTE: These are general recommendations for visualizing data products. There is no 'one-size-fits-all' symbology. Rather, each dataset is unique and requires varying contour intervals and raster symbology to maximize the identification of magnetic anomalies. It is recommended for the user to experiment with these methods to fine the optimal symbology for each dataset.

CONFIDENCE MODEL TOOL

1. Expand the Magnetometer Survey Toolbox.
2. Launch the *Confidence Model* tool by double clicking. This will bring up the user interface.
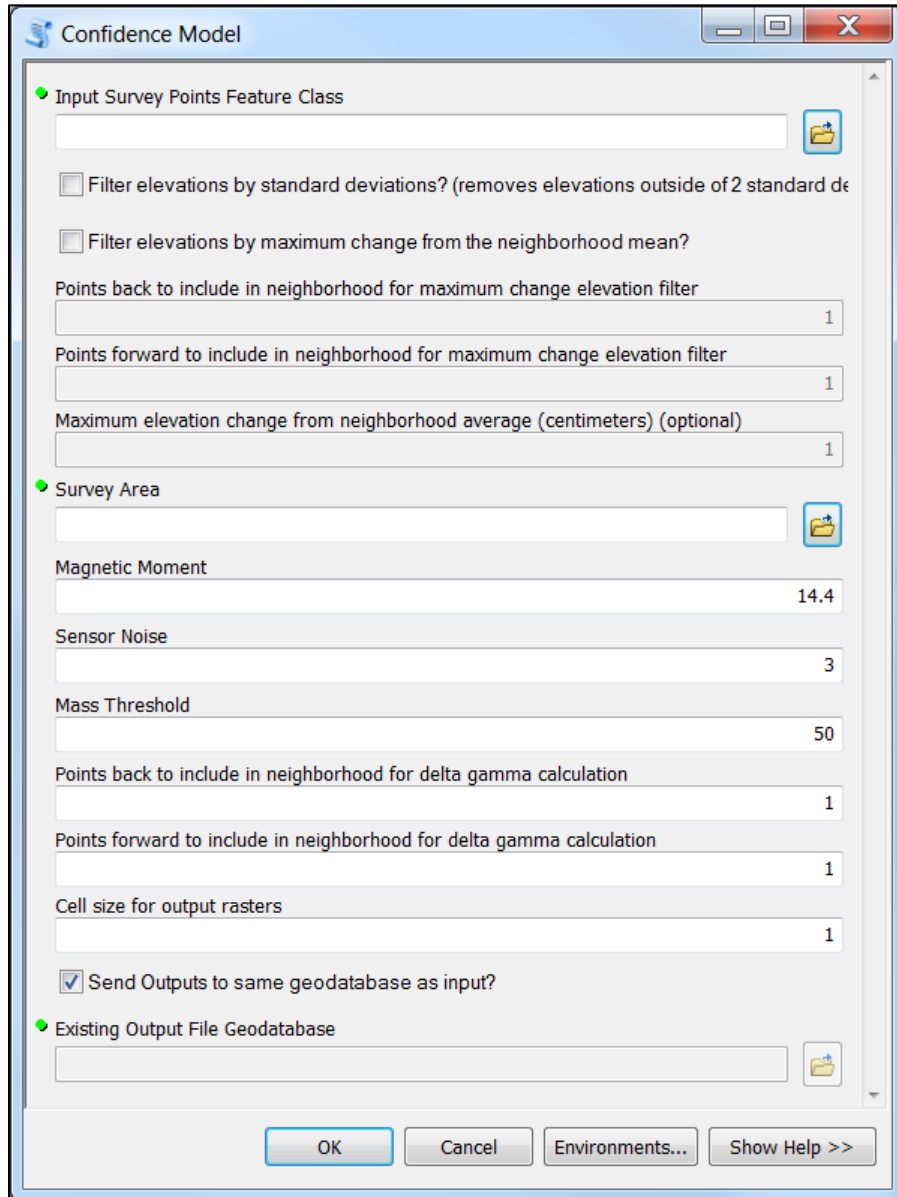
3. Enter all fields in the interface. First, load *rawGamma* data table from the geodatabase created in the *Input Tool*.
4. Load the same survey area used in the *Visualization Tool*.
5. The next prompts deal with filtering altitude. If the data table did not contain altitude value, the *Input Tool* appended each point with the estimated sensor altitude. In this case, all values are the same so no filtering is necessary.

6. If filtering is necessary, select either the statistical method or maximum change from running average.
   a. If using maximum change or running average, define the neighborhood parameters:
      i. How many points back to use for averaging.
      ii. How many points forward to use for averaging.
      iii. The maximum allowable change between a given point and the neighborhood mean.
7. Define the survey area boundary by navigating to its destination folder and selecting.
8. Input a value for Magnetic Moment (m); theoretical values for per ton of iron are between 10 and 100 $*10^4 \frac{emu}{g}$, but archaeologically-relevant values vary depending upon time, location, and target objects. Note, the algorithm calculates according to a metric ton (1000 kg scale). The powers of ten are already factored, so the user need only enter '10,' '50,' or '100,' for example. The output is also scaled so results will appear in kilograms.

*NOTE: Refer to the Magnetic Moment Calculation Spreadsheet accompanying this report to determine a locally relevant value. Using the hyper link embedded in the spreadsheet, navigate to the NOAA NGDC website and enter your geographic location and date of survey. This webpage will provide an ambient magnetic field value (in nT) which can be input directly into the Magnetic Moment Calculation Spreadsheet. The user then inputs an Archaeological Scaling Factor (recommended values between .5 and 1.5). The resulting Magnetic Moment of Archaeological Material can be input into the tool.

9. Input value for sensor noise. Take into account operational parameters, not just manufacturer specifications.
10. Enter an amount in kilograms for the mass threshold calculation; this is used to build the confidence raster, a layer the tool will produce to show in which parts of the survey the area the entered mass would have been detected.
11. Enter an amount of points backwards to use in the Δγ calculation.
12. Enter an amount of points forwards to use in the Δγ calculation.
13. Define the cell resolution of the output rasters. Recommended value is 1.
14. The default settings will save the data products to the same file geodatabase created by the *Input Tool*. If a different destination is desired, un-select and create a new one as per step 10 of the *Input Tool* instructions.
15. In the tool interface, once all inputs are entered, click *Ok* and the tool will execute.
16. Once the geoprocessing is complete, navigate to the output file geodatabase in ArcCatalog.
17. Depending on the elapsed time, you may need to refresh the destination folder. If you do not see the data outputs in the geodatabase, right click it and select *Refresh*.
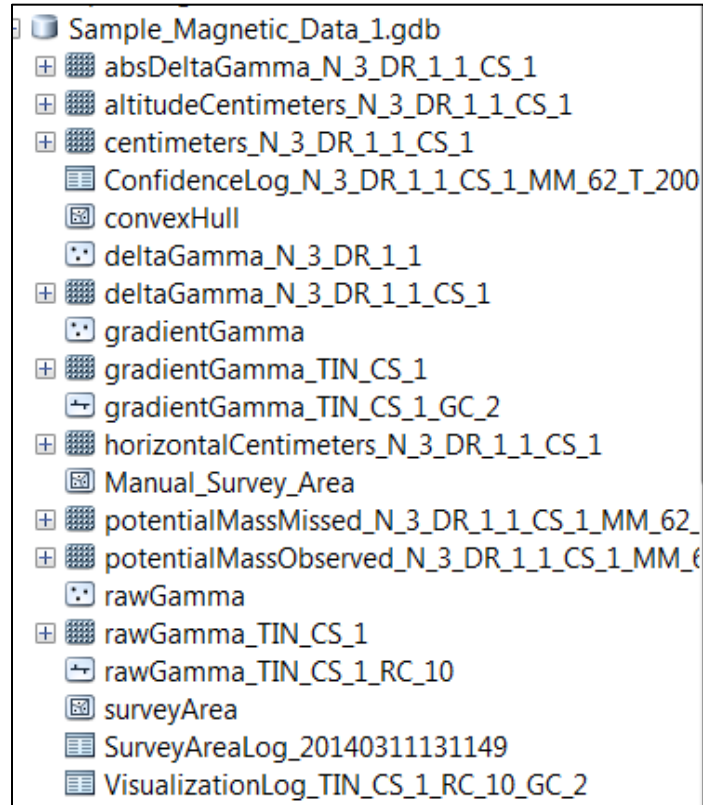
18. The data outputs should appear, along with those from the *Input Tool*, *Generate Survey Boundary* tool (if used), and the *Visualization* tool. Drag and drop these layers into ArcMap and symbolize accordingly.
19. All inputs and parameters used are recorded in the Confidence Log for later reference, and relevant parameters are added as a suffix to each file name. .
20. Use the *potentialMassObserved* raster to determine the calculated masses for observed anomalies. Symbolize in ArcMap and use either the attribute table or the identify features tool to see the mass calculated for a given cell.
21. Use the *potentialMassMissed* raster to calculated thresholds of detection. Use the attribute table to access the calculated masses (*Value*). The *Count* is the number of rasters corresponding to that mass in the layer. If the cell resolution is 1, then the sum of the count's is the area in square meters, otherwise, the count needs to be multiplied by the cell size. Divide this area by the total cell count, and that is the percent of the survey area covered to that mass threshold.

Appendix III
NOAA Survey Permit for IAA Field Testing Operations

UNITED STATES DEPARTMENT OF COMMERCE
National Oceanic and Atmospheric Administration
NATIONAL OCEAN SERVICE

Florida Keys National Marine Sanctuary
P.O. Box 1083
Key Largo, FL 33037

May 15, 2013

John C. Bright
Archeologist
National Park Service
Submerged Resources Center
12795 W. Alameda Pkwy
Lakewood CO 80228

Dear Mr. Bright:

Thank you for your application to the Florida Keys National Marine Sanctuary (FKNMS or sanctuary) for the project, "NPS Submerged Resources Center Magnetic Survey Modeling Experimentation." The application requests conducting remote surveys over artificial reef sites adjacent to Biscayne National Park to further the scientific understanding of magnetic remote sensing.

The work as proposed is not specifically geared towards exploration or documentation of artificial reefs and/or cultural resources. Furthermore, the project is non-intrusive and does not propose undertaking any activities prohibited by FKNMS regulation. Therefore, it has been determined that a permit from FKNMS is not required.

The Office of National Marine Sanctuaries (ONMS) and State of Florida Bureau of Archaeological Research support your project and recognize the value that may be gained from using sanctuary resources to model and characterize the behavior of NPS equipment for future research. As such, FKNMS would appreciate receiving a copy of your results and/or any resulting report(s) that document the work performed in the sanctuary.

Thank you for your cooperation with the ONMS. Please feel free to contact me if you have any questions at brenda.altmeier@noaa.gov or (305) 852-7717 x22.

Sincerely,

Brenda S. Altmeier
Program Support Specialist

APPENDIX IV
MAGNETIC MOMENT CALCULATION STATISTICS

BISC 00020 ANOMALY
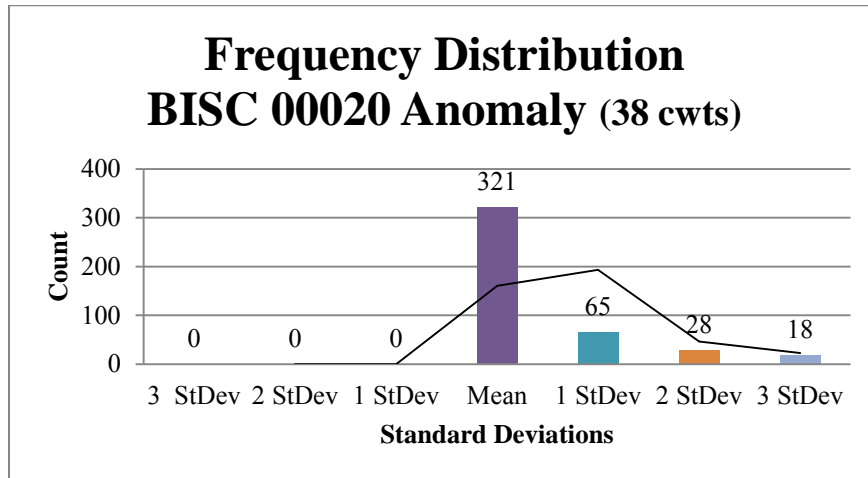
Figure IV-1. Frequency distribution for site BISC 00020 Anomaly calculated at 38 cwts (1930 kg).

Table IV-1
Frequency distribution amounts per standard deviations for BISC 00020 Anomaly calculated at 38 cwts (1930 kg).

Sort Method	Frequency
3 StDev	0
2 StDev	0
1 StDev	0
Mean	321
1 StDev	65
2 StDev	28
3 StDev	18

Table IV-2
Magnetic moment statistics for site BISC 00020 Anomaly calculated at 38 cwts (1930 kg), sample size N=444, including the empirically derived magnetic moment per unit mass (σ) value. All σ units are $\frac{emu}{g}$.

Mean
114.69
Median
33.535
Standard Deviation
173.83
Range
874.329
Empirical σ Value
33.535
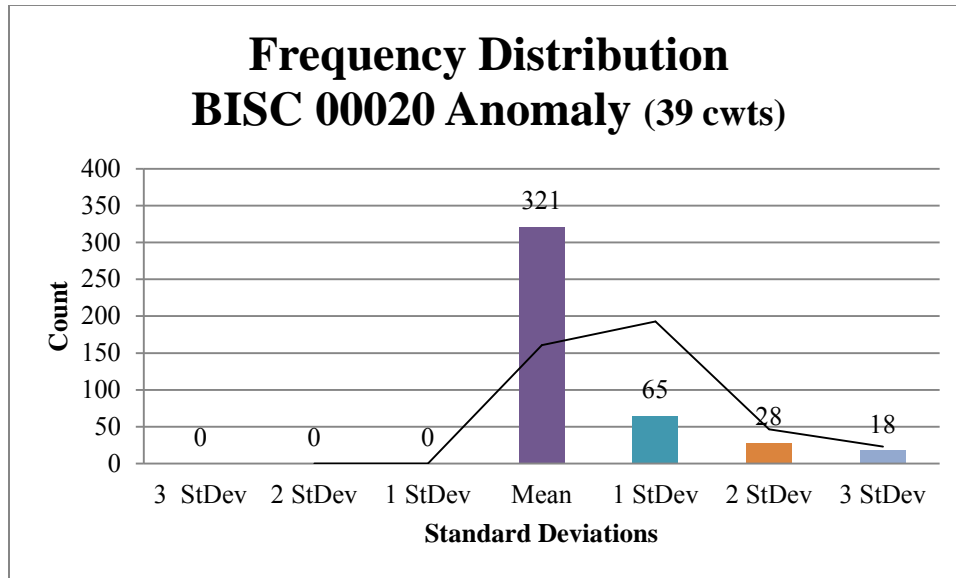
Figure IV-2. Frequency distribution for site BISC 00020 Anomaly calculated at 39 cwts (1981 kg).

Table IV-3

Frequency distribution amounts per standard deviation for BISC 00020 Anomaly calculated at 39 cwts (1981 kg).

Sort Method	Frequency
3 StDev	0
2 StDev	0
1 StDev	0
Mean	321
1 StDev	65
2 StDev	28
3 StDev	18

Table IV-4

Magnetic moment statistics for site BISC 00020 Anomaly calculated at 39 cwts (1981 kg), sample size N=444, including the empirically derived magnetic moment per unit mass (σ) value. All σ units are $\frac{emu}{g}$.

Mean
111.667
Median
31.884
Standard Deviation
169.39
Range
851.820
Empirical σ Value
31.884
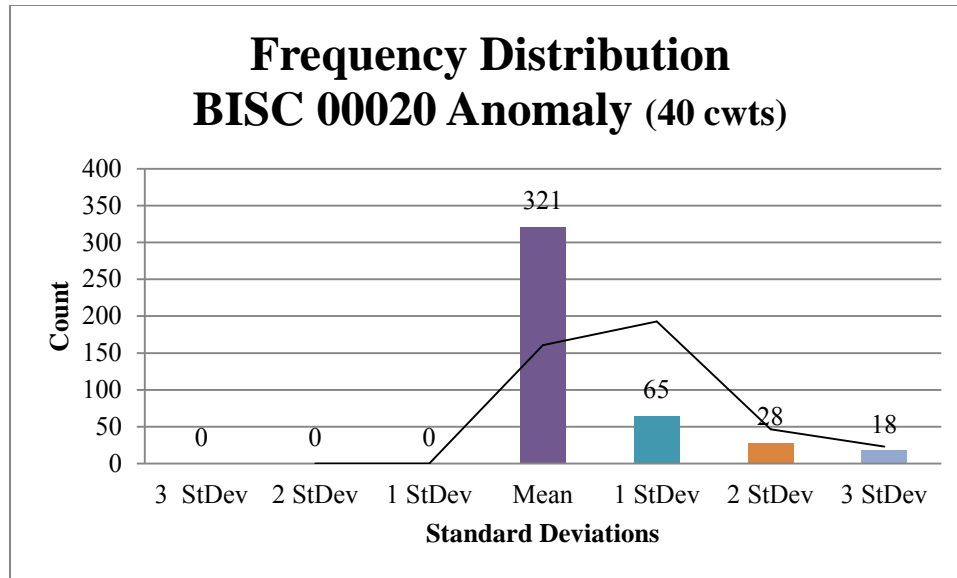
Figure IV-3. Frequency distribution for site BISC 00020 Anomaly calculated at 40 cwts (2032 kg).

Table IV-5
Frequency distribution amounts per standard deviation for BISC 00020 Anomaly calculated at 40 cwts (2032 kg).

Sort Method	Frequency
3 StDev	0
2 StDev	0
1 StDev	0
Mean	321
1 StDev	65
2 StDev	28
3 StDev	18

Table IV-6
Magnetic moment statistics for site BISC 00020 Anomaly calculated at 40 cwts (2032 kg), sample size N=444, including the empirically derived magnetic moment per unit mass (σ) value. All σ units are $\frac{emu}{g}$.

Mean
108.935
Median
31.852
Standard Deviation
164.851
Range
830.442
Empirical σ Value
31.852

BISC 00020 MAIN SITE

**Frequency Distribution
BISC 00020 (6906 kg)**
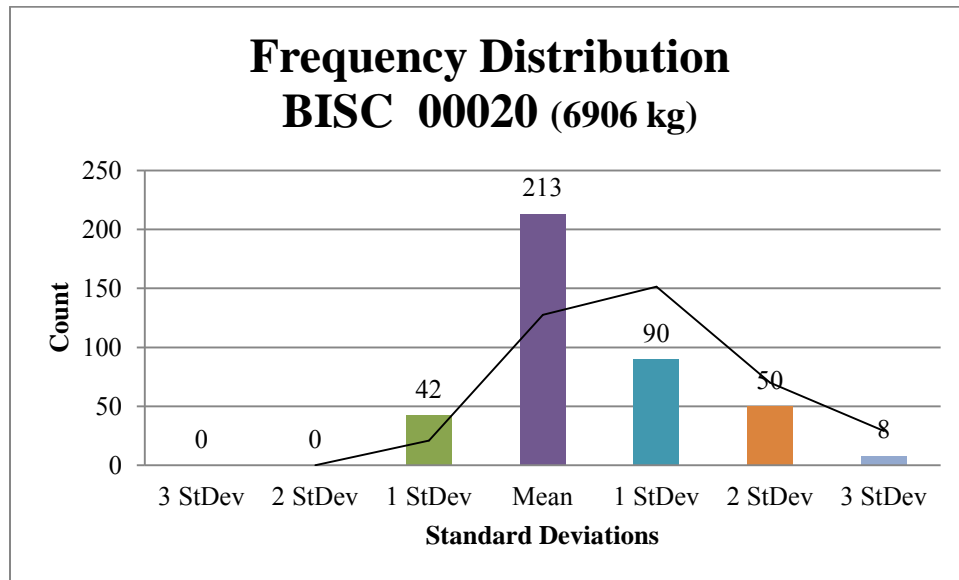
Figure IV-4. Frequency distribution for site BISC 00020 Main Site calculated at 6909 kg.

**Table IV-7
Frequency distribution amounts per standard deviation for BISC 00020 Main Site calculated at 6906 kg.**

Sort Method	Frequency
3 StDev	0
2 StDev	0
1 StDev	42
Mean	213
1 StDev	90
2 StDev	50
3 StDev	8

**Table IV-8
Magnetic moment statistics for site BISC 00020 Main Site calculated at 6909 kg, sample size N=412, including the empirically derived magnetic moment per unit mass (σ) value. All σ units are $\frac{emu}{g}$.**

Mean
17.496
Median
11.782
Standard Deviation
15.553
Range
85.318
Empirical σ Value
11.782

Frequency Distribution
BISC 00020 (6501 kg)
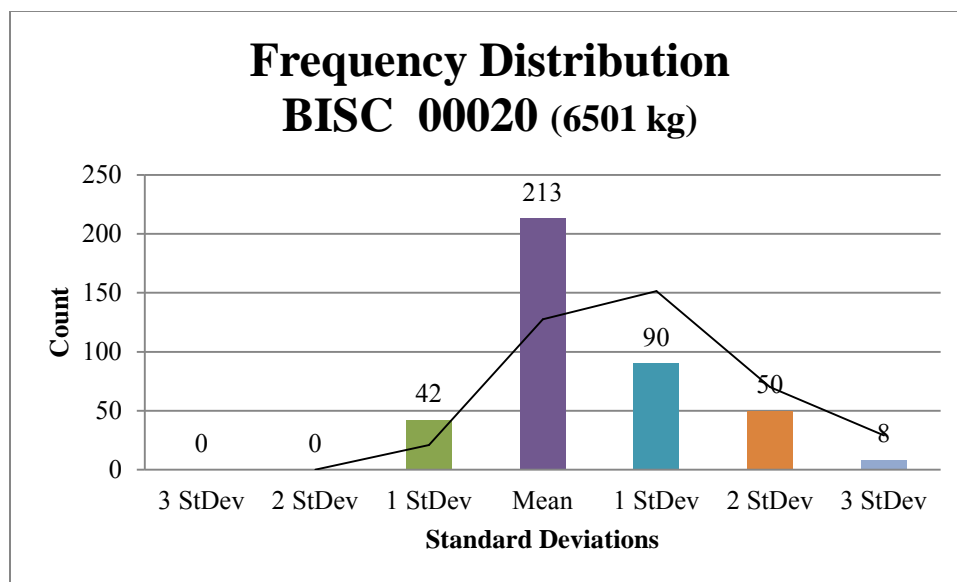
FigureIV-5. Frequency distribution for site BISC 00020 Main Site calculated at 6501 kg.

Table IV-9
Frequency distribution amounts per standard deviation for BISC 00020 Main Site calculated at 6501 kg.

Sort Method	Frequency
3 StDev	0
2 StDev	0
1 StDev	42
Mean	213
1 StDev	90
2 StDev	50
3 StDev	8

Table IV-10
Magnetic moment statistics for site BISC 00020 Main Site calculated at 6501 kg, sample size N=412, including the empirically derived magnetic moment per unit mass (σ) value. All σ units are $\frac{emu}{g}$.

Mean
18.586
Median
12.516
Standard Deviation
16.522
Range
90.633
Empirical σ Value
12.516

BISC 00062
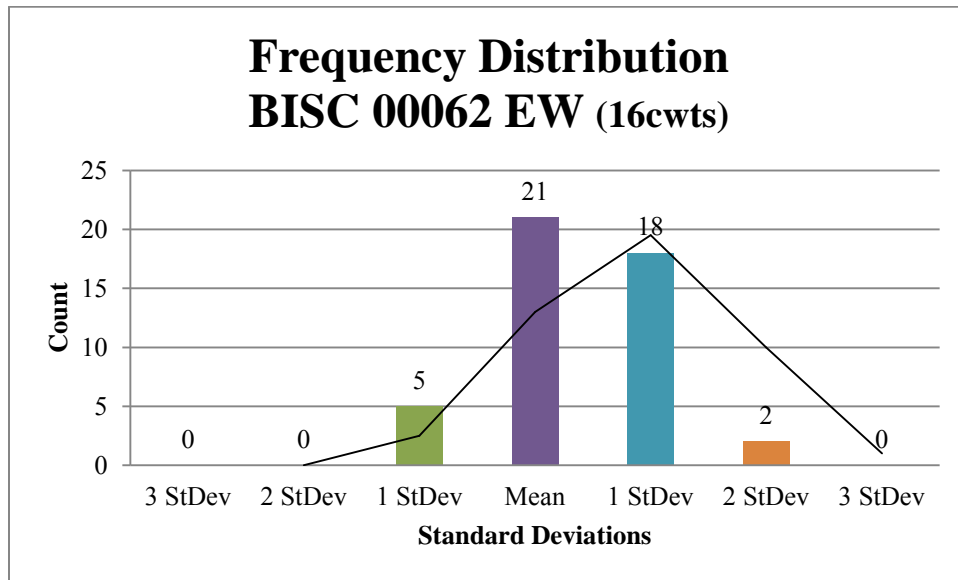
Figure IV-6. Frequency distribution for site BISC 00062 EW calculated at 16 cwts (813 kg).

Table IV-11
Frequency distribution amounts per standard deviation for BISC 00062 EW calculated at 16 cwts (813 kg).

Sort Method	Frequency
3 StDev	0
2 StDev	0
1 StDev	5
Mean	21
1 StDev	18
2 StDev	2
3 StDev	0

Table IV-12
Magnetic moment statistics for site BISC 00062 EW calculated at 16 cwts (813 kg), sample size N=46, including the empirically derived magnetic moment per unit mass (σ) value. All σ units are $\frac{emu}{g}$.

Mean
3.3853
Median
3.001
Standard Deviation
2.52
Range
15.734
Empirical σ Value
3.001
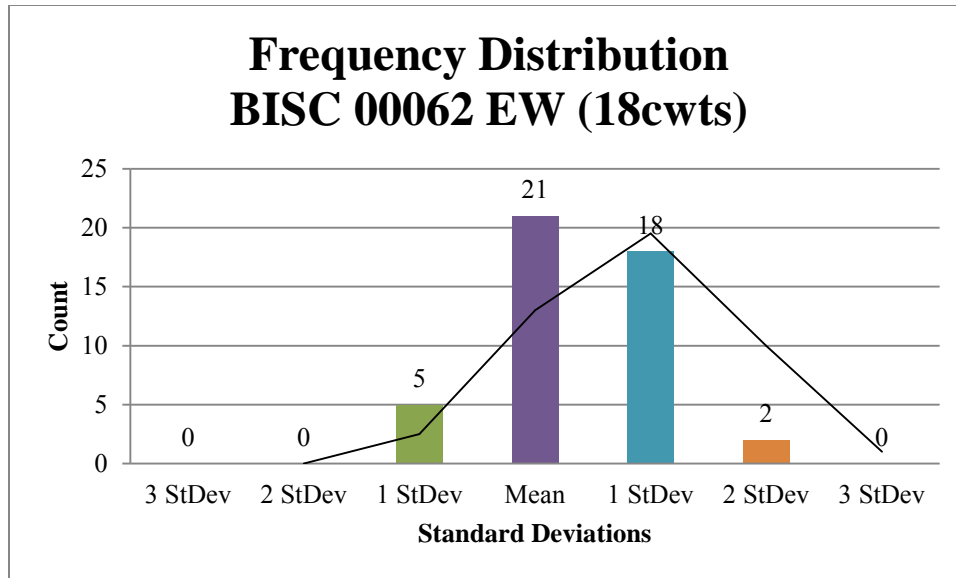
Figure IV-7. Frequency distribution for site BISC 00062 EW calculated at 18 cwts (914 kg).

Table IV-13
Frequency distribution amounts per standard deviation for BISC 00062 EW calculated at 18 cwts (914 kg).

Sort Method	Frequency
3 StDev	0
2 StDev	0
1 StDev	5
Mean	21
1 StDev	18
2 StDev	2
3 StDev	0

Table IV-14
Magnetic moment statistics for site BISC 00062 EW calculated at 18 cwts (914 kg), sample size N=46, including the empirically derived magnetic moment per unit mass (σ) value. All σ units are $\frac{emu}{g}$.

Mean
3.011
Median
2.677
Standard Deviation
2.246
Range
13.995
Empirical σ Value
2.677

Frequency Distribution
BISC 00062 EW (20.5 cwts)
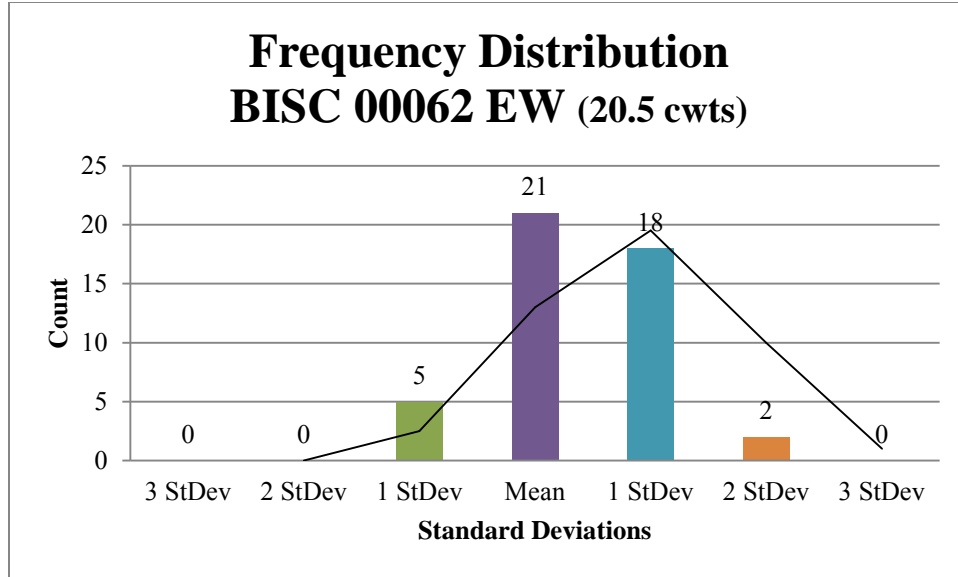
Figure IV-8. Frequency distribution for site BISC 00062 EW calculated at 20.5 cwts (1041 kg).

Table IV-15
Frequency distribution amounts per standard deviation for BISC 00062 EW calculated at 20.5 cwts (1041 kg).

Sort Method	Frequency
3 StDev	0
2 StDev	0
1 StDev	5
Mean	21
1 StDev	18
2 StDev	2
3 StDev	0

Table IV-16
Magnetic moment statistics for site BISC 00062 EW calculated at 20.5 cwts (1041 kg), sample size N=46, including the empirically derived magnetic moment per unit mass (σ) value. All σ units are $\frac{emu}{g}$.

Mean
2.643
Median
2.351
Standard Deviation
1.972
Range
12.288
Empirical σ Value
2.351

Frequency Distribution
BISC 00062 EW (24.5 cwts)
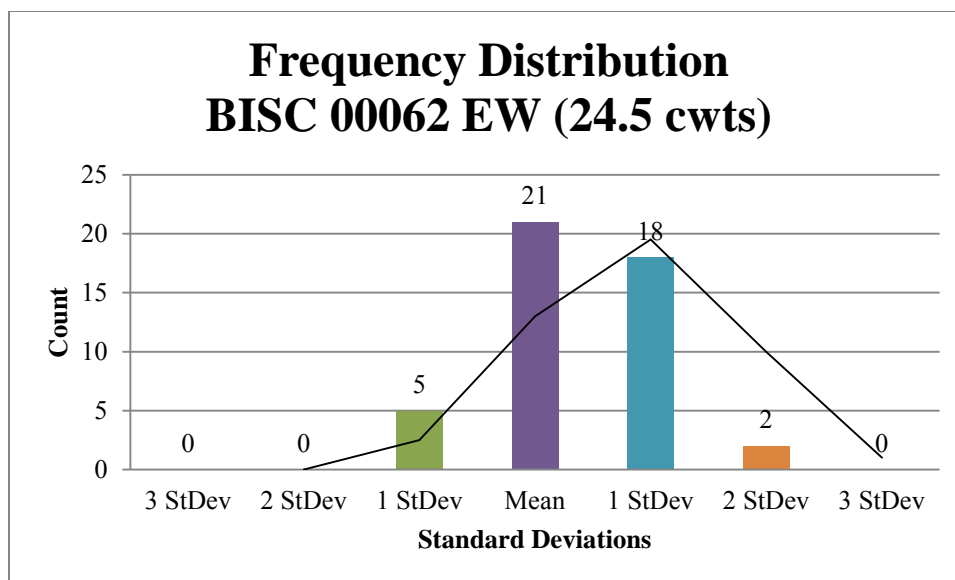
Figure IV-9. Frequency distribution for site BISC 00062 EW calculated at 24.5 cwts (1244 kg).

Table IV-17
Frequency distribution amounts per standard deviation for BISC 00062 EW calculated at 24.5 cwts (1244 kg).

Sort Method	Frequency
3 StDev	0
2 StDev	0
1 StDev	5
Mean	21
1 StDev	18
2 StDev	2
3 StDev	0

Table IV-18
Magnetic moment statistics for site BISC 00062 EW calculated at 24.5 cwts (1244 kg), sample size N=46, including the empirically derived magnetic moment per unit mass (σ) value. All σ units are $\frac{emu}{g}$.

Mean
2.212
Median
1.966
Standard Deviation
1.651
Range
10.282
Empirical σ Value
1.966
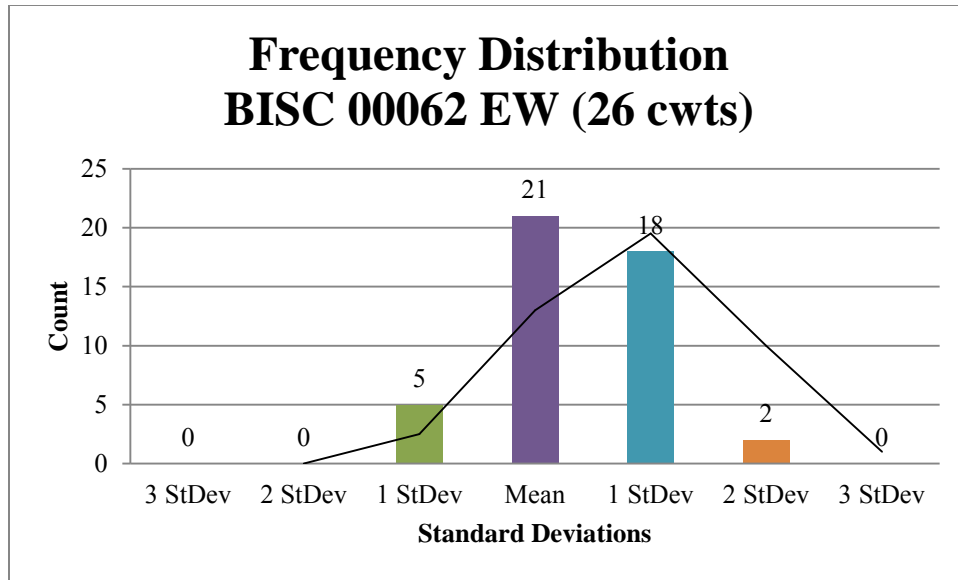
Figure IV-10. Frequency distribution for site BISC 00062 EW calculated at 26 cwts (1320 kg).

Table IV-19
Frequency distribution amounts per standard deviation for BISC 00062 EW calculated at 26 cwts (1320 kg).

Sort Method	Frequency
3 StDev	0
2 StDev	0
1 StDev	5
Mean	21
1 StDev	18
2 StDev	2
3 StDev	0

Table IV-20
Magnetic moment statistics for site BISC 00062 EW calculated at 26 cwts (1320 kg), sample size N=46, including the empirically derived magnetic moment per unit mass (σ) value. All σ units are $\frac{emu}{g}$.

Mean
2.085
Median
1.853
Standard Deviation
1.555
Range
9.691
Empirical σ Value
1.853
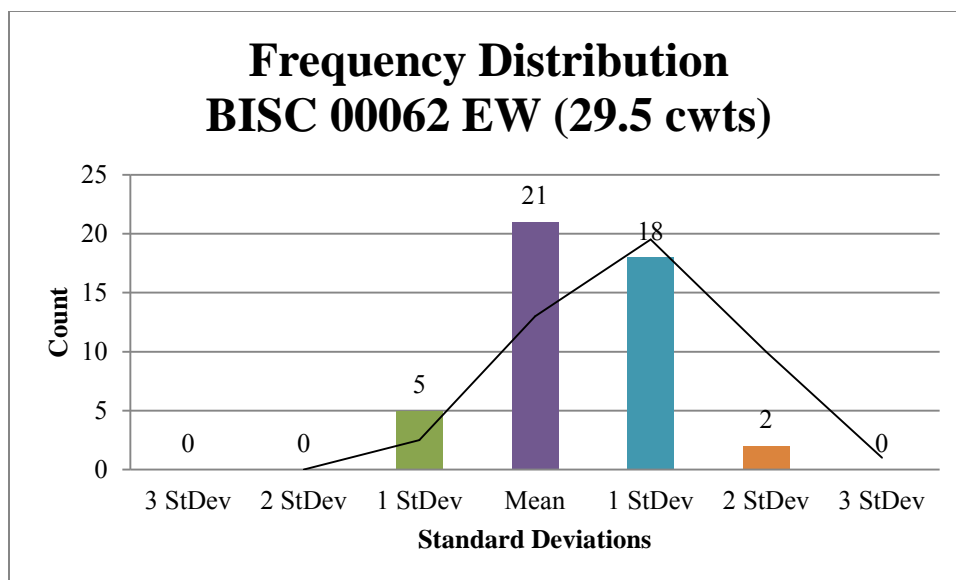
Figure IV-11. Frequency distribution for site BISC 00062 EW calculated at 29.5 cwts (1498 kg).

Table IV-21
Frequency distribution amounts per standard deviation for BISC 00062 EW calculated at 29.5 cwts (1498 kg).

Sort Method	Frequency
3 StDev	0
2 StDev	0
1 StDev	5
Mean	21
1 StDev	18
2 StDev	2
3 StDev	0

Table IV-22
Magnetic moment statistics for site BISC 00062 EW calculated at 29.5 cwts (1498 kg), sample size N=46, including the empirically derived magnetic moment per unit mass (σ) value. All σ units are $\frac{emu}{g}$.

Mean
1.837
Median
1.633
Standard Deviation
1.371
Range
8.539
Empirical σ Value
1.633
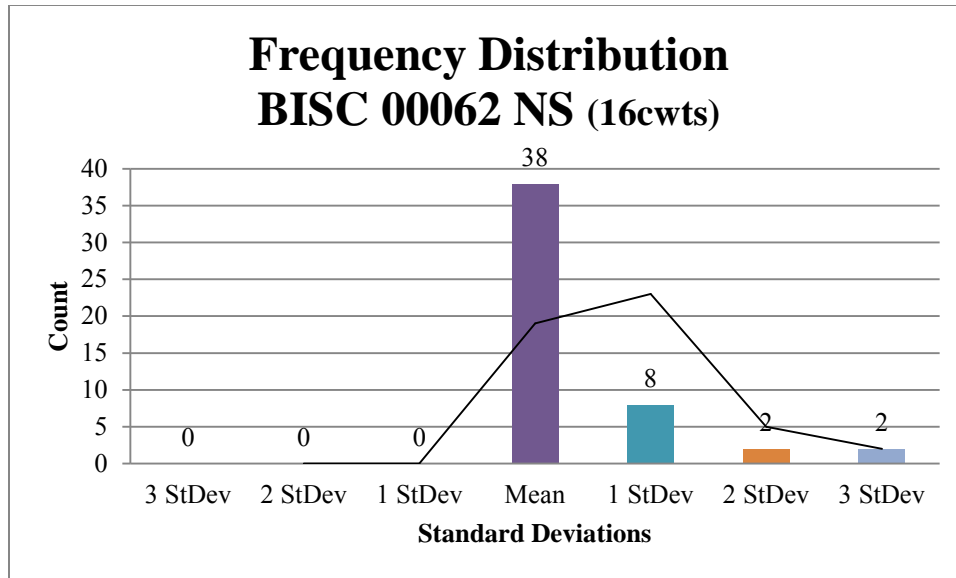
Figure IV-12. Frequency distribution for site BISC 00062 NS calculated at 16 cwts (813 kg).

Table IV-23
Frequency distribution amounts per standard deviation for BISC 00062 NS calculated at 16 cwts (813 kg).

Sort Method	Frequency
3 StDev	0
2 StDev	0
1 StDev	0
Mean	38
1 StDev	8
2 StDev	2
3 StDev	2

Table IV-24
Magnetic moment statistics for site BISC 00062 NS calculated at 16 cwts (813 kg), sample size N=51, including the empirically derived magnetic moment per unit mass (σ) value. All σ units are $\frac{emu}{g}$.

Mean
7.627
Median
5.069
Standard Deviation
7.477
Range
35.452
Empirical σ Value
5.069
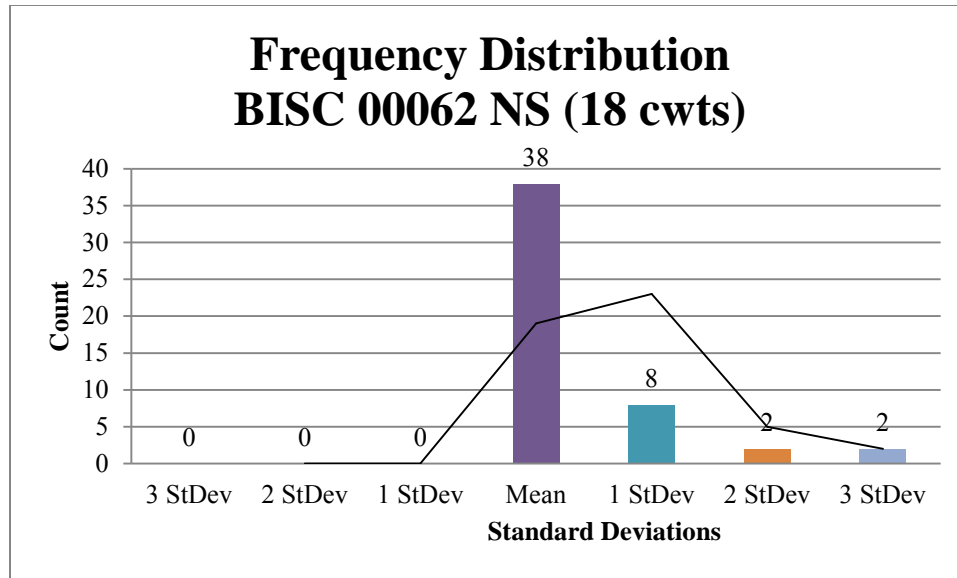
Figure IV-13. Frequency distribution for site BISC 00062 NS calculated at 18 cwts (914 kg).

Table IV-25
Frequency distribution amount per standard deviation for BISC 00062 NS calculated at 18 cwts (914 kg).

Sort Method	Frequency
3 StDev	0
2 StDev	0
1 StDev	0
Mean	38
1 StDev	8
2 StDev	2
3 StDev	2

Table IV-26
Magnetic moment statistics for site BISC 00062 NS calculated at 18 cwts (914 kg), sample size N=51, including the empirically derived magnetic moment per unit mass (σ) value. All σ units are $\frac{emu}{g}$.

Mean
6.784
Median
4.509
Standard Deviation
6.651
Range
31.535
Empirical σ Value
4.509
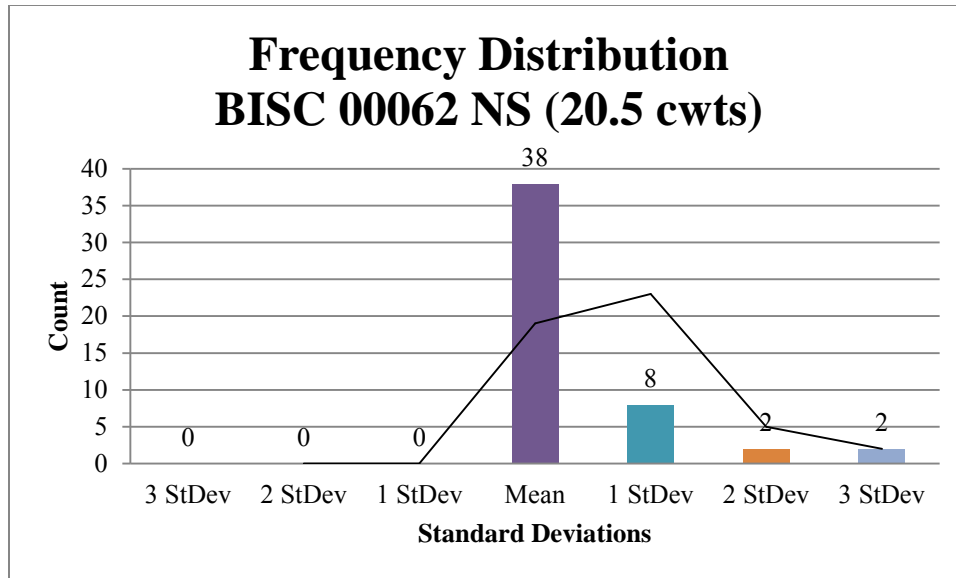
Figure IV-14. Frequency distribution for site BISC 00062 NS calculated at 20.5 cwts (1041 kg).

Table IV-27
Frequency distribution amount per standard deviation for BISC 00062 NS calculated at 20.5 cwts (1041 kg).

Sort Method	Frequency
3 StDev	0
2 StDev	0
1 StDev	0
Mean	38
1 StDev	8
2 StDev	2
3 StDev	2

Table IV-28
Magnetic moment statistics for site BISC 00062 NS calculated at 20.5 cwts (1041 kg), sample size N=51, including the empirically derived magnetic moment per unit mass (σ) value. All σ units are $\frac{emu}{g}$.

Mean
5.956
Median
3.959
Standard Deviation
5.839
Range
27.687
Empirical σ Value
3.959
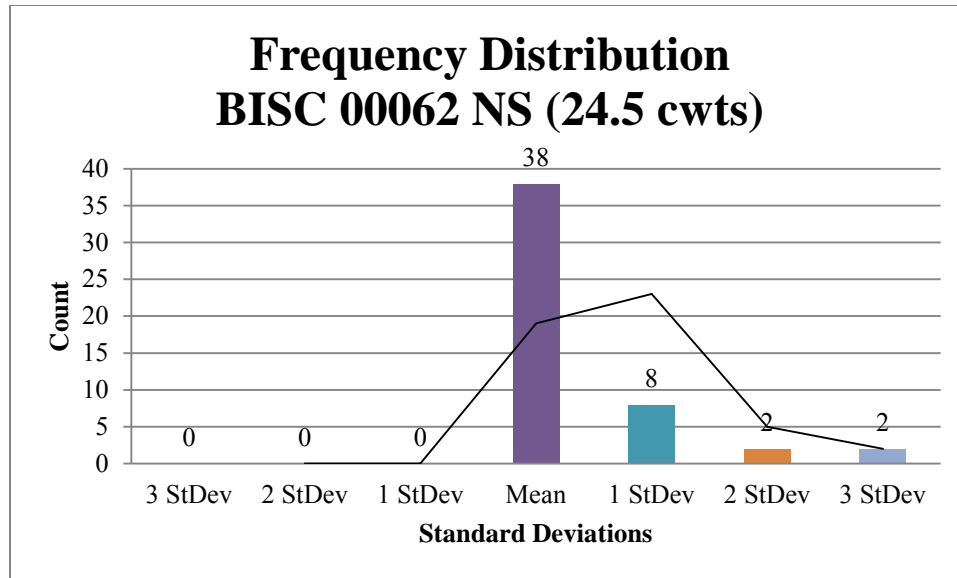
Figure IV-15. Frequency distribution for site BISC 00062 NS calculated at 24.5 cwts (1244 kg).

Table IV-29
Frequency distribution amount per standard deviation for BISC 00062 NS calculated at 24.5 cwts (1244 kg).

Sort Method	Frequency
3 StDev	0
2 StDev	0
1 StDev	0
Mean	38
1 StDev	8
2 StDev	2
3 StDev	2

Table IV-30
Magnetic moment statistics for site BISC 00062 NS calculated at 24.5 cwts (1244 kg), sample size N=51, including the empirically derived magnetic moment per unit mass (σ) value. All σ units are $\frac{emu}{g}$.

Mean
4.984
Median
3.312
Standard Deviation
4.886
Range
23.169
Empirical σ Value
3.312
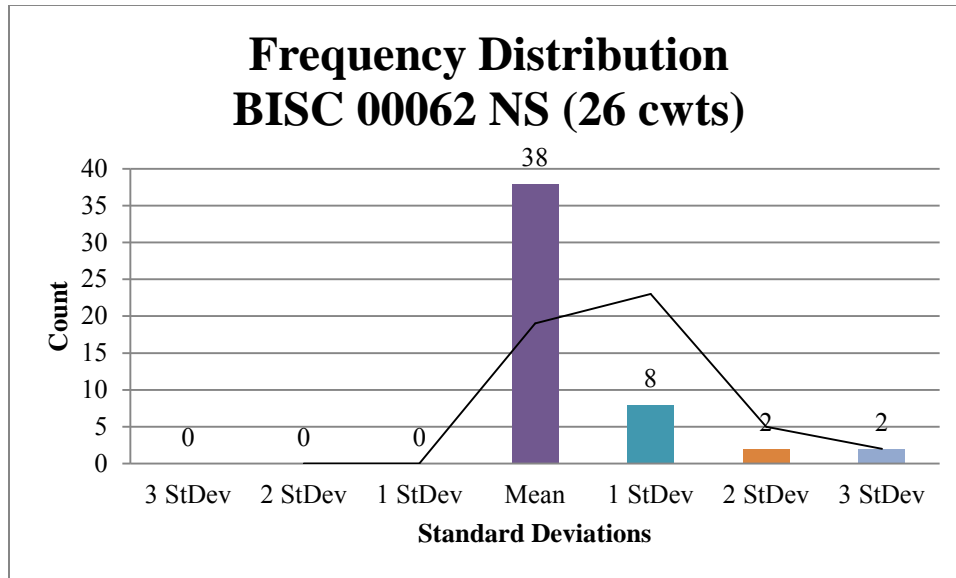
Figure IV-16. Frequency distribution for site BISC 00062 NS calculated at 26 cwts (1320 kg).

Table IV-31
Frequency distribution amount per standard deviation for BISC 00062 NS calculated at 26 cwts (1320 kg).

Sort Method	Frequency
3 StDev	0
2 StDev	0
1 StDev	0
Mean	38
1 StDev	8
2 StDev	2
3 StDev	2

Table IV-32
Magnetic moment statistics for site BISC 00062 NS calculated at 26cwts (1320 kg), sample size N=51, including the empirically derived magnetic moment per unit mass (σ) value. All σ units are $\frac{emu}{g}$.

Mean
4.697
Median
3.122
Standard Deviation
4.605
Range
21.835
Empirical σ Value
3.122
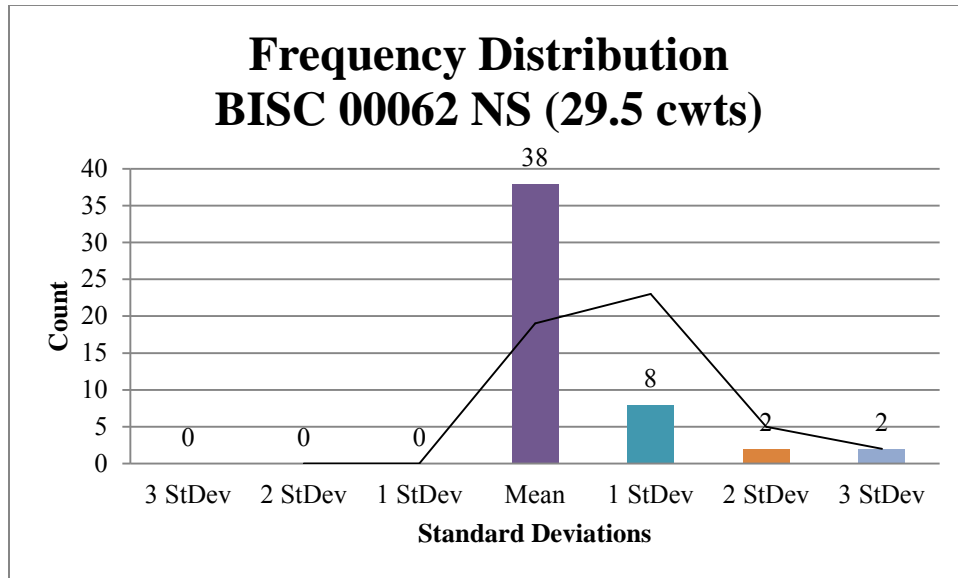
Figure IV-17. Frequency distribution for site BISC 00062 NS calculated at 29.5 cwts (1498 kg).

Table IV-33
Frequency distribution amount per standard deviation for BISC 00062 NS calculated at 29.5 cwts (1498 kg).

Sort Method	Frequency
3 StDev	0
2 StDev	0
1 StDev	0
Mean	38
1 StDev	8
2 StDev	2
3 StDev	2

Table IV-34
Magnetic moment statistics for site BISC 00062 NS calculated at 29.5 cwts (1498 kg), sample size N=51, including the empirically derived magnetic moment per unit mass (σ) value. All σ units are $\frac{emu}{g}$.

Mean
4.139
Median
2.751
Standard Deviation
4.058
Range
19.241
Empirical σ Value
2.751

BISC 00089
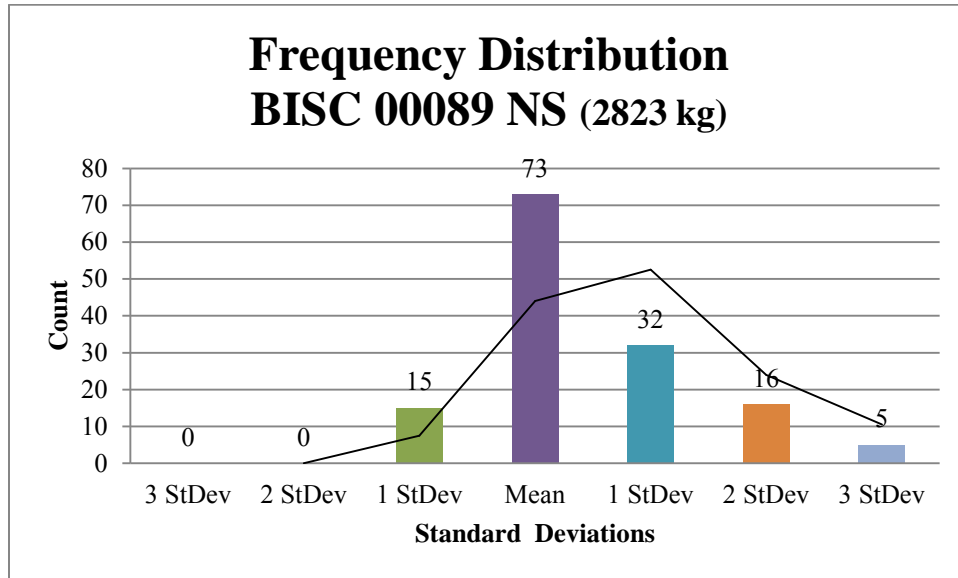
Figure IV-18. Frequency distribution for site BISC 00089 NS calculated at 2823 kg.

Table IV-35
Frequency distribution amounts per standard deviation for BISC 00089 NS calculated at 2823 kg.

Sort Method	Frequency
3 StDev	0
2 StDev	0
1 StDev	15
Mean	73
1 StDev	32
2 StDev	16
3 StDev	5

Table IV-36
Magnetic moment statistics for site BISC 00089 NS calculated at 2823 kg, sample size N=142, including the empirically derived magnetic moment per unit mass (σ) value. All σ units are $\frac{emu}{g}$.

Mean
10.2766
Median
8.122
Standard Deviation
7.824
Range
42.356
Empirical σ Value
8.122

Frequency Distribution
BISC 00089 NS (1684 kg)
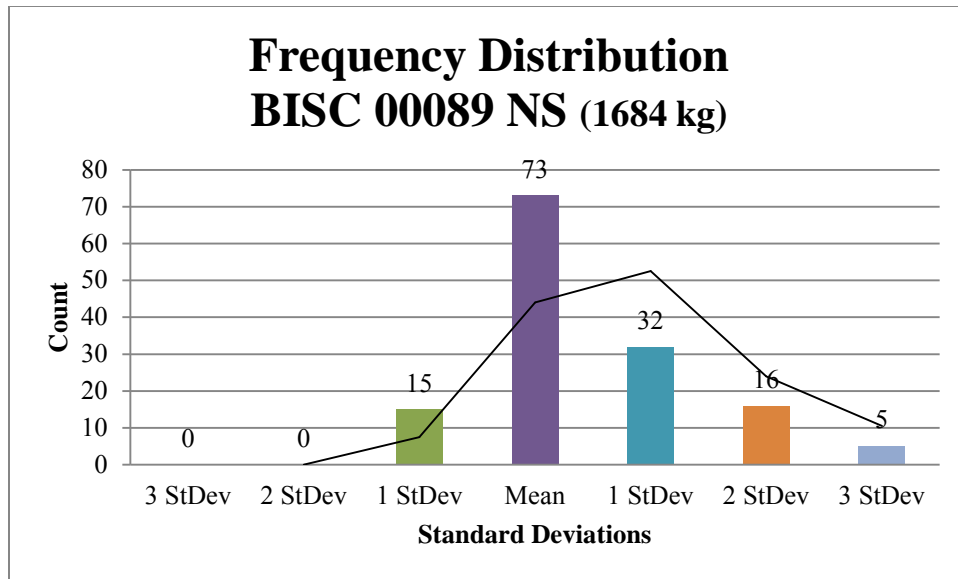
Figure IV-19. Frequency distribution for site BISC 00089 NS calculated at 1684 kg.

Table IV-37
Frequency distribution amount per standard deviation for BISC 00089 NS calculated at 1684 kg.

Sort Method	Frequency
3 StDev	0
2 StDev	0
1 StDev	15
Mean	73
1 StDev	32
2 StDev	16
3 StDev	5

Table IV-38
Magnetic moment statistics for site BISC 00089 NS calculated at 1684 kg, sample size N=142, including the empirically derived magnetic moment per unit mass (σ) value. All σ units are $\frac{emu}{g}$.

Mean
17.223
Median
13.615
Standard Deviation
13.117
Range
70.005
Empirical σ Value
13.615
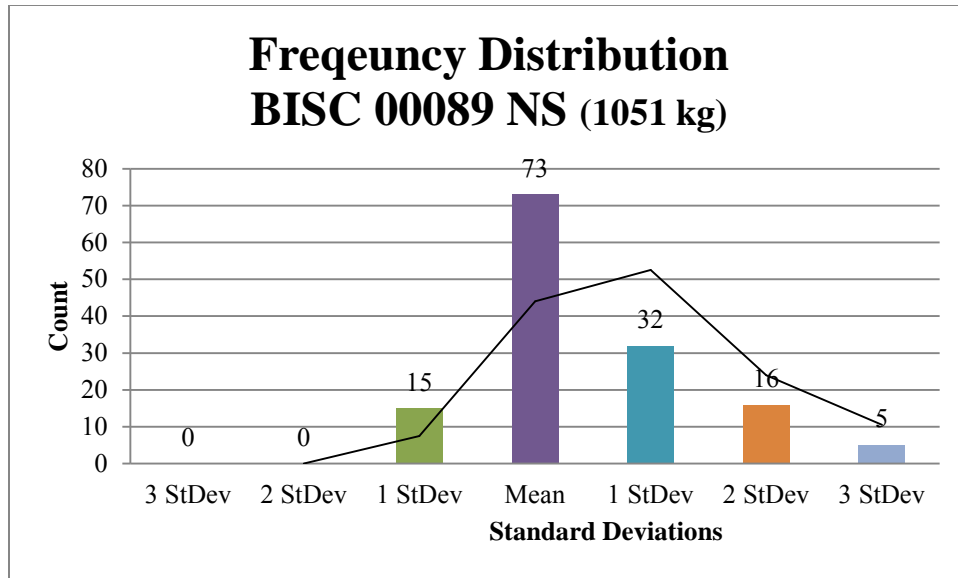
Figure IV-20. Frequency distribution for site BISC 00089 NS calculated at 1051 kg.

Table IV-39
Frequency distribution amount per standard deviation for BISC 00089 NS calculated at 1051 kg.

Sort Method	Frequency
3 StDev	0
2 StDev	0
1 StDev	15
Mean	73
1 StDev	32
2 StDev	16
3 StDev	5

Table IV-40
Magnetic moment statistics for site BISC 00089 NS calculated at 1051 kg, sample size N=142, including the empirically derived magnetic moment per unit mass (σ) value. All σ units are $\frac{emu}{g}$.

Mean
27.603
Median
21.816
Standard Deviation
21.017
Range
113.771
Empirical σ Value
21.816

Frequency Distribution
BISC 00089 EW (2823 kg)
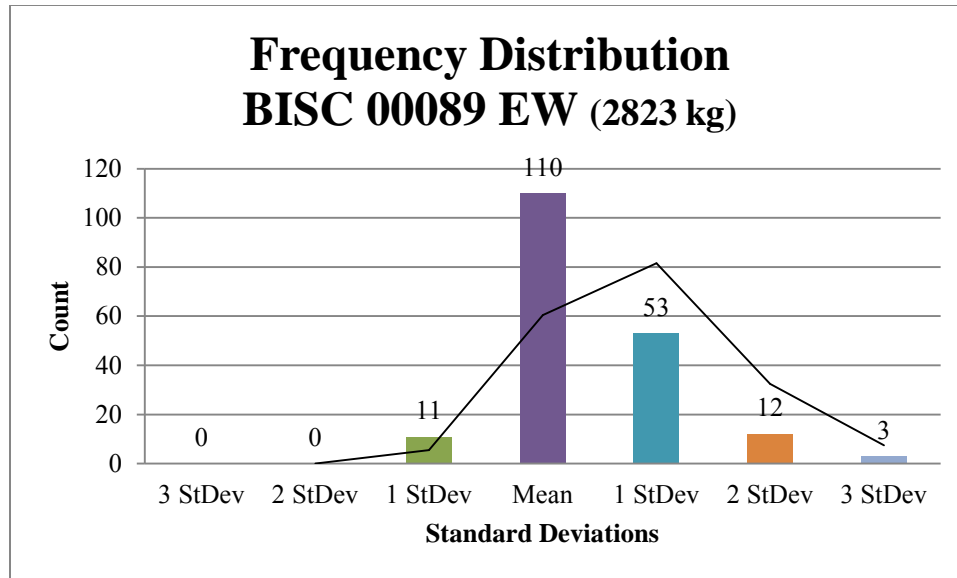
Figure IV-21. Frequency distribution for site BISC 00089 EW calculated at 2823 kg.

Table IV-41
Frequency distribution amount per standard deviation for BISC 00089 EW calculated at 2823 kg.

Sort Method	Frequency
3 StDev	0
2 StDev	0
1 StDev	11
Mean	110
1 StDev	53
2 StDev	12
3 StDev	3

Table IV-42
Magnetic moment statistics for site BISC 00089 EW calculated at 2823 kg, sample size N=195, including the empirically derived magnetic moment per unit mass (σ) value. All σ units are $\frac{emu}{g}$.

Mean
8.535
Median
6.565
Standard Deviation
7.221
Range
41.182
Empirical σ Value
6.565
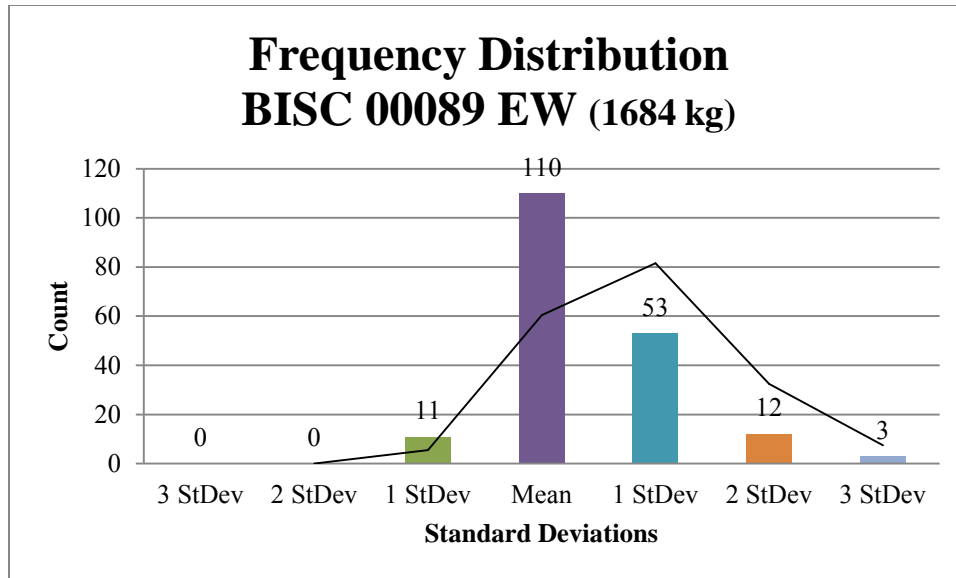
Figure IV-22. Frequency distribution for site BISC 00089 EW calculated at 1684 kg.

Table IV-43
Frequency distribution amount per standard deviation for BISC 00089 EW calculated at 1684 kg.

Sort Method	Frequency
3 StDev	0
2 StDev	0
1 StDev	11
Mean	110
1 StDev	53
2 StDev	12
3 StDev	3

Table IV-44
Magnetic moment statistics for site BISC 00089 EW calculated at 1684 kg, sample size N=195, including the empirically derived magnetic moment per unit mass (σ) value. All σ units are $\frac{emu}{g}$.

Mean
14.307
Median
11.005
Standard Deviation
12.106
Range
69.037
Empirical σ Value
11.005
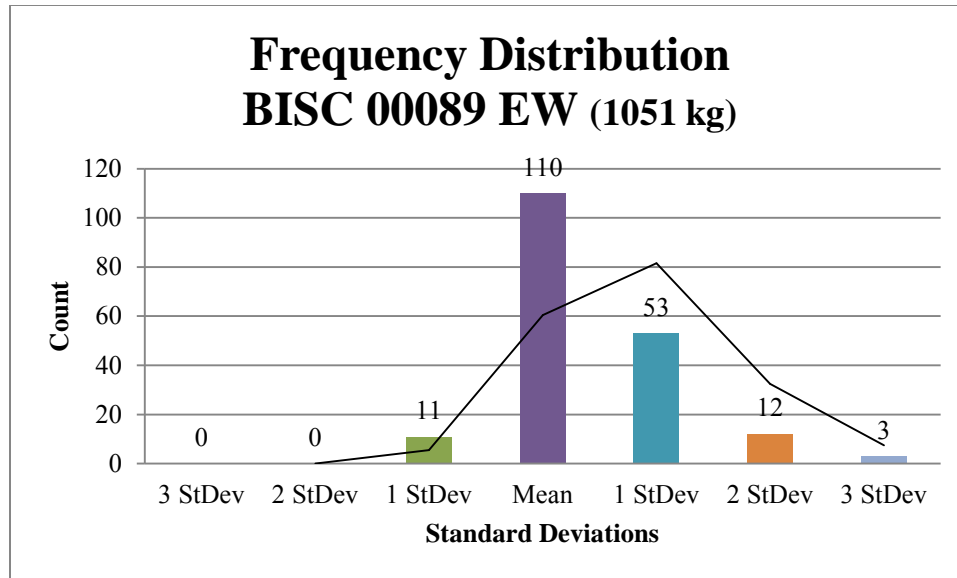
Figure IV-23. Frequency distribution for site BISC 00089 EW calculated at 1051 kg.

Table IV-45
Frequency distribution amount per standard deviation for BISC 00089 EW calculated at 1051 kg.

Sort Method	Frequency
3 StDev	0
2 StDev	0
1 StDev	11
Mean	110
1 StDev	53
2 StDev	12
3 StDev	3

Table IV-46
Magnetic moment statistics for site BISC 00089 EW calculated at 1051 kg, sample size N=195, including the empirically derived magnetic moment per unit mass (σ) value. All σ units are $\frac{emu}{g}$.

Mean
22.925
Median
17.634
Standard Deviation
19.397
Range
110.618
Empirical σ Value
17.634

BISC 00114
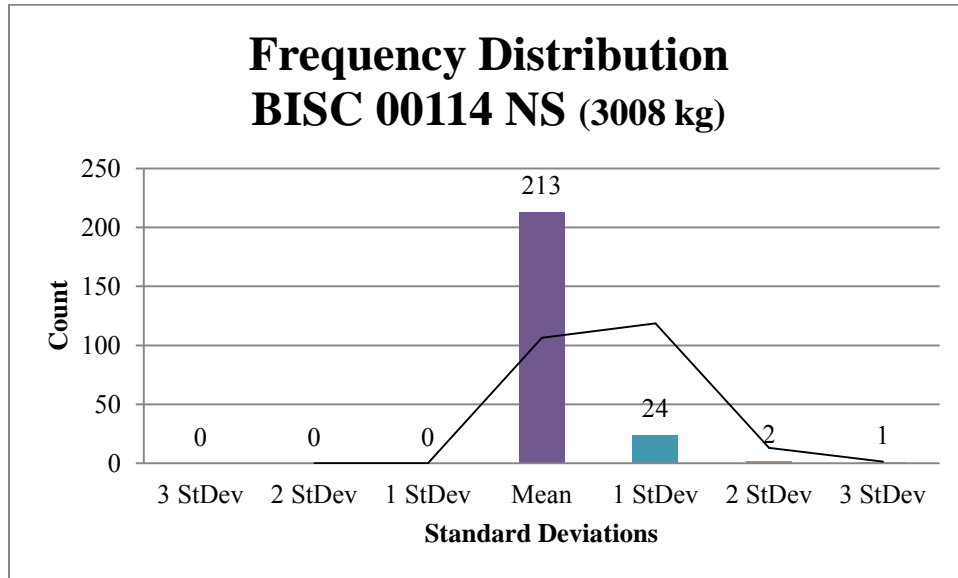
Figure IV-24. Frequency distribution for site BISC 00114 NS calculated at 3008 kg.

Table IV-47
Frequency distribution amounts per standard deviation for BISC 00114 NS calculated at 3008 kg.

Sort Method	Frequency
3 StDev	0
2 StDev	0
1 StDev	0
Mean	213
1 StDev	24
2 StDev	2
3 StDev	1

Table IV-48
Magnetic moment statistics for site BISC 00114 NS calculated at 3008 kg, sample size N=242, including the empirically derived magnetic moment per unit mass (σ) value. All σ units are $\frac{emu}{g}$.

Mean
63.457
Median
23.838
Standard Deviation
270.41
Range
3335.99
Empirical σ Value
23.838

Frequency Distribution
BISC 00114 NS (2970 kg)
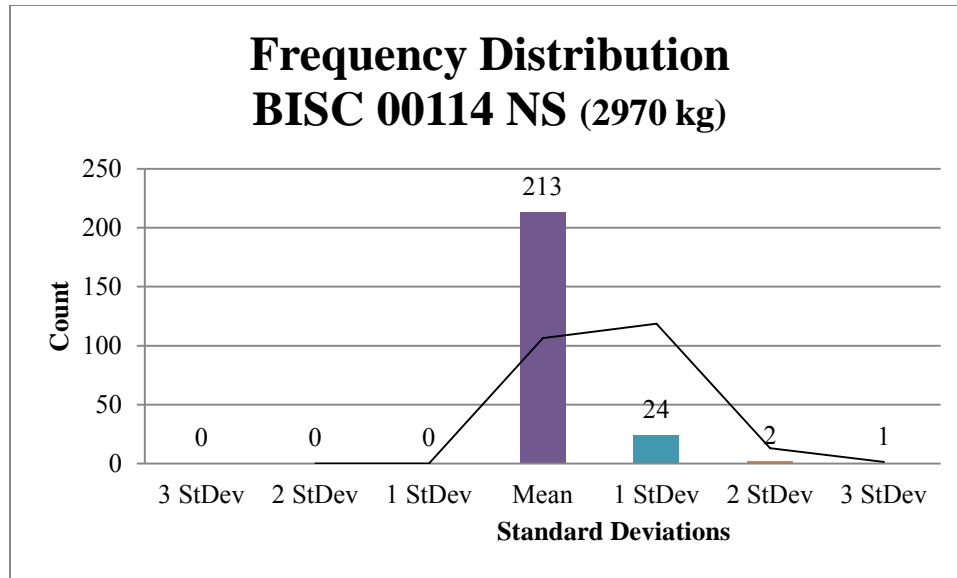
Figure IV-25. Frequency distribution for site BISC 00114 NS calculated at 2970 kg.

Table IV-49
Frequency distribution amounts per standard deviation for BISC 00114 NS calculated at 2970 kg.

Sort Method	Frequency
3 StDev	0
2 StDev	0
1 StDev	0
Mean	213
1 StDev	24
2 StDev	2
3 StDev	1

Table IV-50
Magnetic moment statistics for site BISC 00114 NS calculated at 2970 kg, sample size N=242, including the empirically derived magnetic moment per unit mass (σ) value. All σ units are $\frac{emu}{g}$.

Mean
64.261
Median
24.141
Standard Deviation
273.842
Range
3378.33
Empirical σ Value
24.141
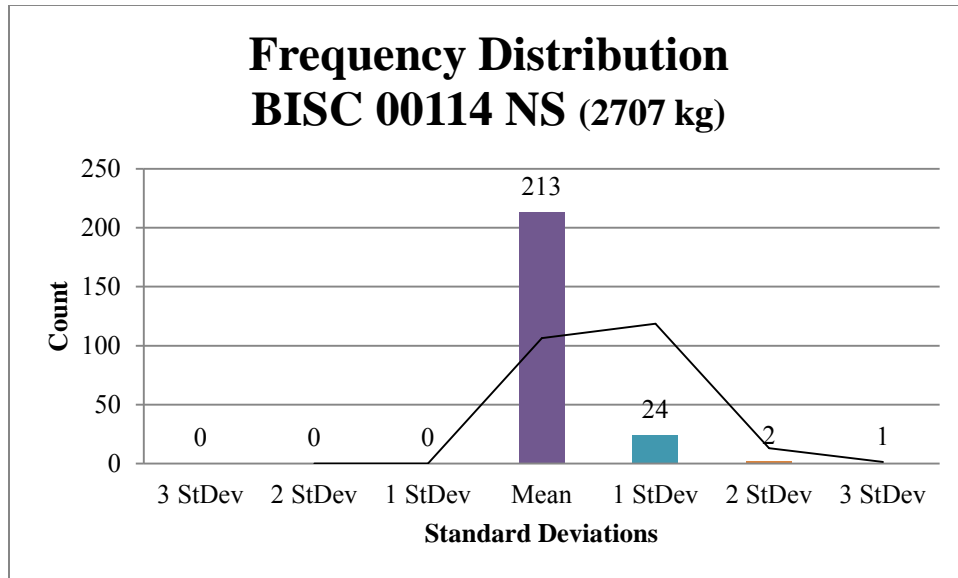
Figure IV-26. Frequency distribution for site BISC 00114 NS calculated at 2707 kg.

Table IV-51
Frequency distribution amounts per standard deviation for BISC 00114 NS calculated at 2707 kg.

Sort Method	Frequency
3 StDev	0
2 StDev	0
1 StDev	0
Mean	213
1 StDev	24
2 StDev	2
3 StDev	1

Table IV-52
Magnetic moment statistics for site BISC 00114 NS calculated at 2707 kg, sample size N=242, including the empirically derived magnetic moment per unit mass (σ) value. All σ units are $\frac{emu}{g}$.

Mean
70.506
Median
26.487
Standard Deviation
300.457
Range
3706.67
Empirical σ Value
26.487
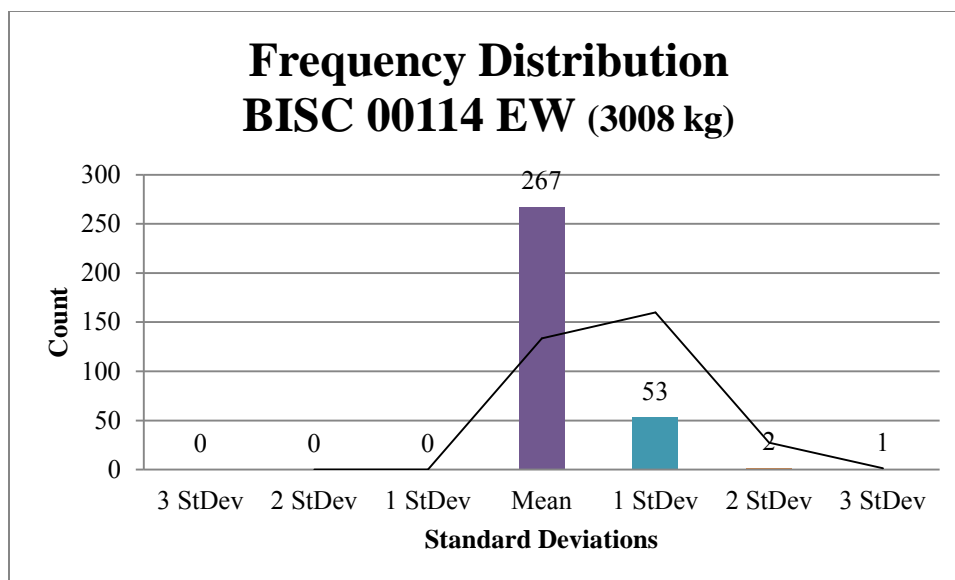
Figure IV-27. Frequency distribution for site BISC 00114 EW calculated at 3008 kg.

Table IV-53
Frequency distribution amounts per standard deviation for BISC 00114 EW calculated at 3008 kg.

Sort Method	Frequency
3 StDev	0
2 StDev	0
1 StDev	0
Mean	267
1 StDev	53
2 StDev	2
3 StDev	1

Table IV-54
Magnetic moment statistics for site BISC 00114 EW calculated at 3008 kg, sample size N=325, including the empirically derived magnetic moment per unit mass (σ) value. All σ units are $\frac{emu}{g}$.

Mean
67.502
Median
25.243
Standard Deviation
286.474
Range
3668.7
Empirical σ Value
25.243
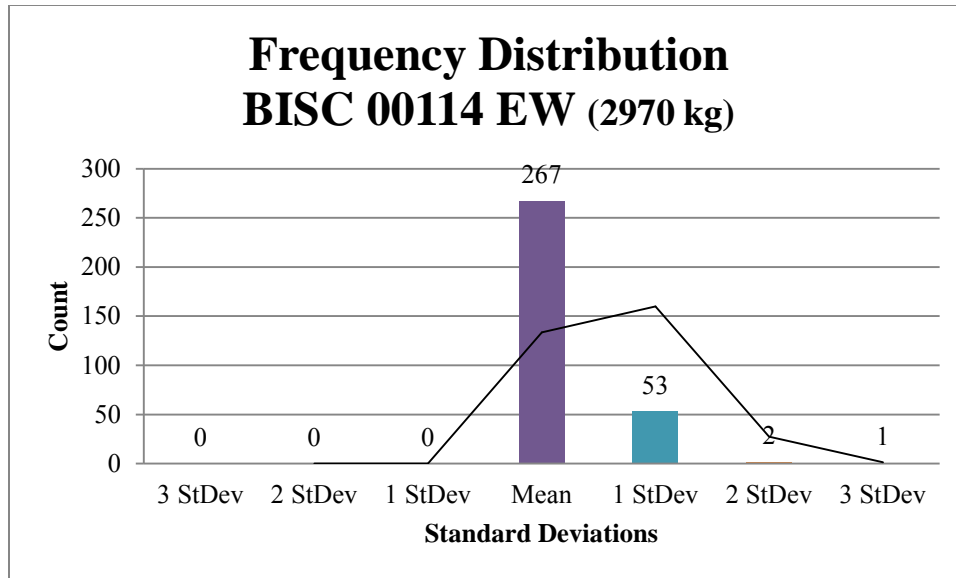
Figure IV-28. Frequency distribution for site BISC 00114 EW calculated at 2970 kg.

Table IV-55
Frequency distribution amounts per standard deviation for BISC 00114 EW calculated at 2970 kg.

Sort Method	Frequency
3 StDev	0
2 StDev	0
1 StDev	0
Mean	267
1 StDev	53
2 StDev	2
3 StDev	1

Table IV-56
Magnetic moment statistics for site BISC 00114 EW calculated at 2970 kg, sample size N=325, including the empirically derived magnetic moment per unit mass (σ) value. All σ units are $\frac{emu}{g}$.

Mean
68.359
Median
25.563
Standard Deviation
290.11
Range
3715.27
Empirical σ Value
25.563

Frequency Distribution
BISC 00114 EW (2707 kg)
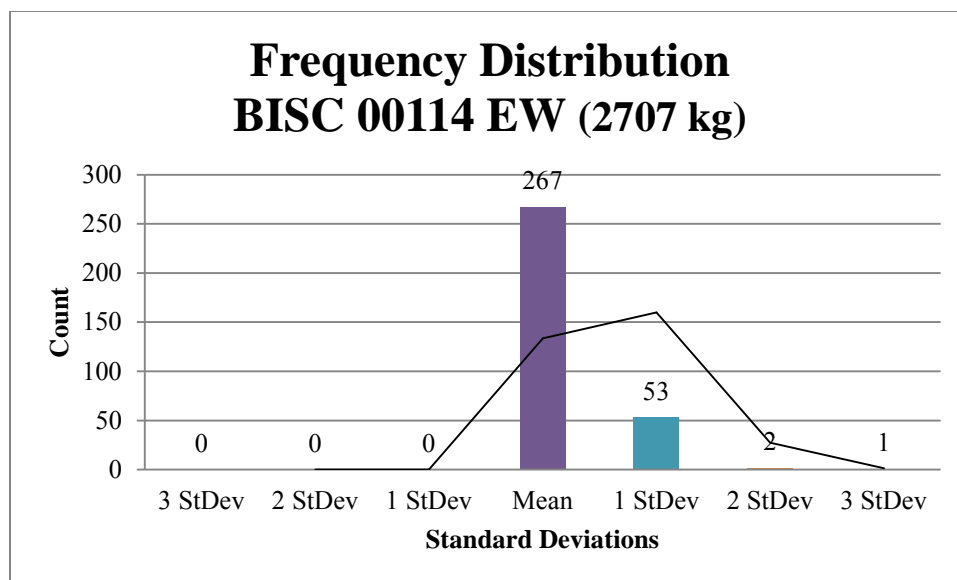
Figure IV-29. Frequency distribution for site BISC 00114 EW calculated at 2707 kg.

Table IV-57
Frequency distribution amounts per standard deviation for BISC 00114 EW calculated at 2707 kg.

Sort Method	Frequency
3 StDev	0
2 StDev	0
1 StDev	0
Mean	267
1 StDev	53
2 StDev	2
3 StDev	1

Table IV-58
Magnetic moment statistics for site BISC 00114 EW calculated at 2707 kg, sample size N=325, including the empirically derived magnetic moment per unit mass (σ) value. All σ units are $\frac{emu}{g}$.

Mean
75.003
Median
28.047
Standard Deviation
318.306
Range
4076.35
Empirical σ Value
28.047

BISC 00122
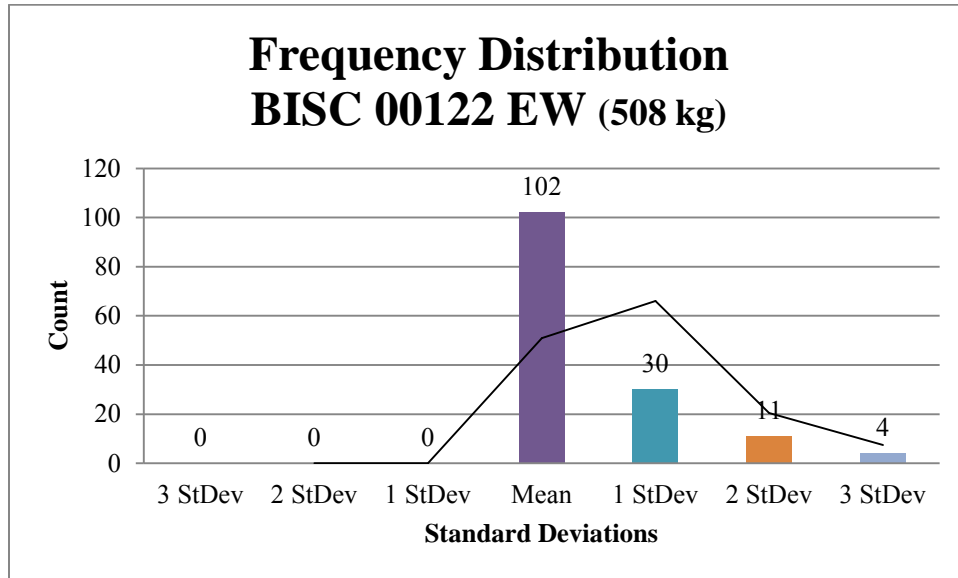
Figure IV-30. Frequency distribution for site BISC 00122 EW calculated at 508 kg.

Table IV-59
Frequency distribution amounts per standard deviation for BISC 00122 EW calculated at 508 kg.

Sort Method	Frequency
3 StDev	0
2 StDev	0
1 StDev	0
Mean	102
1 StDev	30
2 StDev	11
3 StDev	4

Table IV-60
Magnetic moment statistics for site BISC 00122 EW calculated at 508 kg, sample size N=150, including the empirically derived magnetic moment per unit mass (σ) value. All σ units are $\frac{emu}{g}$.

Mean
86.362
Median
27.569
Standard Deviation
121.043
Range
570.003
Empirical σ Value
27.569
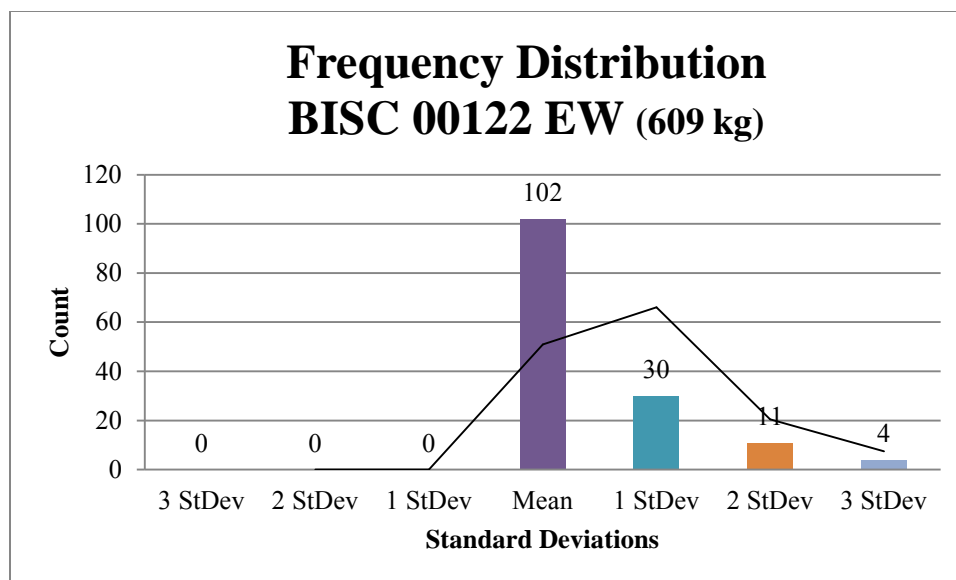
Figure IV-31. Frequency distribution for site BISC 00122 EW calculated at 609 kg.

Table IV-61
Frequency distribution amounts per standard deviation for BISC 00122 EW calculated at 609 kg.

Sort Method	Frequency
3 StDev	0
2 StDev	0
1 StDev	0
Mean	102
1 StDev	30
2 StDev	11
3 StDev	4

Table IV-62
Magnetic moment statistics for site BISC 00122 EW calculated at 609 kg, sample size N=150, including the empirically derived magnetic moment per unit mass (σ) value. All σ units are $\frac{emu}{g}$.

Mean
72.039
Median
22.997
Standard Deviation
100.969
Range
475.469
Empirical σ Value
22.997
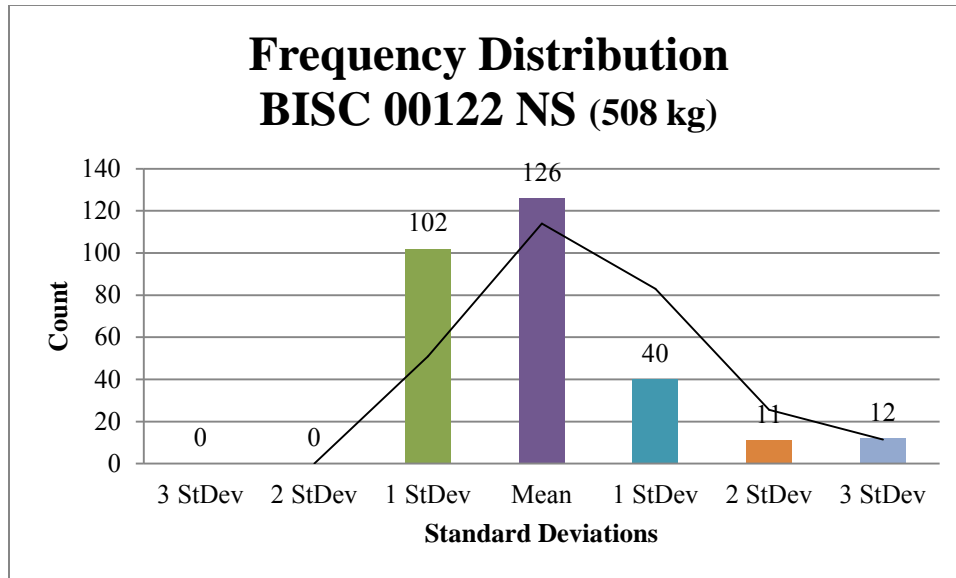
Figure IV-32. Frequency distribution for site BISC 00122 NS calculated at 508 kg.

Table IV-63
Frequency distribution amounts per standard deviation for BISC 00122 NS calculated at 508 kg.

Sort Method	Frequency
3 StDev	0
2 StDev	0
1 StDev	102
Mean	126
1 StDev	40
2 StDev	11
3 StDev	12

Table IV-64
Magnetic moment statistics for site BISC 00122 NS calculated at 508 kg, sample size N=150, including the empirically derived magnetic moment per unit mass (σ) value. All σ units are $\frac{emu}{g}$.

Mean
99.429
Median
58.15
Standard Deviation
85.66
Range
415.223
Empirical σ Value
58.15

Frequency Distribution
BISC 00122 NS (609 kg)
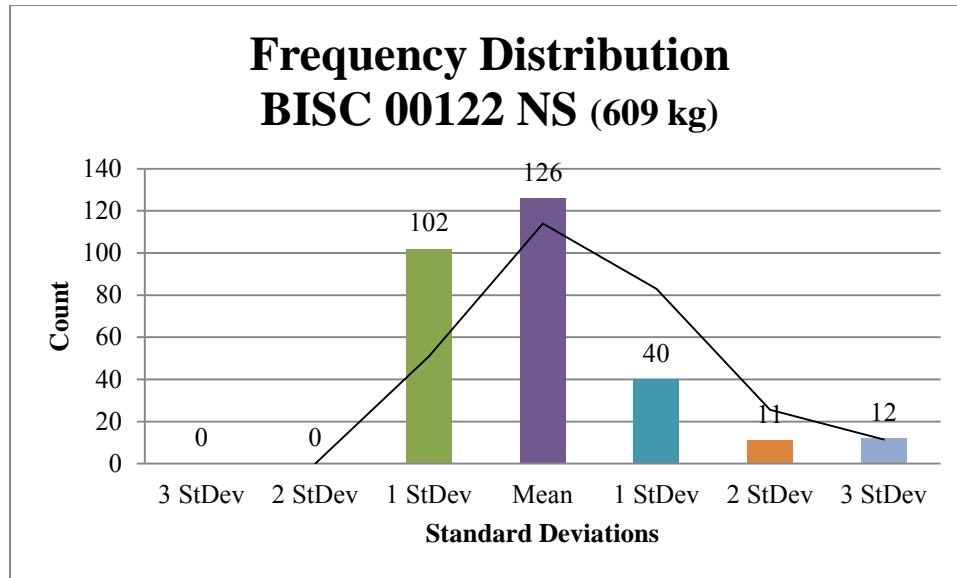
Figure IV-33. Frequency distribution for site BISC 00122 NS calculated at 609 kg.

Table IV-65
Frequency distribution amounts per standard deviation for BISC 00122 NS calculated at 609 kg.

Sort Method	Frequency
3 StDev	0
2 StDev	0
1 StDev	102
Mean	126
1 StDev	40
2 StDev	11
3 StDev	12

Table IV-66
Magnetic moment statistics for site BISC 00122 NS calculated at 609 kg, sample size N=150, including the empirically derived magnetic moment per unit mass (σ) value. All σ units are $\frac{emu}{g}$.

Mean
82.939
Median
48.506
Standard Deviation
71.453
Range
346.36
Empirical σ Value
48.506

BISC 00123
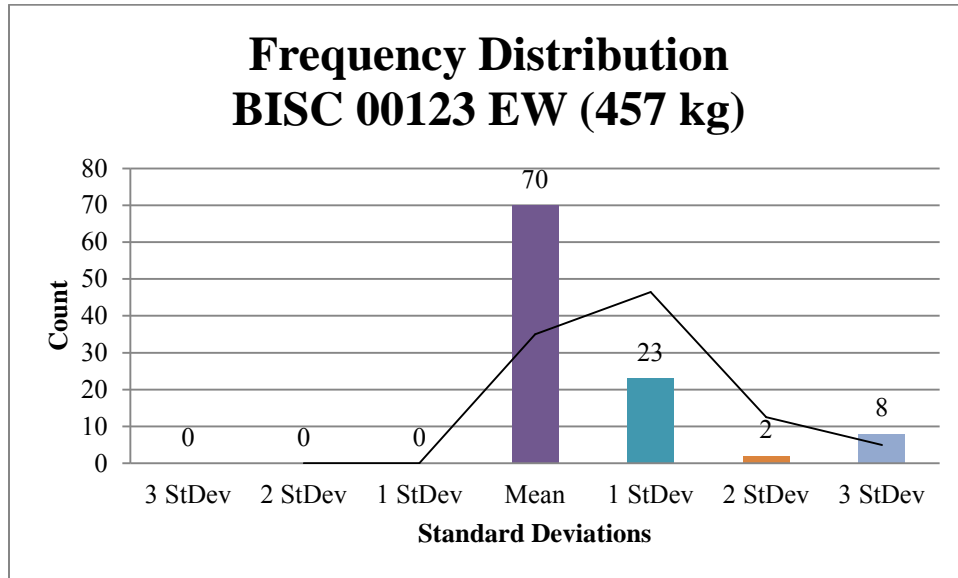
Figure IV-34. Frequency distribution for site BISC 00123 EW calculated at 457 kg.

Table IV-67
Frequency distribution amounts per standard deviation for BISC 00123 EW calculated at 457 kg.

Sort Method	Frequency
3 StDev	0
2 StDev	0
1 StDev	0
Mean	70
1 StDev	23
2 StDev	2
3 StDev	8

Table IV-68
Magnetic moment statistics for site BISC 00123 EW calculated at 457 kg, sample size N=104, including the empirically derived magnetic moment per unit mass (σ) value. All σ units are $\frac{emu}{g}$.

Mean
187.976
Median
84.288
Standard Deviation
261.768
Range
1015.638
Empirical σ Value
84.288

Frequency Distribution
BISC 00123 EW (762 kg)
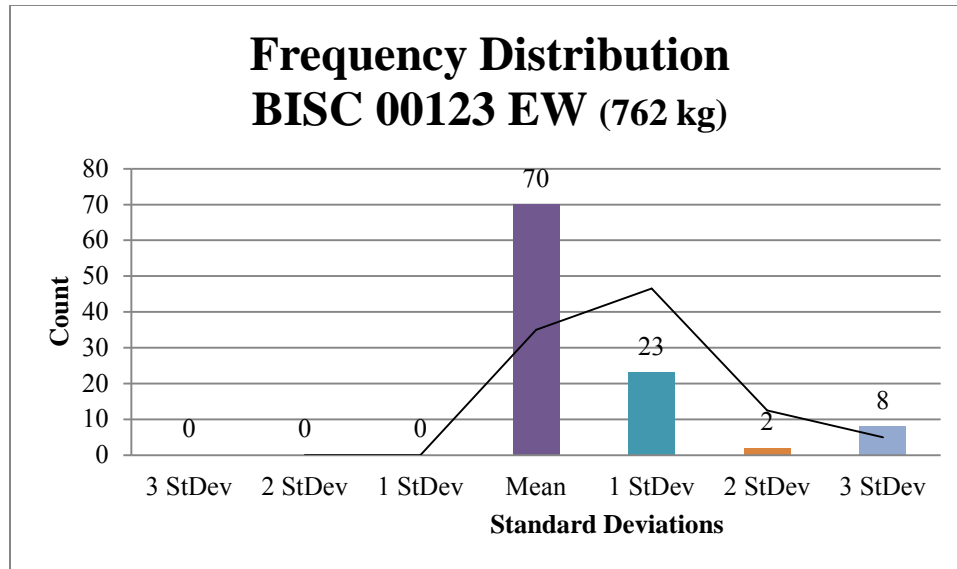
Figure IV-35. Frequency distribution for site BISC 00123 EW calculated at 762 kg.

Table IV-69
Frequency distribution amounts per standard deviation for BISC 00123 EW calculated at 762 kg.

Sort Method	Frequency
3 StDev	0
2 StDev	0
1 StDev	0
Mean	70
1 StDev	23
2 StDev	2
3 StDev	8

Table IV-70
Magnetic moment statistics for site BISC 00123 EW calculated at 762 kg, sample size N=104, including the empirically derived magnetic moment per unit mass (σ) value. All σ units are $\frac{emu}{g}$.

Mean
112.736
Median
50.549
Standard Deviation
156.992
Range
609.116
Empirical σ Value
50.549
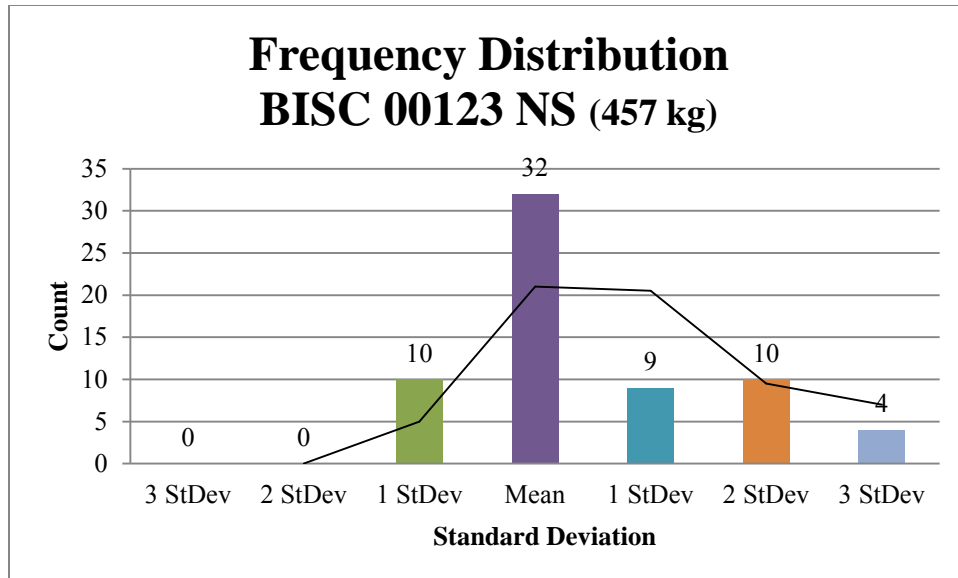
Figure IV-36. Frequency distribution for site BISC 00123 NS calculated at 457 kg.

Table IV-71
Frequency distribution amounts per standard deviation for BISC 00123 NS calculated at 457 kg.

Sort Method	Frequency
3 StDev	0
2 StDev	0
1 StDev	10
Mean	32
1 StDev	9
2 StDev	10
3 StDev	4

Table IV-72
**Magnetic moment statistics for site BISC 00123 NS calculated at 457 kg, sample size N=64, including the
empirically derived magnetic moment per unit mass (σ) value. All σ units are $\frac{emu}{g}$.**

Mean
48.73
Median
37.433
Standard Deviation
46.921
Range
182.825
Empirical σ Value
37.433

Frequency Distribution
BISC 00123 NS (762 kg)
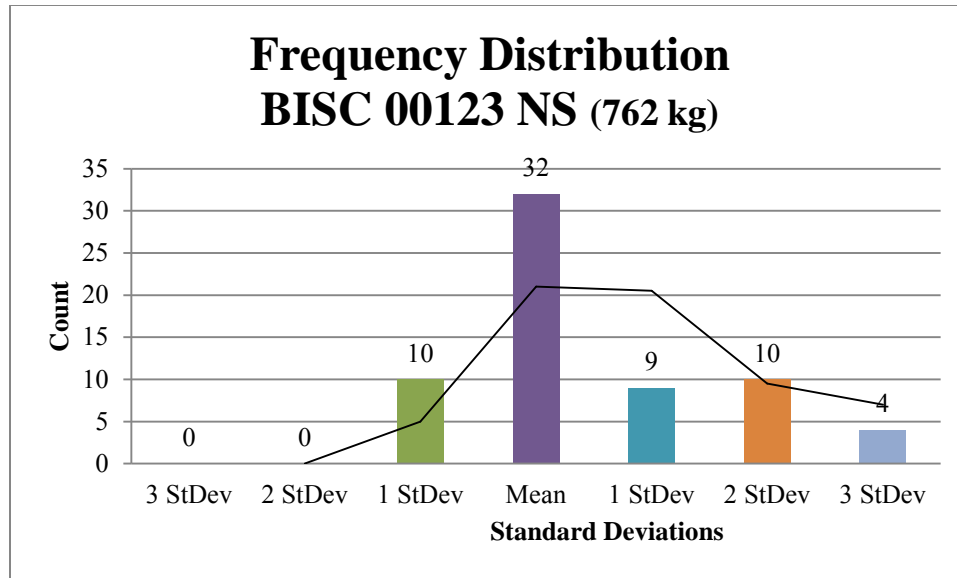
Figure IV-37. Frequency distribution for site BISC 00123 NS calculated at 762 kg.

Table IV-73
Frequency distribution amounts per standard deviation for BISC 00123 NS calculated at 762 kg.

Sort Method	Frequency
3 StDev	0
2 StDev	0
1 StDev	10
Mean	32
1 StDev	9
2 StDev	10
3 StDev	4

Table IV-74
Magnetic moment statistics for site BISC 00123 NS calculated at 762 kg, sample size N=64, including the empirically derived magnetic moment per unit mass (σ) value. All σ units are $\frac{emu}{g}$.

Mean
29.225
Median
22.45
Standard Deviation
28.14
Range
109.648
Empirical σ Value
22.45

BISC 00124
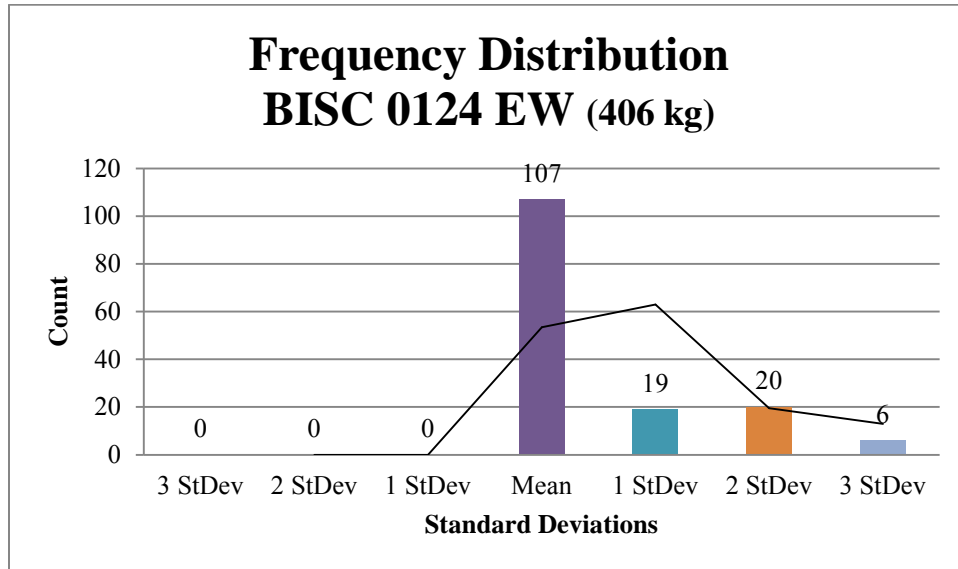
Figure IV-38. Frequency distribution for site BISC 00124 EW calculated at 406 kg.

Table IV-75

Frequency distribution amounts per standard deviation for BISC 00124 EW calculated at 406 kg.

Sort Method	Frequency
3 StDev	0
2 StDev	0
1 StDev	0
Mean	107
1 StDev	19
2 StDev	20
3 StDev	6

Table IV-76

Magnetic moment statistics for site BISC 00124 EW calculated at 406 kg, sample size N=153, including the empirically derived magnetic moment per unit mass (σ) value. All σ units are $\frac{emu}{g}$.

Mean
33.045
Median
19.54
Standard Deviation
33.887
Range
139.963
Empirical σ Value
19.54

Frequency Distribution
BISC 00124 EW (559 kg)
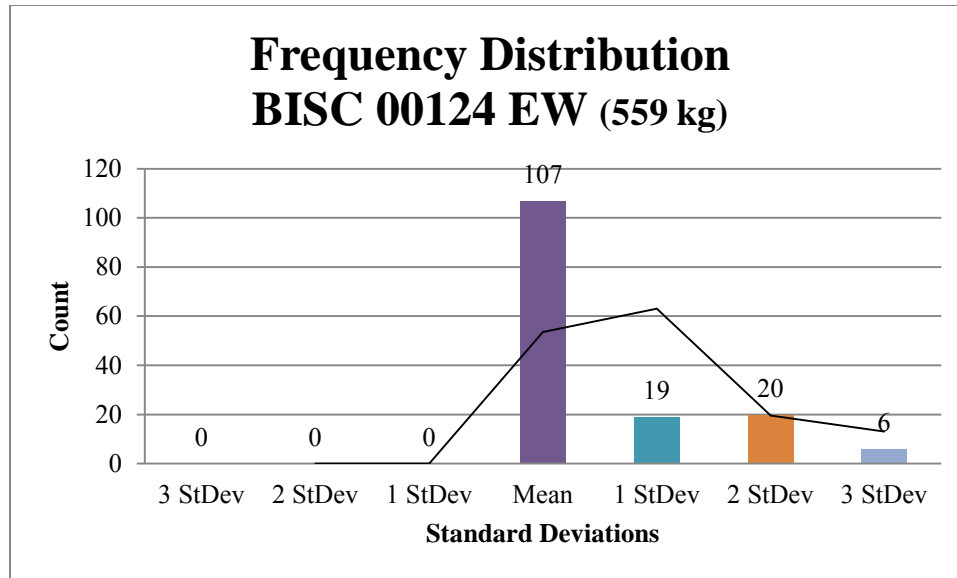
Figure IV-39. Frequency distribution for site BISC 00124 EW calculated at 559 kg.

Table IV-77
Frequency distribution amounts per standard deviation for BISC 00124 EW calculated at 559 kg.

Sort Method	Frequency
3 StDev	0
2 StDev	0
1 StDev	0
Mean	107
1 StDev	19
2 StDev	20
3 StDev	6

Table IV-78
Magnetic moment statistics for site BISC 00124 EW calculated at 559 kg, sample size N=153, including the empirically derived magnetic moment per unit mass (σ) value. All σ units are $\frac{emu}{g}$.

Mean
24.112
Median
14.346
Standard Deviation
24.654
Range
101.828
Empirical σ Value
14.346
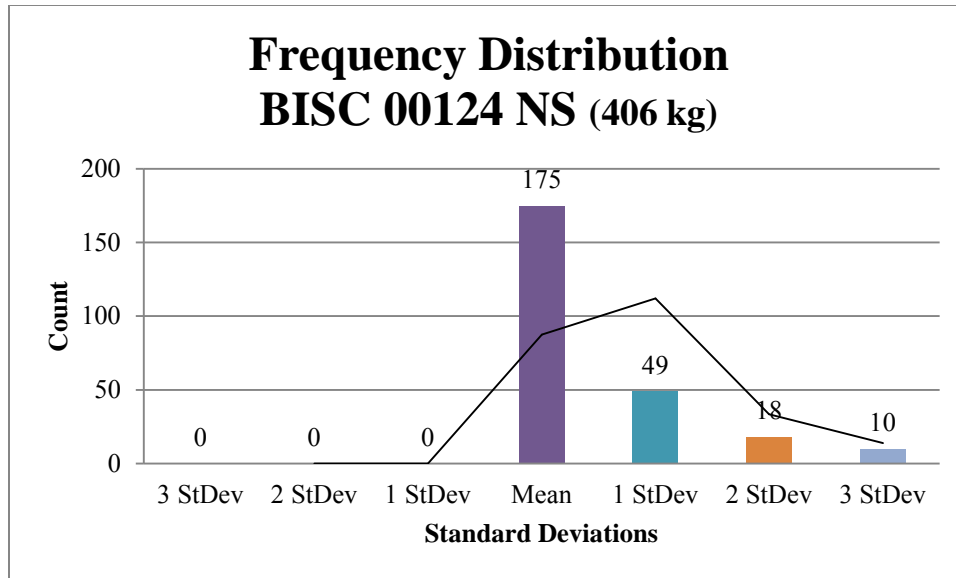
Figure IV-40. Frequency distribution for site BISC 00124 NS calculated at 406 kg.

Table IV-79
Frequency distribution amounts per standard deviation for BISC 00124 NS calculated at 406 kg.

Sort Method	Frequency
3 StDev	0
2 StDev	0
1 StDev	0
Mean	175
1 StDev	49
2 StDev	18
3 StDev	10

Table IV-80
Magnetic moment statistics for site BISC 00124 NS calculated at 406 kg, sample size N=258, including the empirically derived magnetic moment per unit mass (σ) value. All σ units are $\frac{emu}{g}$.

Mean	
71.8	
Median	
30.46	
Standard Deviation	
89.601	
Range	
492.386	
Empirical σ Value	
30.46	

Frequency Distribution
BISC 00124 NS (559 kg)
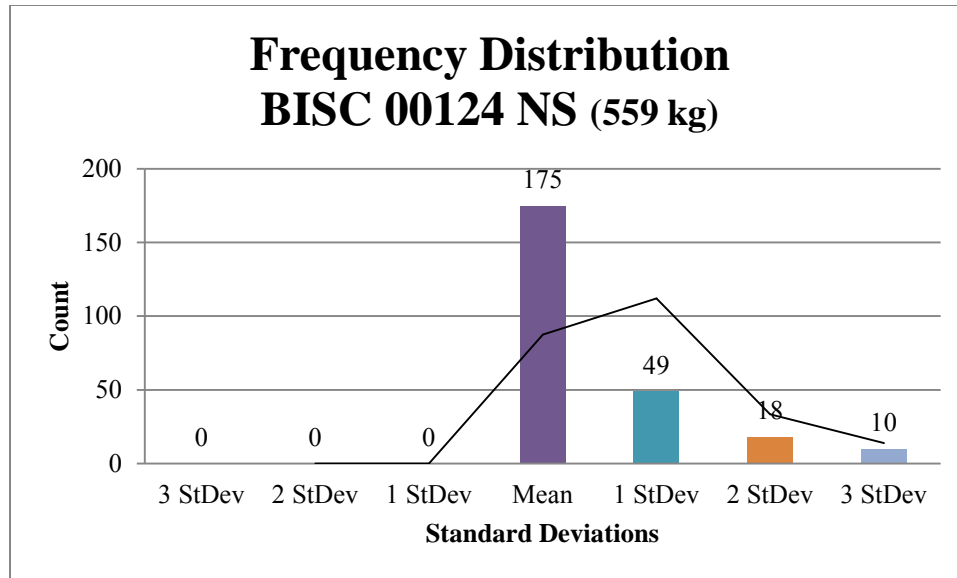
Figure IV-41. Frequency distribution for site BISC 00124 NS calculated at 559 kg.

Table IV-81
Frequency distribution amounts per standard deviation for BISC 00124 NS calculated at 559 kg.

Sort Method	Frequency
3 StDev	0
2 StDev	0
1 StDev	0
Mean	175
1 StDev	49
2 StDev	18
3 StDev	10

Table IV-82
Magnetic moment statistics for site BISC 00124 NS calculated at 559 kg, sample size N=258, including the empirically derived magnetic moment per unit mass (σ) value. All σ units are $\frac{emu}{g}$.

Mean
52.148
Median
22.123
Standard Deviation
65.077
Range
357.618
Empirical σ Value
22.123

ALMIRANTE
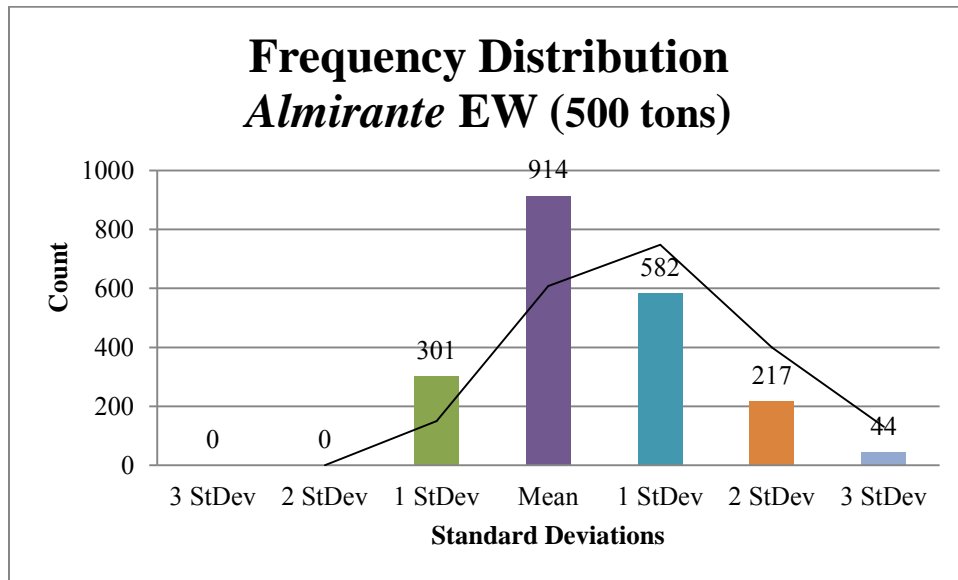
Figure IV-42. Frequency distribution for site *Almirante* EW calculated at 500 tons (453,592 kg).

Table IV-83
Frequency distribution amounts per standard deviation for *Almirante* EW calculated at 500 tons (453,592 kg).

Sort Method	Frequency
3 StDev	0
2 StDev	0
1 StDev	301
Mean	914
1 StDev	582
2 StDev	217
3 StDev	44

Table IV-84
Magnetic moment statistics for site *Almirante* EW calculated at 500 tons (453,592 kg), sample size N=2099, including the empirically derived magnetic moment per unit mass (σ) value. All σ units are $\frac{emu}{g}$.

Mean
79.173
Median
69.052
Standard Deviation
62.735
Range
374.381
Empirical σ Value
69.052
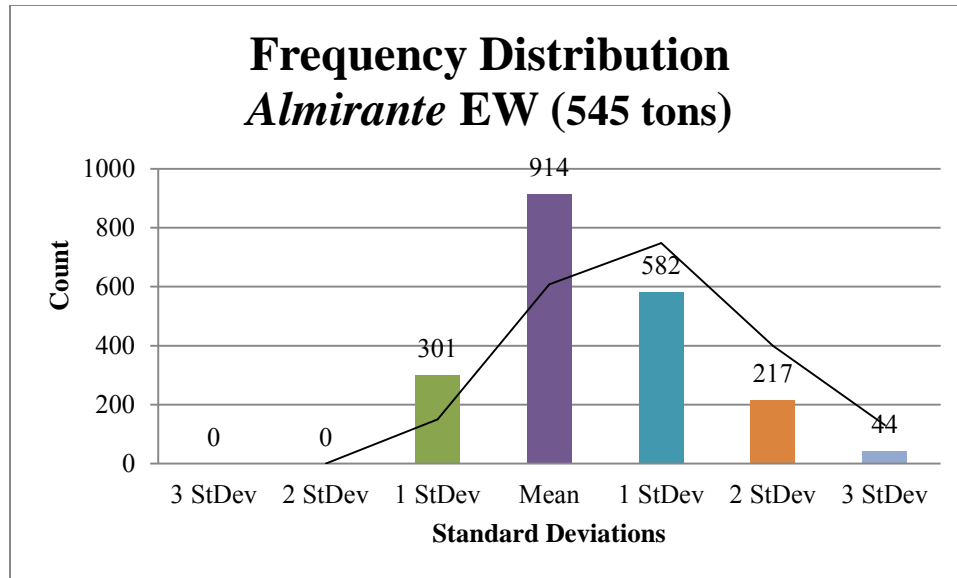
Figure IV-43. Frequency distribution for site *Almirante* EW calculated at 545 tons (553,746 kg).

Table IV-85
Frequency distribution amounts per standard deviation for *Almirante* EW calculated at 545 tons (553,746 kg).

Sort Method	Frequency
3 StDev	0
2 StDev	0
1 StDev	301
Mean	914
1 StDev	582
2 StDev	217
3 StDev	44

Table IV-86
Magnetic moment statistics for site *Almirante* EW calculated at 545 tons (553,746 kg), sample size N=2099, including the empirically derived magnetic moment per unit mass (σ) value. All σ units are $\frac{emu}{g}$.

Mean
64.853
Median
56.562
Standard Deviation
51.388
Range
306.668
Empirical σ Value
56.562
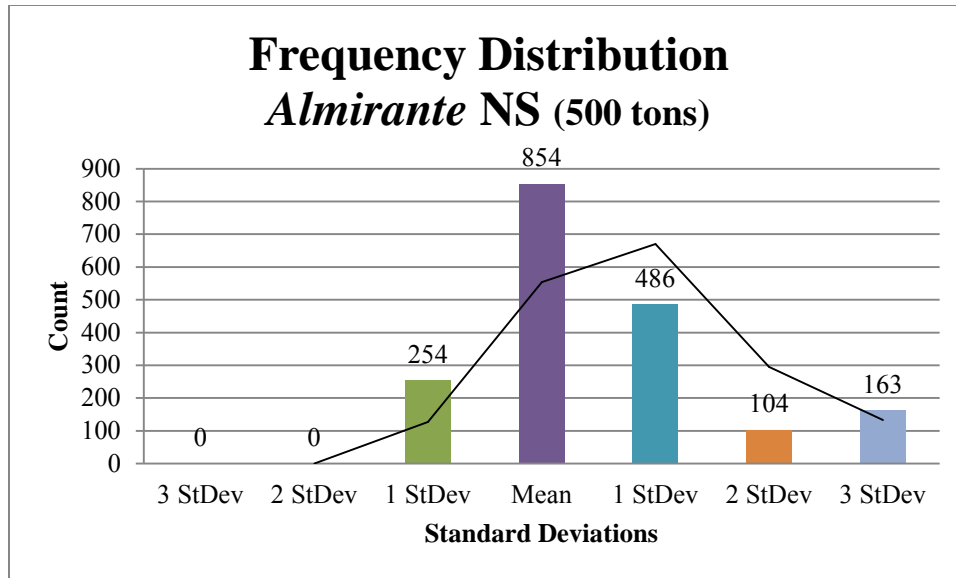
Figure IV-44. Frequency distribution for site *Almirante* NS calculated at 500 tons (453,592 kg).

Table IV-87
Frequency distribution amounts per standard deviation for *Almirante* NS calculated at 500 tons (453,592 kg).

Sort Method	Frequency
3 StDev	0
2 StDev	0
1 StDev	254
Mean	854
1 StDev	486
2 StDev	104
3 StDev	163

Table IV-88
Magnetic moment statistics for site *Almirante* NS calculated at 500 tons (453,592 kg), sample size N=1860, including the empirically derived magnetic moment per unit mass (σ) value. All σ units are $\frac{emu}{g}$.

Mean
74.696
Median
63.32
Standard Deviation
60.265
Range
246.906
Empirical σ Value
63.32
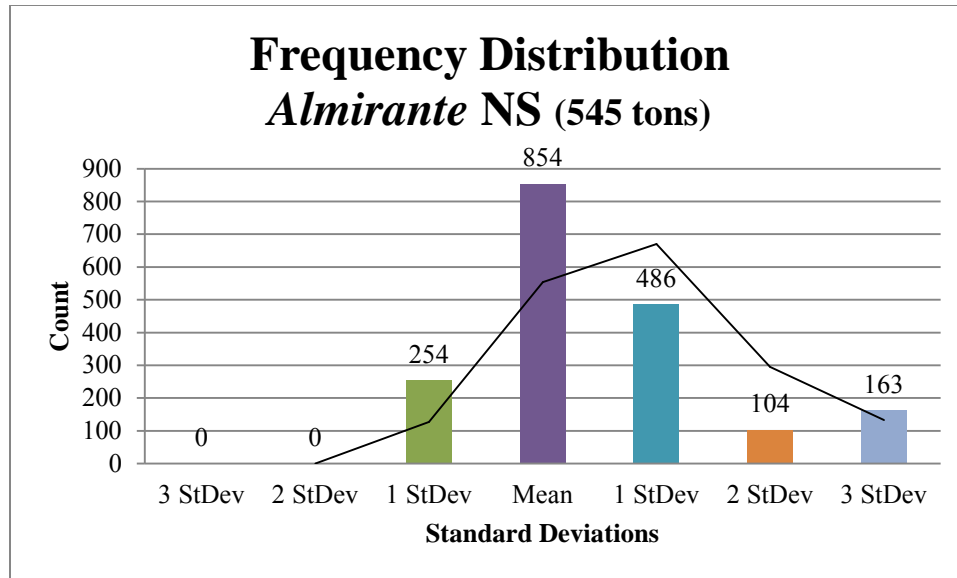
Figure IV-45. Frequency distribution for site *Almirante* NS calculated at 545 tons (553,746 kg).

Table IV-89
Frequency distribution amounts per standard deviation for *Almirante* NS calculated at 545 tons (553,746 kg).

Sort Method	Frequency
3 StDev	0
2 StDev	0
1 StDev	254
Mean	854
1 StDev	486
2 StDev	104
3 StDev	163

Table IV-90
Magnetic moment statistics for site *Almirante* NS calculated at 545 tons (553,746 kg), sample size N=1860, including the empirically derived magnetic moment per unit mass (σ) value. All σ units are $\frac{emu}{g}$.

Mean
61.186
Median
51.867
Standard Deviation
49.365
Range
202.249
Empirical σ Value
51.867

BLUE FIRE
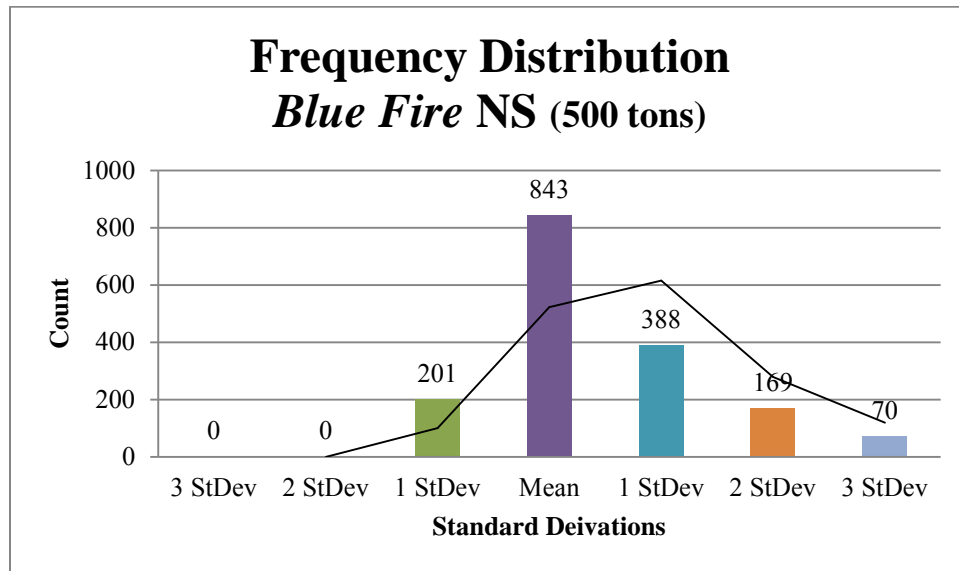
Figure IV-46. Frequency distribution for site *Blue Fire* NS calculated at 500 tons (453,592 kg).

Table IV-91
Frequency distribution amounts per standard deviation for *Blue Fire* NS calculated at 500 tons (453,592 kg).

Sort Method	Frequency
3 StDev	0
2 StDev	0
1 StDev	201
Mean	843
1 StDev	388
2 StDev	169
3 StDev	70

Table IV-92
Magnetic moment statistics for site *Blue Fire* NS calculated at 500 tons (453,592 kg), sample size N=1699, including the empirically derived magnetic moment per unit mass (σ) value. All σ units are $\frac{emu}{g}$.

Mean
56.225
Median
42.279
Standard Deviation
46.843
Range
210.786
Empirical σ Value
42.279
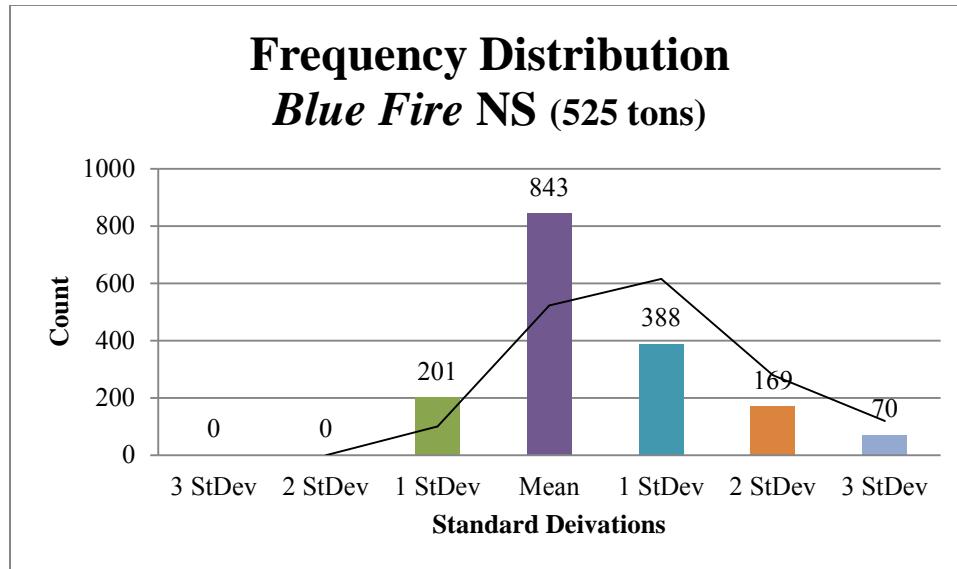
Figure IV-47. Frequency distribution for site *Blue Fire* NS calculated at 525 tons (476,272 kg).

Table IV-93
Frequency distribution amounts per standard deviation for *Blue Fire* NS calculated at 525 tons (476,272 kg).

Sort Method	Frequency
3 StDev	0
2 StDev	0
1 StDev	202
Mean	842
1 StDev	388
2 StDev	169
3 StDev	70

Table IV-94
Magnetic moment statistics for site *Blue Fire* NS calculated at 525 tons (476,272 kg), sample size N=1699, including the empirically derived magnetic moment per unit mass (σ) value. All σ units are $\frac{emu}{g}$.

Mean
53.548
Median
40.266
Standard Deviation
44.605
Range
200.748
Empirical σ Value
40.266
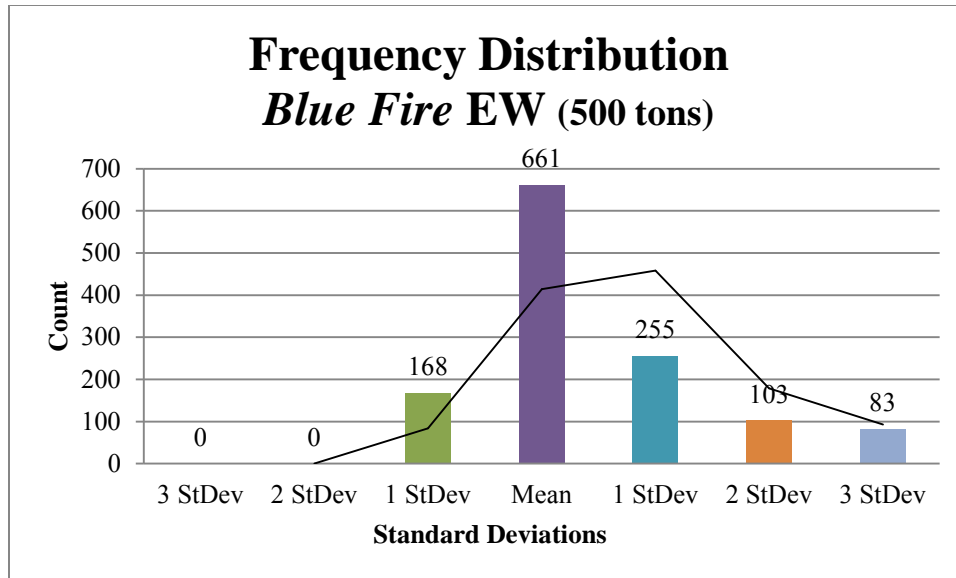
Figure IV-48. Frequency distribution for site *Blue Fire* EW calculated at 500 tons (453,592 kg).

Table IV-95
Frequency distribution amounts per standard deviation for *Blue Fire* EW calculated at 500 tons (453,592 kg).

Sort Method	Frequency
3 StDev	0
2 StDev	0
1 StDev	168
Mean	661
1 StDev	255
2 StDev	103
3 StDev	83

Table IV-96
Magnetic moment statistics for site *Blue Fire* EW calculated at 500 tons (453,592 kg), sample size N=1280, including the empirically derived magnetic moment per unit mass (σ) value. All σ units are $\frac{emu}{g}$.

Mean
65.026
Median
50.329
Standard Deviation
52.386
Range
238.819
Empirical σ Value
50.329
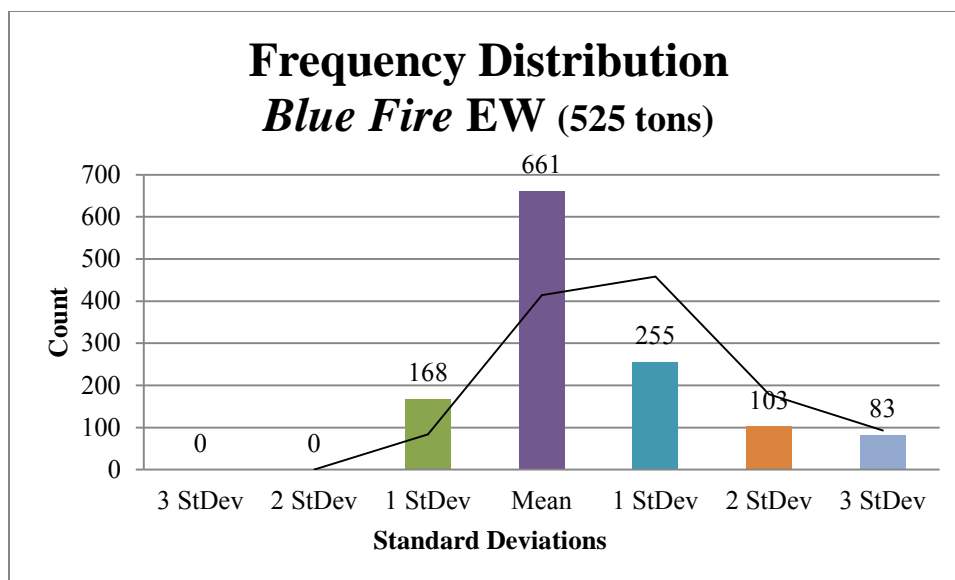
Figure IV-49. Frequency distribution for site *Blue Fire* EW calculated at 525 tons (476,272 kg).

Table IV-97
Frequency distribution amounts per standard deviation for *Blue Fire* EW calculated at 525 tons (476,272 kg).

Sort Method	Frequency
3 StDev	0
2 StDev	0
1 StDev	168
Mean	661
1 StDev	255
2 StDev	103
3 StDev	83

Table IV-98
Magnetic moment statistics for site *Blue Fire* EW calculated at 525 tons (476,272 kg), sample size N=1280, including the empirically derived magnetic moment per unit mass (σ) value. All σ units are $\frac{emu}{g}$.

Mean
61.929
Median
47.933
Standard Deviation
49.887
Range
227.446
Empirical σ Value
47.993

ST ANNE D'AURAY
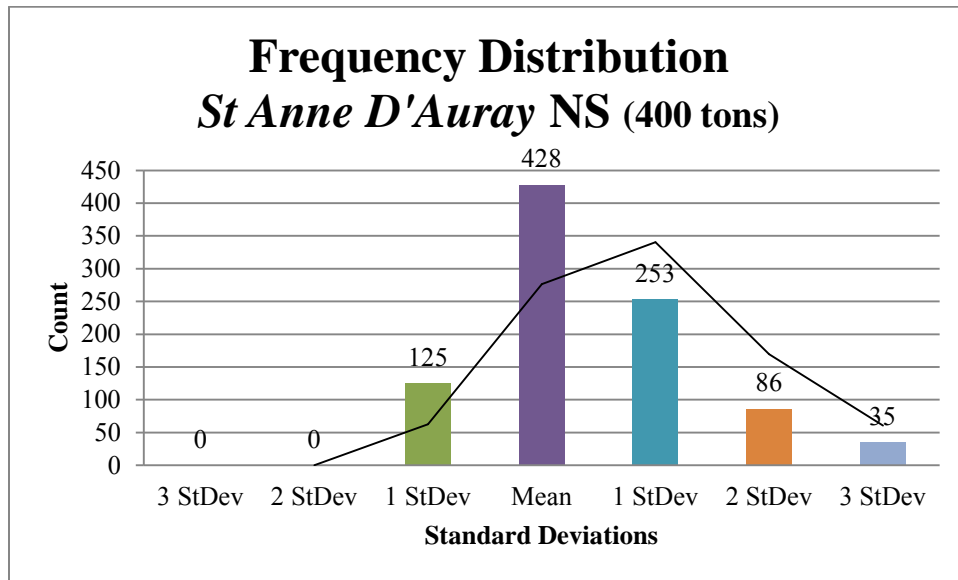
Figure IV-50. Frequency distribution for site *St. Anne D'Auray* NS calculated at 400 tons (362,874 kg).

Table IV-99
Frequency distribution amounts per standard deviation for *St. Anne D'Auray* NS calculated at 400 tons (362,874 kg).

Sort Method	Frequency
3 StDev	0
2 StDev	0
1 StDev	125
Mean	428
1 StDev	253
2 StDev	86
3 StDev	35

Table IV-100
Magnetic moment statistics for site *St. Anne D'Auray* NS calculated at 400 tons (362,874 kg), sample size N=935, including the empirically derived magnetic moment per unit mass (σ) value. All σ units are $\frac{emu}{g}$.

Mean
21.787
Median
17.452
Standard Deviation
16.735
Range
120.434
Empirical σ Value
17.452

Frequency Distribution
St Anne D'Auray NS (350 tons)
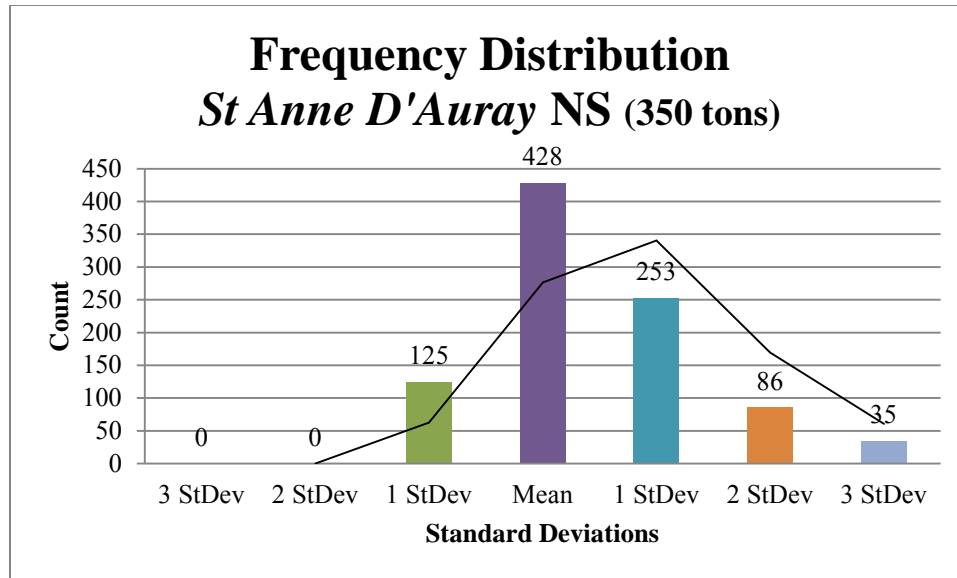
Figure IV-51. Frequency distribution for site *St. Anne D'Auray* NS calculated at 350 tons (317,515 kg).

Table IV-101
Frequency distribution amounts per standard deviation for *St. Anne D'Auray* NS calculated at 350 tons (317,515 kg).

Sort Method	Frequency
3 StDev	0
2 StDev	0
1 StDev	125
Mean	428
1 StDev	253
2 StDev	86
3 StDev	35

Table IV-102
Magnetic moment statistics for site *St. Anne D'Auray* NS calculated at 350 tons (317,515 kg), sample size N=935, including the empirically derived magnetic moment per unit mass (σ) value. All σ units are $\frac{emu}{g}$.

Mean
24.9
Median
19.946
Standard Deviation
19.125
Range
137.639
Empirical σ Value
19.946
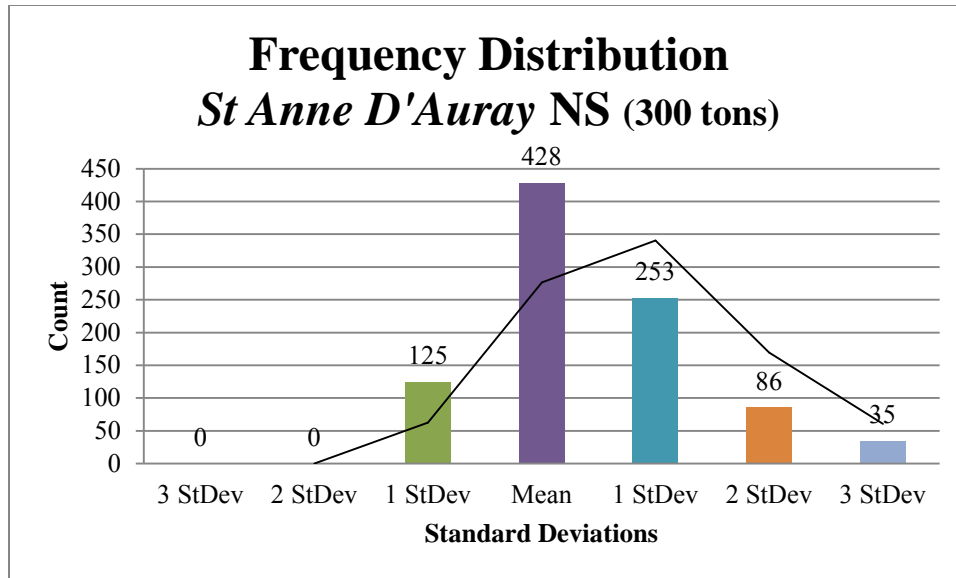
Figure IV-52. Frequency distribution for site *St. Anne D'Auray* NS calculated at 300 tons (272,155 kg).

Table IV-103
Frequency distribution amounts per standard deviation for *St. Anne D'Auray* NS calculated at 300 tons (272,155 kg).

Sort Method	Frequency
3 StDev	0
2 StDev	0
1 StDev	125
Mean	428
1 StDev	253
2 StDev	86
3 StDev	35

Table IV-104
Magnetic moment statistics for site *St. Anne D'Auray* NS calculated at 300 tons (272,155 kg), sample size N=935, including the empirically derived magnetic moment per unit mass (σ) value. All σ units are $\frac{emu}{g}$.

Mean
29.05
Median
23.27
Standard Deviation
22.313
Range
160.579
Empirical σ Value
23.27
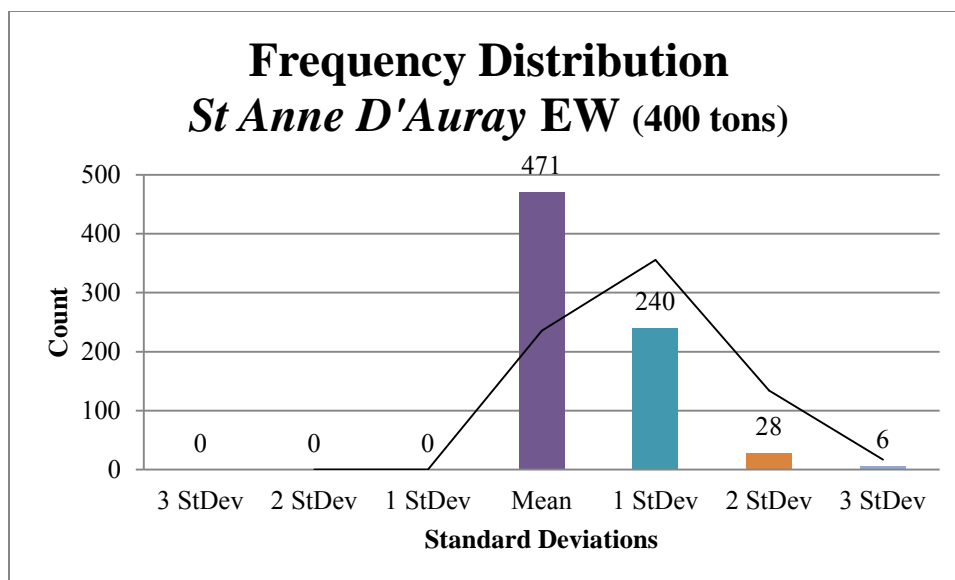
Figure IV-53. Frequency distribution for site *St. Anne D'Auray* EW calculated at 400 tons (362,874 kg).

Table IV-105
Frequency distribution amounts per standard deviation for *St. Anne D'Auray* EW calculated at 400 tons (362,874 kg).

Sort Method	Frequency
3 StDev	0
2 StDev	0
1 StDev	0
Mean	471
1 StDev	240
2 StDev	28
3 StDev	6

Table IV-106
Magnetic moment statistics for site *St. Anne D'Auray* EW calculated at 400 tons (362,874 kg), sample size N=764, including the empirically derived magnetic moment per unit mass (σ) value. All σ units are $\frac{emu}{g}$.

Mean
21.055
Median
14.984
Standard Deviation
22.667
Range
157.713
Empirical σ Value
14.984
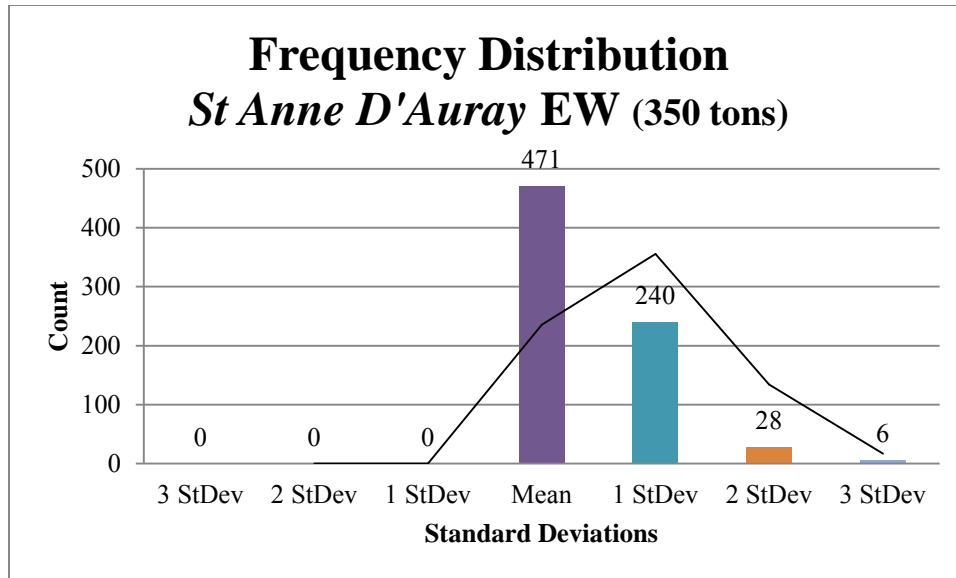
Figure IV-54. Frequency distribution for site *St. Anne D'Auray* EW calculated at 350 tons (317,515 kg).

Table IV-107
Frequency distribution amounts per standard deviation for *St. Anne D'Auray* EW calculated at 350 tons (317,515 kg).

Sort Method	Frequency
3 StDev	0
2 StDev	0
1 StDev	0
Mean	471
1 StDev	240
2 StDev	28
3 StDev	6

Table IV-108
Magnetic moment statistics for site *St. Anne D'Auray* EW calculated at 350 tons (317,515 kg), sample size N=764, including the empirically derived magnetic moment per unit mass (σ) value. All σ units are $\frac{emu}{g}$.

Mean
24.063
Median
17.125
Standard Deviation
25.905
Range
180.243
Empirical σ Value
17.125

Frequency Distribution
St Anne D'Auray EW (300 tons)
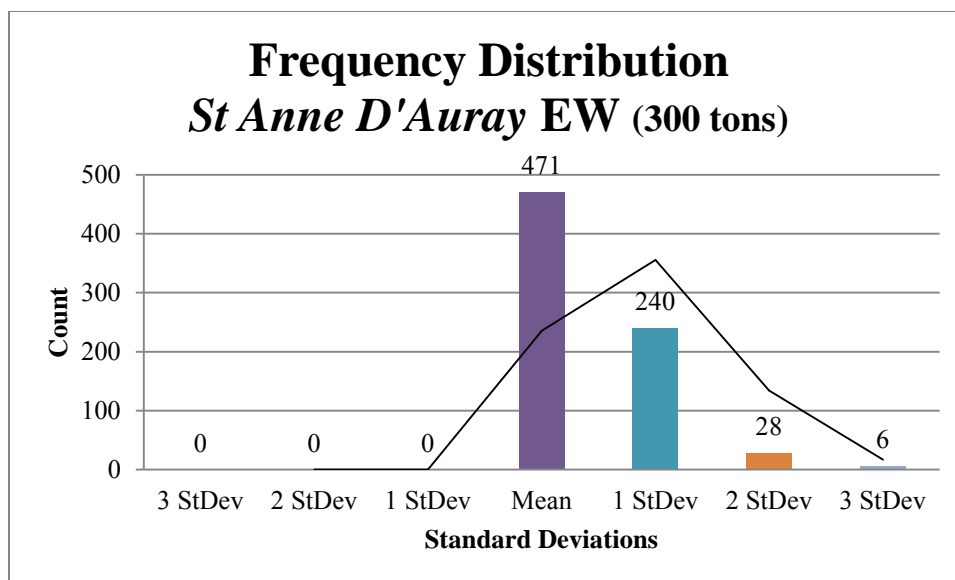
Figure IV-55. Frequency distribution for site *St. Anne D'Auray* EW calculated at 300 tons (272,155 kg).

Table IV-109
Frequency distribution amounts per standard deviation for *St. Anne D'Auray* EW calculated at 300 tons (272,155 kg).

Sort Method	Frequency
3 StDev	0
2 StDev	0
1 StDev	0
Mean	471
1 StDev	240
2 StDev	28
3 StDev	6

Table IV-110
Magnetic moment statistics for site *St. Anne D'Auray* EW calculated at 300 tons (272,155 kg), sample size N=764, including the empirically derived magnetic moment per unit mass (σ) value. All σ units are $\frac{emu}{g}$.

Mean
28.074
Median
19.979
Standard Deviation
30.223
Range
210.284
Empirical σ Value
19.979

DREDGE FLOAT
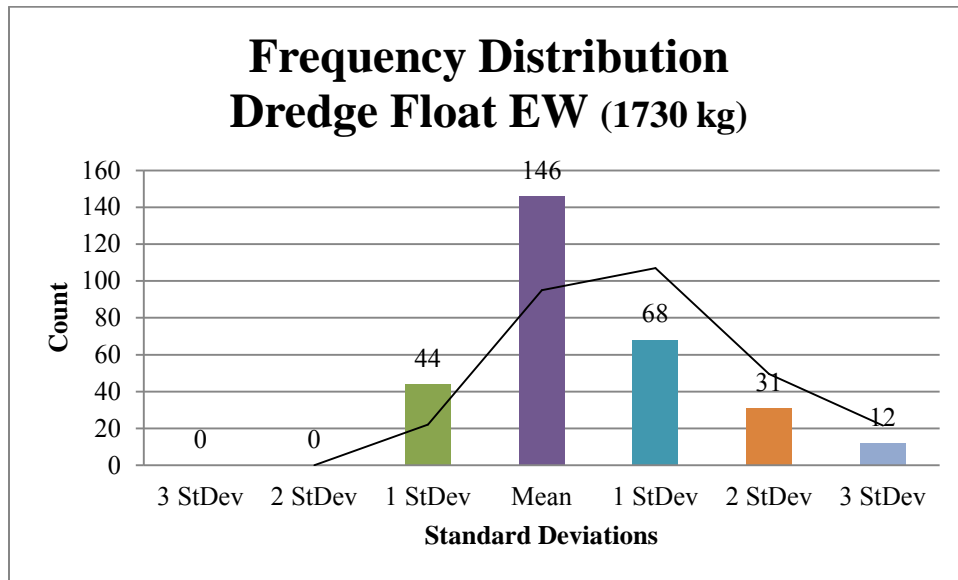
Figure IV-56. Frequency distribution for site Dredge Float EW calculated at1730kg.

Table IV-111
Frequency distribution amounts per standard deviation for Dredge Float EW calculated at1730 kg.

Sort Method	Frequency
3 StDev	0
2 StDev	0
1 StDev	44
Mean	146
1 StDev	68
2 StDev	31
3 StDev	12

Table IV-112
Magnetic moment statistics for site Dredge Float EW calculated at 1730 kg, sample size N=305, including the empirically derived magnetic moment per unit mass (σ) value. All σ units are $\frac{emu}{g}$.

Mean
63.2619
Median
50.042
Standard Deviation
50.504
Range
237.162
Empirical σ Value
50.042

Frequency Distribution
Dredge Float EW (1999 kg)
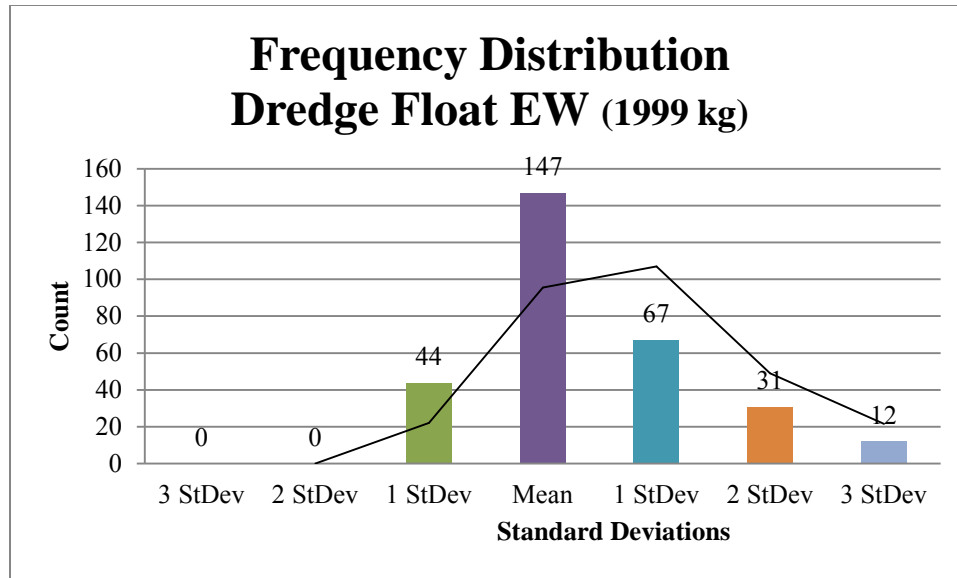
Figure IV-57. Frequency distribution for site Dredge Float EW calculated at 1999 kg.

Table IV-113
Frequency distribution amounts per standard deviation for Dredge Float EW calculated at 1999 kg.

Sort Method	Frequency
3 StDev	0
2 StDev	0
1 StDev	44
Mean	147
1 StDev	67
2 StDev	31
3 StDev	12

Table IV-114
Magnetic moment statistics for site Dredge Float EW calculated at 1999 kg, sample size N=305, including the empirically derived magnetic moment per unit mass (σ) value. All σ units are $\frac{emu}{g}$.

Mean
54.537
Median
42.921
Standard Deviation
43.718
Range
205.248
Empirical σ Value
42.921

Frequency Distribution
Dredge Float NS (1730 kg)
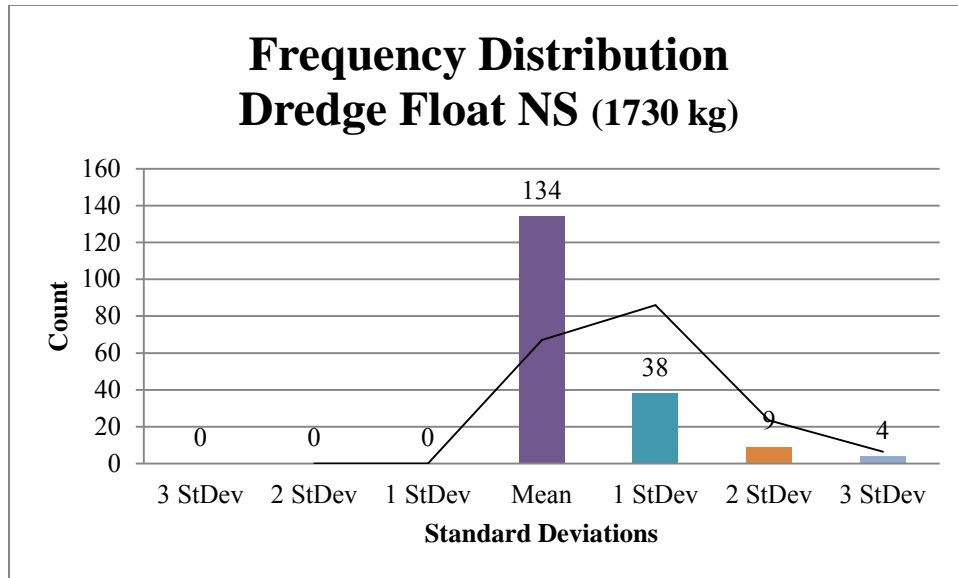
Figure IV-58. Frequency distribution for site Dredge Float NS calculated at1730 kg.

Table IV-115
Frequency distribution amounts per standard deviation for Dredge Float NS calculated at 1730 kg.

Sort Method	Frequency
3 StDev	0
2 StDev	0
1 StDev	0
Mean	134
1 StDev	38
2 StDev	9
3 StDev	4

Table IV-116
Magnetic moment statistics for site Dredge Float NS calculated at 1730 kg, sample size N=305, including the empirically derived magnetic moment per unit mass (σ) value. All σ units are $\frac{emu}{g}$.

Mean
69.105
Median
48.132
Standard Deviation
82.247
Range
791.843
Empirical σ Value
48.132
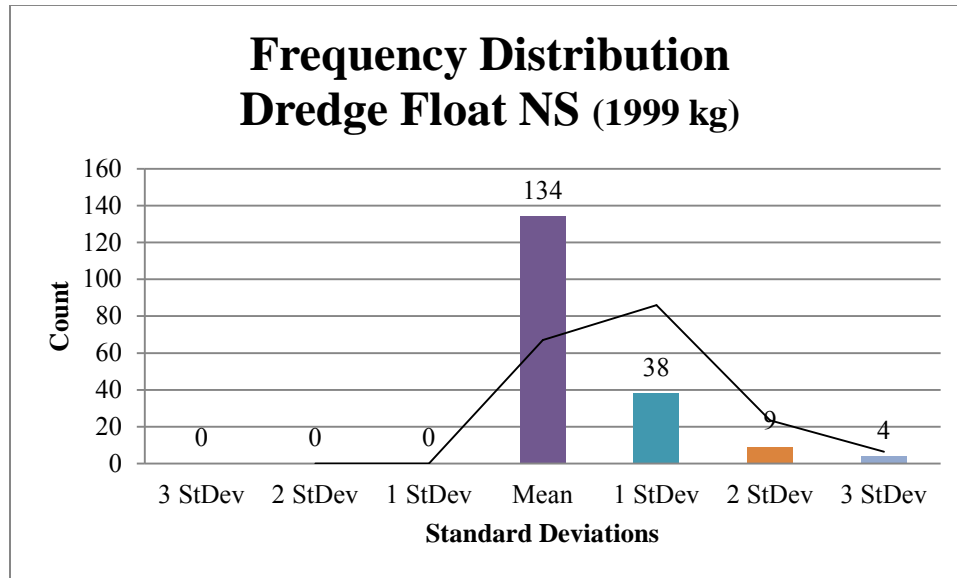
Figure IV-59. Frequency distribution for site Dredge Float NS calculated at1999 kg.

Table IV-117
Frequency distribution amounts per standard deviation for Dredge Float NS calculated at 1999 kg.

Sort Method	Frequency
3 StDev	0
2 StDev	0
1 StDev	0
Mean	134
1 StDev	38
2 StDev	9
3 StDev	4

Table IV-118
Magnetic moment statistics for site Dredge Float NS calculated at 1999 kg, sample size N=305, including the empirically derived magnetic moment per unit mass (σ) value. All σ units are $\frac{emu}{g}$.

Mean
59.806
Median
59.279
Standard Deviation
71.179
Range
685.287
Empirical σ Value
59.279

BOCA CHITA PONTOON SOUTH
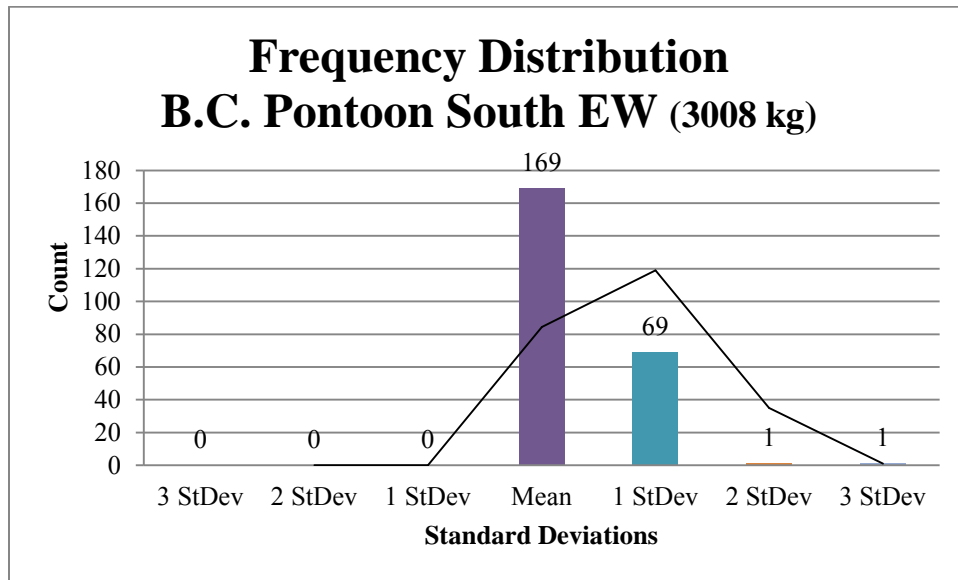
Figure IV-60. Frequency distribution for site Boca Chita Pontoon South EW calculated at3008 kg.

Table IV-119
Frequency distribution amounts per standard deviation for Boca Chita Pontoon South EW calculated at3008 kg.

Sort Method	Frequency
3 StDev	0
2 StDev	0
1 StDev	0
Mean	169
1 StDev	69
2 StDev	1
3 StDev	1

Table IV-120
Magnetic moment statistics for site Boca Chita Pontoon South EW calculated at 3008 kg, sample size N=241, including the empirically derived magnetic moment per unit mass (σ) value. All σ units are $\frac{emu}{g}$.

Mean
93.482
Median
64.845
Standard Deviation
221.886
Range
2683.65
Empirical σ Value
64.845

Frequency Distribution
B.C. Pontoon South EW (3300 kg)
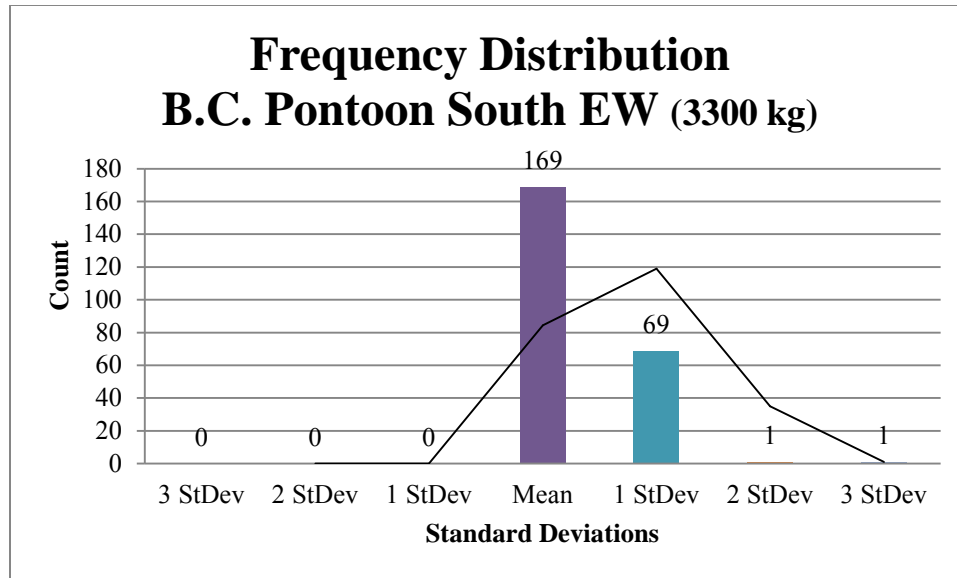
Figure IV-61. Frequency distribution for site Boca Chita Pontoon South EW calculated at 3300 kg.

Table IV-121
Frequency distribution amounts per standard deviation for Boca Chita Pontoon South EW calculated at 3300 kg.

Sort Method	Frequency
3 StDev	0
2 StDev	0
1 StDev	0
Mean	169
1 StDev	69
2 StDev	1
3 StDev	1

Table IV-122
Magnetic moment statistics for site Boca Chita Pontoon South EW calculated at 3300 kg, sample size N=241, including the empirically derived magnetic moment per unit mass (σ) value. All σ units are $\frac{emu}{g}$.

Mean
85.201
Median
59.101
Standard Deviation
202.229
Range
2445.91
Empirical σ Value
59.101
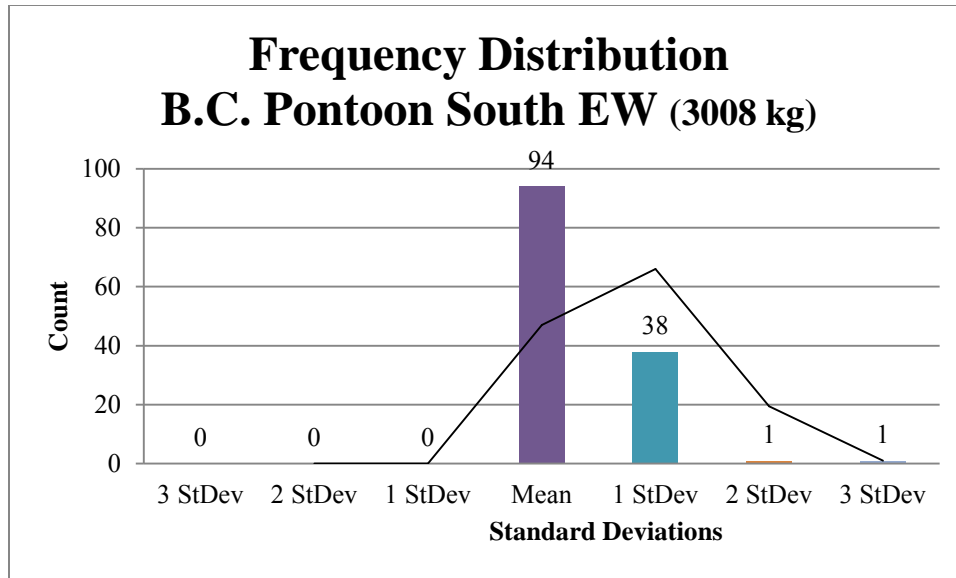
Figure IV-62. Frequency distribution for site Boca Chita Pontoon South NS calculated at 3008 kg.

Table IV-123
Frequency distribution amounts per standard deviation for Boca Chita Pontoon South EW calculated at 3008 kg.

Sort Method	Frequency
3 StDev	0
2 StDev	0
1 StDev	0
Mean	94
1 StDev	38
2 StDev	1
3 StDev	1

Table IV-124
Magnetic moment statistics for site Boca Chita Pontoon South NS calculated at 3008 kg, sample size N=136, including the empirically derived magnetic moment per unit mass (σ) value. All σ units are $\frac{emu}{g}$.

Mean
136.4
Median
63.959
Standard Deviation
269.232
Range
2132.67
Empirical σ Value
63.959
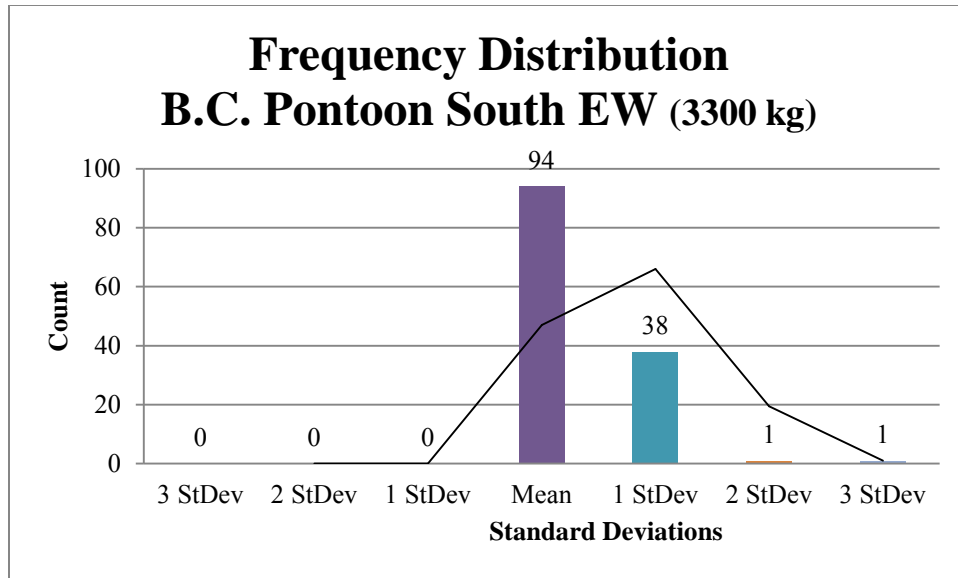
Figure IV-63. Frequency distribution for site Boca Chita Pontoon South NS calculated at3300 kg.

Table IV-125
Frequency distribution amounts per standard deviation for Boca Chita Pontoon South EW calculated at 3300 kg.

Sort Method	Frequency
3 StDev	0
2 StDev	0
1 StDev	0
Mean	94
1 StDev	38
2 StDev	1
3 StDev	1

Table IV-126
Magnetic moment statistics for site Boca Chita Pontoon South NS calculated at 3300 kg, sample size N=136, including the empirically derived magnetic moment per unit mass (σ) value. All σ units are $\frac{emu}{g}$.

Mean
124.317
Median
58.293
Standard Deviation
245.381
Range
1943.73
Empirical σ Value
58.293